UNIVERSITÀ
degli STUDI
di CATANIA

DEPARTMENT OF ELECTRICAL, ELECTRONIC AND COMPUTER ENGINEERING

PH.D. PROGRAMME IN SYSTEMS, ENERGETICS, COMPUTER, AND TELECOMMUNICATIONS ENGINEERING

Giuseppe Bua

Thermo-Mechanical Modelling of Power Electronics Packages and Experimental-Numerical Characterization of Materials under Static and Dynamic Loadings

Academic Supervisor: Prof. Giuseppe Mirone

Academic Co-supervisors: Prof. Gaetano Sequenzia
Prof. Raffaele Barbagallo

Industrial Co-supervisors: Prof. Michele Calabretta
Eng. Alessandro Sitta

PhD. Coordinator: Prof. Paolo Pietro Arena

Academic Year: 2024/2025

Table of Contents

Abstract 19

Introduction 21

Chapter 1: Thermal-mechanical modelling of a SiC-based power module. Effect of layers' deposition geometry on stress distributions 27

1.1 Materials and modelling approach 28

1.2 Results and discussion 34

1.2.1 Sharp edge model 34

1.2.2 Rounded edge model 36

1.2.3 Gradients of stress components through the thickness 37

1.3 Conclusions 39

Chapter 2: Global-Local Finite Element approach for the analysis of stress distributions 40

2.1 Materials and modelling approach for the Global Model 41

2.2 Modelling approach for the Local Model 44

2.3 Results and discussion 46

2.3.1 Assessment of the mesh refinement on stress distributions at local scale 46

2.3.2 Gradients through the thickness extracted from the local model 48

2.4 Application of the Global-Local FEM for assessing the influence of the defects (dry spots) induced from Resin Transfer Molding on local stresses 50

2.5 Conclusions 52

Chapter 3: Finite Element Modelling of the residual stress-state induced at the end of the Resin Transfer Molding process 53

3.1 Resin Transfer Molding Process 54

3.2 Materials and Modelling procedure for the simulation of package encapsulation 56

3.3 Results and discussion 63

3.3.1 Components of stress at different interfaces, evaluated at the maximum temperature 65

3.3.2 Components of stress at different interfaces, evaluated at the end of curing process (residual stresses) 70

3.3.3 Warpage behavior of the package at the end of curing process 74

3.4 Conclusions 76

Chapter 4: Models for the prediction of damage at the package's critical interfaces 78

4.1 Materials and modelling procedure 81

4.2 Results from single thermal cycle: Elastic vs Elastoplastic response 81

4.3 Damage 88

4.3.1 Cohesive Zone Model 88

4.3.2 Modified Tresca Damage Model 91

4.4 Results and discussions 93

4.4.1 Ductile damage of elastoplastic layers 98

4.4.2 Brittle damage of elastic layers 101

4.5 Sensitivity analysis of the Cohesive Zone parameters for the modelling of delamination in SiC-based power modules 106

4.5.1 Results and discussion 110

4.6 Conclusions 113

Chapter 5: Modelling of the mechanical behavior of a SiC-based power module subjected to spatial thermal gradients 115

5.1 Modelling procedure 116

5.1.1 Spatial gradients constant with time 117

5.1.2 Spatial gradient varying with time 118

5.2 Results and discussion 119

5.2.1 First case: spatial gradient of temperature constant with time 120

5.2.2 Second case: spatial gradient of temperature varying with time 125

5.3 Conclusions 129

Chapter 6: Quasi-static tensile response of Polycarbonate 131

6.1 Classical Methodologies for obtaining the tensile stress-strain curve of Polycarbonate round specimens 134

6.1.1 The uniaxial tensile test of Polycarbonate round specimens 135

6.2 Bridgman's Theory for correcting the true stress area-based curve into the material's flow curve 147

6.2.1 Experimental measurements of the necking curvature during the quasi-static tensile test 150

6.3 Finite Element Modelling of the tensile response of Polycarbonate at quasi-static rate 154

6.4 Uniaxial tensile test of Polycarbonate flat specimens 161

6.4.1 First necking and Generalized necking in Polycarbonate 169

6.5 Polycarbonate's material flow curve from the correction of Generalized Neck True curve 173

6.5.1 Finite Element Simulation of the mechanical response of Polycarbonate flat specimens and inverse calibration of the material's flow curve 179

6.6 Conclusions 185

Chapter 7: Dynamic tensile behavior of Polycarbonate 186

7.1 Dynamic tensile tests on Polycarbonate round specimens 187

7.1.1 The Split Hopkinson Tension Bar (SHTB) apparatus 190

7.1.2 Dynamic tensile tests at high strain rates: experimental setup 194

7.1.3 Results and discussion 204

7.2 Conclusions 209

Chapter 8: Mechanical characterization of Polycarbonate at low, intermediate, and high strain rates: combined rate-temperature effect on the post-necking plasticity 211

8.1 Implementation of the PC-DATS model and results from Finite Element modelling 227

8.2 Conclusions 234

Chapter 9: Tensile response of anisotropic sheet metals 236
9.1 Methodologies for the mechanical characterization of ductile sheet metals 237
9.2 Materials and experimental setup 244
9.3 Experimental data and results 247
9.4 Conclusions 253
Conclusions and main contributions of the present work 254
Appendix 266
Fortran Subroutine for the implementation of the Modified Tresca Damage Model 266
Marc Mentat uyield_surface user subroutine for the implementation of the PC-DATS model 268

List of figures

Figure 1: Schematic view of a power module (figure taken from [4]). 21

Figure 2:a) Schematic section of the modeled package (not in scale); b) Exploded axonometric view of the package. 30

Figure 3: Volumetric mesh with Tetra4 elements of the encapsulation. 31

Figure 4: Mesh discretization of copper lead frame, solder, and SiC layers with Hex8-7 elements. 32

Figure 5: a) In-plane view of the meshed Silicon Nitride frame; b) Particular view of the stacked TEOS and Si_3N_4 layers, along a transversal section passing through the diagonal direction of the die. 32

Figure 6: Scheme of the in-plane view of one package's corner. R_{int} and R_{ext} indicate the internal and external fillet radii of the passivation frame. 35

Figure 7: Distributions of the components of stress tensor, along the package's corner diagonal. a) Normal stress, parallel to x direction; b) Normal stress, parallel to y direction; c) Shear stress on the plane x-y; d) Von Mises Stress. 35

Figure 8: Comparisons between the in-plane normal stresses distributions, along the corner's diagonal direction in sharp edge and filleted edge models. These paths are referred to the following levels: a) Si_3N_4 middle plane; b) TEOS middle plane. The distributions were extracted at the maximum temperature (150 °C). 38

Figure 9: Axonometric view of the path plots extracted through the thickness and along the plane of the layers. 38

Figure 10: Components σ_y (a) and τ_{xy} (b) of the stress tensor, plotted through the layers' thickness: comparisons between sharp edge and filleted edge corner. 38

Figure 11: Global and local domain meshed models of the T2PAK power device. 45

Figure 12: Components of stress tensor extracted along the corner's diagonal direction of the passivation frame, at the maximum temperature. The plots refer to the SiC/TEOS interface (TEOS side). The graphs show the comparison between the results obtained from the following models: global model with "coarse mesh", global model with "fine mesh"; local model. 47

Figure 13: Schematic representation of the mesh refinement applied to the modelled subdomain. 47

Figure 14: Path plots through the thickness extracted on the local domain of the modelled package, at maximum temperature. a) discontinuous stress components; b) continuous stress components. 49
Figure 15: Global and local models used for the simulation of the dry spots. 50
Figure 16: Effect of dry spot on stress distributions. 51
Figure 17: Temperature-Time and Degree of Cure-Time representative diagrams for a curing process. 56
Figure 18: Simplified version of a quasi-static curing cycle. Sim1,2, and 3 highlight the time ranges at which all the three sub-analyses are run. 57
Figure 19: Mesh of a quarter model of the simulated package. 59
Figure 20: Flow curves and their fittings for copper [29] and polyimide [30]. 61
Figure 21: Schematic representation of the evolution of the epoxy resin Young's modulus during the curing cycle. The thermal cycle is subdivided in three different simulations indicated by arrows. A zeroing of the plastic strains in the resin takes place at the end of the first simulation. .. 62
Figure 22: a) Schematic representations of the paths extracted at six different interfaces. b) representation of normal and shear stress tensor components on the elementary material's cube: blue arrows indicate the stress components which are equal in each side of the same interface, while the black ones indicate the stress components acting just above or below a specific material. 64
Figure 23: Stress distributions at all interfaces along the paths given in Figure 22 at the peak temperature, T = 200 °C. 67
Figure 24: Minimum, average and maximum stresses along all considered interfaces at the peak temperature, T = 200°C. 68
Figure 25: Stress distributions at all interfaces along the paths given in Figure 22 at the end of cooling, T = 25 °C. 71
Figure 26: Minimum, average and maximum stresses along all considered interfaces at the end of the cooling stage of the curing cycle, T = 25 °C. 72
Figure 27: Distributions of plastic strains at the end of cooling phase of the thermal cycle, T = 25 °C. 73
Figure 28: a) Total equivalent plastic strain along X and Z at the interfaces Resin-SiC, Resin-Polyimide and Resin-Copper and b) History plot the Total equivalent plastic strain, Total elastic strain and Mises stress at the resin location (A), of maximum plastic deformation before the zeroing. 74
Figure 29: Contour plots out-of-plane displacement Uy at the a) peak temperature and a) at the end of cooling stage. 75

Figure 30: Path plots of the out-of-plane displacement at the middle section of the copper layer along the x-axis and z-axis, at the maximum temperature (top) and at the end of cooling stage (bottom).....76

Figure 31: (a) Interfaces at which the stress plots have been extracted. (b) Interface stresses: common (blue) and different (black) stresses between the two interface materials. 82

Figure 32: Comparison between the results obtained from the simulation with all purely elastic materials (dashed lines) and the one with copper, solder and polyimide considered as elastoplastic84

Figure 33: Identification of the critical points in the analyzed interfaces. 85

Figure 34: Single thermal cycle comparison between the results obtained from the simulation with all purely elastic materials (black lines) and the one with copper, solder and polyimide considered as elastoplastic materials (blue lines): Stresses histories in the critical points of the interfaces Copper/Solder_Copper/Resin (a), SiC/Solder (b), SiN/Poly (c), and Resin/Poly (d). 87

Figure 35: Qualitative representation of the bi-linear characteristic curve of the cohesive elements. 89

Figure 36: Fracture data normalized with respect to the uniaxial tensile strength value σcr: experimental fracture data from Morelle et al. (red squares) and Hu et al. (blue circles); MT criterion fracture locus according to Morelle et al. (dashed red line), Hu et al. (blue dotted line), and the present work (black solid line). 92

Figure 37: Elastoplastic simulation of the power module subjected to multiple thermal cycles: histories of plastic strain in the critical points of the elastoplastic layers: Copper a); Solder b); Polyimide c). 95

Figure 38: Elastoplastic simulation of the power module subjected to multiple thermal cycles: path plots of plastic strain, cycle by cycle, along the diagonal of the elastoplastic layers: Copper a); Solder b); Polyimide c). 96

Figure 39: Multiple thermal cycles elastoplastic simulation: comparison of the results implementing different solder constitutive curves (a) in terms of history of plastic strain in the critical point of the solder (b) and path plot of plastic strain, cycle by cycle, along the diagonal of the solder (c). 98

Figure 40: Histories of plastic strain and TF in the critical points of copper and polyimide. 99

Figure 41: Histories of plastic strain and TF in the critical point of solder considering different solder constitutive curves. 100

Figure 42: TF vs plastic strain histories in the critical points of solder, copper, and polyimide considering different solder constitutive curves. 101

Figure 43: Fracture data: experimental fracture data from Morelle et al. (red squares) and Hu et al. (blue circles); MT criterion fracture locus according to Morelle et al. (dashed red line), Hu et al. (blue dotted line), and the present work (black solid line).....102

Figure 44: MT Criterion with τ_{cr}=43.5 MPa, σ_{cr}=73.5 MPa: Path plot of the damage value after one cycle. 103

Figure 45: MT Criterion with different σ_{cr}: history plots of damage in four different nodes of the resin located in the critical area.....103

Figure 46: MT Criterion with σ_{cr}=181 MPa vs CZM: Damage contour plots at the end of the first heating and at the end of the first cycle in the elastic and elastoplastic simulations.....104

Figure 47: CZM: history plots of damage in two different nodes of the resin located in critical area. Comparison between elastic and elastoplastic simulations.....105

Figure 48: Global and local models used for the present analysis.....107

Figure 49: Example of simulation output with delaminated elements and damage plot. 109

Figure 50: Local simulations results: percentage of delaminated area versus %COD/MOD with the curves parametrized with the MOD. Gc is equal to 0.003 in all simulations. 110

Figure 51: Local simulations results: percentage of delaminated area versus MOD with the curves parametrized with the Gc. COD is between 0.005 and 0.05 in all simulations.....111

Figure 52: Local simulations results: percentage of delaminated area versus Gc with the curves parametrized with the MOD. COD is equal to 0.05 in all simulations.....112

Figure 53: Thermal histories measured at specific locations (up) and current cycles (down) imposed on a power module, during an active thermal cycle.(Image taken from [16]) 116

Figure 54: Spatial distribution of temperature in the two modeled cases: a) Constant spatial gradient; b) Time-dependent spatial gradient. 119

Figure 55: Paths and interfaces where stress components were extracted.....120

Figure 56: First case of spatial thermal gradient: stress components (y-axis) plotted along the interfaces (arc length in x-axis) considered in figure Figure 55, at t=50 s (mid-cycle).....122

Figure 57: First case of spatial thermal gradient: stress components (y-axis) plotted along the interfaces (arc length in x-axis) considered in Figure 55, at t=100 s (end of cooling cycle).....123

Figure 58: Distributions of equivalent plastic stains, along four elastoplastic interfaces, at mid-cycle (t=50s) and at the end of cooling phase......124

Figure 59: Second case of spatial thermal gradient: stress components (y-axis) plotted along the interfaces (arc length in x-axis) considered in Figure 55, at t=50 s (mid-cycle). 126

Figure 60: Second case of spatial thermal gradient: stress components (y-axis) plotted along the interfaces (arc length in x-axis) considered in Figure 55, at t=100 s (end of cooling). 127

Figure 61: Distributions of equivalent plastic stains, along four elastoplastic interfaces, at mid-cycle (t=50s) and at the end of cooling phase. 129

Figure 62: (a) Load-Time diagram from a quasi-static tensile test on Polycarbonate round specimen; (b) Plastic strain-Time history from the same test; (c) Frames taken from the recording of the tensile test. 139

Figure 63: Quasi-static (0.01 s^{-1}) tensile stress-strain curves for Polycarbonate round specimens, obtained from four different methodologies. The capital letters from A to D identify the instants of the test captured in Figure 62 c). 143

Figure 64: Summary of the Polycarbonate round specimen stress-strain curves at 0.01 $s^{-.1}$ 143

Figure 65: Comparison between the true stress-strain curves from elongation and area measurements, and the fitting exponential curve 48.5 exp(ε). 145

Figure 66: Area strain vs Global elongation strain for Polycarbonate round specimen at 0.01 s^{-1}. The capital letters from A to D identify the instants of the test captured in Figure 62 c). 146

Figure 67: Quasi-static tensile test on round specimen. Frame taken at total area-based strain of 0.46. The coordinates of the yellow points were manually extracted by the ImageJ software. .. 151

Figure 68: Specimen's contour points and their fitting with a polynomial function, taken at true strain area-based of 0.46. 151

Figure 69: a) Curvature radius vs plastic strain area-based diagram; b) a/R vs plastic strain area-based diagram. 152

Figure 70: Experimental measurements of a/R vs normalized true strain variable. 153

Figure 71: Polycarbonate's material curve at 0.01 s^{-1} and its relative true stress curve from tensile test on round specimens. 154

Figure 72: FEM Modelling of the quasi-static response of Polycarbonate round specimen: meshed axisymmetric model and prescribed boundary condition. 155

Figure 73: Finite Element Modelling of the elasto-plastic response of Polycarbonate at static rate: comparison between experimental data (yellow dots) and FEM results (black line). a) True stress global elongation-based curve; b) True stress area-based curve; c) Area strain vs Elongation strain diagram. 156

Figure 74: Qualitative comparison between quasi-static experiments and FEM results at four relevant instants. 157

Figure 75: Siebel correction vs New approximated correction of the true curve. The difference between the black line and the red dots represents the percentage difference between the first approximation (Siebel) true curve and the experimental one. 158

Figure 76: Comparison between the Finite Element results (black lines) and experimental data (yellow dots). The black solid line and the dashed one indicate, respectively, the results in output from the second approximation and the first approximation of the material's flow curve. 159

Figure 77: Polycarbonate definitive flow curve and its approximation by fitting function (43). 161

Figure 78: Polycarbonate dog bone specimens with rectangular cross section: a) Flat Small specimen; b) Flat Large specimen. 162

Figure 79: Static tensile test of Polycarbonate flat (small) specimen: a) Load vs time diagram; b) area-based strain vs elongation-based strain diagram; c) frames taken from the video recording of the test. 165

Figure 80: Polycarbonate flat (small) specimen tested at quasi-static rates: post-fracture image of the specimen. It is interesting to observe that the minimum resistant cross-section is smaller (red boundary) than the one estimated by assuming a rectangular shape (yellow boundary). 167

Figure 81: Comparison of the strain vs strain diagram for three different geometries: Flat Large (rectangular section with aspect ratio 2.5); Flat Small (rectangular section with aspect ratio 1.5); Round specimen. 168

Figure 82: Quasi-static tensile true stress-strain curves for Polycarbonate round and flat specimens: a) Area-based true curves; b) Elongation-based true curves. 169

Figure 83: First necking section (N1) and generalized one (Ng) during a quasi-static tensile test of Polycarbonate flat specimen. 171

Figure 84: Stages of deformation history experienced by the first necking (N1) and generalized necking section (Ng). 171

Figure 85: a) True stress-strain area-based from first necking and generalized necking. The instants A, B, C, D are referred to Figure 84; b) Strain vs Strain diagram from first necking and generalized necking. 172

Figure 86 : Schematic representation of the moving front of propagation during its approach with the generalized necking section (orange double arrow) (on the left); Bridgman correction factor vs. normalized curvature of the generalized necking section (on the right). 173

Figure 87 : Qualitative differences between flow curve and true curve. 175

Figure 88 : a) Polycarbonate's additive correction function; b) Gen. Neck true curve and flow curve of Polycarbonate at static rates. 176

Figure 89: Area-based strain vs Elongation-based strain for the assessment of the relevanrt points of the additive correction..... 177

Figure 90: Meshed specimens used for the present work: Flat Small and Flat Large. 179

Figure 91: Quasi-static tensile test of Polycarbonate flat specimens: comparison between FEM results (black line) and experimental data (yellow and red dots). Results related to the Flat Large geometry: a) True area-based curve; b) True elongation-based curve; c) Area strain vs elongation strain. Results related to the Flat Small geometry: c) True area-based curve; d) True elongation-based curve; e) Area strain vs elongation strain..... 182

Figure 92: Comparison between the specimen's shape predicted by the Finite Element simulation and the experimental profile in the two tested geometries: Flat Small (top); Flat Large (bottom)..... 183

Figure 93: Comparison between experimental data (yellow dots) and FEM results (black line) for the quasi-static tensile test on Polycarbonate Flat Small specimen (Generalized Necking): a) Generalized Necking true stress strain curve; b) Area-based strain vs Elongation-based strain (Gen. necking)..... 184

Figure 94: Specimen's profile during the propagation phase compared with the profile from FE simulation. 184

Figure 95: Experimental setup for the tests at intermediate strain rate (7 s^{-1}). 188

Figure 96: Tensile tests of Polycarbonate at 0.1 s^{-1}: a) true stress area-based curve; b) true stress elongation-based curve; c) area-based strain vs elongation-based strain..... 189

Figure 97: Tensile tests of Polycarbonate at 7 s^{-1}: true stress area-based curve. 189

Figure 98: Scheme of the Split Hopkinson Tension Bar used for the present work, at the INATECH laboratories (University of Freiburg)..... 194

Figure 99: M8 Threaded Polycarbonate specimen used for dynamic tests. 195

Figure 100: Force waves measurements during a plain pulse test. 197

Figure 101: Calibration curves of the strain gages: Input strain gage (on the top); Output strain gage (on the bottom). 199

Figure 102: Installation procedure of the strain gages on the bars. Note that the multimeter measures a nominal resistance of the strain gage of 350 Ω. 200

Figure 103: Experimental setup for the high strain rate dynamic tests at 1000 s^{-1}. 201

Figure 104: Forces vs time diagram during a tensile test on Polycarbonate round specimen with the Hopkinson bar apparatus. 202

Figure 105: True stress-strain curves for Polycarbonate round specimens at 1000 s^{-1}. a) True stress area-based curve; b) True stress elongation-based curve; c) area-strain vs elongation strain diagram. 203

Figure 106: Quasi-static and dynamic response of Polycarbonate: a) true stress area-based curve; b) true stress elongation-based curve; c) area-based strain vs elongation-based strain. 206

Figure 107: Temperature rising during the tensile tests at nominal strain rate of 0.1 s^{-1}. Comparison with other experimental data derived from compression tests on Polycarbonate. 206

Figure 108: Area-based strain rate histories: linear scale a) and logarithmic scale b) for each tensile test. 207

Figure 109: Measurements of the ratio diameter/necking radius of curvature in the post-necking regime, at different nominal strain rates. 209

Figure 110: Static and dynamic "fixed" flow stress curves of Polycarbonate compared with the corresponding true stress curves. 212

Figure 111: Tensile response of Polycarbonate at low, intermediate, and dynamic strain rates: comparison between the results from FE simulation (black line) with fixed flow curves and experimental data (orange, red, and blue dots). 214

Figure 112: Polycarbonate's material static flow curves at different fixed temperatures (G. Sell et al. [99]*).* 216

Figure 113: Static thermal softening functions of Polycarbonate at four fixed temperatures (from G' Sell et al. [99]*).* 217

Figure 114: Static thermal softening fitting surface and originating experimental data (yellow dots). 218

Figure 115: Comparison between the estimation of temperature rising using fixed TQ coefficient of 0.55 and experimental data. 220

Figure 116: Flow curves at fixed nominal strain rate (dashed lines) and Isothermal flow curves. 221

Figure 117: Dynamic Amplification of Polycarbonate vs true strain rate: a) True strain rate in linear scale; b) True strain rate in logarithmic scale. 222

Figure 118: Derivative of flow stress / Flow Stress ratio vs true strain diagram. 226

Figure 119: Derivative of flow stress/flow stress ratio vs true plastic strain: a) ratio plotted in quasi-static condition at room temperature; b) Effect of dynamic amplification on the slope of the flow curve; c) Effect of the static thermal softening; d) Effect of the adiabatic self-heating. 226

Figure 120: Partial view of the axisymmetric model of SHTB and specimen. 228

Figure 121: Comparison between the flow curves obtained by correcting the experimental true stress curves from the triaxiality effect (dotted curves) and the ones generated by the PC-DATS model, extracted at the center of necking section. 229

Figure 122: Polycarbonate flow curves generated by the PC-DATS model, extracted at the center of two different cross-section. 230

Figure 123: Comparison between the specimen's shape during the test at 1000 s^{-1} predicted by the PC-DATS model (on the top), and the experiment (on the bottom). The pictures are taken at an elongation strain of 0.40 231

Figure 124: Comparison between the results from FEM simulation (black line) using the PC-DATS model and the experimental data (orange dots) for the test at 0.1 s^{-1}. a) True stress area-based curve; b) True stress elongation-based curve; c) area strain vs elongation strain diagram; d) True strain rate history 232

Figure 125: Comparison between the results from FEM simulation (black line) using the PC-DATS model and the experimental data (red dots) for the test at 7 s^{-1}. a) True stress area-based curve; b) True stress elongation-based curve; c) area strain vs elongation strain diagram; d) True strain rate history 232

Figure 126: Comparison between the results from FEM simulation (black line) using the PC-DATS model and the experimental data (blue dots) for the test at 1000 s^{-1}. a) True stress area-based curve; b) True stress elongation-based curve; c) area strain vs elongation strain diagram; d) True strain rate history 233

Figure 127: Schematic representation of the rectangular specimen cut from metallic sheet. 238

Figure 128: Comparison between the local axial strain distribution, the averaged value (true strain), and the DIC local peak strain in three different cross section geometries: a) thin specimen; b) w/t such that $\varepsilon_{DIC}=\varepsilon_{True}$; c) thick specimen. 240

Figure 129: Anisotropic straining of cross-sections: thinning rate smaller (left side) or greater (right side) than isotropic shrinking ratio. 241

Figure 130: Effect of localized necking on the minimum cross-section of the specimen. .. 243

Figure 131: Specimen’s geometry. The thickness t depends on the tested sheet. 246

Figure 132: a) Experimental setup used for the tests; b) frontal view of the painted specimen; c) lateral view of the specimen. 246

Figure 133: Post-mortem images of the specimens' fracture surface. The yellow region distinguishes the net resistant cross-section from the gross one. 247

Figure 134: Experimental data of thickness ratio vs width ratio during a tensile test on anisotropic sheet metal. The diamond dots are related to the pre-necking phase of the material. The green triangles are obtained from the post-mortem measurement of the specimen's fracture surface. The red line is the fitting of the pre-neck data using the power-law having the exponent equal to the Lankford coefficient R. 248

Figure 135: Experimental data of the thickness vs width evolution during the tensile tests performed on CR04 steel. The black circles were obtained from the direct measurements of the thickness by means of a lateral camera. The trend of the black circles deviates from the power-law fitting (constant anisotropic coefficient). The violet dashed line corresponds to a power-law fitting with a variable anisotropic exponent z. 249

Figure 136: True stress-strain curves for the tested anisotropic sheets, obtained from the five approaches proposed in the present work 251

Figure 137: Mean values and corresponding scattering of the necking strain and failure strain estimated by the five approaches proposed in this work. 252

Figure 138: Comparison between the Lankford coefficient derived from elongation and width measurements (blue diamonds), DIC strain measurements (yellow squares), and power-law fitting (red line). 252

List of Tables

Table 1: Electronic package layers' thermal-mechanical properties. 29
Table 2: Summary of the layers' geometric dimensions. 29
Table 3: Contact Table indicating the rigid constrains between adjacent layers. 33
Table 4: Geometric dimensions of the layers of T2PAK power module. 41
Table 5: Details about the discretization of the three layers: SiC, TEOS and Si_3N_4 in the global models. 42
Table 6: Details of the mesh discretization for the local model. 45
Table 7: Main features of the elements discretizing the simulated quarter of power module. 59
Table 8: Linear thermal-mechanical properties of the layers at ambient temperature. 61
Table 9: Cohesive Zone parameters for the copper/resin interface, according to the work of Krieger et al. [66]. 90
Table 10: Cohesive Zone parameters given in input to the Marc Mentat software, for the present work. 91
Table 11: Shape parameter μ from Morelle et al. [68], Hu et al. [67], and used in this work. 92
Table 12: Cohesive Zone parameter sets: MOD, COD, Gc, and σ_{max}, used for the sensitivity analysis. 109
Table 13: Polycarbonate material's constant for the equation (43). 160
Table 14: Additive Correction parameters used for the determination of the material's flow curve. 180
Table 15: Experimental results of the plain pulse tests. 197
Table 16: Polycarbonate flow curves' parameters for the equation (43), at each nominal strain rate. 212
Table 17: Mechanical properties of the four tested steels provided by the manufacturer. 245
Table 18: Chemical composition of the four tested steels. 245
Table 19: Anisotropy and distortion parameters of the four tested steels. 249

List of published or work-in-progress articles

1. Mirone, G.; Barbagallo, R.; Bua, G.; La Rosa, G. Finite Element Simulation and Sensitivity Analysis of the Cohesive Parameters for Delamination Modeling in Power Electronics Packages. *Materials* **2023**, *16*, 4808, doi:10.3390/ma16134808.

2. Mirone, G.; Barbagallo, R.; Bua, G.; De Caro, D.; Ferrea, M.; Tedesco, M.M. A Simple Procedure for the Post-Necking Stress-Strain Curves of Anisotropic Sheet Metals. *Metals* **2023**, *13*, 1156, doi:10.3390/met13071156.

3. Mirone, G.; Barbagallo, R.; Bua, G.; Caro, D.D.; Ferrea, M.; Tedesco, M.M. True Stress-Strain Identification Accounting for Anisotropy of Sheet Metals. In Proceedings of the IOP Conference Series: Materials Science and Engineering; May 1 **2024**; Vol. 1306, p. 012005.

4. Mirone, G.; Barbagallo, R.; Bua, G.; Sitta, A.; Calabretta, M.; Sequenzia, G. Thermal-Structural Modeling of Power Electronic Package: Effects of Deposition Geometry and Dry Spot on the Stress Distributions. *IOP Conf. Ser.: Mater. Sci. Eng.* **2024**, *1306*, 012012, doi:10.1088/1757-899X/1306/1/012012.

5. Mirone, G.; Barbagallo, R.; Bua, G. Static and Dynamic Tensile Behaviour of Polycarbonate Connected to the Deforming Specimen Shape. In Proceedings of the IOP Conference Series: Materials Science and Engineering; May 1 **2024**; Vol. 1306, p. 012006.

6. Mirone, G.; Barbagallo, R.; Bua, G.; Licignano, P.; Tedesco, M.M. An Enhanced Approach for High-Strain Plasticity in Flat Anisotropic Specimens with Progressively Distorting Neck Sections. *Metals* **2024**, *14*, 578, doi:10.3390/met14050578.

7. Barbagallo, R.; Mirone, G.; Landi, L.; Bua, G. Tensile Behavior of Polycarbonate: Key Aspects for Accurate Constitutive Modelling and Simulation. *Applications in Engineering Science* **2024**, *18*, 100183, doi:10.1016/j.apples.2024.100183.

8. Mirone, G.; Barbagallo, R.; Bua, G. Experimental Characterization and Plastic Modeling of Polycarbonate at Static and Dynamic Rates. *International Journal of Impact Engineering* **2025**, *203*, 105329, doi:10.1016/j.ijimpeng.2025.105329.

9. Mirone, G.; Barbagallo, R.; Corallo, L.; Bua, G.; La Rosa, G.; Fargione, G.; Giudice, F. Nonlinear Elastoplastic Response and Damage Modeling in Power Electronics Packages Under Thermal Cycling. In Proceedings of the AIAS 2024; MDPI, April 16 **2025**; p. 50.

10. Mirone, G.; Corallo, L.; Barbagallo, R.; Bua, G. Modelling of residual stress, plastic deformation, and permanent warpage induced by the resin moulding process in SiC-based power modules, *Energies*, **2025**, 18, 5364, https://doi.org/10.3390/en18205364.

11. Barbagallo, R.; Bua, G.; Costanza, G.; Giudice, F.; Mirone, G.; Sili A.; Tata, M.E. Theoretical-experimental investigation on mechanical response of Al honeycomb sandwich under static compression and ballistic impact, **2025** (*work in progress*).

Abstract

Power modules are electronic devices employed for the conversion of electrical energy across a wide range of application fields. These systems are composed of multiple layers of different materials (e.g., metals, ceramics, and polymers) capable of operating under conditions of high voltages and currents.

The dissipation of electrical power into heat induces significant cyclical temperature variations within the device, often on the order of hundred degrees. The thermo-mechanical mismatch among the layers is the primary cause of stresses and thermal strains that, in many cases, lead to delamination phenomena at critical interfaces, accumulation of plastic strain and, consequently, ductile damage, as well as brittle fracture in the semiconductor layer or in the encapsulating resin.

Over the years, Finite Element (FE) simulations have gained considerable relevance in industrial practice for modeling stress distributions and damage mechanisms in power modules, enabling predictive assessments of the average number of operating cycles a device can withstand before failure. The accuracy of FEM simulations of power packages strongly depends on the accuracy of the methodologies for characterizing the mechanical response of the constituent layers, both in the elastic and plastic regimes, while accounting for the effects of temperature and strain rate.

This doctoral thesis is structured into two main parts. The first part is entirely devoted to the thermo-structural numerical modeling of SiC-based power modules for automotive applications. Numerical simulations were employed to characterize the critical interfaces through the accurate analyses of the stress distributions. Specifically, the following aspects were investigated: the effect of deposition geometry of passivation layers on local stress distributions; permanent deformations and residual stresses arising from specific steps of the manufacturing process; delamination models and ductile/brittle damage mechanisms; and, finally, the comparison between purely elastic and elastoplastic responses.

The accuracy of the results delivered by the Finite Element Analyses of power modules are strongly influenced by the constitutive material models implemented to simulate the mechanical behavior of each layer of the package. Actually, the first part of my PhD activity was generally focused on demonstrating the importance of properly including the nonlinear elastoplastic response of copper, solder and polyimide layers in simulating the thermomechanical behavior of Power electronics devices, whereas most simulations in the current literature still rely on first-approximation linear elastic approaches. Therefore, the second part of this doctoral thesis is focused on the

investigation of experimental-numerical methodologies for characterizing the tensile response of structural materials subjected to static and dynamic strain rates. Specifically, the plastic response of Polycarbonate and anisotropic sheet metals is deeply examined, connecting their peculiar deformation mechanisms, in the post-necking regime, to the corresponding true stress-strain curve and the material flow curve. Although the specific materials investigated in the second part of the thesis (i.e., Polycarbonate and anisotropic sheets) are not directly employed in the manufacturing of the Power Electronics packages analyzed, the distinctive features characterizing their elastoplastic response, such as the pronounced hardening-softening behavior observed in Polycarbonate and the inherent anisotropy of the rolled sheets, provide critical insights. Such knowledge is suitable to refine the constitutive modeling approaches for the analogous behaviors exhibited by the metallic and polymeric layers present within the modules, thereby enhancing the overall simulation reliability.

Introduction

APPLICATIONS OF MODULES AND STATE OF THE ART

During the last decade, the progressive electrification of transport systems, the diffusion of renewable energy sources, and the increasing demand for high-performance and reliable electronic systems have prompted significant innovation in the field of power conversion technologies. Among these, power modules have emerged as central components in power electronic architectures due to their ability to control, convert, and transmit large amounts of electrical energy with high efficiency and compactness.

These devices are widely employed in hybrid and electric vehicles, high-speed rail systems, wind turbines, photovoltaic inverters, industrial drives, aerospace applications, and data centers. Power modules are complex multi-material and multi-layered systems, designed to ensure optimal thermal management, mechanical integrity, and electrical performance in harsh operating environments. Power modules integrate various functional layers assembled into a compact encapsulated device. The core of a Power Module is the semiconductor die, fabricated from materials such as *Silicon* (Si), *Silicon Carbide* (SiC), or *Gallium Nitride* (GaN) [1–3].

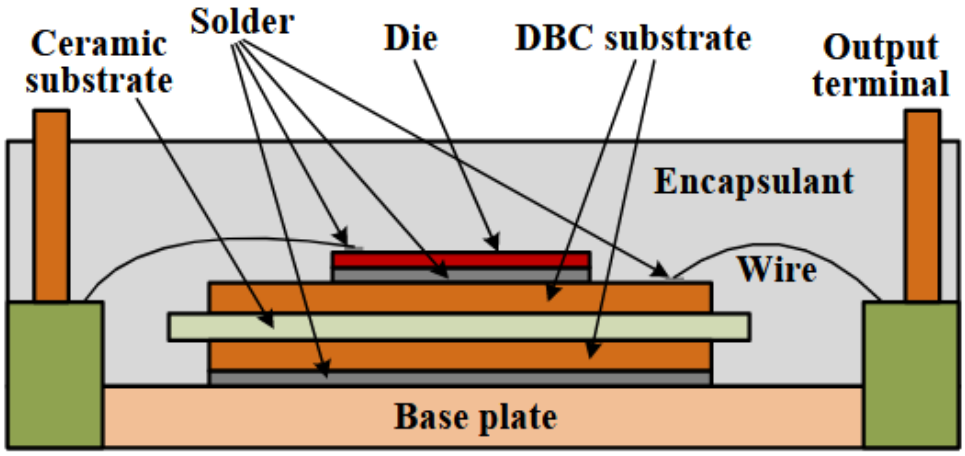


Figure 1: Schematic view of a power module (figure taken from [4]).

In recent years, the transition toward wide bandgap semiconductors like SiC and GaN has become increasingly widespread due to their superior breakdown voltage, thermal conductivity, switching frequency, and overall performance in high-power and high-temperature applications [1]. The adoption of wide bandgap semiconductors, while offering substantial performance advantages, introduces further complications in thermal management and packaging reliability. The SiC-based dies, for instance, can operate at junction temperatures exceeding 300 °C [5], but the actual generation of materials commonly employed in the packages, especially solder alloys and epoxy resins, are limited by their thermal stability and degradation behavior up to 150 °C-200 °C. Traditional solders tend to soften or creep under such high temperatures, leading to premature failure, while the epoxy compounds experience the transition from glassy to rubbery state, losing their mechanical integrity and adhesion.

The semiconductor dies are bonded to copper-based substrates using the so-called *die attach* process, in which solder alloys such as SnAg or PbSnAg are typically employed, or alternatively, silver-based sintering pastes that offer improved thermal and mechanical performances.

The substrate on which the dies are mounted usually consists of a ceramic insulating core, made of materials like alumina (Al_2O_3), aluminum nitride (AlN), or silicon nitride (Si_3N_4), jointed between two copper plates by means of manufacturing processes such as the *Direct Bonded Copper* (DBC) [6] or the *Active Metal Brazing* (AMB) [7]. The ceramic layer of a substrate ensures electrical insulation while providing thermal conductivity and mechanical stiffness [8]. The upper copper layer of the substrate features patterns to electrically interconnect multiple dies, forming conductive pathways that are linked to the module terminals through *wire bonding*, *clip bonding*, or advanced *direct lead bonding techniques* [9,10].

The entire metallic-ceramic-semiconductor assembly is encapsulated using an epoxy molding compound (EMC), typically applied through a transfer molding process, which provides protection against humidity, contaminants, and other corrosive agents while contributing to electrical insulation [11].

Beneath the substrate lies a *Thermal Interface Material* (TIM) layer, often composed of thermally conductive pastes or compliant compounds, that facilitates heat transfer between the substrate and a metallic baseplate. The baseplate, typically made of copper or metal matrix composites like aluminum silicon carbide, acts both as a mechanical support and as a thermal interface to external heat sinks or cooling systems [12].

This vertically stacked architecture, while ensuring compactness and high performance, introduces numerous structural integrity challenges arising from the mismatch of material properties across the layers. In particular, the coefficients of thermal expansion and elastic moduli differ significantly between copper, ceramics, encapsulants, and solders, leading to the accumulation of stresses and strains during thermal excursions [13,14]. These considerations explain why the mechanical design and the mechanics of materials have gained a paramount importance in the multi-physics design of power electronics, which was likely unthinkable a decade ago.

The analysis of the mechanical response of power modules and the number of operating cycles they can withstand before failure is carried out by testing these devices on special benches that allow them to be cyclically cooled and heated at a controlled rate. The thermal cycles used for reliability testing are classified as: *passive cycles* and *active cycles*.

MECHANICAL-STRUCTURAL ISSUES AND CHALLENGES

During a passive thermal cycle imposed to power module, in which the device is tested in a climatic chamber, the temperature may change from -65°C to 150°C or higher at a quasi-static rate (≈ 0.1 °C/s), reproducing the operating conditions encountered in harsh environments [15].

On the contrary, an active thermal cycle involves repeatedly heating and cooling the power module by applying controlled electrical power. This causes the device to heat up from the inside and then cool down, simulating real operating conditions. During these cycles, the temperatures at different points of the device are monitored to evaluate how heat flows through the system and how the module reacts over time. This type of testing helps assess the long-term reliability of the module under realistic working conditions [16].

During each thermal cycle, ductile materials such as copper or solder undergo plastic deformation once their yield strength is exceeded, while brittle layers such as ceramics and epoxy may develop microcracks due the reaching of a critical stress states [17,18].

The accumulation of plastic strain over multiple cycles results in permanent warpage, a bending of the entire package that compromises the planarity of the leads and induces residual stresses within the package. Moreover, cyclic thermal loading induces fatigue damage in solder joints and sintered layers, where stresses are concentrated at geometric or material discontinuities. These regions are prone to damage initiation, including delamination, void growth, and crack propagation, which can eventually compromise the module's thermal performance and electrical isolation [19–21].

Another failure mechanism in power modules is the *delamination*, particularly problematic at interfaces with high thermal-mechanical mismatch, such as the die-encapsulant or copper-encapsulant boundaries, where tensile and shear stress gradients are most pronounced [22,23].

MECHANICS OF MATERIALS FOR POWER ELECTRONICS

Addressing these failure mechanisms requires a combination of robust experimental techniques and predictive numerical modeling. Finite Element Method (FEM) simulations have become indispensable tools in the design and validation of power modules, allowing engineers to predict, with a certain approximation: stress evolution, thermal gradients, plastic strain accumulation, and potential sites of damage initiation under realistic loading scenarios. Advanced FEM models incorporate nonlinear temperature-dependent material behavior, including elasto-plasticity, creep, viscoelasticity, and damage. In order to ensure accurate numerical predictions, an extensive material characterization is required. The campaign of materials' characterization includes uniaxial tensile tests on metals at room and high temperatures; creep tests on solder joints to evaluate the time-dependent strains; Dynamic Mechanical Analysis (DMA) on EMCs to evaluate the storage and loss moduli variation, glass transition temperature, and coefficient of thermal expansion.

CONTEXTUALIZATION OF THE THESIS

The first part of this doctoral thesis is devoted to the development and application of advanced finite element modelling (FEM) procedures for simulating the thermo-mechanical response of silicon carbide (SiC)-based power modules subjected to both passive and active thermal cycling. The research activity regarding the modelling of power modules has been carried out within the framework of my industrial PhD program funded by STMicroelectronics (STM), a leading international company in the fields of Microelectronics and Power Electronics.

The first part of the thesis is structured into five chapters, each addressing a specific aspect of the modelling process. Following a review of the state of the art and of the main reliability issues related to power modules, the numerical methodologies adopted in this work are discussed. The work is focused on the simulation of cyclic thermal loading, both passive and active, and to the resulting analysis of stress and strain distributions in the constituent materials and at the critical interfaces of the package. Attention is then devoted to the modelling of damage mechanisms, including ductile and

brittle failure of the layers, as well as interfacial delamination, which represent some of the most critical degradation phenomena affecting the long-term reliability of power electronic packages.

It is noteworthy that the accuracy of the results delivered by the Finite Element Analyses of power modules are strongly influenced by the constitutive material models implemented to simulate the mechanical behavior of each layer of the package. Actually, the first part of my PhD activity was generally focused on demonstrating the importance of properly including the nonlinear elastoplastic response of copper, solder and polyimide layers in simulating the thermomechanical behavior of Power electronics devices, whereas most simulations in the current literature still rely on first-approximation linear elastic approaches. Therefore, the second part of this doctoral thesis is focused on the investigation of experimental-numerical methodologies for characterizing the tensile response of structural materials subjected to static and dynamic strain rates. Specifically, the plastic response of Polycarbonate and anisotropic sheet metals is deeply examined, connecting their peculiar deformation mechanisms, in the post-necking regime, to the corresponding true stress-strain curve and the material flow curve. Although the specific materials investigated in the second part of the thesis (i.e., Polycarbonate and anisotropic sheets) are not directly employed in the manufacturing of the Power Electronics packages analyzed, the distinctive features characterizing their elastoplastic response, such as the pronounced hardening-softening behavior observed in Polycarbonate and the inherent anisotropy of the rolled sheets, provide critical insights. Such knowledge is suitable to refine the constitutive modeling approaches for the analogous behaviors exhibited by the metallic and polymeric layers present within the modules, thereby enhancing the overall simulation reliability.

The characterization of Polycarbonate under quasi-static and dynamic strain rate conditions has represented a significant activity of my doctoral research, conducted largely at the University of Catania and further pursued during my period as a Visiting PhD Student at the INATECH laboratories of the University of Freiburg, Germany.

STRUCTURE OF THE THESIS

Chapter 1 focuses on the FEM simulation of four different design variants of a reference power modules, assessing the influence of the layer deposition geometry on the local stress distributions within the device. This section is followed, in Chapter 2, by a detailed sensitivity analysis on the mesh, exploring the effects of mesh refinement on the accuracy in predicting the stress distributions. In this context, a Global-Local FEM strategy is presented for evaluating the local stress field in a

region of interest, by modelling only a subdomain of the complete power package, thereby reducing computational cost while preserving accuracy in critical regions.

Chapter 3 is dedicated to the mechanical modelling of the Resin Transfer Molding (RTM) process, which is used for the encapsulation of the internal layers. Particular attention is given to the mechanical interaction between the copper-solder-die subassembly and the encapsulating resin, which undergoes polymerization and evolves its thermo-mechanical properties during the curing stage of the RTM process.

Chapter 4 addresses the damage analysis of power modules at selected critical interfaces. In this framework, damage models are described and implemented, including those suitable for ductile and brittle materials, as well as interface damage phenomena such as delamination or debonding.

Chapter 5 deals with the thermo-mechanical modelling of power modules subjected to spatially varying thermal gradients with a spherical distribution.

In Chapter 6 the elastoplastic characterization of the tensile response of Polycarbonate at static rate is discussed, posing particular attention to its deformation mechanism in round and rectangular specimens. Two methodologies for correcting the experimental true stress-strain curves into the material's flow curve are proposed in the present work.

Chapter 7 extends the investigation of the mechanical response of Polycarbonate under dynamic loadings. The tensile tests performed at low, intermediate, and high strain rates are accurately discussed and the resulting true stress-strain curves are shown and corrected into the material's flow curve, by applying the same methodologies proposed in Chapter 6.

In Chapter 8, a novel material model is proposed for Polycarbonate, comprehending the coupled effect of temperature and strain rate on its mechanical response.

Finally, in Chapter 9, the investigation of the mechanical response of sheet metals is discussed, as well as an enhanced approach for extending the true stress-strain curve in the post-necking region, accounting for anisotropy and high strain distortion of the specimen's cross section.

A significant part of the methodologies and results reported in this doctoral thesis have already been published in peer-reviewed journals and presented at national conferences [13,14,24].

Chapter 1: Thermal-mechanical modelling of a SiC-based power module. Effect of layers' deposition geometry on stress distributions

In this chapter the Finite Element modeling procedure of a part of a whole power module will be described. It is formed, from the bottom to the top, by a copper lead frame, a PbSnAg solder alloy, a SiC (Silicon Carbide) based die, two passivation layers: TEOS (Tetra-ethyl-orthosilicate) and Si_3N_4 (Silicon Nitride), and the encapsulating material. The encapsulation is realized by a thermosetting epoxy resin, filled with silica (Epoxy Molding Compound, or briefly EMC). The filling particles aim to improve the mechanical strength of the resin and tend to increase its glass transition temperature up to 150 °C.

The aim of this work is the assessment of the effect caused by the deposition geometry of the edge termination structures, which are regions designed to mitigate the effect of electric field crowding (i.e., the corners of TEOS and Si_3N_4 layers), on the local stress distributions.

In power modules, passivation layers play a crucial role in electrically isolating the die from the external environment, providing a higher degree of protection than that offered by epoxy resin encapsulation alone. These layers, such as Si_3N_4, are deposited directly onto the die as thin films, typically on the order of micrometers, using advanced techniques such as Chemical Vapor Deposition (CVD).

Si_3N_4 is particularly valued for its high dielectric strength (approximately 20 MV/cm[1]), to effectively suppress electric field crowding near the edges of the die. However, in applications where the package is subjected to significant thermal cycling, the mismatch in thermo-mechanical properties between the passivation layers, the underlying die, and the overlying resin can give rise to thermal stresses. These stresses may, in turn, lead to delamination phenomena or the formation of microcracks within the passivation stack.

In a manner analogous to electric field distribution, mechanical stress components can also become highly localized and amplified, depending on the geometry of the passivation layer deposition. It is well established in the fields of Solid Mechanics and Fracture Mechanics that rounded

[1] Value taken from the datasheet available at the following link: https://www.azom.com/properties.aspx?ArticleID=53

or filleted geometries serve to mitigate such local stress concentrations. In this study, four finite element analyses (FEM) were carried out to model SiC-based power modules featuring variant geometries of the passivation layers. In particular, three models were developed with rounded in-plane geometries for the TEOS and Si_3N_4 layers, and were compared against a reference model characterized by sharp-edged passivation layers of identical material composition and thickness. To evaluate this geometrical effect, the stress distributions within the passivation layers were extracted during the post-processing phase of the simulations. The modelling procedure and the results reported in the present chapter have already been published in the conference paper entitled *Thermal-Structural Modeling of Power Electronic Package: Effect of Deposition Geometry and Dry Spot on the Stress Distributions* [13].

1.1 Materials and modelling approach

The simulated model is supposed to be subjected to a passive quasi-static heating between -65 °C and 150 °C. According to the JEDEC standard [15], a passive thermal cycle consists of a heating/cooling cycle completed in one hour, imposing a temperature change rate of approximately 15 °C/min in the climatic chamber. Tests in the climatic chamber are conducted with a controlled heating rate to avoid thermal transients within the device. Under this hypothesis, it is then reasonable assuming that all the points are in thermal equilibrium for each time step, and dynamic transient is not taken into account.

In this modelling, it is also hypothesized that all the possible mechanical effects derived from previous manufacturing processes on the package (e.g., soldering, resin molding or chemical deposition of the passivation layers) are neglected at the temperature of -65 °C. In this case, the initial temperature of the heating ramp is assumed as *stress-free temperature*, that is the temperature at which the package is totally unstressed and undeformed.

As first approximation, all the material properties for each layer are assumed to be linear, elastic, isotropic, and temperature independent. Their thermal-mechanical properties are summarized in the Table 1[2].

[2] The mechanical properties of the layers at room temperature (25 °C) were made available by STMicroelectronics company.

	Elastic Modulus [MPa]	Poisson's ratio [-]	Coefficient of Thermal Expansion [10^{-6} °C^{-1}]
Copper	125000	0.3	17.5
PbSnAg solder	5600	0.4	29
SiC	410000	0.28	4
Si_3N_4	300000	0.29	3.4
TEOS	59000	0.25	1
EMC	24000	0.34	12

Table 1: Electronic package layers' thermal-mechanical properties.

The model has the following dimensions: 14.5 mm x 10 mm x 5 mm. The solder, the die, and the two passivation layers have a square shape with a 3.5 mm edge. Their thicknesses are respectively: 45 μm; 180 μm; 1.6 μm for the TEOS layer and 1 μm for the Si_3N_4 layer. The two passivation layers are deposited are deposited on the SiC as two stacked frames featuring a square cavity with an edge equal to 2.85 mm. During the resin transfer molding process, the EMC has the possibility to fill this cavity, adhering on the top of the SiC die. As explained before, the die is directly soldered on the copper lead frame, having the dimensions of 12.5 mm x 8 mm x 1.27 mm. These dimensions are reported in Table 2, accompanied by two schematic overviews of the modeled package.

	In-plane dimensions [mm]	Thickness [μm]
Copper	12.5 x 8	1270
PbSnAg solder	3.6 x 3.6	45
SiC	3.6 x 3.6	180
Si_3N_4	3.6 x 3.6	1
TEOS	3.6 x 3.6	1.6
EMC	14.5 x 10	5000

Table 2: Summary of the layers' geometric dimensions.

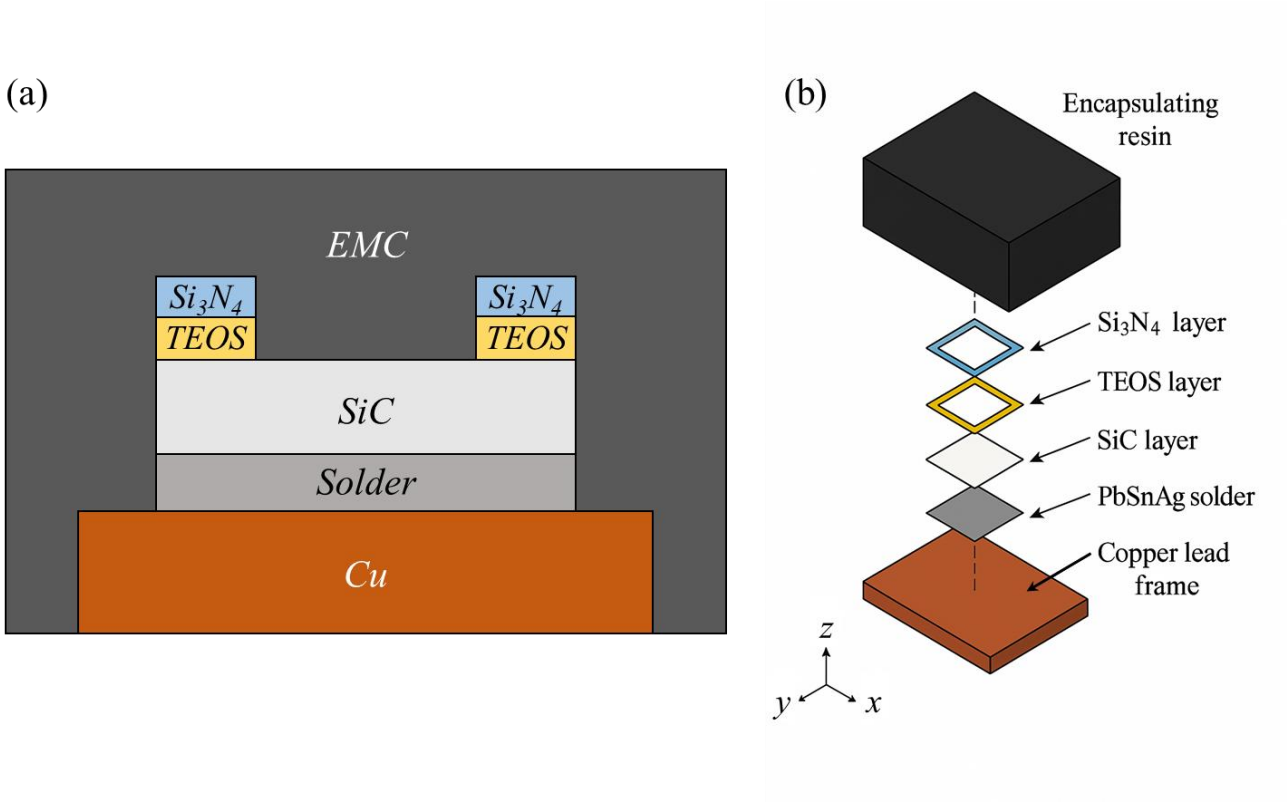


Figure 2:a) Schematic section of the modeled package (not in scale); b) Exploded axonometric view of the package.

The Finite Element simulations have been carried out on the Hexagon software MSC Marc Mentat ® v2023.4. In order to assess the effect of the deposition geometry of the TEOS and Si_3N_4 layers on local stress distributions, four models have been created: a reference model with all sharp corners, and three variants with round corners. The modelling procedure for the package with sharp corners is described below; the same approach applies to the other variants.

Since the thicknesses of the TEOS and Si_3N_4 layers are thousand times smaller than the encapsulating resin, a crucial aspect during the mesh discretization is combining different subdivision modes (e.g., coarse/fine meshing, non-coherent meshing between adjacent layers) and element formulations (e.g., solid or planar elements) for each material, controlling the total number of elements and consequently reducing the computational cost of the modelling. The cartesian axes have been fixed maintaining the plane x-y parallel to the layers, while the z direction is orthogonal to them.

The package's encapsulation has been discretized by the volumetric Patran auto-mesher using tetrahedral elements with 4 nodes and full integration formulation (Tetra4-134 in Marc). As shown in Figure 3, the mesh tends to densify toward the center of the package, in the region at the interface with the die (the maximum mesh density is 44 elements/mm^2), where the evaluation of stress distributions needs to be as accurate as possible.

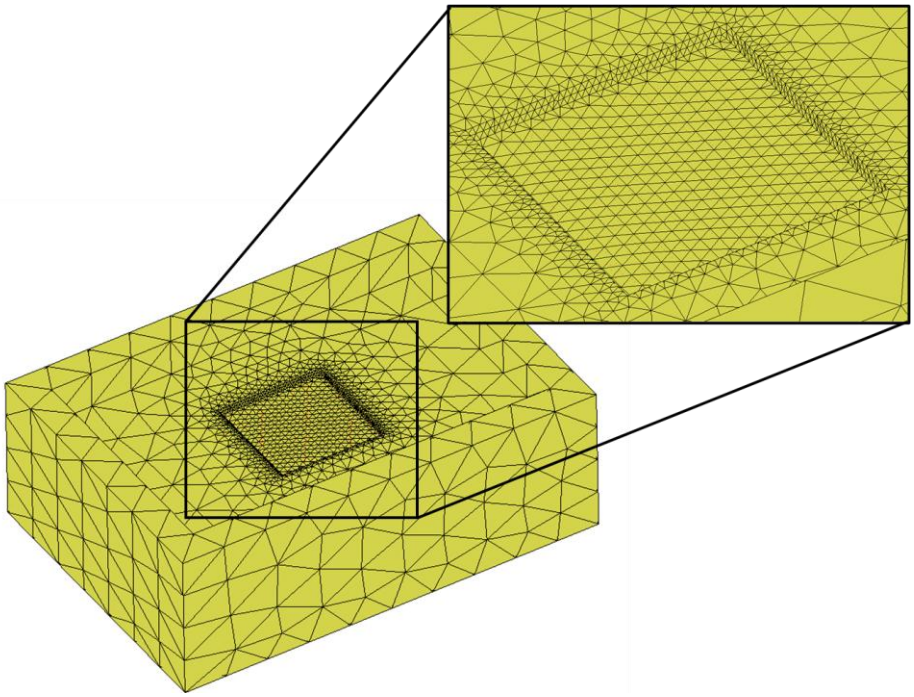


Figure 3: Volumetric mesh with Tetra4 elements of the encapsulation.

The copper lead frame, the solder and SiC layers have been meshed with hexahedral elements having 8 nodes, plus the full integration formulation (Hex8-7 in Marc, Figure 4). I will refer to these solid elements calling them, simply, bricks. The copper lead frame has been subdivided into 4 bricks through the thickness, 25 along the y direction and 40 along the x direction. The solder layer has 2 subdivisions through the thickness, and 80 along each edge (elements' thickness/length aspect ratio is 0.5). The SiC layer has been divided into 8 elements through the thickness, and 80 along each edge (elements' thickness/length aspect ratio approximately equal to 0.53).

Finally, the TEOS and Si_3N_4 frames, and the part of encapsulating resin filling the square cavity inside the frames, due to their micrometric thickness, have been modeled with shell elements with 4 nodes, full integration, and thick shell formulation (Quad4-75 in Marc, see Appendix A for more details). 50 divisions along the edge, and 10 divisions along the frame's width have been imposed (Figure 5).

Once each layer is opportunely discretized, it is necessary to stabilize the type of interaction between them. As a first approximation, it was assumed that the contact between two adjacent layers is ideally rigid. This means assuming that at the contact surface the components of the displacement field are continuous above and below the interface plane.

(1) $$u_i(x,y,z)^+ = u_i(x,y,z)^- \quad i = 1,2,3$$

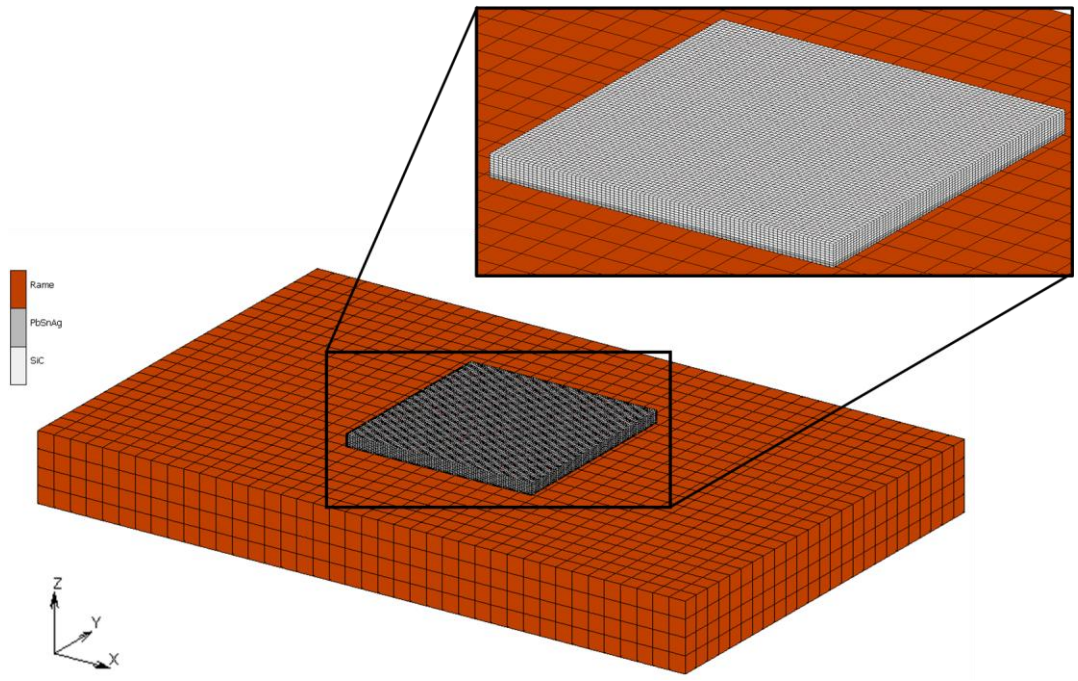


Figure 4: Mesh discretization of copper lead frame, solder, and SiC layers with Hex8-7 elements.

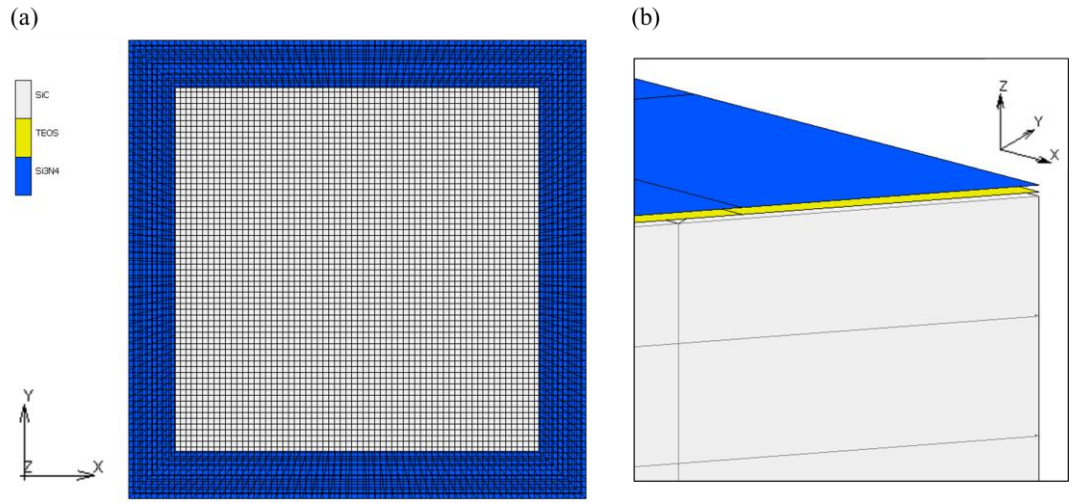


Figure 5: a) In-plane view of the meshed Silicon Nitride frame; b) Particular view of the stacked TEOS and Si_3N_4 layers, along a transversal section passing through the diagonal direction of the die.

In Marc Mentat software, it is possible to implement the rigid contact between two layers by using the Glued Contact Interaction. Each solid or planar meshed layer is defined as Meshed Deformable Contact Body. The Glued Interaction is built by the so-called Contact Table, which is a sort of connectivity matrix between the defined bodies. The set Contact Table is shown in Table 3

(note that the capital letter G means Glued Contact). The implemented contact algorithm for this model is the segment-to-segment [25].

A problem related to the planar meshed layers is the fact that shell elements do not support the algorithm of contact interaction on both sides. This issue is easily by-passable combining the contact with rigid links. Indeed, structural rigid links implement the same constrain condition of the Glued Contact, but they require a 1-to-1 node correspondence. Then, between coherent meshes (same number of nodes for each layer, in the plane of the interface) N-to-N rigid links have been implemented (e.g., TEOS layer – Si_3N_4 layer).

	(1)	*(2)*	*(3)*	*(4)*	*(5)*	*(6)*	*(7)*	*(8)*
Encapsulating resin (tetra) (1)		G		G			G	
Copper (brick) (2)	G							G
TEOS (quad) (3)				G	G			
Si_3N_4 (quad) (4)	G		G					
SiC (brick) (5)			G			G		G
Resin filling the square cavity – layer TEOS (quad) (6)					G		G	
Resin filling the square cavity – layer Si_3N_4 (quad) (7)	G					G		
Solder (brick) (8)		G			G			

Table 3: Contact Table indicating the rigid constrains between adjacent layers.

During the heating process of the whole package, this is supposed to be simply posed on the bench of the climatic chamber, and it is free to bend and expand along all the directions. In order to model this boundary condition, assuming that the bench is the z = 0 plane, 2 rollers constrains and 1 spherical hinge have been imposed on three model's vertexes lying on this plane:

$$(2)\quad \begin{cases} u_x = u_y = u_z = 0 \;\; at\; vertex\; 1\; (spherical\; hinge) \\ u_x = u_z = 0\; at\;\; vertex\; 2, lying\; on\; y - direction\; (y\; roller) \\ u_y = u_z = 0\; at\; vertex\; 3, lying\; on\; x - direction\; (x\; roller) \end{cases}$$

The combination of these constrains with the double symmetry of the package's geometry, ensure that stresses and strains distributions are equal on each corner of the die. Then, the numerical results have been extracted only on one corner. The analysis has been carried out taking into account the possible geometrical non-linearities with the option *large strain*. The time discretization has been set imposing only 4 steps.

1.2 Results and discussion

1.2.1 Sharp edge model

The assessment of the effect of the deposition geometry of the passivation layers on the stress distributions was performed at the instant when the package reaches the maximum temperature (150 °C), or the maximum thermal variation of 215 °C. For the sharp edge model, at this temperature, three path plots were extracted along the corner's diagonal, identified as the direction of maximum stress, at the following interfaces: SiC/TEOS, TEOS/Si_3N_4, Si_3N_4/Resin.

For the filleted edge models, only two representative levels for the path plots were chosen: TEOS middle plane and Si_3N_4 middle plane. Taking as reference the in-plane view of the passivation frame (Figure 6), the starting point of the path is the point O; point P1 is located on the external boundary of the passivation frame, while the point P2 indicates the end of the frame. R_{int} and R_{ext} represent the fillet radii of the boundaries, respectively, on the internal and external side of the passivation frame. The chosen fillet radii at the frame's external boundary are: 0.1 mm, 0.25 mm, and 0.32 mm, while on the internal boundary they are respectively: 0.05 mm, 0.125 mm, and 0.16 mm.

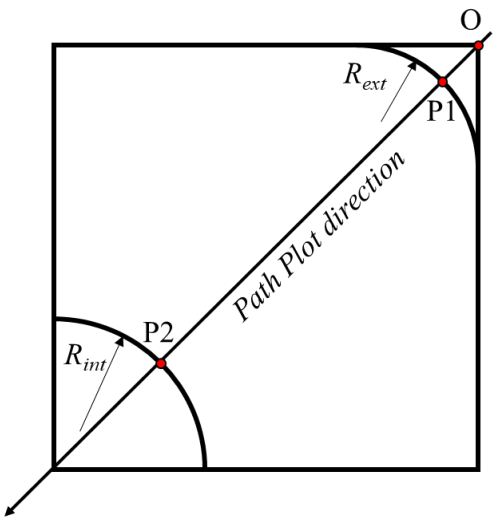


Figure 6: Scheme of the in-plane view of one package's corner. R_{int} and R_{ext} indicate the internal and external fillet radii of the passivation frame.

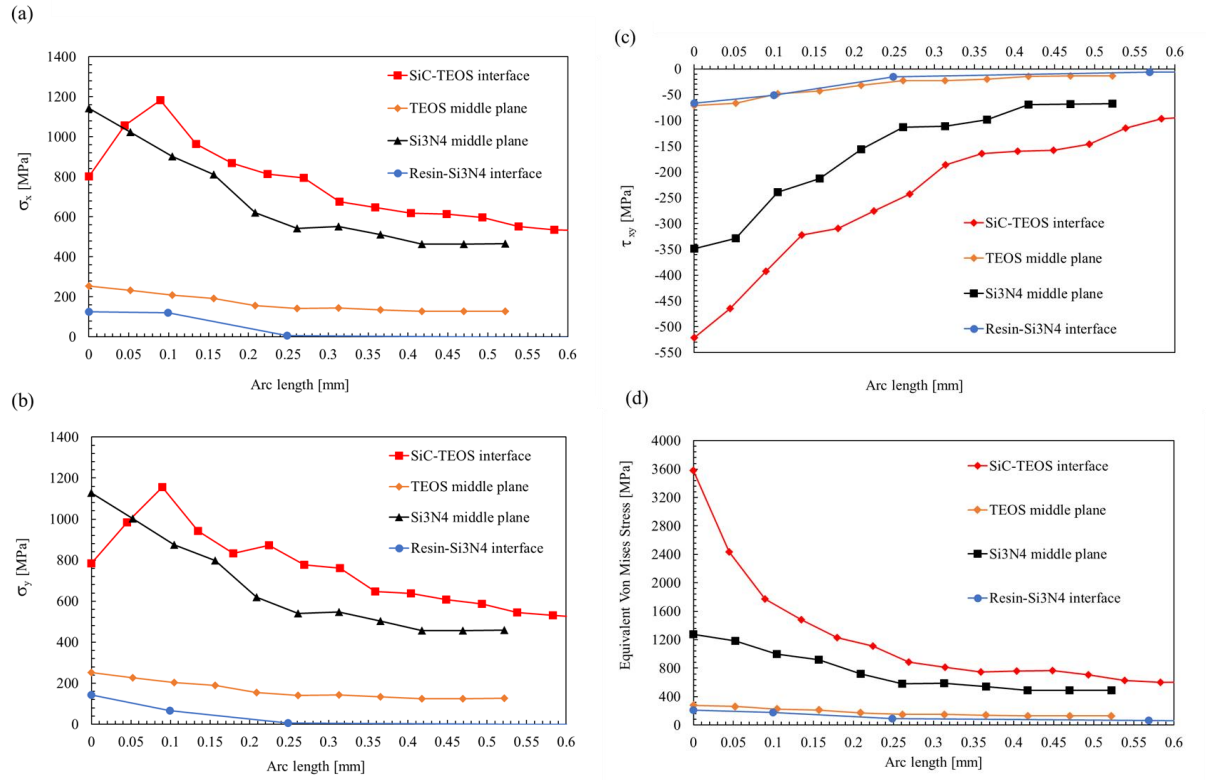


Figure 7: Distributions of the components of stress tensor, along the package's corner diagonal. a) Normal stress, parallel to x direction; b) Normal stress, parallel to y direction; c) Shear stress on the plane x-y; d) Von Mises Stress.

Since TEOS and Si_3N_4 layers are discretized with shell elements, no information about the interlaminar shear stresses is available. Then, the components of stress tensor extracted from the analyses were: two normal stresses parallel to the x and y directions (σ_x and σ_y), the shear stress τ_{xy},

and the Equivalent Von Mises stress. For shell elements, these quantities were evaluated on their middle plane.

For the "sharp edge" model, the distributions of the components of stress tensor are shown in Figure 7. As expected σ_x and σ_y are equal to each other throughout, due to the symmetry of the model and the prescribed boundary conditions. The diagrams highlight the effect of stress concentrations induced by sharp edge configuration, particularly on all interfaces/planes. Indeed, it is observable that the stress components increase along the extracted paths, from a plateau level of stress reached "far" from the sharp edge to a maximum one near the edge termination. For the TEOS and Si_3N_4 planes, all the components of stress tensor are quite uniform in the path range between 0.4 and 0.52 mm.

For the TEOS/SiC interface, the normal components of stress σ_x and σ_y are monotonically increasing from point P2 towards point P1, until they reach a local maximum at 0.1 mm from the sharp edge. On the other hand, the Von Mises stress strongly increases from a value of 800 MPa at 0.6 mm far from the edge, up to 3600 MPa on it. This value represents just a number in output from the simulation, and does not have a real physical meaning. Indeed, sharp corners are singularity points for the stress components, and they tend to diverge in the proximity of these boundaries. Then, the output results derived from the analysis of the sharp edge model are approximately unaffected by the point of singularity excluding 2-3 elements close to it.

1.2.2 Rounded edge model

Looking at the stress distributions σ_x and σ_y, derived in output from the analyses on the filleted frames (Figure 8), it is possible to notice that all the results are quite aligned onto a common curve. The only difference is the maximum value reached by the stress component, which obviously depends on the external fillet radius and the mesh discretization.

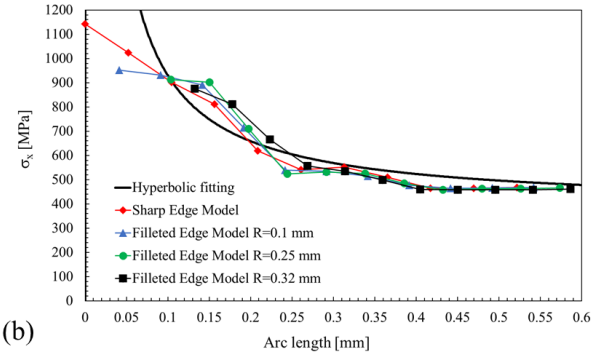
This information allows, in theory, a fast prediction of the maximum stress correspondent to a fixed fillet radius, by performing only one simulation on the sharp edge corner model. Indeed, taking a simple hyperbolic fitting of the results reported with the red line/dots, the maximum stress is achieved when the arc length abscissa assumes the value of the position of point P1. For instance, assuming a value of external fillet radius of 0.3 mm, the external boundary of the frame is located at $s1 = 0.3 * \left(\sqrt{2} - 1\right) \cong 0.124\, mm$. The maximum value of the component σ_x at the point s_1 is approximately 840 MPa, while σ_y is equal to 185 MPa.

1.2.3 Gradients of stress components through the thickness

The mismatch between the thermal-mechanical properties of two layers in contact, leads to gradients of stress through the layers' thickness. For this reason, another path plot passing through the middle point of the corner's diagonal and orthogonal to the x-y plane is reported, in order to evaluate the effect of the in-plane fillet radius on these distributions (Figure 9). The starting point of this path is located 5 μm above Si_3N_4-Resin interface (inside the encapsulating resin) and the ending one is 11.6 μm below the SiC-TEOS interface (inside the SiC layer). The plotted components of the stress tensor σ_y and τ_{xy} are shown in Figure 10. Colored rectangles have been added in the diagrams to highlight the position of the layers' materials along the arc length.

The path plots through the thickness feature that the in-plane filleted geometries do not have a significant effect on the distributions of the considered stress components (Figure 10 a) and b)), or their gradients. On the other hand, it is possible to observe the huge amount of the amplitude of the stress discontinuities, along the arc length, due to the transition from one layer to the adjacent one. Taking as reference the component σ_y, stress gradient is 550 MPa at Resin-Si_3N_4 interface, 400 MPa passing from Si_3N_4 middle plane to TEOS middle plane, and about 450 MPa at SiC-TEOS interface. For the component τ_{xy}, stress gradients assume these following values: 90 MPa at Resin-Si_3N_4 interface, 75 MPa along the transition from Si_3N_4 middle plane to TEOS middle plane, and about 110 MPa at SiC-TEOS interface.

(a)



(b)

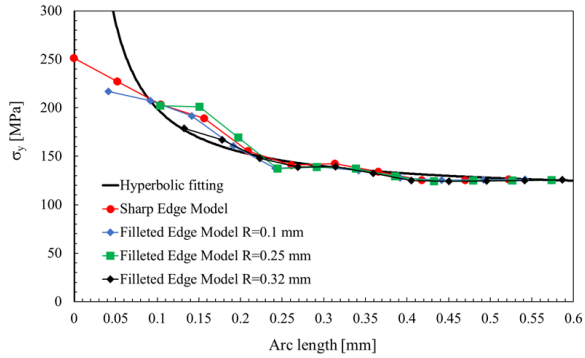


Figure 8: Comparisons between the in-plane normal stresses distributions, along the corner's diagonal direction in sharp edge and filleted edge models. These paths are referred to the following levels: a) Si_3N_4 middle plane; b) TEOS middle plane. The distributions were extracted at the maximum temperature (150 °C).

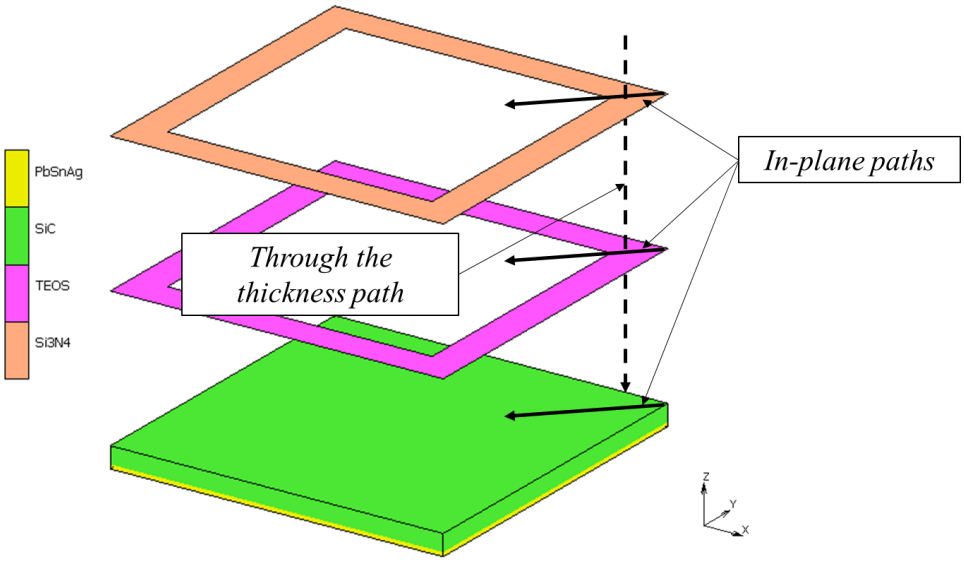


Figure 9: Axonometric view of the path plots extracted through the thickness and along the plane of the layers.

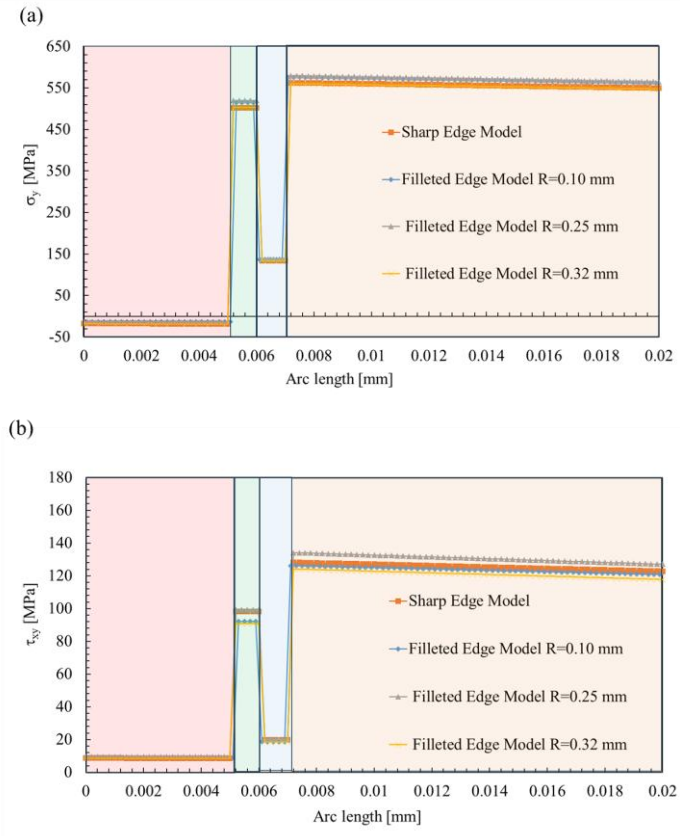


Figure 10: Components σ_y (a) and τ_{xy} (b) of the stress tensor, plotted through the layers' thickness: comparisons between sharp edge and filleted edge corner.

1.3 Conclusions

FEM simulations carried out in this study demonstrated that the geometry of the passivation layers affects local stress distributions in power modules. Specifically, the present study focused on predicting stress distributions induced by a quasi-static heating process. The analyzed interfaces were resin/silicon nitride, TEOS/silicon carbide. Stress distributions were also extracted in the TEOS and silicon nitride layer. The influence of deposition geometry on stress distribution was investigated through numerical simulations. A sharp edge reference model was compared with three variants incorporating different fillet radii. For the sharp edge model, normal and shear components of the stress tensor were analyzed along four diagonal paths at different levels to assess stress concentrations at the corners of the passivation frame, recognized as critical sites for mechanical damage such as crack initiation and delamination under thermo-mechanical cycling. Models with filleted edges revealed a significant role of fillet radius in reducing maximum stresses: while the overall stress distribution shape remains nearly unaffected by the fillet size, the fillets significantly reduce stress in the proximity of the external boundary of the frame, where stress gradients are steep. Larger fillet radii eliminate a greater portion of these stressed regions. This finding suggests that the fillet radius can be selected based on the maximum allowable stress, using only the sharp-edge stress distribution as a reference, thereby potentially avoiding further time-consuming finite element analyses. These insights underscore the importance of integrating geometric and material design considerations early in power module development to optimize passivation layers and mitigate failure risks.

Chapter 2: Global-Local Finite Element approach for the analysis of stress distributions

In the previous section, the modeling procedure of a complete power electronics package was discussed. In such model, the passivation layers of the die were discretized using shell elements, while the encapsulating resin was meshed with tetrahedral elements. Moreover, an additional passivation layer interposed between the resin and the silicon nitride was not included in the model. This omitted layer was the polyimide.

Polyimide is commonly employed in electronic packages for several reasons: it provides an additional barrier that enhances electrical insulation between the die and the surrounding environment, particularly in cases where the resin fails to ensure complete encapsulation of the TEOS and silicon nitride layers. Furthermore, polyimides are well known for their thermal stability, and thermoplastic polyimides also exhibit a certain degree of ductility.

When a polyimide film is inserted between the encapsulating resin and the silicon nitride passivation layer, it acts as a soft layer, accommodating the expansion/contraction of these two materials and reducing stress gradients across the thickness arising from the large thermo-mechanical mismatch between the encapsulant and the passivation layer.

This section will introduce different enhancements to the previous modelling approach. Specifically, the polyimide layer deposited on top of the silicon nitride will be explicitly modeled; the resin encapsulation will be discretized using hexahedral elements with uniform divisions between the inner and outer sides of the package; and finally, a mesh sensitivity analysis will be carried out on a representative interface in order to assess whether the mesh refinement level adopted in the models is adequate to accurately capture the stress distributions.

The mesh refinement operation is particularly delicate, as increasing the number of divisions, both in-plane and through the thickness, would lead to a substantial rise in the total number of elements and nodes in the model. This would substantially increase the computational cost of the analysis and the simulation time.

In order to avoid the simulation of models containing hundreds of thousands of nodes and elements, the use of a global-local modeling approach will be introduced. This approach involves the analysis of a global model that includes all components of a complex structure, discretized with a coarse mesh. From this model, a local subdomain (finely meshed) is extracted to represent a region where accurate information on stress and strain distributions is needed.

This approach allows for a compromise between the total number of elements in the model, the associated computational cost, and the level of accuracy required in the evaluation of stress components at local scale.

In this section, the procedure followed for the global-local modeling of a power electronics package will be described. Three models will be presented: i) two global models: one with a "fine" mesh, locally refined around the SiC, TEOS, and Si_3N_4 layers, and one with a "coarse" mesh; ii) a third model simulating a local subdomain. This local model, extracted by one corner of the die, includes the SiC, TEOS, Si_3N_4, polyimide, and resin layers. These analyses enable the evaluation of the sensitivity of local stress components to three different levels of mesh refinement.

In the final section of this paragraph, the application of the Global-Local approach will be described to evaluate the effect of stress concentration caused by defects arising during the manufacturing and assembly process of the package. One such defect is the formation of dry spots, namely localized regions at the interface between the encapsulating resin and the die, where partial or complete loss of adhesion between the two components occurs. Therefore, the second objective of this work is to assess the impact of dry spots on local stress distributions.

2.1 Materials and modelling approach for the Global Model

The model analyzed in this section is based on a commercial T2PAK package developed by ST Microelectronics[3], for which the geometric details were provided by the company. The dimensions of the constituent layers used in the model are slightly different from those reported in the previous section 1.1. These dimensions are summarized in the following Table 4.

	In-plane dimensions [mm]	Thickness [μm]
Copper	10.40 x 6.40	1270
PbSnAg solder	4.95 x 4.23	45
SiC	4.95 x 4.23	180
Si_3N_4	4.88 x 4.16	1
TEOS	4.88 x 4.16	2.4
Polyimide	4.95 x 4.23	5.6
EMC	14 x 10	3500

Table 4: Geometric dimensions of the layers of T2PAK power module.

[3] The datasheets for the packages are available at the following webpage: https://www.st.com/en/power-transistors/stpower-n-channel-mosfets-gt-200-v-to-700-v/documentation.html

The polyimide layer is deposited so as to encapsulate the two overlapping passivation layers of TEOS and Si_3N_4. For this reason, the frame width of the latter two layers is smaller than that of the polyimide. The stack of the three passivation layers features a rectangular cavity with dimensions 4.28 mm × 3.56 mm.

Regarding the considerations discussed in the previous section about the symmetry of the package, the uniformity of the thermal load, and the constraints imposed to the model, only one quarter of the full geometry will be analyzed in the present study.

As previously mentioned, in the current model, the encapsulating resin has been discretized using hexahedral elements with 8 nodes (Hex 8), obtained by extruding a two-dimensional mesh of the package cross-section (lying in the x–z plane) along the orthogonal y-direction. The two-dimensional mesh of the package's cross-section was generated using the planar *automesh* tool available in MSC Marc Mentat®, after prescribing a suitable subdivision of the boundary of the region to be discretized.

For the resin block, the mesh was divided into 34 elements along the y-direction, 22 along the x-direction, and 15 along the z-direction, resulting in a total of 19625 elements. The copper, solder, and SiC layers were also discretized using 8-node hexahedral elements.

The copper layer was meshed with 20 divisions along x, 30 along y, and 10 along z. The solder layer was divided into 37 parts along x, 32 along y, and 3 along z. The SiC, TEOS, and Si_3N_4 layers are the ones affected by mesh refinement; therefore, it is necessary to distinguish the number of divisions used, respectively, in the *global coarse mesh* model and in the *global fine mesh* model. To simplify the reading, the mesh specifications for these two model variants are summarized in the following Table 5.

	Global Coarse Mesh			*Global Fine Mesh*		
	Div. along x-direction[4]	*Div. along y-direction*	*Div. along z-direction*	*Div. along x-direction*	*Div. along y-direction*	*Div. along z-direction*
SiC	23	20	5	46	40	5
TEOS	10	50	1	20	50	1
Si_3N_4	10	50	1	20	50	1

Table 5: Details about the discretization of the three layers: SiC, TEOS and Si_3N_4 in the global models.

[4] The divisions along x and y direction, for TEOS and Si_3N_4 layers, are counted respectively along the frame's width and length.

The TEOS, Si_3N_4, and polyimide layers were discretized using *solid shell elements*, a formulation implemented in the Marc Mentat software[5]. This choice was made to improve the accuracy of the results in output from the traditional planar shell elements, avoiding the limitations associated with the Kirchhoff assumptions inherent to thin shell formulations.

Solid shell elements offer a significant advantage in this context: they provide a full three-dimensional strain and stress field description, while still being suitable for modeling thin structures. Unlike classical shell elements, solid shells do not require explicit definition of reference surfaces and their normal directions, and they can take into account interfacial stresses. Additionally, solid shells are fully compatible with *glued contact* definitions in Marc, which allows for a physically consistent modeling of perfect adhesion between adjacent layers in multilayered electronic packages. -particularly important in thermal and mechanical load conditions where interlaminar stresses develop.

From a mathematical standpoint, the formulation of solid shell elements in Marc accounts for thickness changes during the deformation history. This feature becomes especially important in large deformation scenarios, where the assumption of constant thickness made by traditional shell formulations may lead to significant inaccuracies in the computed stress state.

A quasi-static time–temperature profile ranging from −65 °C to 150 °C was applied to the global model, uniformly across all nodes. The considered materials properties were the same ones of the previous section (Table 1), adding the following properties for the Polyimide layer: Young's modulus 3000 MPa, Poisson's ratio 0.34, Coefficient of Thermal Expansion $5x10^{-5}$ $°C^{-1}$. As in the previous model, all layers were assumed to be perfectly bonded using *glued contact*. The chosen glued contact algorithm is segment-to-segment[6].

Two symmetry constraints were applied using *Symmetry* contact conditions: one on the x–z plane and one on the y–z plane. Additionally, a spherical hinge constraint was imposed on a node located on the model's axis of symmetry and lying on the bottom surface of the package. This setup effectively suppresses all rigid body motions of the package, while still allowing it to expand or contract in space and to warp due to bending effects. The following section outlines the procedure adopted for the construction of the local model.

[5] Further details about the solid shell formulation are reported in the Marc Mentat documentation volume B: Element Library

[6] Further details about the segment-to-segment contact algorithm are reported in the Marc Mentat documentation volume A: Theory and User information

2.2 Modelling approach for the Local Model

As previously anticipated, an alternative strategy to mesh refinement, aimed at enhancing the accuracy of local stress evaluation, is the adoption of the global-local finite element approach (GL-FEM).

Let us consider a deformable continuum domain denoted by Ω, subjected to externally applied forces and/or moments and subjected to boundary conditions. Under these conditions, each material point within the domain Ω experiences a stress state represented by the stress tensor $\boldsymbol{\sigma}$.

Let $\Omega' \subset \Omega$ be a subdomain of the global continuum. As a result of external loads and boundary constraints applied to the global domain Ω, a displacement field $\boldsymbol{u}=\boldsymbol{u}(\mathbf{x}, t)$ is uniquely induced on the boundary of the subdomain Ω', where $\mathbf{x}$ denotes the position vector in the deformed configuration of the body, and t is time.

The global-local approach is founded on the principle that the internal stress state at any point within the subdomain Ω', when subjected to the boundary displacement field $\boldsymbol{u}=\boldsymbol{u}(\mathbf{x}, t)$, is identical to the stress state experienced by the same point when considered as part of the original global domain Ω under the corresponding global loading and constraint conditions.

This equivalence allows for an efficient multiscale modeling framework, in which a coarse global model captures the overall behavior of the structure, while local sub-models with refined discretization are employed to accurately capture stress and strain fields in regions of interest, without further increasing the computational cost due to the refinement of the entire domain.

The FE software Marc Mentat is able to easily apply the global-local boundary conditions, expressed in terms of displacement distributions, onto a local subdomain extracted from the global model. The local subdomain on which this work focuses corresponds to a corner region of the package, containing the following material layers: SiC, TEOS, Si_3N_4, polyimide, and encapsulating resin**.**

The Si_3N_4 and TEOS passivation layers feature rounded geometries designed to mitigate stress concentration effects. The outer edge of the frame is filleted with a radius of 0.4 mm, while the inner edge features a fillet radius of 0.1 mm. The total volume of the modeled domain measures 0.5 mm × 0.5 mm × 0.131 mm. This volume includes a 50 μm thick part of the encapsulating resin layer (placed above the polyimide) and a 72 μm thick portion of the SiC layer (located beneath the TEOS layer). A schematic representation of the local model is provided below (Figure 11).

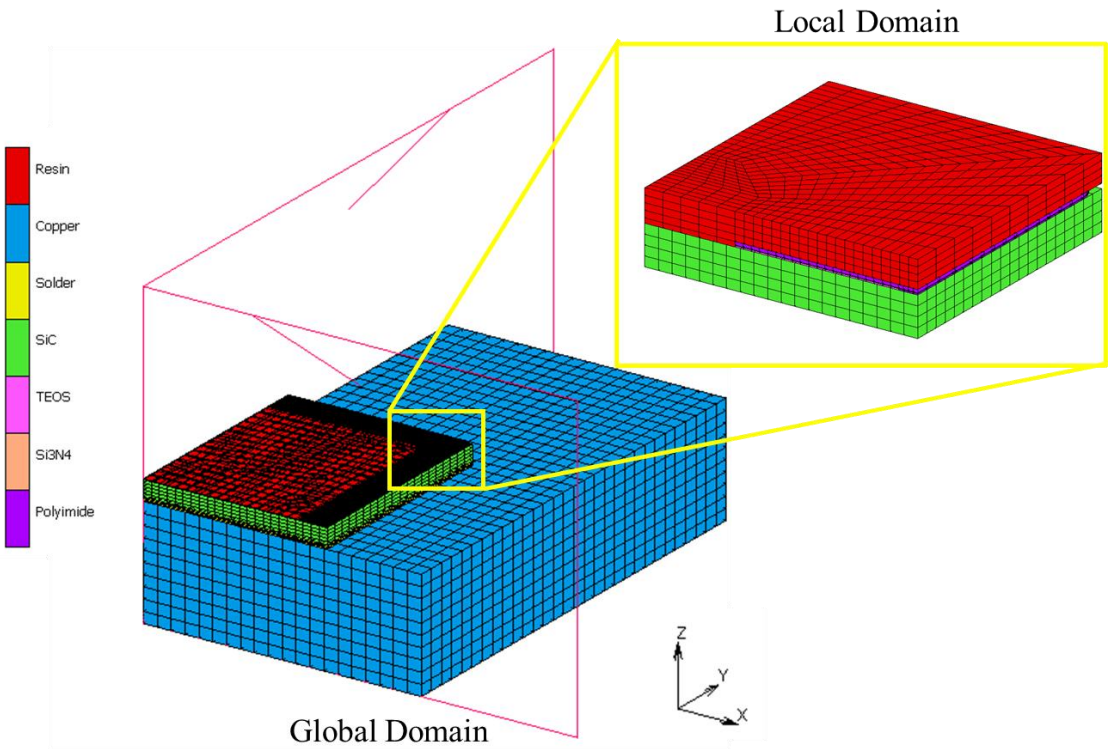


Figure 11: Global and local domain meshed models of the T2PAK power device.

The details concerning the mesh subdivisions of the internal layers in the local model are reported in the following Table 6.

	Local Model Mesh		
	Div. along x-direction	*Div. along y-direction*	*Div. along z-direction*
SiC	20	20	4
TEOS	20	20	1
Si_3N_4	20	20	1
Polyimide	24	24	1
Resin	non uniform mesh		4

Table 6: Details of the mesh discretization for the local model.

In the following paragraph, the results obtained from the analyses of these three FEM models will be presented and compared.

2.3 Results and discussion

2.3.1 Assessment of the mesh refinement on stress distributions at local scale

As a first step, the stress distributions obtained from the simulations of the three FEM models described above were compared along a representative interface affected by mesh refinement. The selected interface is the SiC/TEOS interface. The results presented in Figure 12 were extracted along a path oriented diagonally with respect to the filleted corner of the TEOS passivation frame. The results were extracted at the nodes lying on the TEOS side.

The plotted stress components include: the in-plane normal stress component σ_x (which, due to the symmetry considerations discussed in the previous section, is equal to σ_y), and the in-plane shear stress τ_{xy}. These three components exhibit discontinuities when transitioning from one material layer (A) to another (B). The remaining three components correspond to the so-called "interfacial stresses": the out-of-plane normal stress σ_z, and the interlaminar shear stresses τ_{xz} (equal to τ_{yz} by the symmetry).

The comparison involved the three FEM models in which mesh refinement and the global-local approach were implemented: the *global coarse mesh model*, the *global fine mesh model*, and the *local model*. As illustrated in Figure 12, comparing only the results from the two global models, the mesh refinement at the SiC/TEOS interface leads to a maximum variation in the stress distributions of approximately 10%.

Considering also the results extracted from the local model, it is noteworthy that:

- In the spatial distribution of the σ_x component, no significant stress variations are observed due to the additional refinement (i.e., no significant variation comparing the results from the global model with fine mesh and the local model);
- Considering the stress component τ_{xy}, a difference of 4.2 MPa is observed between the coarse mesh and the local model, compared to a plateau value of approximately 9.5 MPa in the local Model;
- Pronounced discrepancies are found in the interfacial stress distributions: for τ_{xz}, a maximum difference of about 13 MPa is observed between the global coarse and local models; for σ_z, while the value is nearly zero in both global models, it reaches an average value of approximately −22 MPa along the path in the local model.

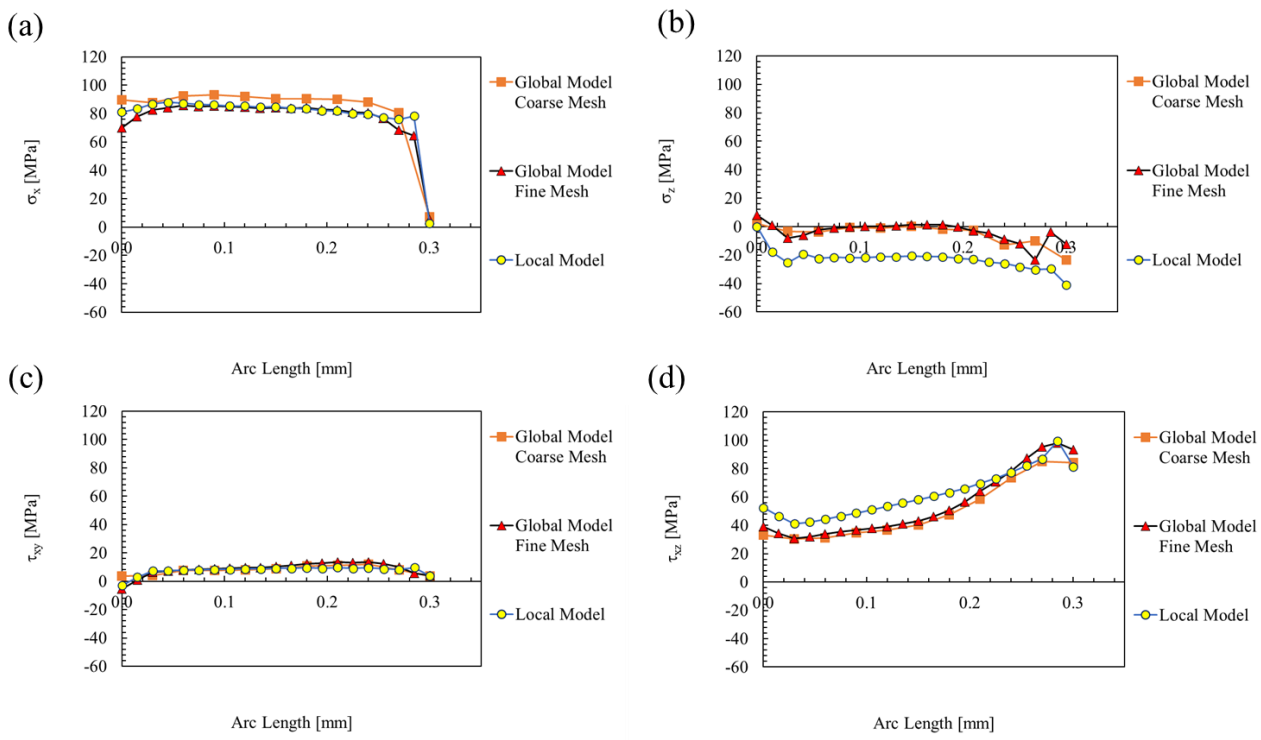


Figure 12: Components of stress tensor extracted along the corner's diagonal direction of the passivation frame, at the maximum temperature. The plots refer to the SiC/TEOS interface (TEOS side). The graphs show the comparison between the results obtained from the following models: global model with "coarse mesh", global model with "fine mesh"; local model.

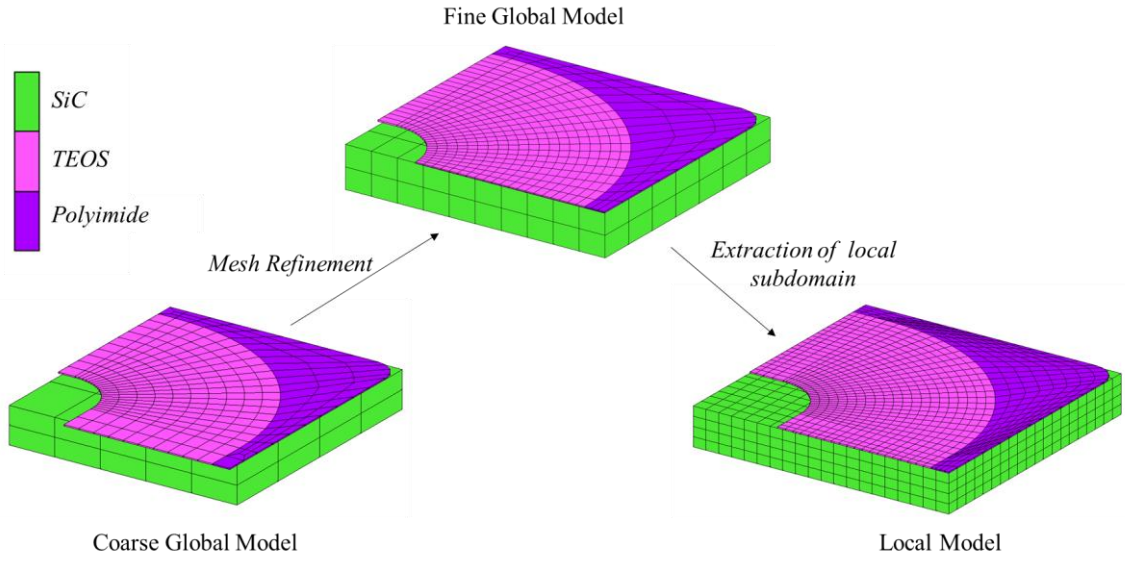


Figure 13: Schematic representation of the mesh refinement applied to the modelled subdomain.

These differences in the stress distributions are, in part, attributable to the increase in the number of in-plane subdivisions. However, it is important to note that, despite the refinement, the

element proportions at the TEOS/SiC interface remain significantly different across the three models: approximately 1:26 in the coarse mesh model, 1:9 in the fine mesh model, and 1:2 in the local model.

This mismatch in element dimensions, when non-coherent meshes are placed in contact, has a substantial impact on the computed interfacial stresses. It is, therefore, reasonable to attribute the discrepancies observed above to the disproportionate mesh densities across the SiC/TEOS interface. The local model can thus be considered the most accurate in capturing the stress distributions at the interface.

2.3.2 Gradients through the thickness extracted from the local model

Following the above considerations regarding mesh refinement, a path plot through the thickness was extracted directly from the local model in order to assess the stress gradients in this direction, as well as the effect of the polyimide layer interposed between the Si_3N_4 and the resin. The results reported in the following graphs Figure 14 were compared with the corresponding ones presented in Figure 10.

The path was defined along a straight segment starting from the bottom side of the SiC layer and ending at the top surface of the resin, intersecting the midpoints of the passivation frames. The total length of the path is therefore 131.1 μm.

Considering the in-plane normal stress component σ_x, it increases from 224 MPa to 265 MPa through the SiC, as the path approaches the TEOS layer. At z = 72 μm, a discontinuity occurs at the SiC/TEOS interface, where σ_x drops to approximately 83.6 MPa and remains nearly uniform throughout the TEOS layer. At z = 74.4 μm, the second interface (TEOS/Si_3N_4) is encountered, across which σ_x increases from 83.6 MPa to 266 MPa within the Si_3N_4 layer. A third stress gradient occurs at z = 75.4 μm, where the stress decreases from 266 MPa to –53.3 MPa. Finally, in the resin layer - ranging from z = 81.1 μm to z = 131.1 μm- σ_x gradually increases from –20.6 MPa to 2.4 MPa.

Regarding the in-plane shear stress component $\tau_{x\gamma}$, it increases from 46.9 MPa to 58.7 MPa through the SiC, approaching the TEOS layer. At z = 72 μm, corresponding to the SiC/TEOS interface, $\tau_{x\gamma}$ drops to 8.9 MPa. Inside the Si_3N_4 layer, it increases again to 46.5 MPa. Notably, $\tau_{x\gamma}$ approximately vanishes across the thickness of the polyimide layer and, in the resin, varies between 10.8 MPa and 16.5 MPa.

The out-of-plane normal stress component σ_z -normal to the interfaces- is entirely negative (i.e., compressive) along the thickness, varying approximately linearly from –10 MPa to –33 MPa.

Finally, the interlaminar shear stress τ_{xz} varies between 17 MPa and 54.2 MPa within the polyimide layer, and subsequently decreases to 35.5 MPa within the resin.

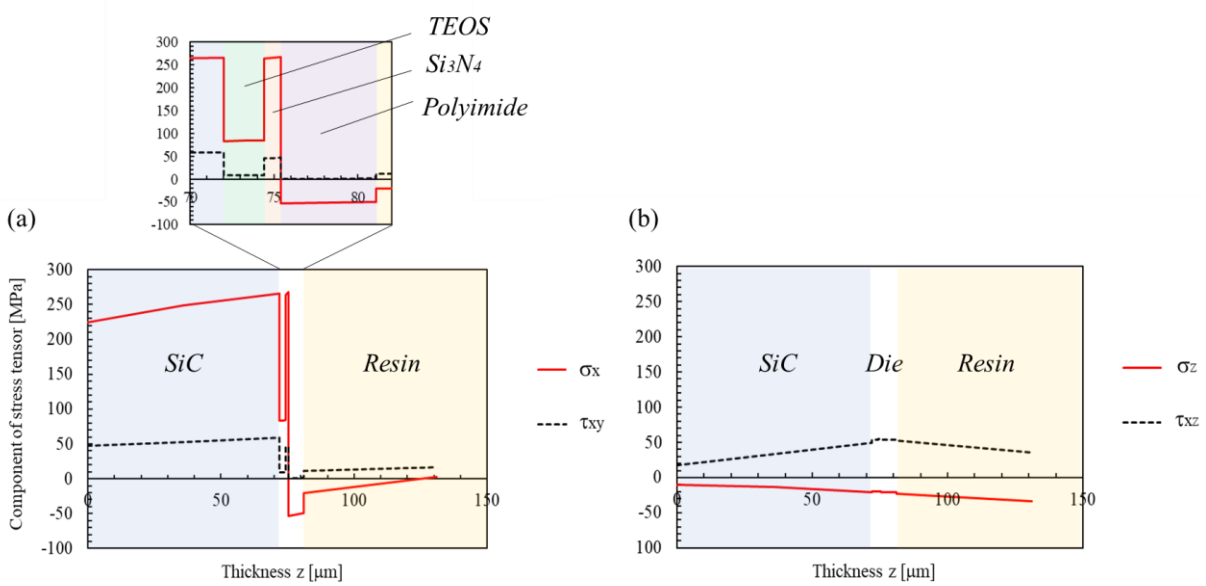


Figure 14: Path plots through the thickness extracted on the local domain of the modelled package, at maximum temperature. a) discontinuous stress components; b) continuous stress components.

By comparing the through-thickness path plot shown in Figure 14 with that of Figure 10, it is clearly observed that the presence of the polyimide layer, being in direct contact with both the silicon nitride and the SiC layers, contributes to a substantial reduction, approximately by half, of the internal stresses σ_x and τ_{xy} in these layers.

Polyimide exhibits the lowest elastic modulus among all the materials used in the package and is therefore capable of accommodating most of the resin-induced deformations without accumulating significant elastic stress.

Since this material is also ductile and capable of undergoing plastic deformation, it would be of great interest to evaluate the effect of polyimide's plastic strains and strain hardening behavior on the internal stress distributions within the die. This topic will be further explored in the subsequent sections.

2.4 Application of the Global-Local FEM for assessing the influence of the defects (dry spots) induced from Resin Transfer Molding on local stresses

During the packaging process of a power module, the thermosetting resin is injected into a mold containing the metallic-ceramic layers and partial or total lack of adhesion may occur between the encapsulation and die or copper leadframe. The de-bonded areas have small dimensions (approximately 0.05 mm^2) compared to the in-plane dimension of Si_3N_4 frame, so the modelling of these critical interfacial regions requires finer mesh than other parts of the package. Then, the Global-Local Finite Element Analysis (GL-FEA) has been used in order to accurately investigate the stresses distributions near the discontinuity induced by the dry spot.

In this work, a dry spot of dimensions 0.128 mm x 0.332 mm has been modelled in the middle region of the Si_3N_4 frame, sufficiently far from the two corners, neglecting other edge effects. The presence of the Polyimide passivation layer was neglected as done in the first model described in section 1.1.

The representative volume element chosen for the analysis has the following dimensions: 0.5 mm x 0.17 mm x 0.0426 mm (see Figure 15). A portion of resin lying on the two lateral sides of the TEOS and Si_3N_4 frames has been included in the local model in order to capture the in-plane transition from a layer to the encapsulating resin. For the modelling of the dry spot, the elements belonging to the Si_3N_4 contact body at the interface with resin elements have been excluded from the glued interaction.

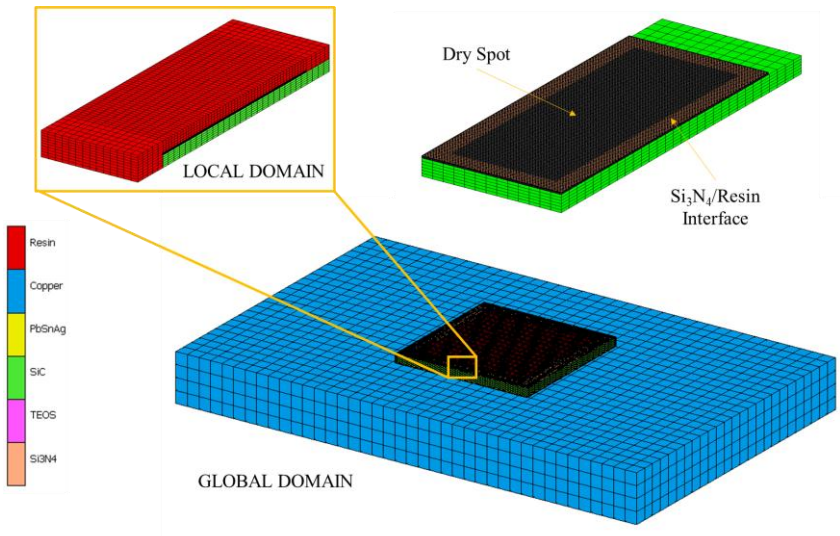


Figure 15: Global and local models used for the simulation of the dry spots.

Taking as reference the local model of Figure 15, one path parallel to the passivation frame and passing through the center of the dry spot have been chosen for the evaluation of this de-bonded area on stresses amplifications. Two representative components of stress tensor have been chosen for the comparison: the in-plane normal component σ_x and the interlaminar shear stress τ_{yz}. The obtained results are shown in Figure 16, where the arc length interval between the two dashed lines indicates the region where dry spot is present.

Observing the normal component of stress σ_x, the effect of the dry spot is negligible. Indeed, the average value of the difference between stress in presence and in absence of dry spot (delta stress reported in secondary axis) is about 15 MPa compared with the average value of σ_x of 600 MPa (difference of 2.5 %). Local peaks of stress of 25 MPa and 80 MPa are located, respectively, at arc length 0.024 mm and 0.147 mm, where there is the in-plane transition from the "glued zone" to the de-bonded one.

A relevant local amplification effect is observed on the interlaminar shear component τ_{yz}. Within the dry spot region, far from the boundary edges, this component passes from a mean value of -50 MPa to zero MPa. Also in this case, the peak stresses of -350 MPa and -400 MPa occur at the glued-dry spot transition.

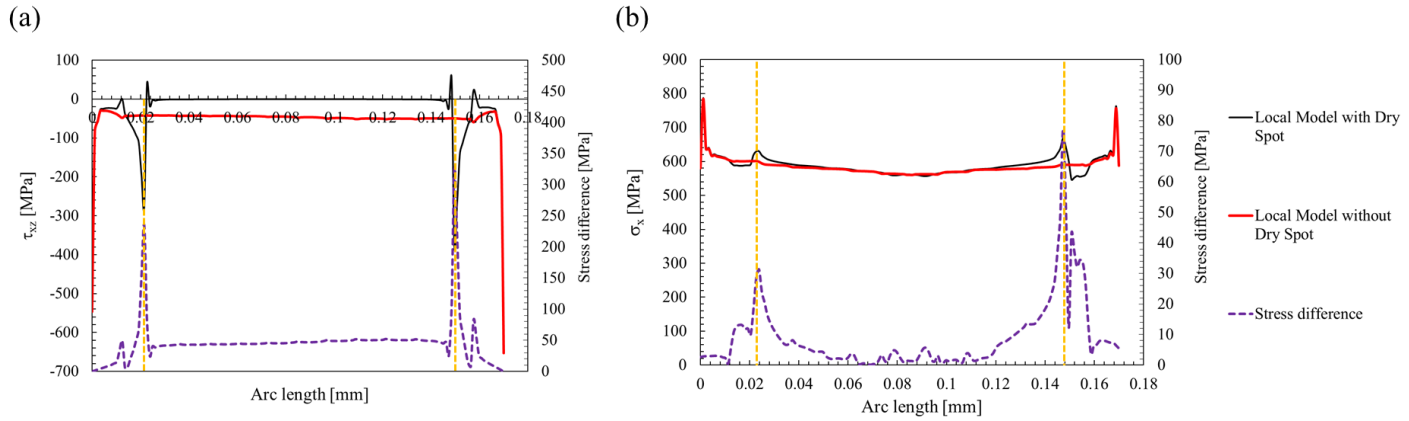


Figure 16: Effect of dry spot on stress distributions.

2.5 Conclusions

The present study has demonstrated the critical importance of accurately modeling the multilayer structure of power electronics packages, particularly through the inclusion of the polyimide layer and the use of refined mesh strategies. The global-local finite element approach enabled an effective balance between computational efficiency and local accuracy, revealing that mesh refinement significantly influences the prediction of stress distributions at critical interfaces, especially the SiC/TEOS boundary. The local model, with its finer and more coherent mesh, provided the most reliable stress estimations, capturing complex interfacial stress states that coarser meshes tend to underestimate or smooth out. Furthermore, the explicit modeling of the polyimide layer highlighted its vital role as a soft interlayer that substantially reduces stress magnitudes and gradients within the adjacent silicon nitride and resin layers. This reduction is primarily due to the polyimide's lower elastic modulus and its ability to accommodate resin-induced strains, thereby mitigating the thermo-mechanical mismatch effects. These insights are particularly valuable for improving the mechanical reliability and longevity of power electronic packages, as high interfacial stresses are known to contribute to delamination, cracking, and premature failure. The outcomes of this work provide a robust framework for future studies aimed at incorporating polyimide plasticity and strain hardening behavior, which will further enhance the predictive capability of numerical models.

Moreover, the Global-Local modeling approach was applied to investigate the effect of dry spots, i.e., localized defects at the interface between the encapsulating resin and the die, where partial or total adhesion loss occurs. The study showed that the presence of a dry spot induces a local stress amplification effect in the vicinity of the defect. In particular, the distributions of two components of the stress tensor were analyzed along a path parallel to the passivation frame at the Si_3N_4/resin interface level. The presence of the dry spot causes a local amplification of the interlaminar shear stress component up to 7 times (in absolute value) the average value along the path. The in-plane normal stress component, on the other hand, was locally amplified by up to 13% compared to the average stress value along the path.

Chapter 3: Finite Element Modelling of the residual stress-state induced at the end of the Resin Transfer Molding process

Simulations of power modules performed by industries typically assume a stress-free state before applying the thermal loads, neglecting the residual stresses and plastic deformations induced by the manufacturing process at the initial temperature. This hypothesis was applied also in the simulations described in chapter 1 and 2.

Many authors in the literature use this simplified approach in the modelling of power electronics packages.

For instance, in the study of Mirone et al. [8], a semi-assembled part of a power module, featuring residual strains due to the production processes, was simulated under the assumption that the model was undeformed and unstressed at a conventional "stress-free temperature", different from the initial one (i.e., room temperature).

Dudek et al. [26] modeled the delamination phenomenon in power packages subjected to thermal cycling, assuming a stress-free condition at 175 °C, where all stresses are considered to relax at this temperature and above.

Gschwandl et al. [27] studied the residual stresses generated during the manufacturing process of an epoxy molding compound used as the encapsulation material in a D2PAK power package. To characterize the material behavior, they conducted tensile tests at various temperatures and performed Differential Scanning Calorimetry (DSC) measurements to determine the curing kinetics.

These experimental results were used to model the curing process in finite element (FE) simulations using the Prout–Tompkins model. Additionally, the Cure Hardening Instantaneous Linear Elastic (CHILE) approach was adopted.

In the CHILE framework, the evolution of the epoxy molding compound's stiffness is divided into three distinct phases: initially, the resin is uncured and exhibits negligible stiffness; subsequently, as curing progresses, the elastic modulus gradually increases. Finally, once the material is fully cured, the stiffness reaches a plateau.

The numerical results in [27] indicate that the combined effects of the manufacturing process and the thermal mismatch between the metallic components and the resin are the primary drivers of residual stresses and plastic deformation.

In this section, it will be described the modelling procedure useful to take into account the effect of a specific manufacturing process, that is the Resin Transfer Molding, on the stress-strain history of a representative SiC-based power electronics package, subjected to a passive power cycling of heating and cooling.

The thermosetting resins used in the Resin Transfer Molding process have peculiar physical properties that strongly change during the curing phase. Curing denotes an irreversible reaction, where the polymeric chains of a viscous resin start crosslinking, increasing the viscosity, the elastic modulus, and the Poisson's ratio.

The modelling procedure explained in this section is able to reproduce the change of the mechanical and adhesion properties of the encapsulating resin during the molding process, in order to assess its effect on the final state of the whole package, in terms of local stress, plastic and elastic strains, and permanent warpage (global out-of-plane displacement at the end of the power cycling).

The Resin Transfer Molding may be considered representative of other manufacturing processes of a power modulus, where the single layers are progressively bonded together despite their differing thermo-mechanical properties. As a result, the final state of the partial assembly is deformed and subjected to residual stresses. Indeed, similar considerations may also apply to the soldering process between Copper and SiC and, perhaps to lower extents, to the application of Polyimide layer on top of passivation layers.

No experimental data are available for this process due to its general representativeness and the industrial confidentiality surrounding manufacturing details. Nevertheless, some numerical aspects of the modeling strategy employed here, such as post-yield material behavior, interlayer contact modeling, and mesh sensitivity, have already been validated in previous studies where less sensitive experimental data were accessible [8,28]. The contents presented in this chapter are currently reported in a journal article under submission entitled: *Modelling of Residual Stress, Plastic Deformation, and Permanent Warpage Induced by the Resin Moulding Process in SiC-Based Power Modules*.

3.1 Resin Transfer Molding Process

When an electronic package completes all the steps of the entire manufacturing process and assembly, the strain history within the device is strongly influenced by the following heating and cooling cycles at which each layer (or a stacked sequence of layers) is subjected. One of the most relevant processes in the fabrication of power module is the Resin Transfer Molding, during which

the bonded metallic-ceramic-polymeric substrates are encapsulated in a thermosetting resin filled with silica particles to increase the glass transition temperature of the matrix.

Once the manufacturing stages preceding resin molding are assumed to be complete, the Copper layer supporting the soldered SiC die, the deposited passivation layers of TEOS, Si_3N_4 and Polyimide are considered a unique semi-worked body. In the description of the modelling procedure of the process, this body is defined as “Copper-to-Poly” assembly for brevity.

During the initial phase of the molding process, the resin is pre-heated from the ambient temperature (25 °C) up to the *Curing Start Temperature* of (here assumed at 50 °C), maintaining its liquid viscous state at which the monomers are not yet linked by covalent bonds. Then, this fluid is pressurized into the mold, filling all the void spaces and pushing against the Copper-to-Poly assembly. At this stage, the bonded layers experience the rise in temperature and the hydrostatic pressure exerted by the fluid.

As the resin starts to wet the materials of the assembly, the adhesion forces develop at the interfaces, creating a contact with negligible stiffness. Once the mold is full, the temperature gradually increases up to 200 °C. Above the curing start temperature, the polymerization reaction takes place in the resin. This reaction is exothermic and involves the growth of the main polymeric chains and the formation of networks (cross-linking agents are added to the liquid resin, in order to promote the formation of bridges of covalent bonds) between the chains themselves. The fraction of cured resin that forms covalent bonds and cross-links is defined as Degree of Cure α, and it is considered an important state-variable on the modelling of the chemical kinetic of the curing process. Obviously, a value of $\alpha=1$ means that the material is in a solid state and fully polymerized.

As result of the polymerization, the chemical and physical properties of the thermosetting resin (elastic modulus, Poisson’s ratio, viscosity, thermal conductibility, coefficient of thermal expansion, glass transition temperature, and so on) increase progressively until it is assumed fully solidified at a temperature of 150 °C, denoted as *Curing Finish Temperature*.

Between the glassy solid state and the liquid one, the thermosetting polymer passes through the so-called rubbery gel zone, when the Degree of Cure is approximately 0.5 and the chemical-physical properties of the resin continue to increase slowly, until they reach an asymptotic value. A representative temperature-time diagram of the curing process is reported in Figure 17.

3.2 Materials and Modelling procedure for the simulation of package encapsulation

The simulation of the mechanical response of the metallic-ceramic-polymeric assembly (Copper-to-Poly), during the encapsulation in the thermosetting resin, was divided into three sub-analyses in order to model the complex behavior of the resin (which passes from viscous liquid to gel, and finally to a glassy polymer), its interaction with the assembly itself, and the irreversible nature of the curing reaction.

The epoxy resin's phase transition and mechanical properties, during the polymerization reaction, has been strongly simplified by avoiding the simulation of all the transients involving the heat transfer phenomena and the kinetics of the chemical reaction.

Indeed, since the heating rate of a curing cycle is in the order of 1 °C/min=0.017 °C/s, it is reasonable to assume that the Copper-to-Poly assembly has ''sufficient'' time to reach the thermal equilibrium inside it and with the resin itself. Then, all the points have the same equilibrium temperature at each instant of time.

Moreover, as observed in the diagram of Figure 17, the degree of cure of the epoxy compound is strictly related with the temperature. Knowing that all the physical properties of this material are monotonically dependent on the degree of cure, then it is possible to express these properties directly with the temperature, bypassing the simulation of the chemical reaction into the Finite Element software.

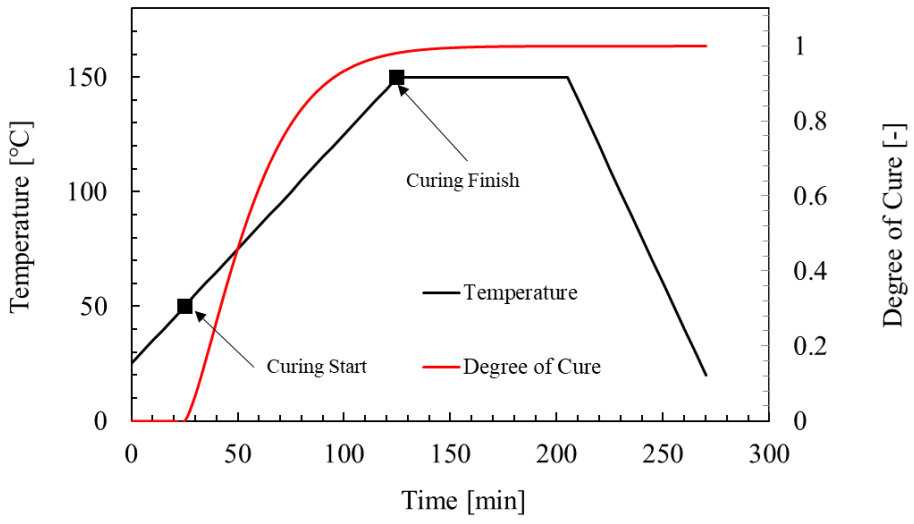


Figure 17: Temperature-Time and Degree of Cure-Time representative diagrams for a curing process.

The first type of thermomechanical load acting on the Copper-to-Poly assembly is due to the pre-heating phase between 25 °C and 50 °C (Curing start), where such assembly deforms and is stressed as a result of its own heterogeneous multi-layered nature, but its deformation/stress states are not quite affected by the interaction with the fluid resin.

In the second heating phase beyond 50 °C, the curing resin progressively solidifies and increases its elastic modulus, gradually introducing more and more intense constraints to the deformation of the Copper-to-Poly assembly, until the temperature of 150 °C is reached. At 150 °C, the solidification is assumed completed and the package becomes a single structural solid body. Beyond 150 °C, the resin stiffness does not change further.

Then, in the final part of the heating process, from 150 °C to 200 °C, as well as in the subsequent cooling phase down to 25 °C, the thermomechanical loading history is applied to a "new-born" structural component which is already pre-loaded and pre-strained due to the previous stages of the molding process.

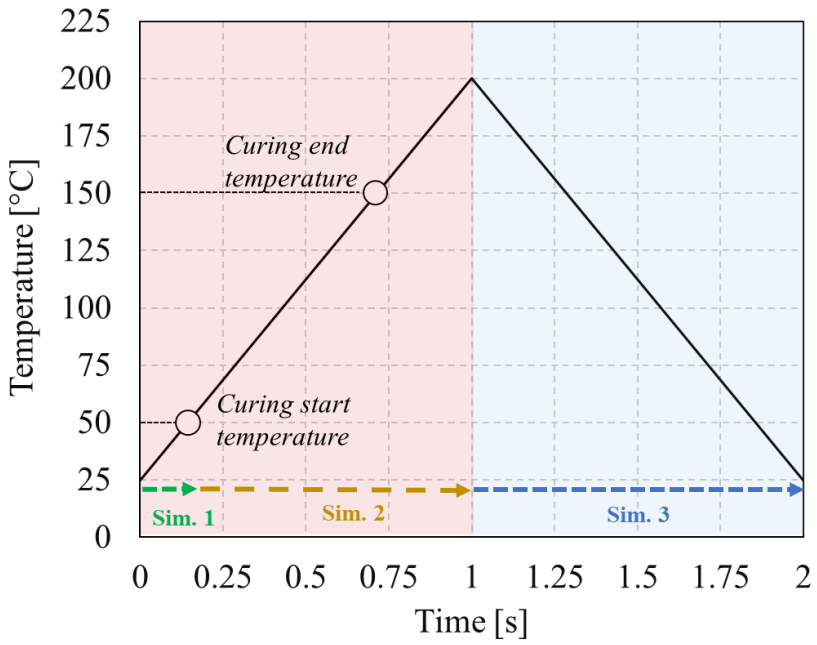


Figure 18: Simplified version of a quasi-static curing cycle. Sim1,2, and 3 highlight the time ranges at which all the three sub-analyses are run.

Numerical simulations of the resin molding process were performed by the commercial finite element code MSC Marc Mentat® v2023.4. Only a quarter of the package was modelled, taking into account the symmetries described in the paragraph 1.2. A schematic representation of the meshed package is given in Figure 19.

The resin volume above the polyimide, copper, and SiC layers was modelled using fully integrated eight-node iso-parametric hexahedral solid elements (SE) (Hex8-7 in Marc), while the

solder, TEOS, Si_3N_4, polyimide and internal resin (i.e., the part of resin filling the cavity formed by the passivation frame) were modelled using solid shell elements (SSE) having eight-node brick topology (Hex8-185 in Marc). The choice of these type of elements and formulations allows a better definition of the contact between the different layers as well as a better discretization of the resin mesh, without excessively increasing the computational cost of the analysis.

In this simulation, the epoxy encapsulation was manually generated, without using the automatic meshing tool. Due to the simplicity of the model, the mesh was generated by first creating a planar subdivision of a model section (e.g., the section lying in the x–y plane), and then extruding these planar elements along the third orthogonal direction (e.g., the z-direction). This approach provides finer control over the elements' aspect ratio compared to what is typically achievable with automatic meshing procedures. The other ‘’thick’’ layers have been discretized diving their thickness into, respectively: 10 elements for the Copper layer; 4 elements for the Solder layer; 5 elements for the SiC layer. The thinner layers such as: TEOS, Si_3N_4, Polyimide, and Internal resin feature only one division along their thickness.

The overall model counts of 16176 elements and 20101 nodes. Table 7 compiles the dimensions of each component as well as details on the mesh used for their discretization, i.e., elements type, number of elements and the average element size.

The interaction between adjacent layers was considered perfectly rigid as well as done in the paragraphs 1.1 and 2.1. Then, the internal constrains have been implemented by using the Glued contact in Marc Mentat. The contact table connecting the layers is the same of that one reported in the Table 3, except for the addition of Polyimide layer, which is perfectly glued on both its faces (one in contact with the Si_3N_4 layer, and the other with the resin encapsulation above).

The external constraints previously described in the paragraph 1.1 were replaced with a rigid plane in touching contact at the base of the model (x-z plane or y=0). This alternative contact formulation allows the implementation of the following mathematical condition (3):

(*3*) $$y \geq 0 \; for\ each\ node\ in\ contact\ with\ the\ rigid\ plane$$

The conditions expressing the symmetry of the quarter of model are the following (Eq. (4):

(*4*) $$\begin{cases} u_z = \phi_x = \phi_y = 0 & for\ each\ node\ belonging\ to\ z = 0\ plane\ (x - y\ plane) \\ u_x = \phi_z = \phi_y = 0 & for\ each\ node\ belonging\ to\ x = 0\ plane\ (z - y\ plane) \end{cases}$$

where ϕ_i is the rotation around the i direction. The combination of Eqs. (3) and (4) locks the vertical rigid motion of the package, without constraining its deformation displacements along all directions.

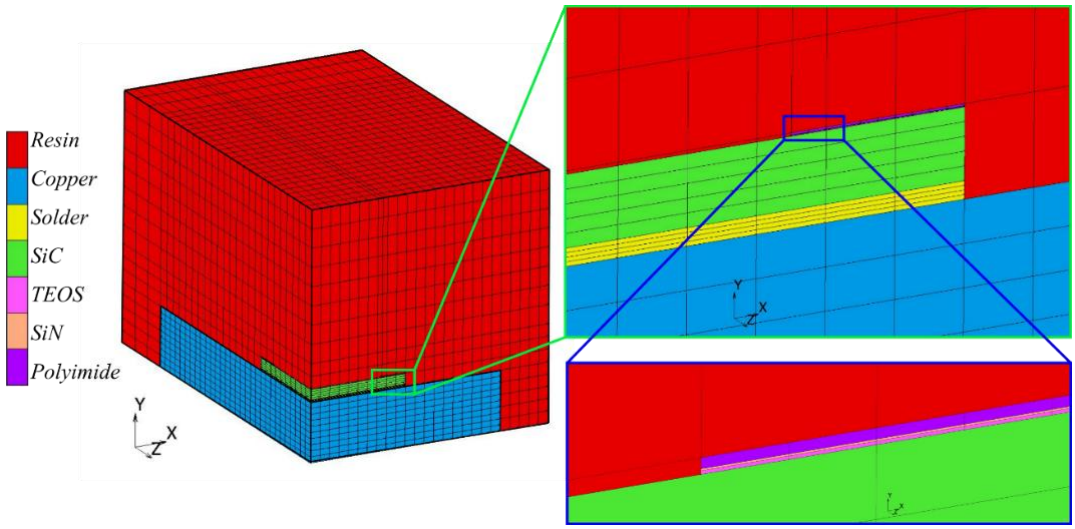


Figure 19: Mesh of a quarter model of the simulated package.

	Length along x [mm]	*Length along z [mm]*	*Thickness [mm]*	*Element Geometry and Formulation*	*Avg. Element size (x-z-y) [mm x mm x mm]*	*Number of Elements [-]*
External Resin	5	7.5	5	Brick Hex8	0.2x0.25x0.24	8628
Internal Resin	1.5	1.5	9×10^{-3}	Solid Shell Hex8	0.2x0.25x0.009	48
Polyimide	2	2	6×10^{-3}	Solid Shell Hex8	0.05x0.15x0.006	200
Si_3N_4	2	2	1×10^{-3}	Solid Shell Hex8	0.05x0.15x0.001	200
TEOS	2	2	2×10^{-3}	Solid Shell Hex8	0.05x0.15x0.002	200
SiC	2	2	0.2	Brick Hex8	0.2x0.2x0.04	500
Solder	2	2	0.05	Solid Shell Hex8	0.2x0.2x0.0125	400
Copper	4	6	1.2	Brick Hex8	0.2x0.2x0.12	6000

Table 7: Main features of the elements discretizing the simulated quarter of power module.

The meshing features adopted here (mesh sizes, subdivisions of layers thickness, aspect ratios, model zones where to adopt refined/coarser meshes) complied with the knowledge previously acquired in 2.3.1, where a global-local approach demonstrated the suitability of the opportune global mesh to fairly reproduce the mechanical response of the package beyond the effect of mesh sensitivity.

According to the Figure 18, the thermal load has been modelled as a heating-cooling cycle between the ambient temperature (25 °C) and the maximum temperature of 200 °C. This temperature was uniformly imposed all over the entire package.

The material properties of the brittle layers such as: SiC, TEOS, and Si_3N_4 were assumed linear, pure elastic and, as first approximation, temperature independent. The linear thermal-mechanical properties of all layers, considered at ambient temperature, are summarized in the

Table 8.

The ductile layers (copper, solder, and polyimide) were considered to be elastoplastic. The adopted plasticity model was the classic Von Mises/ J2-plasticity, combined with isotropic hardening. The experimental data of the copper and polyimide elastoplastic curve were obtained from the works of Kabaar et al. [29] and Agag et al. [30]. The equations of the materials' flow curves, expressing the relationship between the equivalent/effective stress and the equivalent/effective plastic strain are reported below (Figure 20). The copper and polyimide curves are fitted by means of a simple Ludwick's law.

$$\sigma_{eq} = \begin{cases} 43.5 + 10.7\epsilon_{eq} & (PbSnAg\ solder)\ ^{7} \\ 31.95 + 641.96\,\epsilon_{eq}^{0.67} & (Copper) \\ 95 + 165.79\,\epsilon_{eq}^{0.34} & (Polyimide) \end{cases} \quad (5)$$

Regarding the resin, as mentioned before, its mechanical behavior is strongly linked to the curing start and curing end temperatures. The evolution of its Young's modulus, during the reaction of polymerization, was assumed temperature dependent and approximable by a simple linear piecewise function (Figure 21).

	Mass density	Young's Modulus	Poisson's Ratio	Isotropic Thermal Expansion
	[tonnes / mm^3]	*[MPa]*	*[-]*	*[10^{-6} ºC^{-1}]*
Resin (after curing)	1.21 x 10^{-9}	25000*	0.34	12.0
Copper	8.96 x 10^{-9}	125000	0.3	17.5

[7] The PbSnAg solder flow curve was estimated based on the data reported in the Matweb datasheet, at the following link: https://www.matweb.com/search/datasheet.aspx?matguid=3a5c8bc670914d588b26ab0b994d88cb&ckck=1 (accessed on 1 November 2025).

Solder	6.54 x 10^{-9}	5600	0.4	29.0
SiC	3.21 x 10^{-9}	410000	0.28	4.0
TEOS	1.04 x 10^{-9}	59000	0.25	1.0
Si_3N_4	3.17 x 10^{-9}	300000	0.29	3.4
Polyimide	1.15 x 10^{-9}	3000	0.34	50.0

Table 8: Linear thermal-mechanical properties of the layers at ambient temperature.

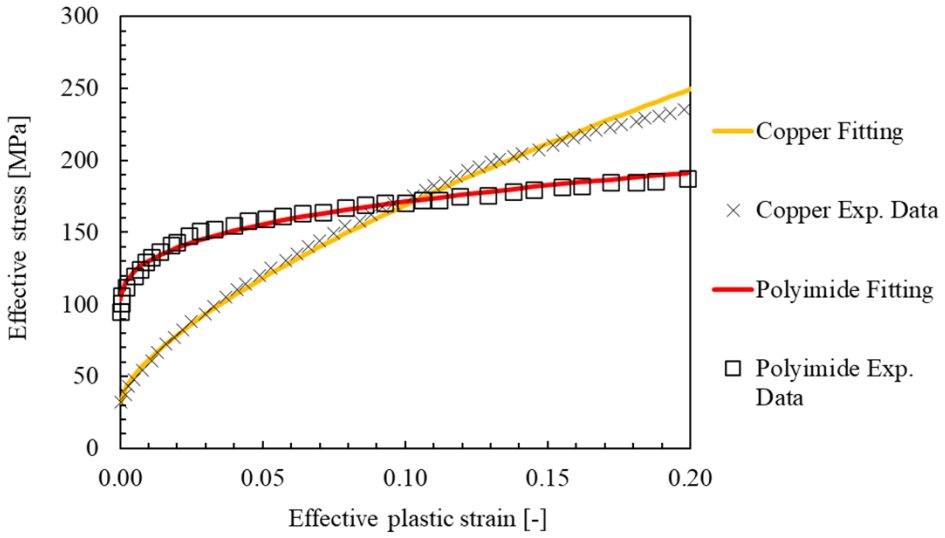


Figure 20: Flow curves and their fittings for copper [29] and polyimide [30].

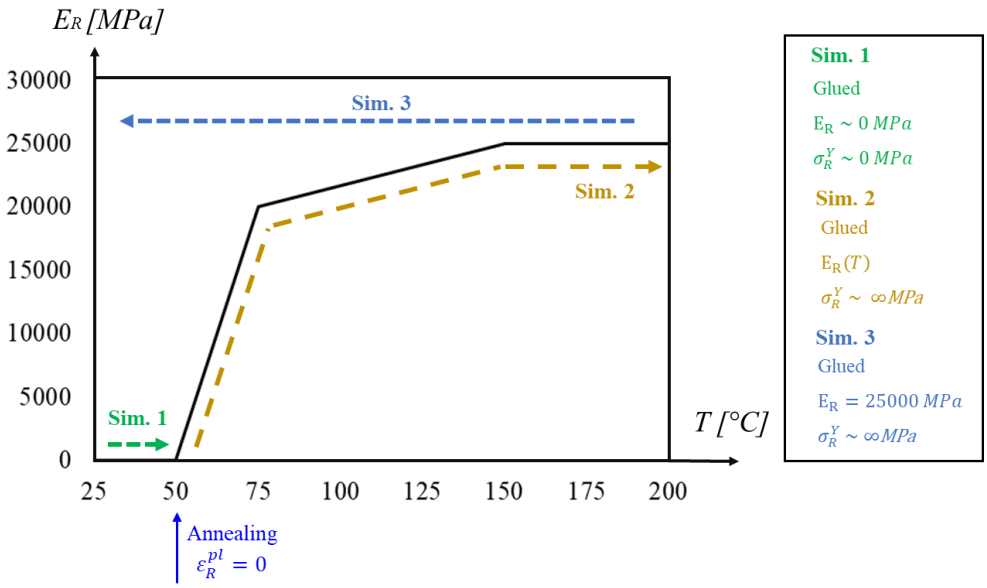


Figure 21: Schematic representation of the evolution of the epoxy resin Young's modulus during the curing cycle. The thermal cycle is subdivided in three different simulations indicated by arrows. A zeroing of the plastic strains in the resin takes place at the end of the first simulation.

The mechanical interaction between the Copper-to-Poly assembly and the adhering resin, experiencing a fluid to solid phase change, was approached by subdividing the simulation of the whole molding process into three sub-analyses, where the boundary conditions, the stress state and the constraints derived from an analysis constitute the input to the successive one.

This splitting of the load case was necessary to implement modifications to the model between an analysis and the successive, trying to simulate the irreversible process involving the resin.

In the first analysis (*Sim. 1*), the resin was assumed to be a perfect elasto-plastic solid with negligible yield stress and elastic modulus, in order to mimic its behavior during the liquid state.

This assumption is a relevant approximation in the modelling of the viscous behavior of the resin, but it is suitable for avoiding other difficult approaches regarding the solid-fluid interaction. As a result of the first analysis, the modelled resin follows the thermal deformation of the Copper-to-Poly assembly without opposing significant resistance, in analogy to what the fluid resin does in the real molding process.

It is important to note that, in this stage, the extremely low yield stress assigned to the resin guarantees that it plastically deforms without accumulating elastic strain. Such permanent deformation is then zeroed at the end of the first analysis, so that the strain history of the resin during its fluid phase is reset.

It might be tempting to model the resin in Sim. 1 as a purely elastic material with an extremely low stiffness. However, preliminary simulations showed that this simplification leads to significant issues. Specifically, it results in large elastic strains that cannot be reset during the annealing step, which only affects the plastic strain component. These residual elastic strains remain inactive -as long as the resin's elastic modulus is negligible in the fluid phase- but they become problematic in later stages. As the resin cures and its stiffness increases, these previously negligible strains "awaken", generating unrealistically high stresses and compromising the accuracy of the simulation.

At 50 °C the Resin is completely stress-free while the "Copper-to-Poly" assembly is not in this condition. The resin is stretched and deformed, following the warped shape of the "Copper-to-Poly" assembly, but it is not generating any stress nor is it storing any elastic strain which would generate ''unrealistic'' stresses in the successive simulation stages.

In the second simulation phase (*Sim. 2*), the temperature increases from 50 °C (curing-start temperature) to 200 °C. Now the resin is simulated as purely non-linear elastic material, having very

high yield stress, with Young's modulus evolving according to the reference curve of Figure 21. Note that, in *Sim. 2*, the elastic modulus evolves gradually together with the temperature, which triggers the progressive build-up of possible relative deformation between different layers and, consequently, the gradual continuous development of internal stresses and strains. The temperature of 150 °C is assumed to be the *curing-end temperature*, at which the solidification of the resin is completed and its elasticity modulus reached the final value, maintaining it constant for the rest of the simulation. At the end of this stage, the package is finally formed, and no further changes in its physical properties occur.

If the elastoplastic properties of ductile layers are properly considered in the simulation, then permanent deformations and residual stresses are predicted during the thermal load history, especially during the post-cure heating phase up to 200 °C and the successive cooling stage to room temperature. Obviously, such plastic strains are added to those ones already cumulated during the curing reaction, between 50 °C and 150 °C.

The further increase in temperature above 150 °C reflects a practice adopted in the industry to ensure that all the resin into the mold is totally cured (degree of cure > 90 %) and it is perfectly adherent to the Copper-to-Poly assembly. This practice prevents the formation of dry spots, which are local defects potentially leading stress concentration phenomena and electric failure due to the lack of insulation.

The last sub-simulation (*Sim. 3*) regards the cooling phase of the thermal cycle, from 200 °C to 25 °C, during which the reaction of polymerization stops into the solid resin and no further changes in its mechanical properties take place, while the ductile layers can plastically deform. Then, in *Sim. 3*, the elastic modulus of the resin is assumed fixed to its asymptotic value reached at the curing-end temperature, independently of the decreasing temperature imposed to the package. This approximation can be improved considering a cured resin's elastic modulus dependent on the temperature, but its variation (three order of magnitude less than the variation featured during the chemical reaction) has a negligible effect on the thermal stress at the end of the strain history.

3.3 Results and discussion

The modelling procedure described before allows to reproduce the interplaying changes of the structural features and the thermo-mechanical loading modes occurring together as the encapsulating resin interacts with the copper-to-poly assembly, in conjunction with the progression of the curing reaction. Considering the frame of reference Ox-y-z shown in Figure 22a, all the six components of

the stress tensor were taken along the paths highlighted with the dashed arrows at different interfaces. These interfaces are the following: Interface 1 is the copper/solder interface if the path's arc length varies between 0 and 2.83 mm (Figure 22a), assuming the origin in the y-axis. It changes in Copper/Resin interface as the arc length lies between 2.83 mm and 5.66 mm. Interface 2 is the Solder/SiC interface. Interface 3 is the SiC/Resin if the arc length is between 0 and 2.12 mm, and SiC/TEOS interface in the last part of the path (between 2.12 and 2.83 mm). Interface 4 is the TEOS/Si_3N_4 interface, while the Interface 5 is the Si_3N_4/Polyimide interface. Remember that these passivation layers have the shape of a square frame, then the relevant information are extracted along the diagonal paths, for an abscissa between 2.12 and 2.83 mm. Finally, the last Interface 6 denotes the Polyimide/Resin interface.

These diagonal paths show the variation of the stress distributions due to the changing of material through the thickness (y-direction) and through the path itself. In the denomination of the stress components, the numbers 1, 2, and 3 will be used in substitution to the letters x, y and z (1=x, 2=y, 3=z).

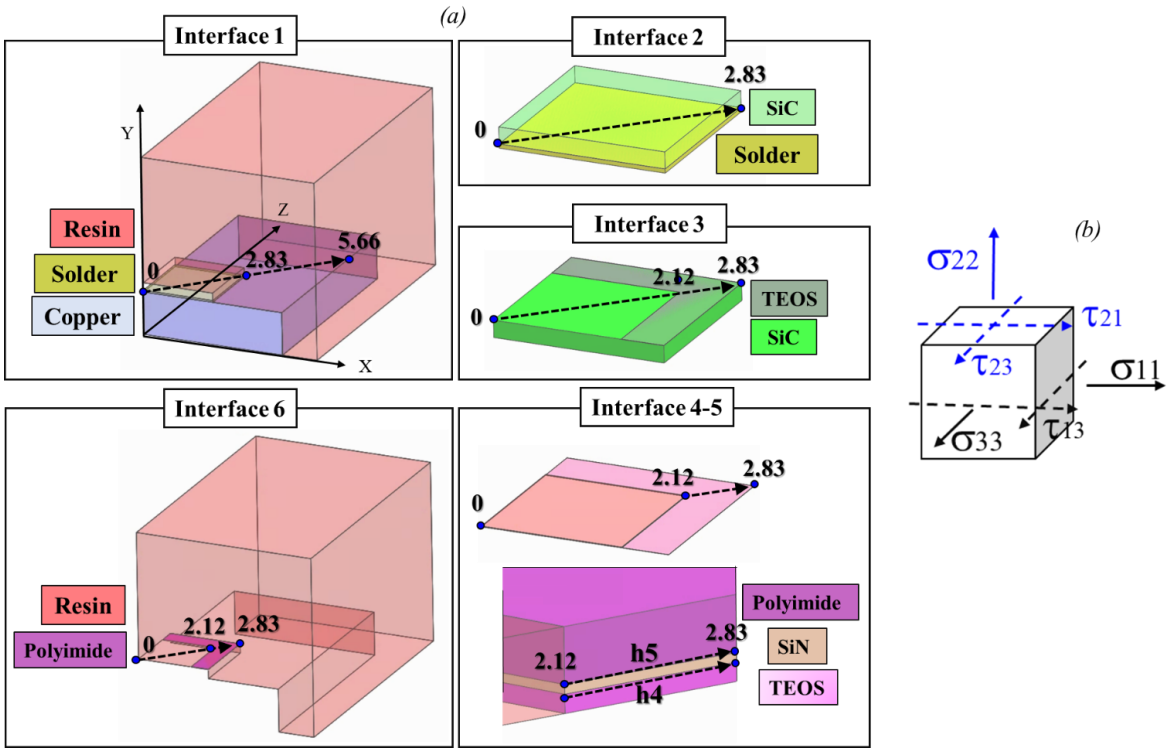


Figure 22: a) Schematic representations of the paths extracted at six different interfaces. b) representation of normal and shear stress tensor components on the elementary material's cube: blue arrows indicate the stress components which are equal in each side of the same interface, while the black ones indicate the stress components acting just above or below a specific material.

Figure 22b provides a schematic representation of all the stress components considered, with the x-z plane corresponding to the plane parallel to all the layers. The blue arrows indicate one normal

stress, σ_{22}, and two shear stresses, τ_{21} and τ_{23}, acting at generic interface between two adjacent layers. From a trivial consideration deriving by the action-reaction principle of the dynamics, these stress components must be continuous across the interface, since they are identical just above and below the plane of the interface. They are the primary contributors to the initiation of interlaminar damage. Moreover, in the case of a symmetric package, the two shear stress components along the considered path are equal in absolute value.

In contrast, the other stress components, two normal stresses, σ_{11} and σ_{33}, and the remaining in-plane shear stress, τ_{13}, act within the single layer and they are discontinuous across the interfaces. Their gradients through the thickness depend on the mismatch between the thermal-mechanical properties (coefficient of thermal expansion and elastic modulus) of the materials in contact. These components are the primary drivers of the interfacial debonding or delamination, but may lead to damage within the bulk materials themselves.

In the following sections, all stress components are quantified along selected paths both at the peak temperature (200 °C) and at the end of the cooling phase (25 °C). Subsequently, the residual plastic deformation at 25 °C in copper, solder, and polyimide is evaluated and discussed. Finally, the onset of out-of-plane deformation (warpage) is analyzed both at 200 °C and after the production process is complete (residual warpage).

3.3.1 Components of stress at different interfaces, evaluated at the maximum temperature

Figure 23 presents the distribution of all stress components along the defined paths at each individual interface (as also indicated in Figure 22), evaluated at the peak process temperature of 200 °C. Each horizontal row corresponds to a specific interface within the package, while the columns distinguish between: components of stress in common (or continuous) at the interface between material A and B, components of stress above the interface (material A), components of stress below the interface (material B).

To make clear the comparison of stress levels across all critical regions of the package, uniform color scales have been applied to the plots in Figure 23. This approach emphasizes the location and relative magnitude of stress peaks, even though it may obscure finer details in low-stress regions. Among all layers, the silicon carbide (SiC) die exhibits the highest stress levels at 200 °C, due to its significantly higher stiffness compared to the surrounding materials. Nevertheless, the absolute stress values in each layer must be assessed in relation to the mechanical limits of the

corresponding material -such as yield strength or ultimate strength - to evaluate their potential role in initiating failure.

For improved clarity, Figure 24 compiles the maximum, average, and minimum stress values at each interface. The stress state at 200 °C is particularly important, as it represents the most critical thermal condition experienced during the manufacturing process, where thermal expansion induces significant mechanical loading. Finally, the peak interface stresses (in absolute terms) are compared against relevant material strength data from the literature, in order to assess the likelihood of failure or damage initiation.

In [29], the authors reported three tensile stress-strain curves for copper specimens produced via different processes: no annealing, annealing and free cooling, annealing and free cooling when the copper is attached to a ceramic layer. This last specimen is particularly important for the present work as it reproduce a semi-worked assembly similar to the three-layer structure copper-solder-SiC.

In the case of no-annealed copper, the failure stress is about 330 MPa. On the contrary, as expected, the annealed metal presents lower fracture stress of about 250 MPa but larger ductility (approximately 2.5 times greater than the no-annealed copper). The last copper-ceramic specimen given in [29], similar to the one used in power electronic applications, presents lower fracture stress and ductility, about 155 MPa and slightly above 0.15, respectively. In the FE simulation the greatest (in absolute value) compressive stress is found at the Interface 1, located precisely at the copper/solder interface (copper side), i.e., $\sigma_{11} = -34$ MPa.

In [31], the authors investigated the mechanical properties of a PbSn based solder joints used for electronics components. They reported a failure stress in tension between 60-80 MPa, while in this FE model, the maximum (compressive) stress found at the copper/solder interface (solder side) is $\sigma_{11} = -27$ MPa. Similarly, according to the data given in the Matweb online datasheet[8], the ultimate tensile strength of an eutectic PbSn solder is of 52 MPa. Even though the ultimate tensile strength does not directly give an indication on the failure stress, it suggests that also at the maximum temperature, the material still remains in the uniform deformation regime and no stress/strain localization takes place.

[8] Mechanical properties of eutectic solder 63Sn-37Pb. Link at the online datasheet: Eutectic Solder (63Sn-37Pb) - ASTM B 32 Grade Sn63 (accessed on 1 November 2025).

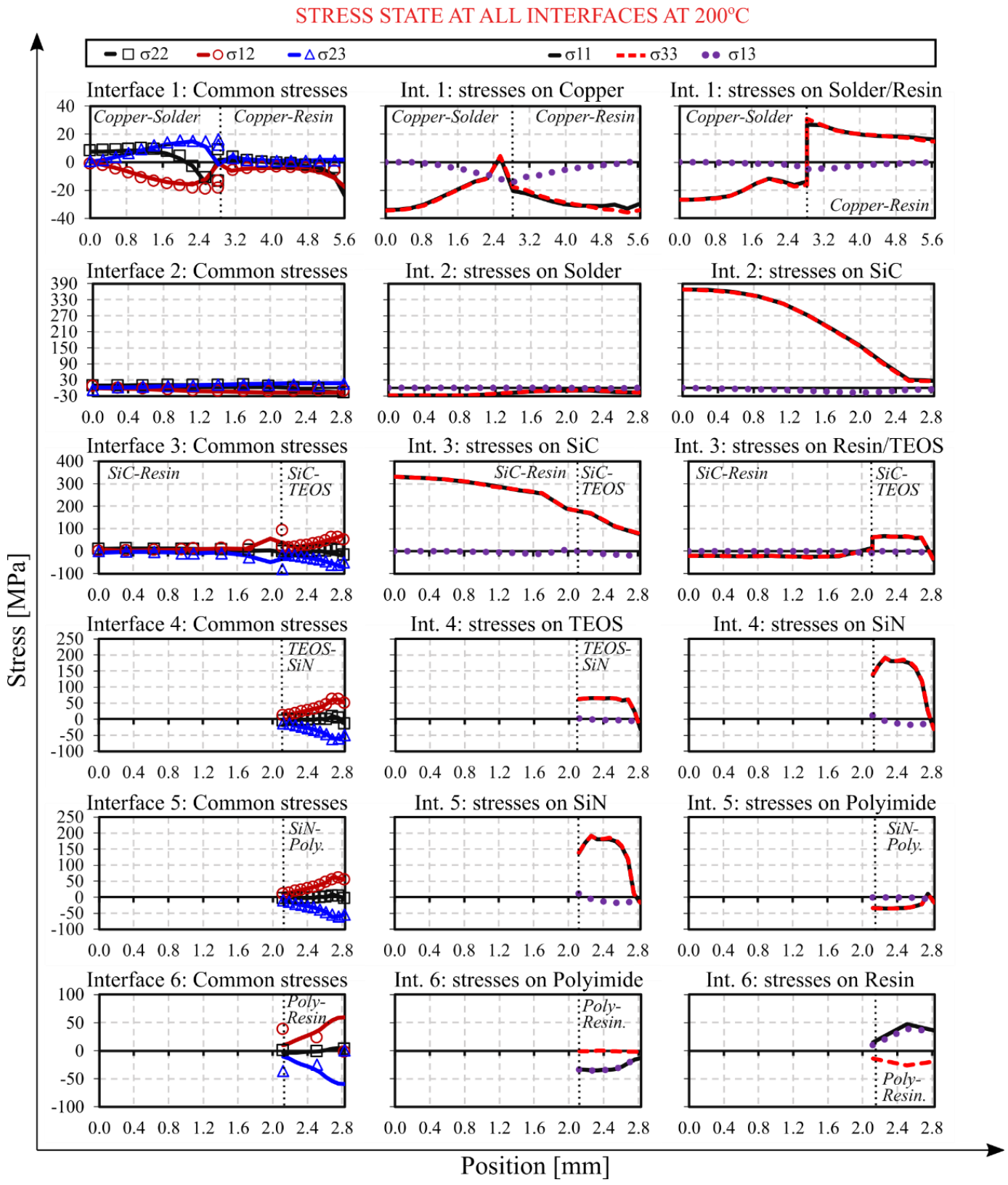


Figure 23: Stress distributions at all interfaces along the paths given in Figure 22 at the peak temperature, T = 200 °C.

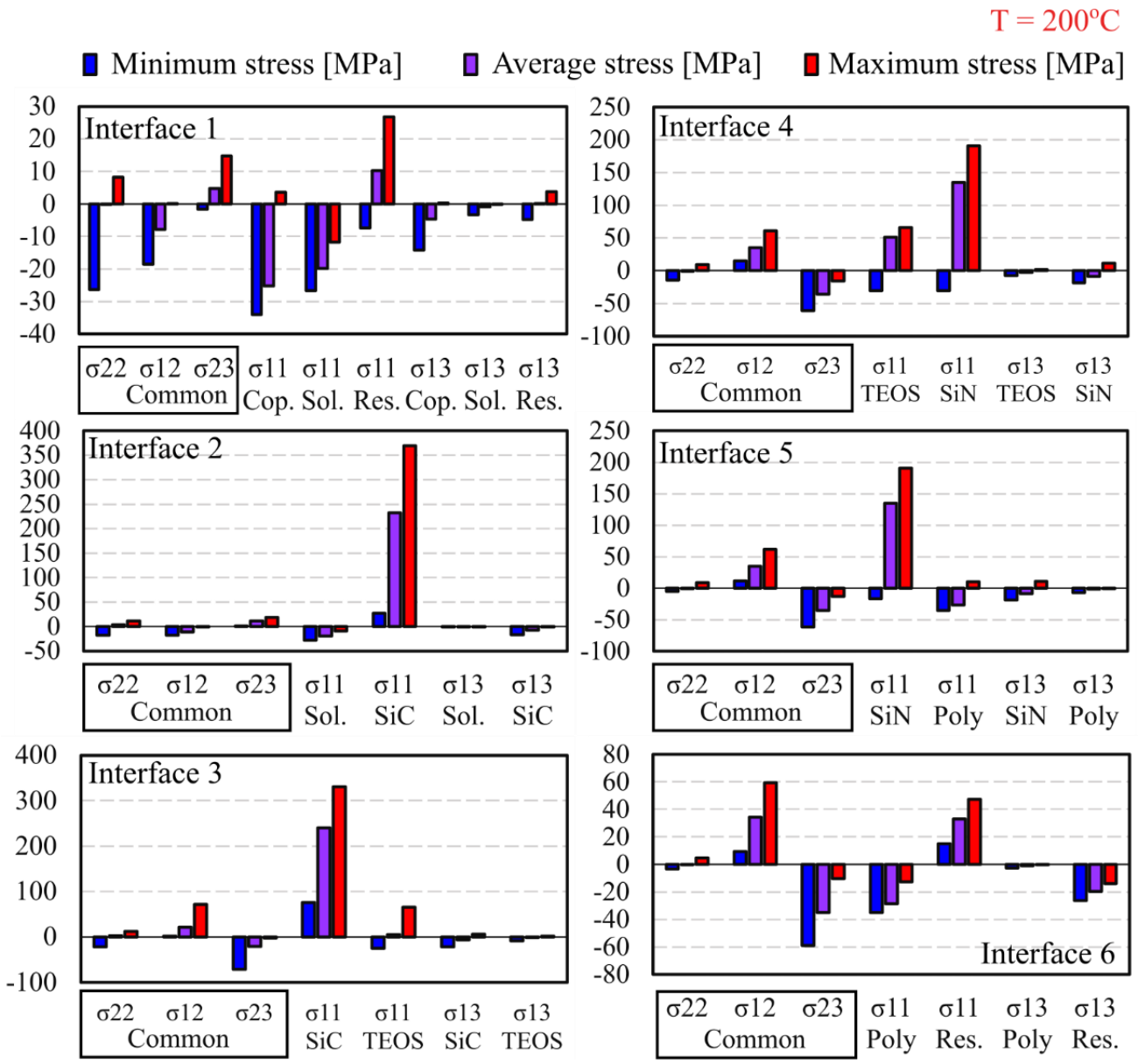


Figure 24: Minimum, average and maximum stresses along all considered interfaces at the peak temperature, T = 200°C.

It is possible to observe that the most stressed layer of the package is the SiC one, due to its high elastic modulus. In particular, the Interface 2 (Solder/SiC) features a maximum (tensile) normal of 369 MPa on the SiC side. This value is crucial for the reliability of the package and its total lifetime, since this critical interface is frequently subjected to failure phenomena documented in the literature [32,33]. Considering a α-SiC, the tensile strength values at room temperature have been found to range between 180 and 270 MPa [34]. In contrast, four-point and three-point bending tests yield flexural strength values between 330 and 400 MPa. The comparison between these experimental values and FE results highlights that stress gradients -particularly at the Solder/SiC interface- may

originate from the manufacturing process itself. Such gradients could potentially lead the initiate damage in the SiC layer and thereby compromise the mechanical integrity of the entire component. No experimental data regarding the mechanical response of the TEOS have been found in the literature and no reference data are available for comparison with FE results. However, it is worth reporting a moderate maximum tensile stress from FE, $\sigma_{11} = 66$ MPa, and almost negligible shear stress $\tau_{13} = -6$ MPa. Numerous investigations have examined the mechanical response of silicon nitride (Si_3N_4) under dynamic cyclic loadings and creep tests [35,36]. With regard to its static mechanical properties at room temperature, the study in [36] reported tensile strength values ranging from 500 to 700 MPa. In the present FE simulation, at the maximum temperature, a peak of normal stress of σ_{11} = 191 MPa is reached in the Si_3N_4 layer. As reported in the Matmake online datasheet[9], the polyimides feature an ultimate tensile strength ranging between 70 and 150 MPa. According to the results of the FE simulation performed for this work, at the maximum temperature, the polyimide layer experiences a normal stress of σ_{11} = –35 MPa and a negligible in-plane shear stress of τ_{13}= –3 MPa. At interface 6 (polyimide/resin), the simulation reveals a peak value of interlaminar shear stress of τ_{12} = 59 MPa. These results indicate that interface 6 may represent another critical location for damage initiation, primarily driven by interlaminar shear stresses.

According to the data reported in the Matweb online datasheet, the ultimate tensile strength of an epoxy molding compound[10] can vary between 14 and 300 MPa, depending on its chemical composition and the parameters governing its production process. In the work of Bouzakis et al. [37], the authors investigated the tensile response of another epoxy resin. The authors reported values of maximum tensile strength ranging between 30 and 45 MPa. As observed in the diagram of Figure 24 (polyimide/resin interface 6), the maximum tensile stress acting within the resin layer is $\sigma_{11} = 47$ MPa. On the other hand, the maximum interlaminar shear stress is $\tau_{12} = 59$ MPa. Concerning the stresses acting at the interfaces, the greatest normal stress is found at the copper/resin interface, $\sigma_{22} = -26$ MPa. This stress component might be responsible for the fracture mode I at the interface between these two materials. On the other hand, the maximum interlaminar shear stress, responsible for the fracture mode II and III, is found at the SiC/TEOS and is equal to 72 MPa.

[9] Mechanical properties of polyimides. Link at the Matmake datasheet: Polyimide (PI) - Properties (accessed on 1 November 2025).

[10] Overview of the mechanical properties of Epoxy Molding Compound (EMC). Link at the online datasheet: Overview of materials for Epoxy Molding Compound (accessed on 1 November 2025).

3.3.2 Components of stress at different interfaces, evaluated at the end of curing process (residual stresses)

The plots reported in Figure 25 shows the distributions of the six components of the stress tensor taken along the paths at each interface, as shown in Figure 22, at the end of the cooling phase of the curing cycle (T=25 °C). For improving the readability and highlighting the key results of the analysis, the maximum, average and minimum stresses, for each path, are summarized in the following Figure 26. As it is observable from these two figures, the power module remains internally stressed at the end of the curing cycle, featuring significant residual stresses. This aspect is crucial for the reliability analyses of these electronic devices, since these components are generally assumed perfectly unstressed and undeformed once they complete all the stages of the manufacturing process.

This FE simulation highlights that if the elasto-plastic behavior of the materials inside the multilaminar component is properly taken into account, the curing cycle and other manufacturing stages involving thermal loads give a significant contribution in the accumulation of plastic (irreversible and permanent) strains within the structure.

Another interesting observation deriving from the comparison of the results reported into the diagrams of Figure 24 and Figure 26 is that some stress components change their sign during the strain history. For instance, the copper layer passes from a compressive stress state at 200 °C to a tensile state at 25 °C. On the contrary, the resin encapsulation is subjected to a tensile stress state at 200 °C while it is compressed at 25 °C. In general, the change of sign in the thermomechanical stresses throughout the curing process is related to the changing of the deformed shape assumed by the whole package, which alters an upward concavity (smiling) to upward convexity (crying) or vice versa.

During heating, at each interface, the layers with higher coefficients of thermal expansion (CTE) tend to experience compression, while those with lower CTE are subjected to tension. This occurs due to the mutual mechanical interaction, where the expansion of the former is constrained and the extension of the latter is enhanced. Additionally, plastic strains in ductile layers further influence this overall behavior.

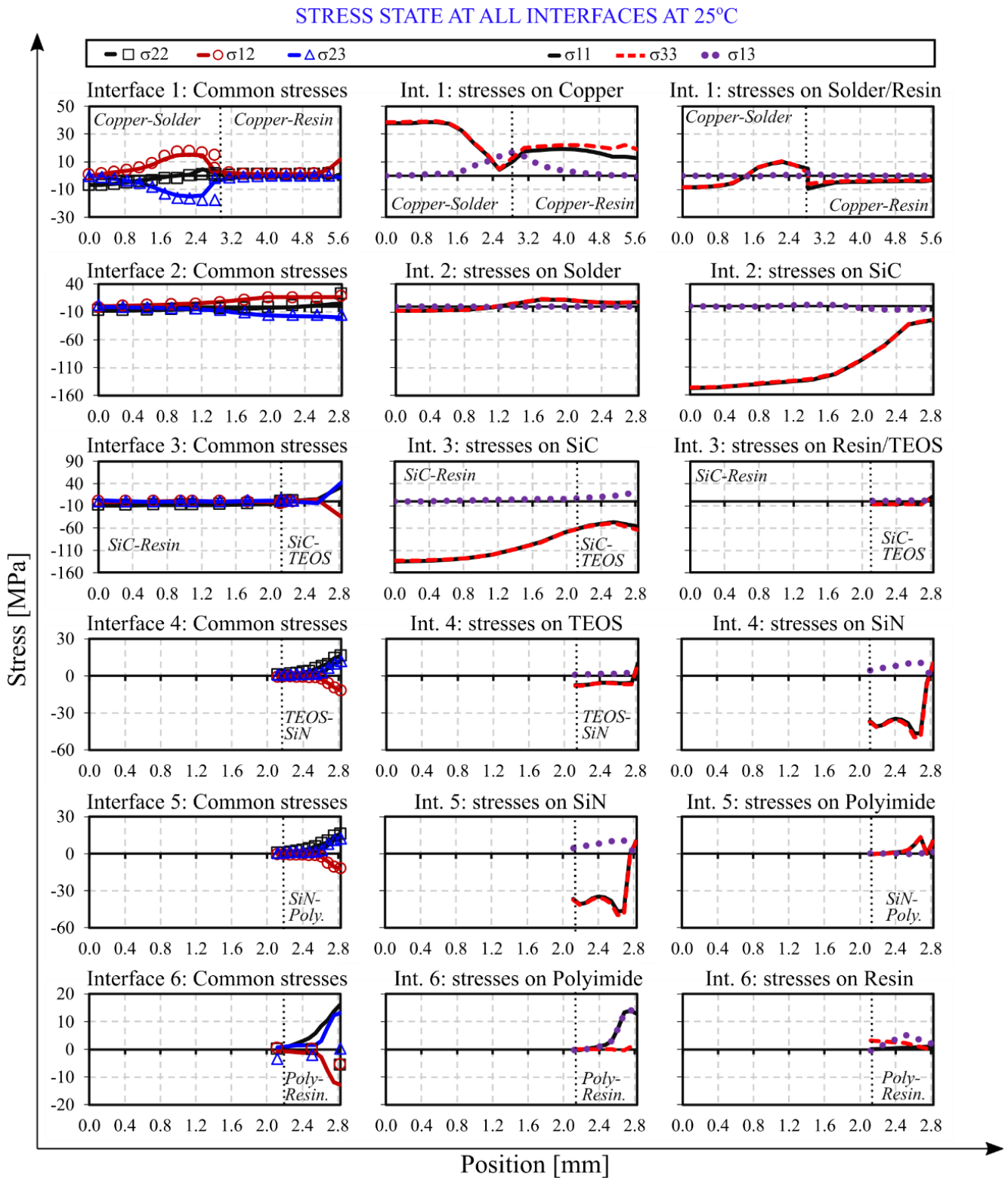


Figure 25: Stress distributions at all interfaces along the paths given in Figure 22 at the end of cooling, T = 25 °C.

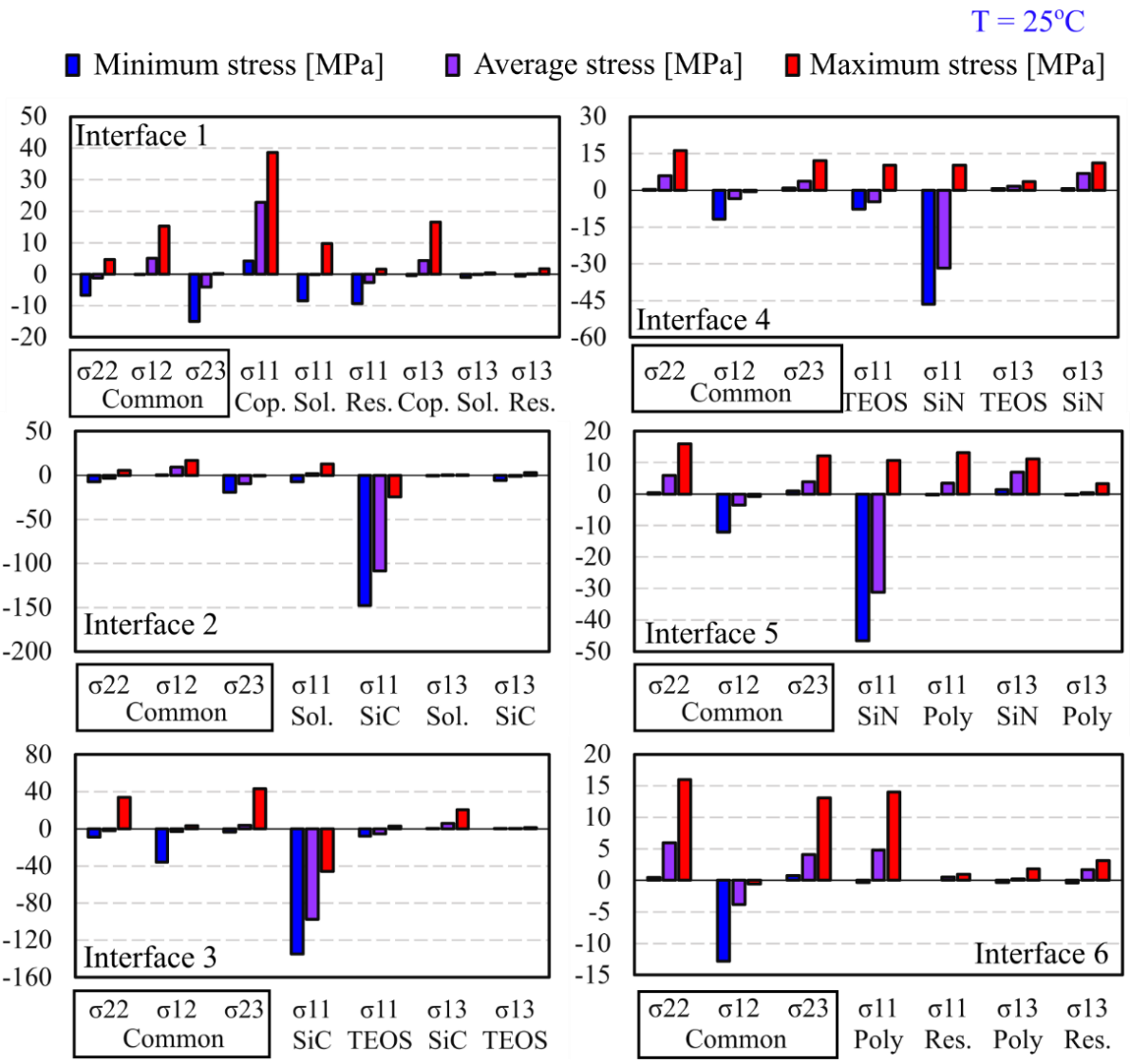


Figure 26: Minimum, average and maximum stresses along all considered interfaces at the end of the cooling stage of the curing cycle, T = 25 °C.

The following Figure 27 shows the distributions of the plastic strains accumulated at 200 °C and 25 °C at the interfaces where ductile layers are present. In particular, in Figure 27a, the equivalent accumulated plastic strain is considered in both nodes belonging to copper (solid line) and to solder (full square dots). During cooling, both copper and solder accumulate plastic deformation. On the other hand, no plastic deformation is accumulated in the polyimide irrespective of the considered interface.

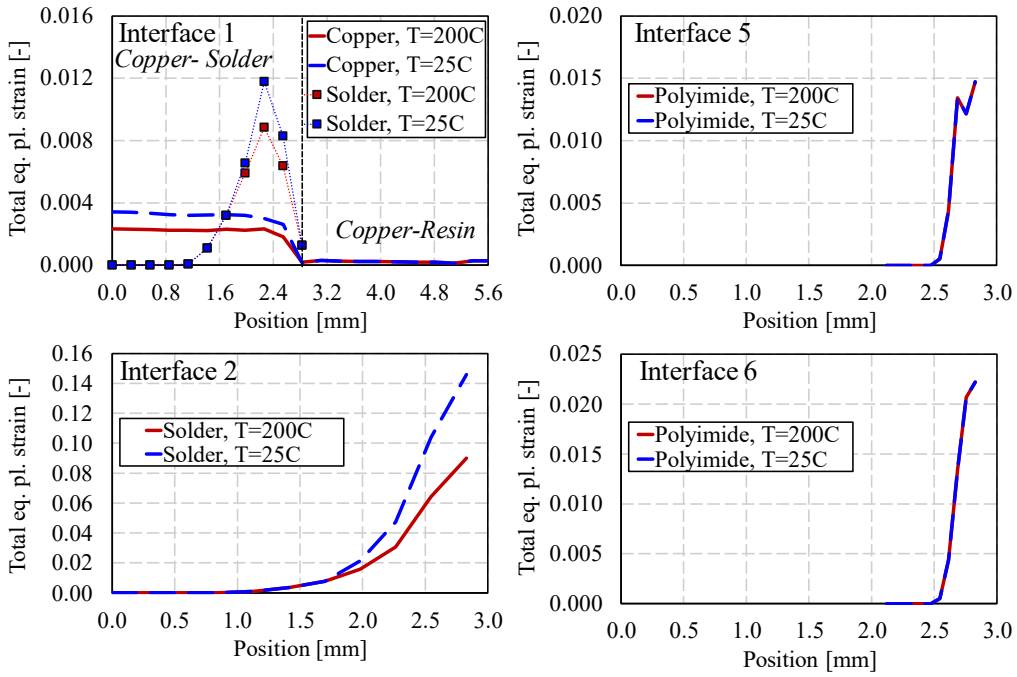


Figure 27: Distributions of plastic strains at the end of cooling phase of the thermal cycle, T = 25 °C.

When the temperature of the whole package returns to the ambient one, the distribution of equivalent plastic strain of the copper layer, taken just below the plane of the copper/solder interface, is almost uniform along the path and equal to 0.3%. On the other hand, looking at the same interface but just above it, this distribution on the solder is strongly variable, from nearly zero at the origin of the path, up to a maximum value of about 0.012 in the proximity of the sharp edge. The other side of the solder layer, at the interface with the SiC (interface 2) features higher values of plastic strain, reaching a maximum of 0.16.

In the polyimide layer, the distribution of plastic deformation exhibits a maximum value of 0.015 above the interface 5 (on the Si_3N_4 side) and 0.022 below the interface 6 (resin side), at the corner of its external boundary.

Figure 28 illustrates the equivalent plastic strain accumulated by the resin at the interfaces with SiC, polyimide, and copper before the start of curing. In Sim. 1 (between 25 °C and 49 °C), although the resin behaves as a viscous material, plastic strains appear due to the approximated modeling approach, not actual material behavior. The resin, with negligible yield stress, conforms to package deformation without developing internal stresses. At 50 °C, these strains are zeroed, setting a stress-free state for the curing phase. In Simulations 2 and 3, the resin is modelled as a non-linear elastic material -first with temperature-dependent modulus, then with constant modulus -without further plastic strain, accurately representing the variation in the mechanical properties during the polymerization.

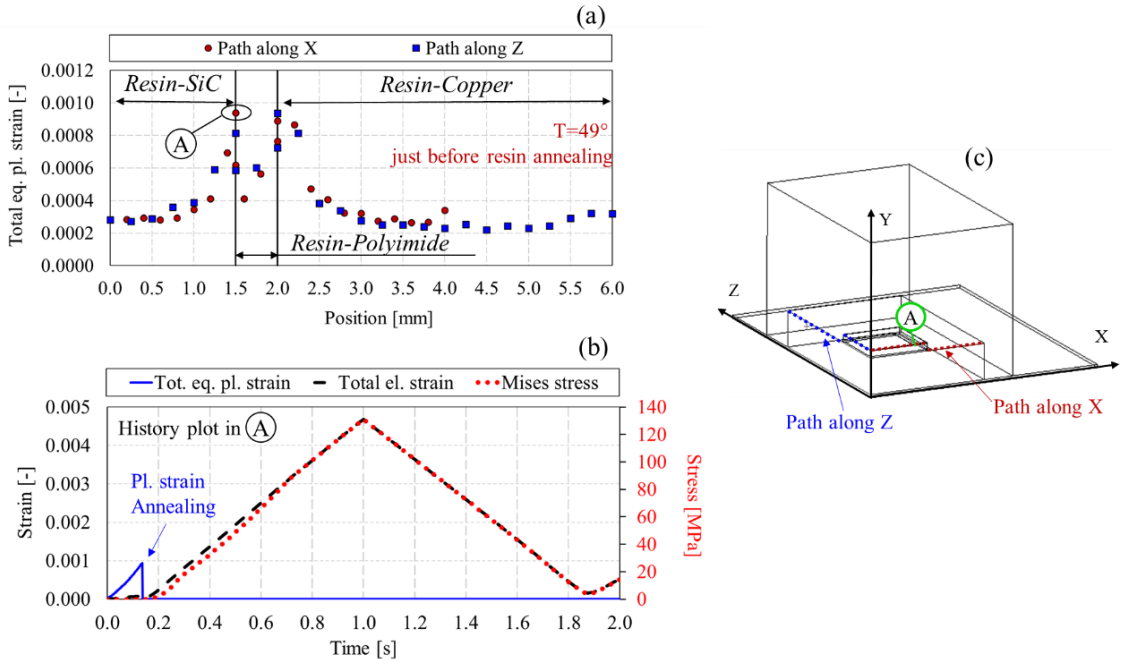


Figure 28: a) Total equivalent plastic strain along X and Z at the interfaces Resin-SiC, Resin-Polyimide and Resin-Copper and b) History plot the Total equivalent plastic strain, Total elastic strain and Mises stress at the resin location (A), of maximum plastic deformation before the zeroing.

3.3.3 Warpage behavior of the package at the end of curing process

In reliability studies conducted by industries on power modules, one of the key parameters measured is the warpage of the device, i.e., the out-of-plane displacement of the package points when it is subjected to thermal loads. The ideal condition would be the achievement of zero warpage at the end of each stage of the packaging manufacturing process. Zero warpage corresponds to perfectly planar layer surfaces, which would optimize the bonding between the different layers and improve thermal exchange within the power module when it is soldered onto the heat sink. Furthermore, if the module exhibits warpage phenomena, these are also associated with residual stresses within the device, which can lead to premature failure or degradation of its performance during operational life. Several works in the literature [8,28,38] confirm that cyclic thermomechanical loads in power modules result in their warpage. The warpage of the of the component modelled for the present work was analyzed, evaluating the out-of-plane displacement at the top side of the resin at the peak temperature 200 ℃ as well as at 25 °C, after the resin molding process is completed. Figure 29 shows that the solidification process can turn in a remarkable warpage at the top surface of the resin capsule.

Particularly, at 200 °C the greatest positive out-of-plane displacement is found at the outer corner of the component (“smiling” shape of the package), while after cooling down at 25 °C the

permanent deformations acquired confer higher positive out-of-plane displacements to the center points of the package (“crying” shape).

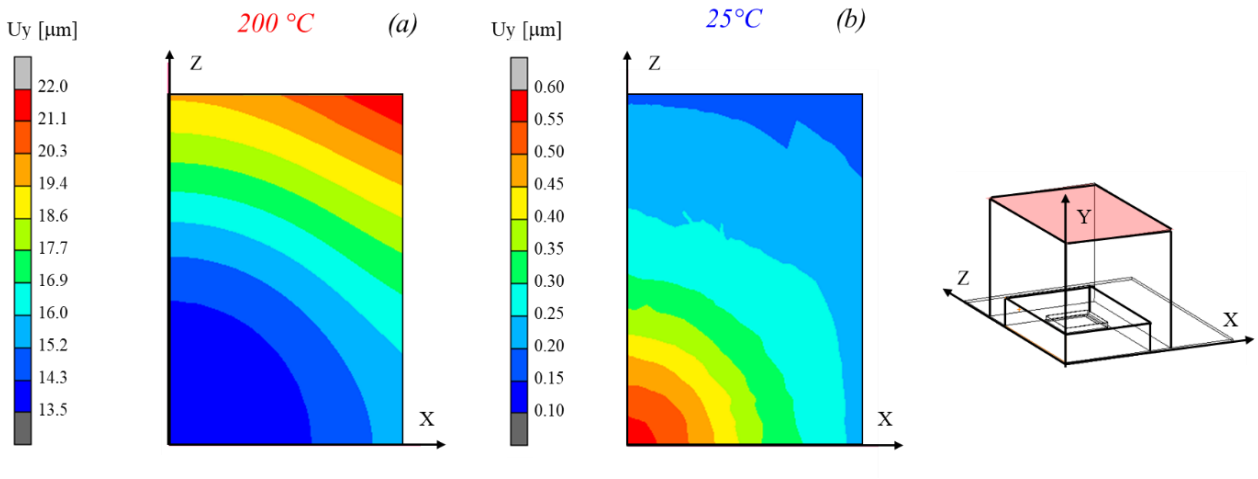


Figure 29: Contour plots out-of-plane displacement Uy at the a) peak temperature and a) at the end of cooling stage.

The warpage of the device is further examined by evaluating the out-of-plane displacement profiles along two orthogonal paths, one parallel to the x-axis and the other to the z-axis, both intersecting the center of the package’s top view at the mid-plane of the copper layer (see Figure 30).

At 200 °C, the displacement trends along both directions are nearly identical, indicating an almost symmetrical deformation pattern. However, after cooling to 25 °C, the trends along the X and Z directions tend to diverge, pointing to the development of an asymmetric deformed shape. Notably, the maximum out-of-plane displacement along the Z-direction does not occur at the copper edge (6 mm), as it does along the X-direction, but rather around 4 mm from the center. This behavior further supports the emergence of a "crying-type" deformation following the manufacturing process. The simulations clearly highlight that the geometry changes induced during the packaging process are non-negligible and that the initial post-process condition of the material must be properly accounted for in subsequent analyses. This finding highlights that the assumption of undeformed package as reference starting configuration in the reliability assessment of power modules [39–41] is approximated.

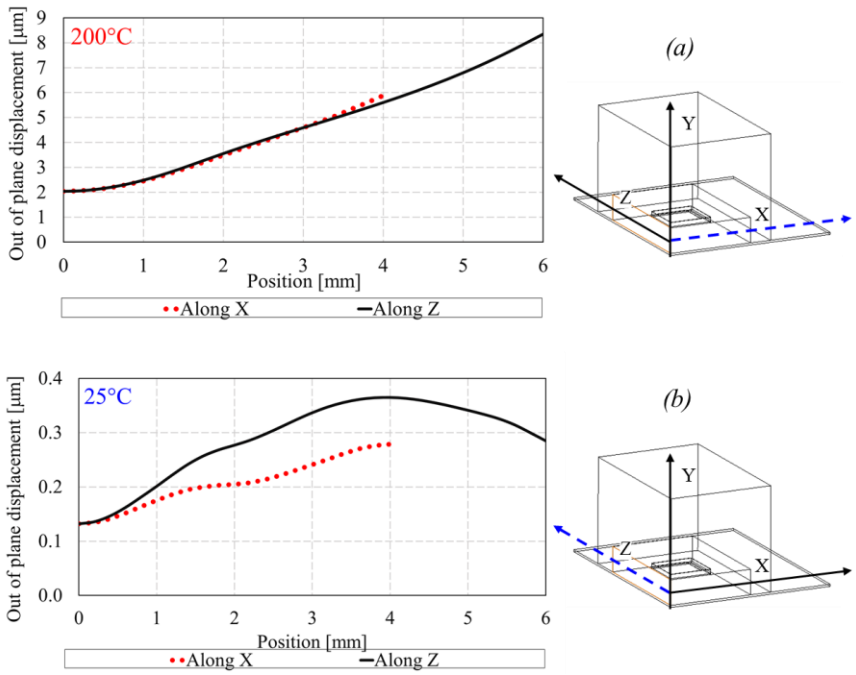


Figure 30: Path plots of the out-of-plane displacement at the middle section of the copper layer along the x-axis and z-axis, at the maximum temperature (top) and at the end of cooling stage (bottom).

3.4 Conclusions

In the present work, a thermo-mechanical modelling procedure for a Resin Transfer Molding (RTM) process has been proposed, as one of the manufacturing steps in the production of a power module package. The numerical study presented in this section specifically focuses on modelling the irreversible curing process of an epoxy molding compound and the mechanical interaction between the thermosetting polymer and the ceramic-metal substrate during the heating and cooling thermal cycle required for resin polymerization.

The chemical reaction, during which the mechanical properties of the resin evolve, was modelled as an irreversible non-linear mechanical behavior through three sub-simulations. In this approach, the resin's elastic modulus varies with temperature, starting from a very low value (typical of a viscous mechanical state) and progressively increasing to a plateau value corresponding to the glassy state.

The focus of the present study is on the stress and strain fields developed throughout the thermal cycle. The most stressed interfaces, both at the peak curing temperature and at the end of the cooling phase, are the SiC/solder, SiN/polyimide, and polyimide/resin interfaces. At the first two

interfaces, in-plane normal stress components are dominant, which can promote brittle fracture or ductile damage within the individual layers. At the last interface, interlaminar shear stresses are more critical, as they are responsible for delamination between the two materials.

The numerical analysis showed that, when the elasto-plastic properties of ductile materials (i.e., copper, solder, and polyimide) are properly taken into account, even a single curing thermal cycle can induce significant plastic deformation in these materials. As a result, a warpage of the entire package is observed, characterized by a positive concavity ("smiling" shape) at the curing temperature peak and a negative concavity ("crying" shape) after cooling.

It should be emphasized that, in order to validate the FEM analysis, experimental measurements of warpage on a commercial device with the same geometry as the simulated model are required. However, such experimental data are currently not available, as they are confidential and subjected to access restrictions by ST Microelectronics company.

Chapter 4: Models for the prediction of damage at the package's critical interfaces

During their operational life, power electronic packages must be able to work in different thermomechanical conditions and they are susceptible to various failure modes. One of the most critical failure mechanisms is delamination [42]. Delamination refers to the separation or detachment of layers at their interfaces, leading to performance degradation, compromised reliability, operational failure of electrical functions, and even catastrophic failure as the whole package breaks. Delamination can result from various factors, including mechanical stresses induced by temperature cycling, thermal expansion mismatch, and mechanical loading during operation. Understanding and predicting the behavior of delamination in power electronics packages is essential for ensuring their long-term reliability and optimal performance. Delamination issues primarily affect the interfaces between two joined materials. The mechanical properties of an interface are influenced not only by the mechanical properties of the individual materials involved in the joint, but also by the manner in which the interface itself has been created. For instance, in Active Metal Brazing (AMB) processes -used to join copper and silicon nitride layers- or in die passivation processes, where passivation layers are directly deposited onto the semiconductor wafer, bonding between layers is achieved through atomic diffusion and the development of adhesion forces between the two materials. In AMB brazing, as well as in die soldering onto copper, the formation of intermetallic compounds may occur at the transition zone between materials.

Although delamination is one of the most common failure modes in power packages, other types of damage can also occur within the bulk of individual layers, affecting both ductile and brittle materials. With regard to the metals employed in packaging, ductile damage mechanisms are of critical importance -particularly due to their relationship with fracture after a certain number of working cycles, as in the case of thermal fatigue in power modules. Ductile damage is characterized by a progressive degradation process within the material, generally articulated into three stages: void nucleation, void growth and coalescence, and finally, fracture propagation. Voids may originate from pre-existing material defects induced by processing or metallurgical treatments, or from the presence of inclusions or impurity atoms embedded in the microstructure. Local ductile damage phenomena are governed by a variety of factors, including the material's intrinsic properties, plastic deformation history, specimen geometry, and loading conditions (tension, compression, torsion, mixed-mode, etc.).

Another failure mechanism that can occurs in the electronic packages is the brittle fracture in the epoxy molding compounds used for the encapsulation. It is a critical failure mode arising from the inherently rigid and highly crosslinked molecular structure of these materials. Due to the absence of molecular mobility, thermosets exhibit negligible plastic deformation prior to fracture, making their failure behavior strongly brittle in nature. Crack initiation typically occurs at pre-existing microstructural defects such as voids formed from polymerization shrinkage, entrapped air bubbles, inhomogeneous crosslink density, or weak interfacial adhesion with fillers or fibers. Once a critical stress is reached, cracks propagate rapidly and unstably across the matrix, with minimal energy dissipation through plastic flow. The resulting fracture surfaces often display glassy, irregular morphologies with features such as chevron patterns or mirror zones indicative of brittle propagation [43].

Traditional experimental methods for studying these failure phenomena are time-consuming and costly and are limited by the ability to access critical regions within the package. Therefore, numerical simulations have emerged as a valuable tool to investigate and analyze delamination behavior in a more efficient and cost-effective manner.

In recent years, researchers have been utilizing Finite Element simulations to study the damage phenomena in power electronics packages and gain insights into their initiation and propagation mechanisms [26,44], despite the latter being significantly mesh dependent. In this field, the cohesive zone models (CZMs) approach has gained popularity in recent years due to its capability of modeling the complex interfacial behavior between layers. CZMs provide a phenomenological description of the fracture process by defining a class of mathematical formulations describing the traction-separation relationships along the delamination interfaces. By incorporating CZMs into FE simulations, it becomes possible to capture the complex behavior of delamination, including crack initiation, propagation, and interaction with other structural features. In the literature, CZM has been implemented to simulate the many kinds of interfaces, including some applications related to polymers [45] and bonded joints [46,47]. Regarding power electronics applications, CZM has been used in copper-to-resin adhesion [48], solder joint interface delamination [49], the bonding/debonding behavior of bond pad structures [50], the debonding process of stiff film/compliant substrate systems [51], the failure mechanisms of stretchable electronics [52], the solder layer and semiconductor chip interface [53], and thermal fatigue [54], among others.

Regarding the models available for investigating ductile damage within the metallic layers, various mathematical models have been proposed over the years. A subset of these falls within the framework of Continuum Damage Mechanics (CDM), among which the models developed by

Gurson-Tvergaard [55,56], Lemaitre [57], and Bonora [58] are particularly noteworthy. CDM models are based on the evolution of micro voids within a representative volume element of the material. As these voids grow and coalesce, the material's resistant cross-section and elastic modulus progressively degrade, ultimately leading to failure. Other modeling approaches are instead directly derived by experimental-numerical data, obtained from tensile, compressive, torsional, plane-stress, and mode-mixed tests, carried out on notched specimens with varying geometries. These models, often referred to as Phenomenological Damage Models, are founded on the empirical observation that the onset of ductile damage is closely related to the evolution of the first invariant of the stress tensor (I_1) and the second and third invariants of the deviatoric stress tensor (J_2 and J_3), as plastic strain accumulates locally.

The earliest models incorporating all three invariants include those by McClintock [59] and Rice-Tracey [60], but more recent and relatively easy to calibrate models have also been proposed, such as those by Bao-Wierzbicki [61], Cockcroft-Lathan [62], Mirone-Corallo [63], Xue-Wierzbicki [64], and Coppola-Cortese [65], among others.

Brittle damage models are not inherently dependent on the deformation history of a material point. In the case of brittle fracture, a modeling approach based on the assumption that damage initiates when a local maximum stress or maximum strain criterion is reached, has proven to be effective. In general, it should be sufficient to conduct mechanical tests under different loading conditions, collect the corresponding fracture stress data in the principal stress plane (or space), and construct a failure surface that describes the locus of stress states leading to fracture.
Among the failure criteria commonly employed for the analysis of brittle materials are the Von Mises, Tresca, and Mohr-Coulomb surfaces, each of which defines a specific mathematical formulation for the onset of fracture under multi-axial loading conditions.

This chapter is structured as follows: in the first part, the results of finite element analyses on a representative power electronics package subjected to a single thermal cycle are compared. Two modelling approaches are adopted: in the first analysis, the layers are described using only the elastic properties of the constituent materials, while in the second analysis, the ductile materials are assigned elastoplastic properties. The second part of this chapter is dedicated to damage modelling. Specifically, two damage models have been implemented: a cohesive zone model for simulating delamination at the resin/copper interface, and a Tresca-based model for representing brittle fracture within the encapsulating resin. Regarding the solder, which is particularly sensitive to fatigue-induced damage, the evolution of two key variables: accumulated plastic strain and triaxiality factor has been evaluated, as these have previously been identified as critical indicators of ductile damage. In the

final part of the chapter, a sensitivity analysis is presented on the cohesive zone model used to simulate delamination at the Si_3N_4/resin interface. Overall, this chapter provides a synthesis of modelling approaches for damage phenomena in power modules, and encompasses the key concepts published in the articles *Finite Element Simulation and Sensitivity Analysis of the Cohesive Parameters for Delamination Modeling in Power Electronics Packages* and *Nonlinear Elastoplastic Response and Damage Modeling in Power Electronics Packages Under Thermal Cycling*.

4.1 Materials and modelling procedure

Taking as a reference the model analyzed in the section 3.2, and maintaining the same mesh, contact definitions, and material properties, the finite element analyses were performed using the software MSC Marc Mentat v2023.4®. A quasi-static thermal cycle of –65 °C / 150 °C / –65 °C was uniformly applied to all nodes of the model as the boundary condition. The package was assumed to be in a stress-free state at –65 °C, meaning that no initial stresses or strains resulting from prior manufacturing or assembly processes are present. The following section presents the results obtained from two separate analyses: the first one considers all layers as purely elastic and linear, whereas the second one incorporates the elastoplastic response of the copper**,** solder, and polyimide layers.

4.2 Results from single thermal cycle: Elastic vs Elastoplastic response

In Figure 31a, the critical interfaces analyzed are identified, specifically those where at least one of the two interfacing materials was simulated as elastoplastic. In Figure 31b, the interface stresses are schematically shown. In particular, the three stress components equal on both sides of the interface are indicated in blue, while the three discontinuous ones are shown in black. Consequently, for a complete analysis of each interface, a total of nine stresses should be displayed, namely the three common ones and the three discontinuous ones for the two materials. In the present analysis, for better readability, the data have been reduced by considering only one between σ_{11} and σ_{33}, as they are very similar due to the system geometry, and by neglecting τ_{13} because it is much less compared to the others.

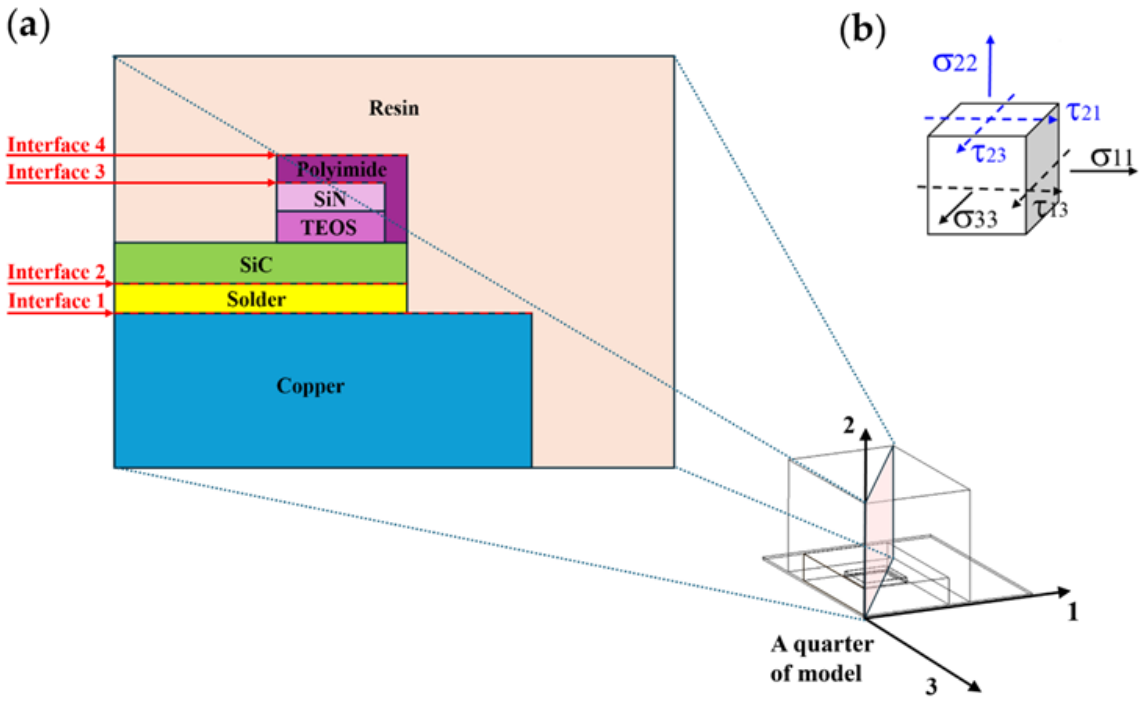


Figure 31: (a) Interfaces at which the stress plots have been extracted. (b) Interface stresses: common (blue) and different (black) stresses between the two interface materials.

In Figure 32, the resulting stress distributions from the two variant analyses are reported in the considered interfaces, at the end of the heating phase and at the end of the thermal cycle (heating + cooling). The blue arrows in the graphs serve as spatial references along a generic path. The term "Frame" in the graphs refers to the stacked sequence of layers: TEOS-Si_3N_4-polyimide.

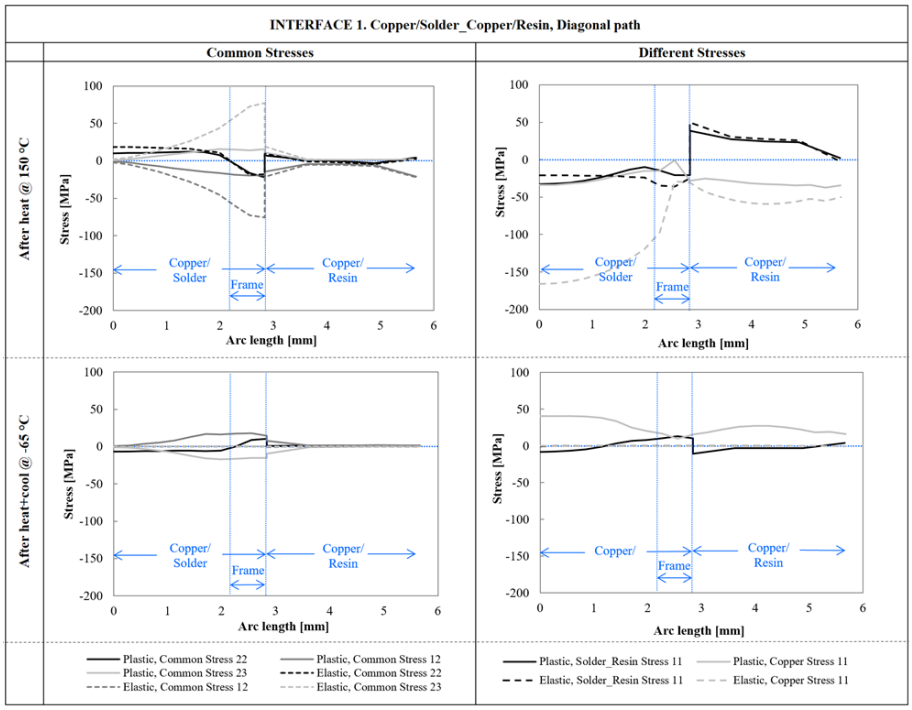
As observed, the analyses of stress distributions during a single thermal cycle reveal significant differences between the elastic and elastoplastic material models. The purely elastic model tends to overestimate stress levels at the end of the heating phase, producing higher peak values due to its inability to account for plastic deformation occurring at elevated temperatures.

Conversely, the elastic model predicts no residual stresses after cooling, which represents a fundamental limitation when employing linear-elastic analyses for such problems. This behavior is consistent across all analyzed interfaces.

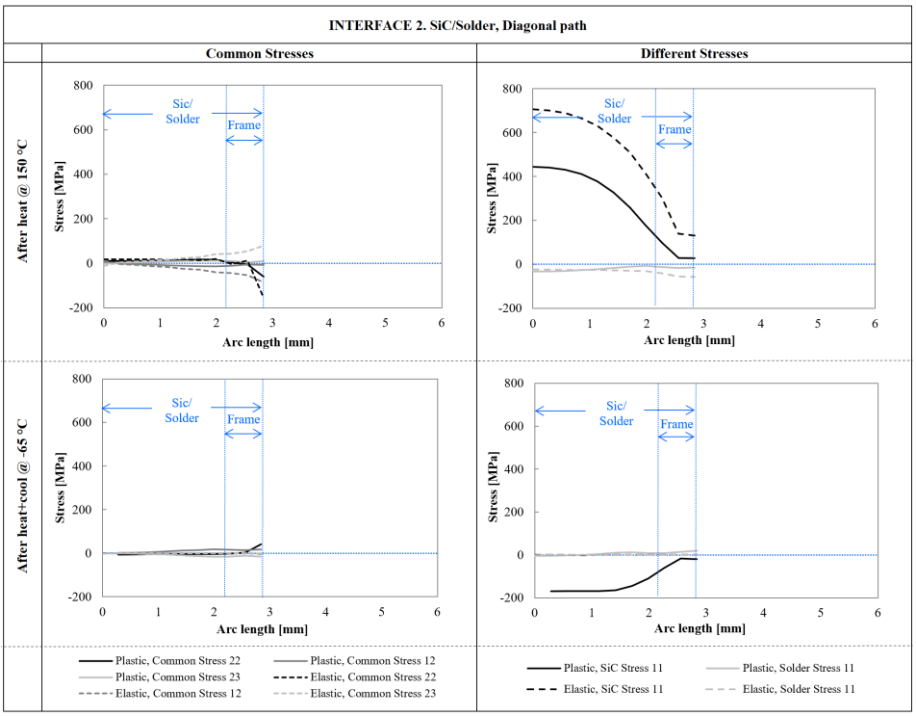
In contrast, the elastoplastic model provides a more accurate representation of the materials' response. By considering plastic deformation, this model yields lower stress levels at the end of the heating phase compared to the elastic model. Furthermore, it captures residual stresses that persist following the cooling phase, which are critical for assessing the long-term reliability of the package.

It is worth highlighting that the stress overestimation by the elastic model may lead to peak values exceeding the actual admissible strength of the materials involved, as exemplified by the SiC

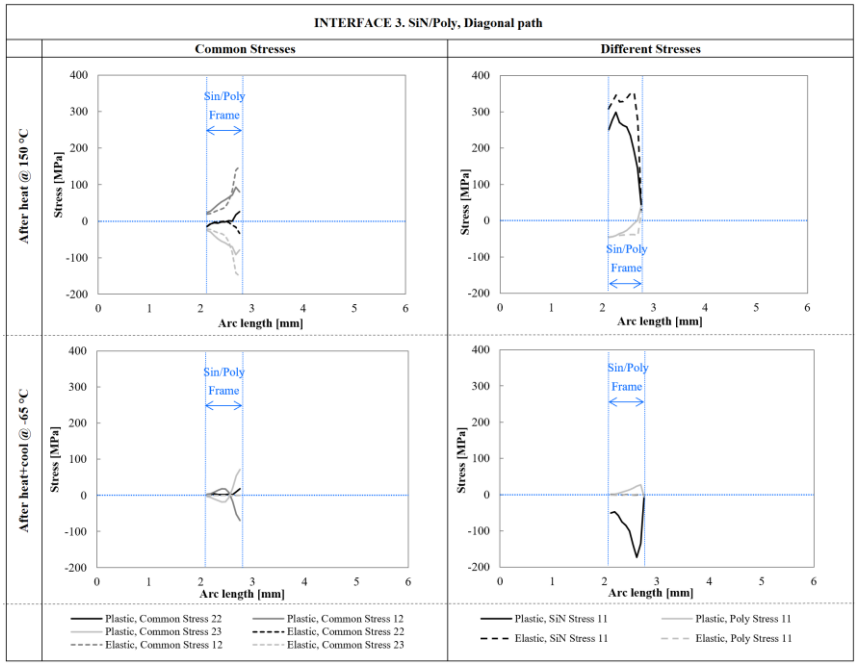
at the SiC–solder interface. These findings emphasize the importance of incorporating elastoplastic material behavior to reliably predict the actual stress state of power electronics packages under thermal cycling conditions.



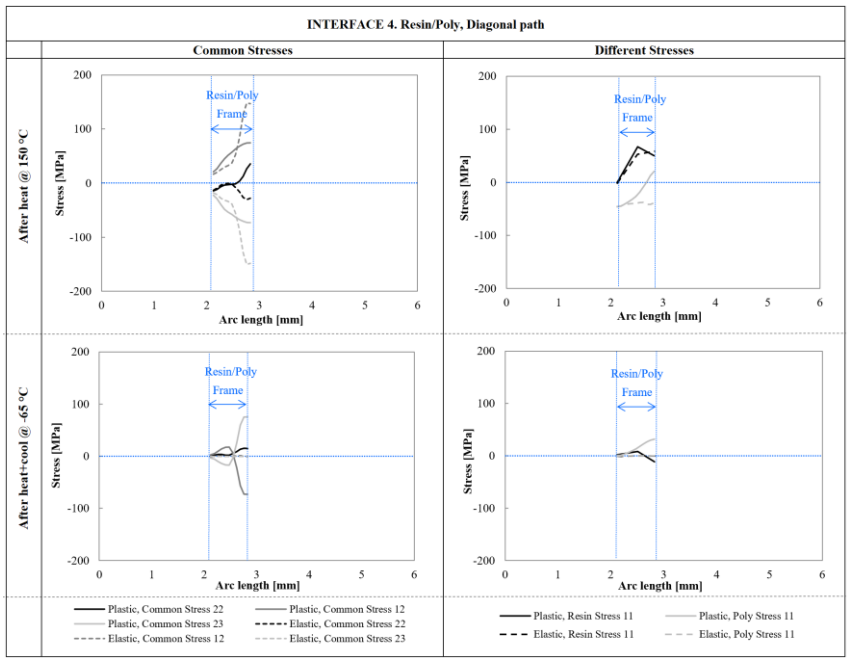
(a)



(b)



(c)



(d)

Figure 32: Comparison between the results obtained from the simulation with all purely elastic materials (dashed lines) and the one with copper, solder and polyimide considered as elastoplastic materials (solid lines): Stresses path plots in the considered interfaces (Copper/Solder_Copper/Resin (a), SiC/Solder (b), Si_3N_4/Poly (c), Resin/Polyimide (d)) at the end of the heating phase and of the heating + cooling entire cycle.

The analysis of the package subjected to a single thermal cycle was performed comparing the results obtained from the simulation with all purely elastic materials and the one with copper, solder and polyimide considered as elastoplastic materials. From the previous analyses of the stress distributions at the considered interfaces, the critical points of each one of them were identified and are shown Figure 33. At these points, the histories during the entire thermal cycle of Von Mises, maximum shear, and in-plane stress were analyzed, once again comparing the results obtained from the simulation with all materials considered elastic to those obtained by considering copper, polyimide, and solder as elastoplastic.

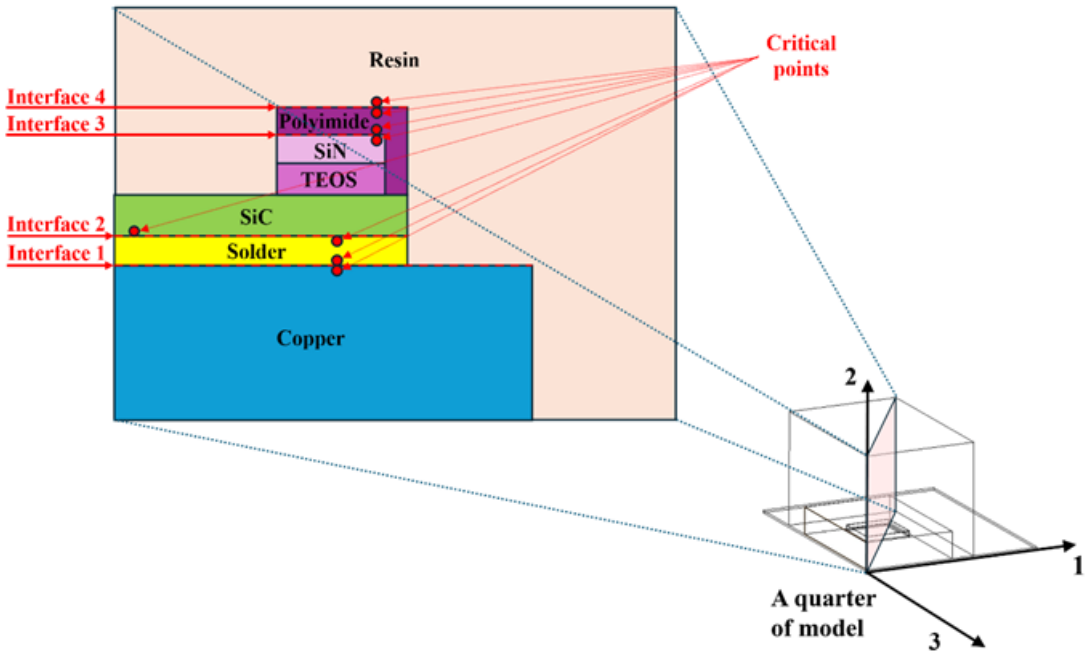


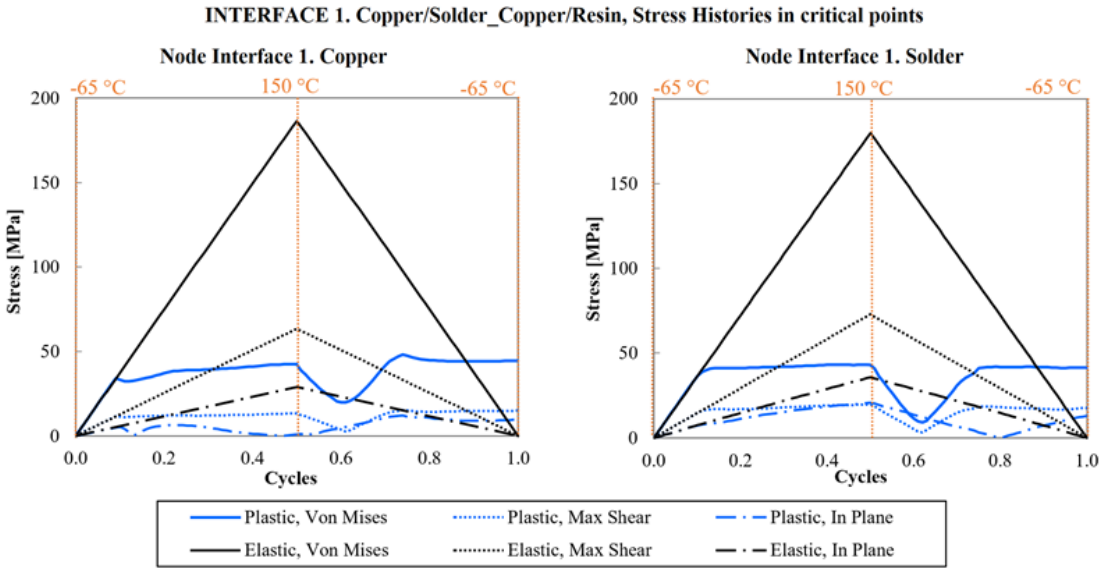
Figure 33: Identification of the critical points in the analyzed interfaces.

The results obtained are presented in Figure 34. The analysis of stress evolution during a single thermal cycle, focusing on critical points within the package, provides important insights into the contrasting behaviors of elastic and elastoplastic material models. The elastic model consistently overestimates the maximum stress values, producing a triangular stress pattern that directly follows the imposed temperature cycle and exhibits no residual stresses upon completion. This overestimation arises from the model's assumption that the material undergoes purely elastic deformation, neglecting any plasticity, which does not reflect actual material behavior under operational conditions.

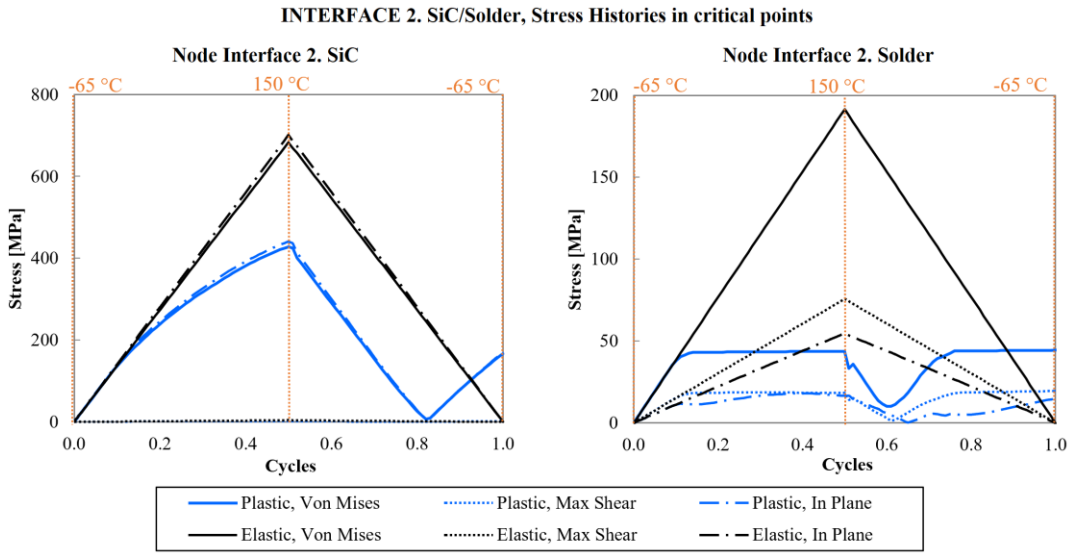
In contrast, the elastoplastic model reveals that the stress response deviates from the triangular temperature profile. Stresses accumulate within the package following more complex trends and result in residual stresses after the cooling phase. Notably, these residual stresses are observed not

only in the elastoplastic materials but also in the resin and SiC layers. Such residual stresses are critical as they can contribute to progressive damage accumulation over multiple thermal cycles. This phenomenon is particularly pronounced at the Resin/Polyimide and Si_3N_4/Polyimide interfaces.

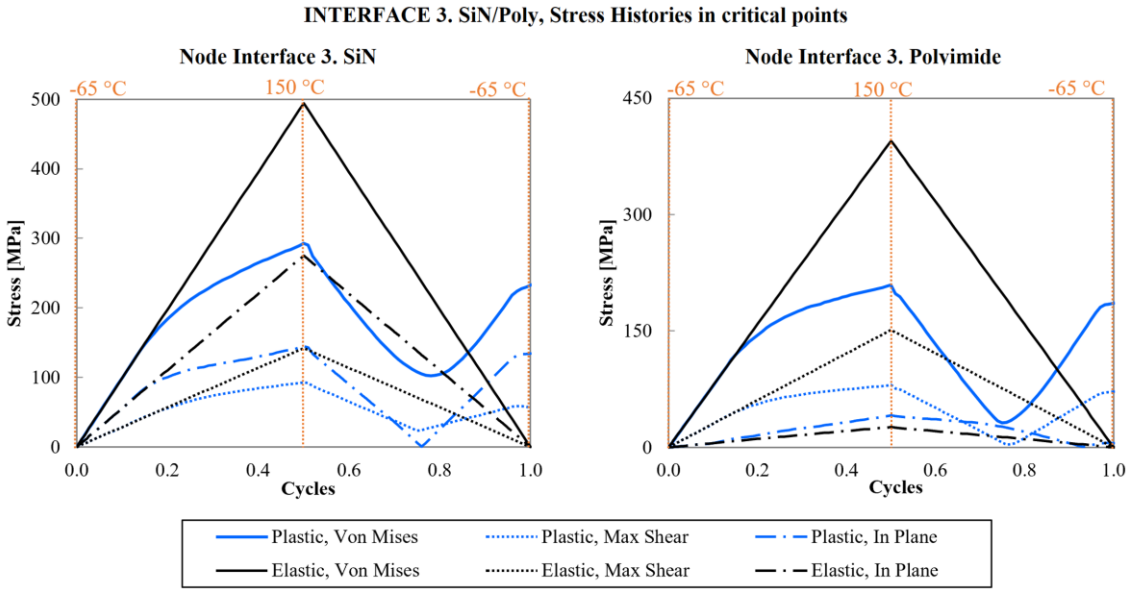
A good agreement between elastic and elastoplastic models is observed up to very low plastic strain levels, beyond which Figure 34 clearly illustrates the divergence between the two responses. These findings confirm that elastoplastic modeling provides a more accurate and realistic evaluation of the package's durability under operational thermal cycling, effectively predicting residual stresses and their evolution over time. Consequently, subsequent analyses involving multiple thermal cycles will be performed exclusively using the elastoplastic model.



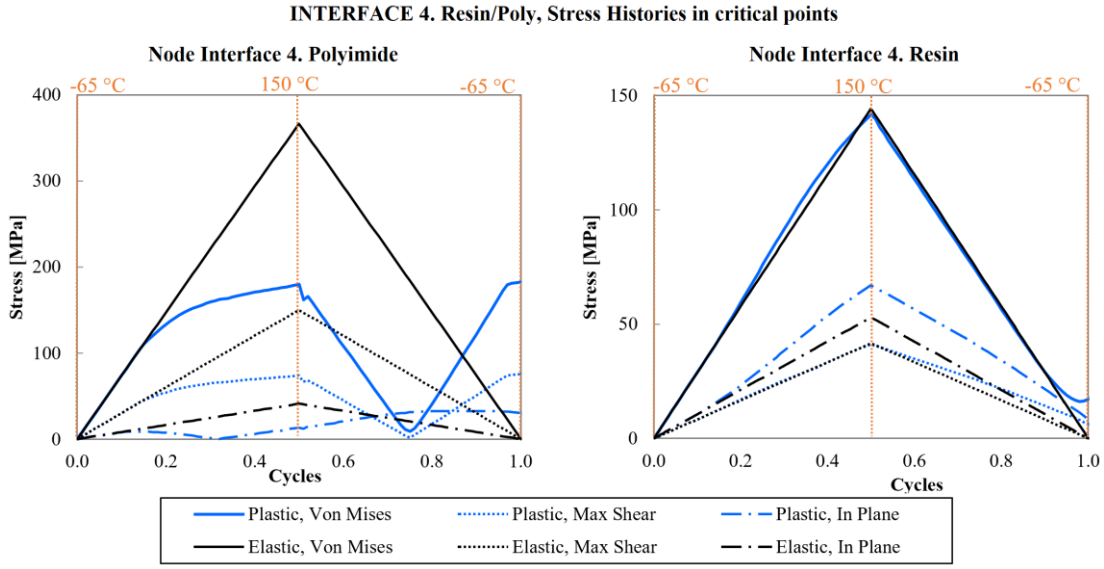
(a)



(b)



(c)



(d)

Figure 34: Single thermal cycle comparison between the results obtained from the simulation with all purely elastic materials (black lines) and the one with copper, solder and polyimide considered as elastoplastic materials (blue lines): Stresses histories in the critical points of the interfaces Copper/Solder_Copper/Resin (a), SiC/Solder (b), SiN/Poly (c), and Resin/Poly (d).

4.3 Damage

Considering damage, the objective of the study is twofold: to analyze the fundamental damage parameters in elastoplastic materials and to model the purely elastic damage in the resin. Resin is taken as a reference for a general damageable elastic material; the same approach can be followed for the other elastic materials.

In the case of the elastic materials, two different approaches to damage modeling are considered: the Modified Tresca (MT) criterion to be applied to the bulk material, and the Cohesive Zone Model (CZM), implemented for simulating interface delamination between the resin and the rest of the package.

4.3.1 Cohesive Zone Model

According to CZM, the interface is discretized with elements behaving as non-linear springs in which the reaction force per unit interface area, also called traction t, depends on the relative displacements between the upper and the lower edge of the element, also called separation δ. The relative displacement modulus between a single pair of integration points or nodes is obtained by the vectorial sum of one normal and two shear components. There is a wide variety of traction-separation laws proposed in the literature in the context of the cohesive zone modelling. The simplest law, used for the present work is a bi-linear traction-separation model. Until the separation reaches a particular value defined as the critical opening displacement (COD), which corresponds to a maximum stress σ_{max}, the cohesive interface is characterized by a traction force linearly increasing with the separation. Afterwards, the damage initiates and causes the degradation of the stiffness K of the cohesive zone, in terms of an irreversible loss of stiffness (softening behavior). The element becomes fully damaged when the separation becomes equal to the maximum opening displacement (MOD).

The cohesive element response described before, accounting for the damage initiation and its progression, is expressed by the so-called *traction-separation law*. The integral of the traction with respect to the separation, i.e., the area beneath the traction-separation law, expresses the potential energy released per unit crack growth area in a given crack opening mode. In the fracture mechanics literature, this is also called the *critical strain energy release rate* or *cohesive energy* G_c. Thus, there are essentially three independent parameters to calibrate in CZM: COD, MOD, and G_c. A qualitative representation of the bi-linear triangular characteristic curve of the implemented elements is shown in Figure 35.

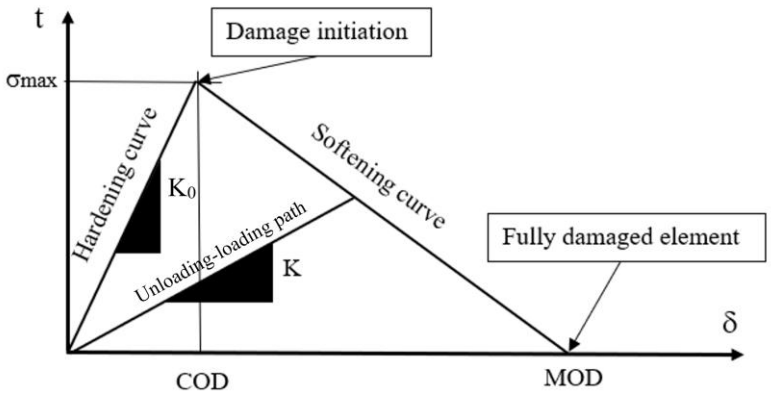


Figure 35: Qualitative representation of the bi-linear characteristic curve of the cohesive elements.

Equation (6) shows the mathematical formulation of the bi-linear model, where $K_0 = \frac{\sigma_{max}}{COD}$ is the element's stiffness in the elastic region, a $= \frac{\sigma_{max}}{COD-MOD}$, and b $= MOD\,\frac{\sigma_{max}}{MOD-COD}$.

(6) $$t(\delta) = \begin{cases} K_0\delta & if\ \delta \leq COD \\ a\delta + b & if\ \delta > COD \end{cases}$$

In this case, it is immediately possible to evaluate the cohesive energy G_c by using the formula for the triangle's area (Eq. (7)). Indeed, the triangle's height is equal to σ_{max} and the base is equal to the MOD.

(7) $$G_c = \frac{1}{2}\,\sigma_{max} \cdot MOD$$

The law presents an initial linear reversible section, during which the interface's stiffness K_0 remains constant, followed by a linear irreversible response during which the stiffness gradually decreases as the damage evolves according to equation (8).

(8) $$D = 1 - \frac{K}{K_0}$$

K is the element's stiffness during the unloading/re-loading transformation, which starts from a point lying in the softening curve Figure 35. When δ reaches the COD value, the stiffness is still equal to the elastic hardening region value and the damage variable is equal to zero. When δ reaches the MOD value, the element's stiffness degenerates to zero and the cohesive element is fully damaged (D = 1).

The Cohesive Zone Model (CZM) is, in principle, capable of simulating the phenomenon of delamination, i.e., the separation between two materials in contact at an interface, under different fracture modes. Specifically, it can model Mode I fracture, where the applied load is perpendicular to

the crack propagation plane; Mode II fracture, where the load is parallel to both the interface plane and the crack propagation direction; and Mode III fracture, where the load is parallel to the interface plane but perpendicular to the crack propagation direction.

For each individual crack opening mode, it is possible to define and calibrate a triangular cohesive law using numerical-experimental methods. This law is characterized by three parameters: the critical energy release rate G_c, the critical crack opening displacement (COD), and the maximum opening displacement (MOD). Since, in general, the applied load may be inclined in a direction that does not correspond to one of the three pure modes described above, the crack opening mode may be of a mixed type. Under mixed-mode conditions, the triangular cohesive law is defined such that the parameters G_c, COD, and MOD become functions of the corresponding values in pure Mode I, II, and III. If the delamination problem is two-dimensional and there are no force components contributing to Mode III crack opening, then at most two experimental tests are required to calibrate a complete Cohesive Zone Model (CZM). Specifically, a Double Cantilever Beam (DCB) test, in which the interface opens predominantly in Mode I, and an End Notch Flexural (ENF) test, in which crack propagation occurs mainly in Mode II. From these two tests, it is possible to reliably determine the strain energy release rates from the load-crack opening displacement curves. The remaining two parameters of the cohesive model are typically identified through combined numerical -experimental inverse procedures. This approach exposes the cohesive zone model to the issue of non-uniqueness in the identification of its parameters. Given the lack of specific experimental data on the package modeled in this thesis, the cohesive parameters were taken as reference from the study by Krieger et al. [66]

	Mode I parameters	Mode II parameters
σ_{max}[Mpa]	30	400
$MOD[\mu\text{m}]$	2.320	11.080
$COD[\mu\text{m}]$	0.232	1.108

Table 9: Cohesive Zone parameters for the copper/resin interface, according to the work of Krieger et al. [66].

It is worth emphasizing that in the FEM software Marc Mentat, the cohesive zone model (CZM) is already implemented natively, without the need for user-defined subroutines. However, it presents a significant limitation: the model can only accept five independent input parameters. Three of these define the crack opening behavior in pure Mode I, while the remaining two are scaling factors that linearly map the Mode I triangular law onto a Mode II triangular law, assuming the maximum opening displacement (MOD) to be invariant. The scaling factors are defined as follows: α = Mode

II cohesive energy / Mode I cohesive energy, and β = Mode II maximum traction / Mode I maximum traction. The cohesive parameters used for modeling delamination at the copper/resin interface in the package investigated in this work are summarized in the following Table 10.

σ_{maxI} [MPa]	COD I [μm]	MOD I [μm]	$\alpha=Gc_{II}/Gc_I$	$\beta=\sigma_{maxII}/\sigma_{maxI}$	MOD II [μm]
30	0.232	2.320	63.678	13.333	2.320

Table 10: Cohesive Zone parameters given in input to the Marc Mentat software, for the present work.

4.3.2 Modified Tresca Damage Model

The Modified Tesca (MT) criterion is employed to assess damage in materials subjected to multiaxial stress states, with particular emphasis on the behavior within the bulk material. This model is formulated in terms of the principal and hydrostatic stress component. The relationship representing the condition of failure of this criterion is shown in eq. (9), where $\sigma_1 < \sigma_2 < \sigma_3$ are the principal stresses, $\sigma_H = \frac{\sigma_1+\sigma_2+\sigma_3}{3}$ is the hydrostatic stress, τ_{cr} is the critical failure shear stress in condition of zero hydrostatic stress, and μ is the coefficient of internal friction. Obviously, when $\sigma_H = 0$ the model is reduced to the Tresca criterion.

(9) $$\frac{|\sigma_1-\sigma_3|}{2} = \tau_{cr} + \mu\sigma_H$$

The two parameters characterizing this model are μ and τ_{cr}, which regulate the shape and the size of the fracture locus respectively.

In theory, the calibration of the Modified Tresca model requires only two uniaxial tests: one in tension and one in compression. Based on this consideration, the following system of two equations in two unknowns can be derived (eqs. (10)).

(10) $$\begin{cases} Uniax.tension:\ \sigma_1 > 0,\ \sigma_3 = 0,\ \sigma_1 = \sigma_T, \sigma_H = \frac{\sigma_T}{3} \rightarrow \frac{\sigma_T}{2} = \tau_{cr} + \mu\frac{\sigma_T}{3} \\ Uniax.compression:\ \sigma_1 < 0,\ \sigma_3 = 0,\ \sigma_1 = -|\sigma_C|, \sigma_H = -\frac{|\sigma_C|}{3} \rightarrow \frac{|\sigma_C|}{2} = \tau_{cr} - \mu\frac{|\sigma_C|}{3} \end{cases}$$

From a practical standpoint, using the previously identified parameters μ and τ_{cr}, the failure surface would accurately intersect two experimental points corresponding to pure tension and pure compression. However, it would approximate with significant error the remaining data points associated with other stress states. To address this limitation, and by incorporating the experimental

data reported by Hu et al. [67] and Morelle et al. [68], the shape of the failure surface (represented by the parameter μ) was refined by minimizing the discrepancy between an initial trial normalized surface and the two aforementioned experimental datasets. This procedure was carried out using stress values normalized with respect to their corresponding failure stresses. The minimization procedure was carried out by using the Excel® Solver minimization (Generalized Reduced Gradient, Nonlinear). The obtained value is reported in Table 11 together with the ones from the considered literature references. Then, Figure 36 shows all the considered fracture data normalized with respect to the uniaxial tensile critical value σ_{cr}, i.e., the experimental fracture data from Morelle et al. (red squares) and Hu et al. (blue circles) and the MT criterion fracture locus according to Morelle et al. (dashed red line), to Hu et al. (blue dotted line), and the present work (black solid line).

Morelle et al. [68]	Hu et al. [67]	Present work
-0.441	-0.200	-0.275

Table 11: Shape parameter μ from Morelle et al. [68], Hu et al. [67], and used in this work.

Having defined the shape parameter μ, only the size parameter τ_{cr} remains as the single tunable parameter. Moreover, given μ, a value of the failure shear stress τ_{cr} corresponds uniquely to a single value of uniaxial tensile critical value σ_{cr}. Consequently, the size of the fracture locus can be defined as needed by the value of τ_{cr} or σ_{cr}. The full calibration of the size of the fracture locus will be discussed in the following sections. The MT criterion has been implemented in the FEM software via Fortran subroutine (see Appendix).

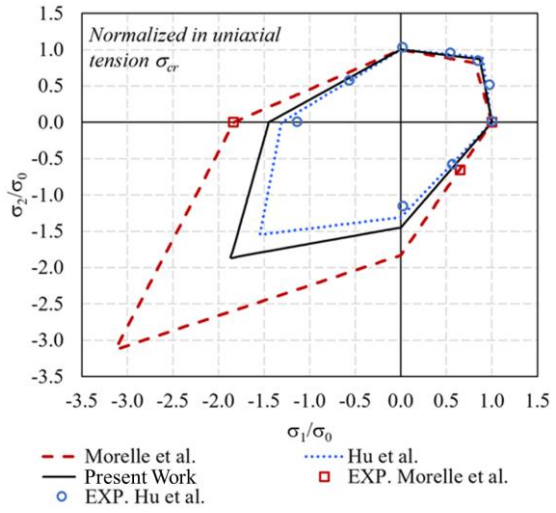


Figure 36: Fracture data normalized with respect to the uniaxial tensile strength value σ_{cr}: experimental fracture data from Morelle et al. (red squares) and Hu et al. (blue circles); MT

criterion fracture locus according to Morelle et al. (dashed red line), Hu et al. (blue dotted line), and the present work (black solid line).

4.4 Results and discussions

The analysis of plastic strain accumulation over a series of thermal cycles reveals significant insights into the long-term behavior of materials used in power electronics packages. In Figure 37 are shown the histories of plastic strain in the critical points of the elastoplastic bodies considering ten consecutive thermal cycles. It shows that plastic deformation evolves differently across various critical points in the package, with some regions experiencing more pronounced deformation than others.

In the case of copper, the three critical points exhibit practically the same evolution of plastic strain, as the critical area appears to be deformed quite uniformly, which tends to saturate from the beginning. Moreover, the maximum strain is relatively low, around 0.02, and far from concerning levels in terms of damage.

In the case of polyimide, in all the three critical points, the plastic strain increases sharply in the first cycle before gradually approaching saturation. In this case, there is a significant difference between the two most deformed points and the third one, highlighting a marked gradient in the deformation from the corner inward. In this case, the maximum plastic deformation seems to saturate at a consistent level of about 0.25, which is to be monitored regarding damage initiation.

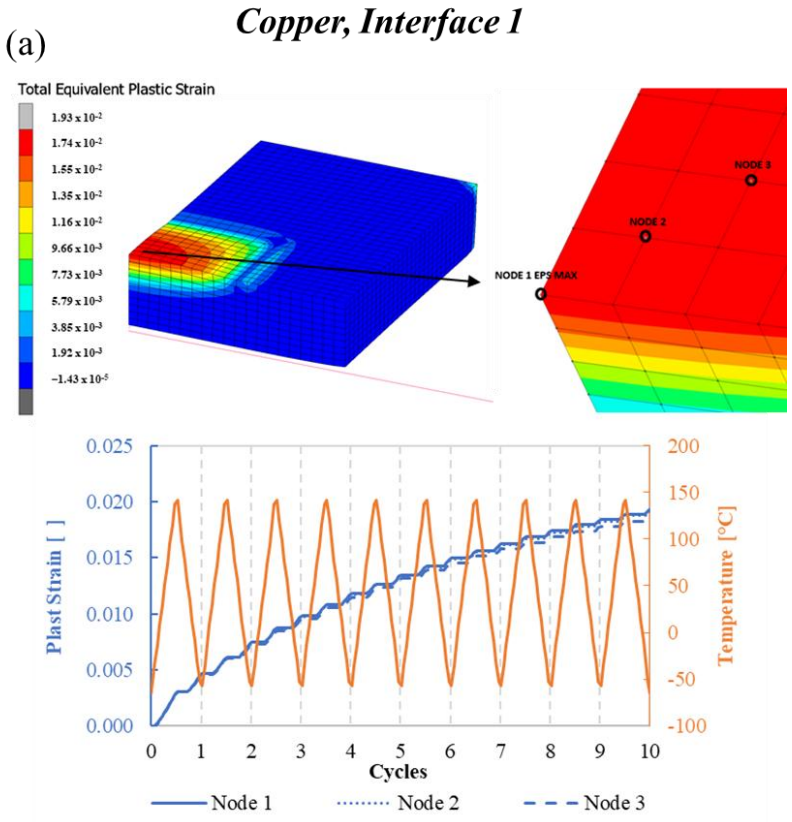
The solder material is highlighted as the critical component due to its substantial plastic deformation (i.e., up to 1.1 at local scale). The analysis demonstrates that the deformation is not uniform across the solder joint, leading to very consistent strain gradients. It must be noted that the history of plastic strain accumulated in the solder layer is strongly influenced by the elastoplastic properties of this material, as it is demonstrated in the following.

Figure 38 shows the path plots of plastic strain, cycle by cycle, along the diagonal line of the elastoplastic bodies. Analyzing the distribution of plastic deformation across multiple thermal cycles, there are significant differences in how deformation accumulates in various regions of the power electronics package. In all the considered bodies, plastic deformation is not uniformly distributed.

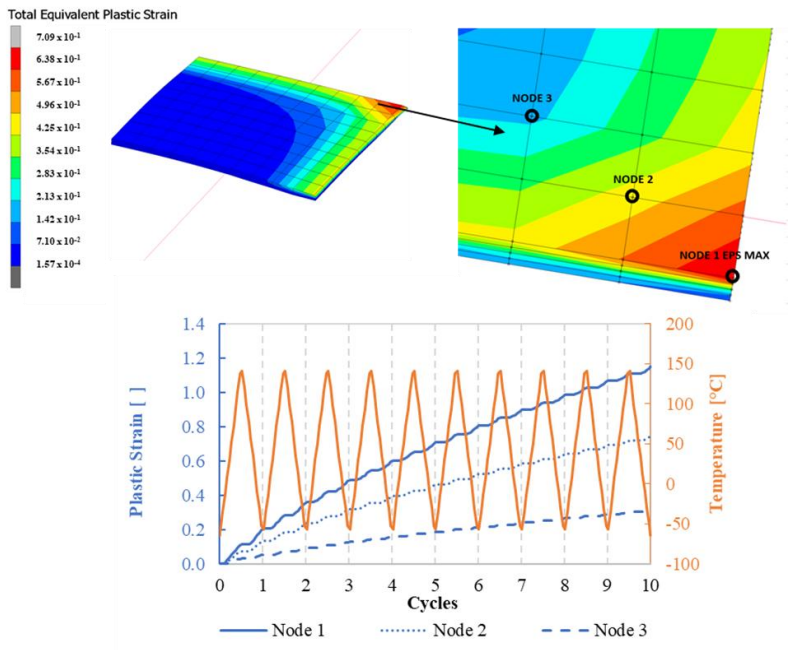
In the case of copper, there are very low strains concentrated in the central area of the package. The growth is saturating with increasing cycles. Solder confirms to be the critical body, with very high strains still showing significant growth and with a very consistent strain gradient. In the case of

polyimide, there are high deformations, but almost fully saturated, with large deformation gradient between the first two nodes and the rest.

(a)



(b)



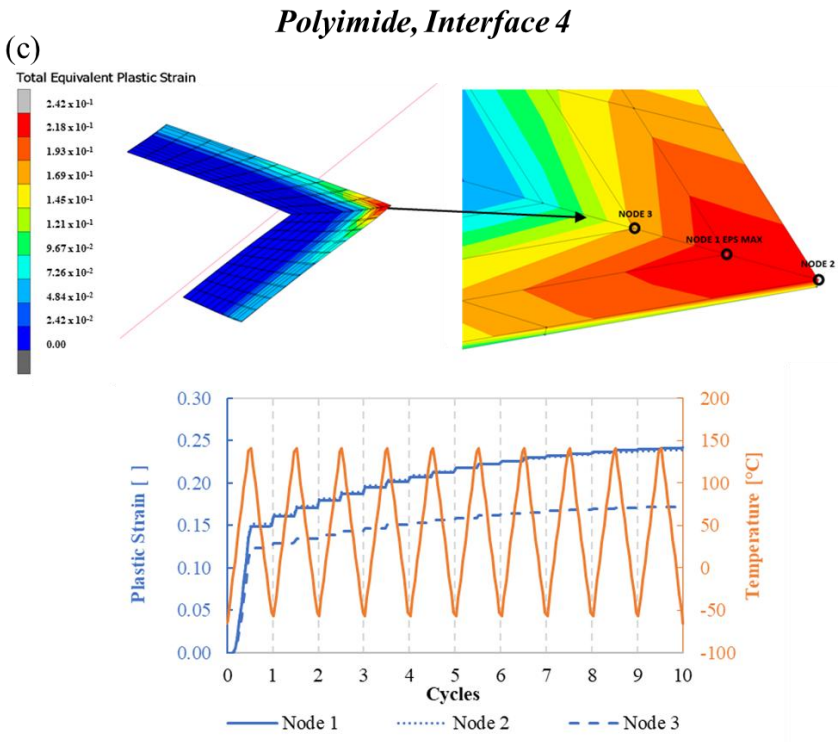
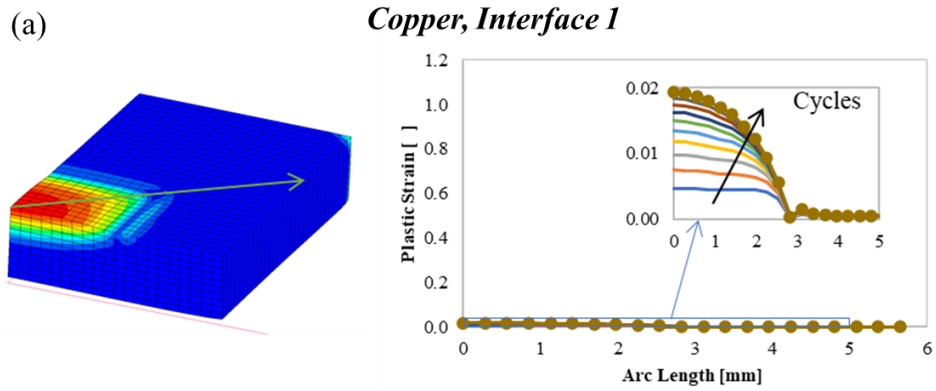


Figure 37: Elastoplastic simulation of the power module subjected to multiple thermal cycles: histories of plastic strain in the critical points of the elastoplastic layers: Copper a); Solder b); Polyimide c).

The findings from this analysis suggest that certain materials within the package, particularly the solder, are more susceptible to plastic deformation and therefore more prone to failure under repeated thermal cycling.



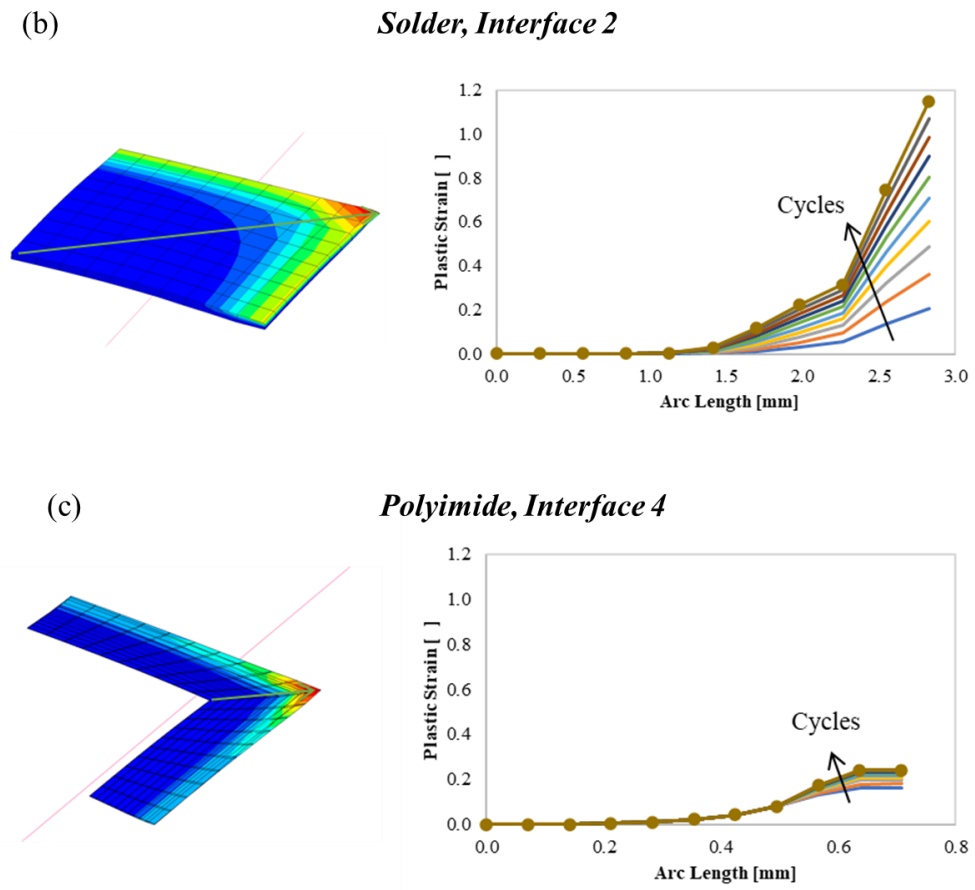


Figure 38: Elastoplastic simulation of the power module subjected to multiple thermal cycles: path plots of plastic strain, cycle by cycle, along the diagonal of the elastoplastic layers: Copper a); Solder b); Polyimide c).

This analysis emphasizes the critical role of the solder material's constitutive curve. Its parameters strongly influence the accumulation of plastic deformation during repeated thermal cycles. To evaluate this effect, a sensitivity analysis of the solder elastoplastic flow curve was performed, focusing on the plastic strain accumulated over ten thermal cycles. Three variants of the reference flow curve, defined in equation (5), were considered: *Flat* (FL), *Slope+Flat* (SL+FL), and *Shifted* (SH).

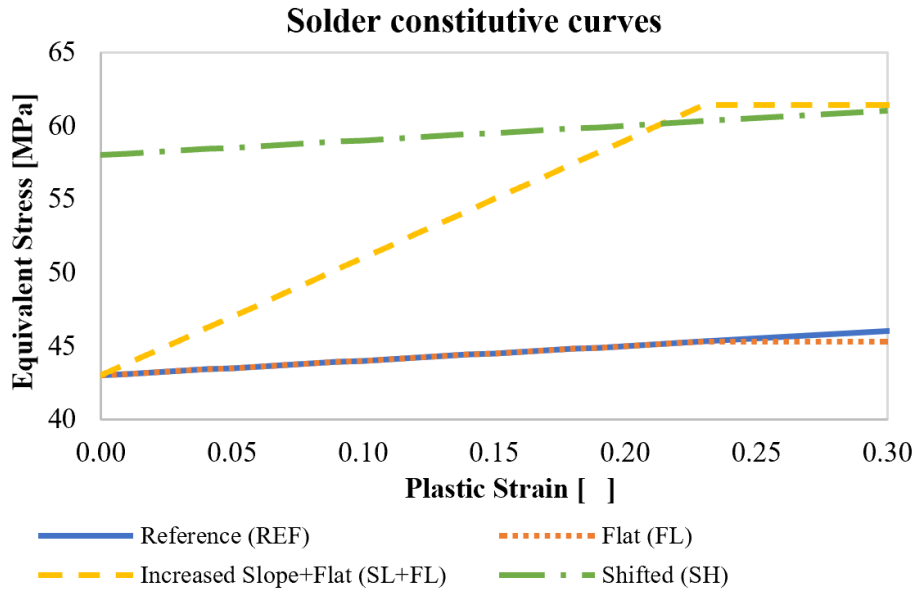
The *Flat* (FL) curve was constructed by matching the reference curve in the strain range 0–0.22, after which it was assumed to behave as ideally plastic. This configuration leads to a faster and more pronounced accumulation of plastic strain, which accelerates with each cycle. A solder material exhibiting such behavior could considerably increase the likelihood of damage initiation and propagation, making it a critical reliability concern for the package.

The *Slope+Flat* (SL+FL) curve is characterized by a steeper initial slope compared with the reference. This results in a more gradual accumulation of plastic deformation in the early stages.

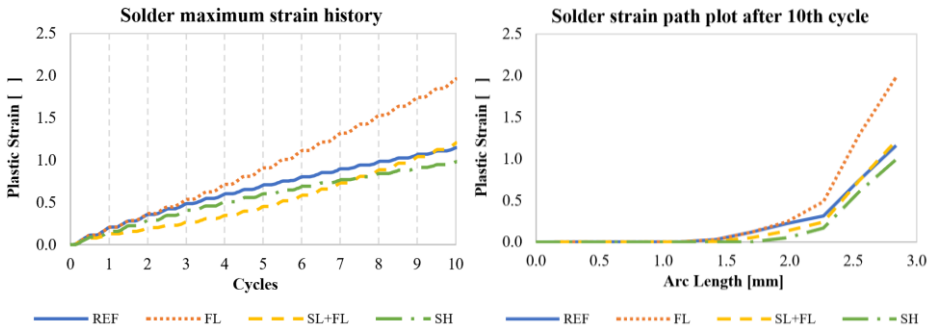
However, once the curve transitions to the flat regime, strain begins to accumulate rapidly, ultimately reaching values higher than those predicted by the reference curve at the end of the tenth cycle.

The *Shifted* (SH) curve, on the other hand, is defined by a higher yield strength while maintaining the same hardening slope as the reference. This behavior leads a reduction in plastic strain accumulation and therefore a lower risk of damage accumulation under thermal cycling.

Overall, the results highlight the importance of carefully selecting solder materials and accounting for strain-rate and temperature effects on their flow curves. By choosing materials that exhibit reduced plastic deformation under thermal loading, the reliability and long-term performance of power electronic packages can be significantly improved. At the same time, this analysis underlines the necessity of an accurate material characterization before the design phase of the devices to ensure that FEM simulations can reliably predict their mechanical response during the operative conditions.



(a)



(b)

(c)

Figure 39: Multiple thermal cycles elastoplastic simulation: comparison of the results implementing different solder constitutive curves (a) in terms of history of plastic strain in the critical point of the solder (b) and path plot of plastic strain, cycle by cycle, along the diagonal of the solder (c).

4.4.1 Ductile damage of elastoplastic layers

From the elastoplastic Finite Element analysis performed on the considered power device, the evolution of plastic strain and Triaxiality Factor (TF) was assessed in copper and polyimide layers during multiple thermal cycling, considering the reference solder constitutive curve. The Triaxiality Factor, which is the measure of the ratio between the hydrostatic stress and the equivalent stress, provides useful insight into the materials' susceptibility to damage.

A measure of the so-called damage variable D is related to the integral of the local triaxiality factor over the deformation history. A simple damage criterion, such as Bao–Wierzbicki or Cockcroft–Latham, states that the onset of local damage occurs when the variable D reaches a critical value D_{cr}. In order to determine D_{cr}, it is necessary to test specimens of the material under investigation to different loading modes (tension, compression, torsion, etc.). The present work did not focus on the experimental–numerical characterization of damage in the ductile layers, but rather on the numerical analysis of the evolution of the variables involved in the phenomenon (TF and accumulated plastic strain), using material data provided by STMicroelectronics or available in the literature. Understanding how TF and plastic deformation evolve is essential for predicting the long-term reliability of the package, as it highlights the most vulnerable regions to failure.

For the copper layer, the TF exhibits a behavior that fluctuates around zero, with TF values becoming negative during the heating phase and positive during the cooling phase. This pattern indicates that copper experiences compressive stresses during heating, which can reduce the likelihood of immediate damage, but these stresses shift to tensile during cooling, which increases the risk of damage initiation. Despite these fluctuations, the maximum and minimum levels of TF in copper remain relatively stable across the thermal cycles, with significant variations only occurring at specific peaks.

In the case of polyimide, the TF remains consistently positive, with the highest peaks occurring during the cooling phases of the thermal cycles. These peaks tend to increase with the number of cycles. This behavior is particularly significant because may suggest that even polyimide can accumulate ductile damage over time due to thermal cycling.

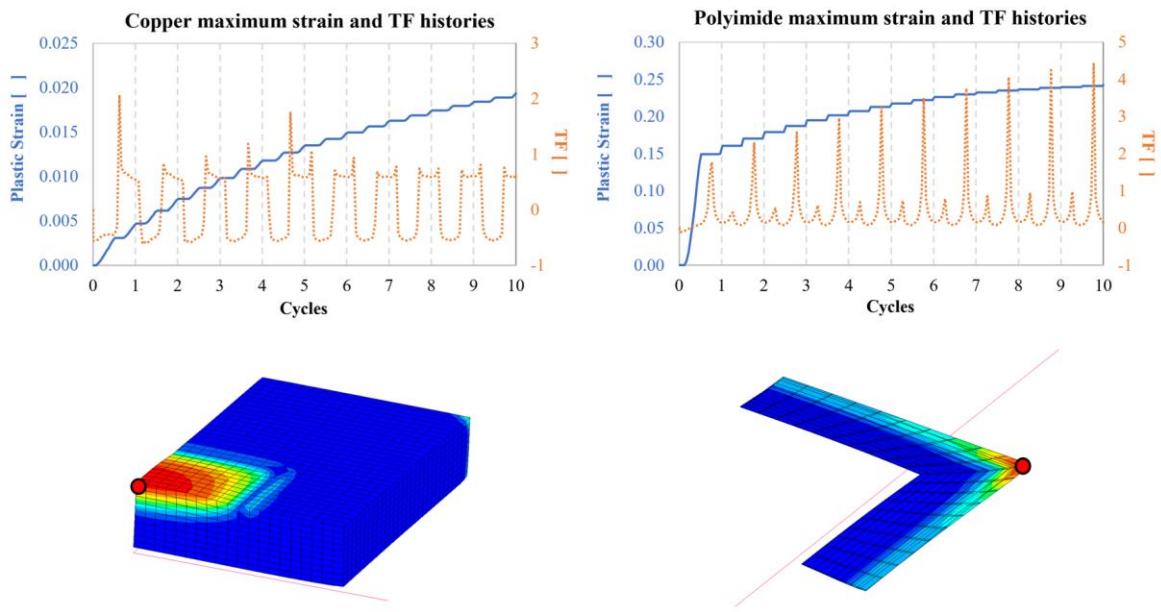


Figure 40: Histories of plastic strain and TF in the critical points of copper and polyimide.

The analysis shown in Figure 41 focuses on the impact of different solder constitutive curves on the history of TF and plastic deformation at the critical point of the solder layer.
Considering the reference curve, TF fluctuates around zero, with its value becoming negative during the heating phases and positive during the cooling phases. The maximum and minimum values of TF oscillations, after a first decreasing period, tend to increase with the number of cycles, posing a further problem of the accumulation of damage over time.

The alternative Flat solder curve results in significantly higher plastic strain accumulation, as previously shown, but TF oscillations seem to remain stable with the cycles. However, the greatly increased plastic deformation can lead to a greater likelihood of damage initiation.

A solder behavior modelled with the Slope + Flat constitutive curve exhibits remarkable TF oscillations in the first cycles of the thermal history, which tend to stabilize after seven cycles.

The Shifted curve features both accumulated plastic strain and TF peaks lower than the reference curve. Then, this study reveals useful insights into the relationship between the solder material's constitutive curve, plastic strain, and TF. The modifications in the solder's flow curve that lead to lower strain growth tend to result in higher peaks of TF, and conversely, those that increase strain tend to reduce TF peaks. Moreover, increasing the overall yield strength level of the constitutive curve not only reduces the strain growth but also diminishes the TF peaks.

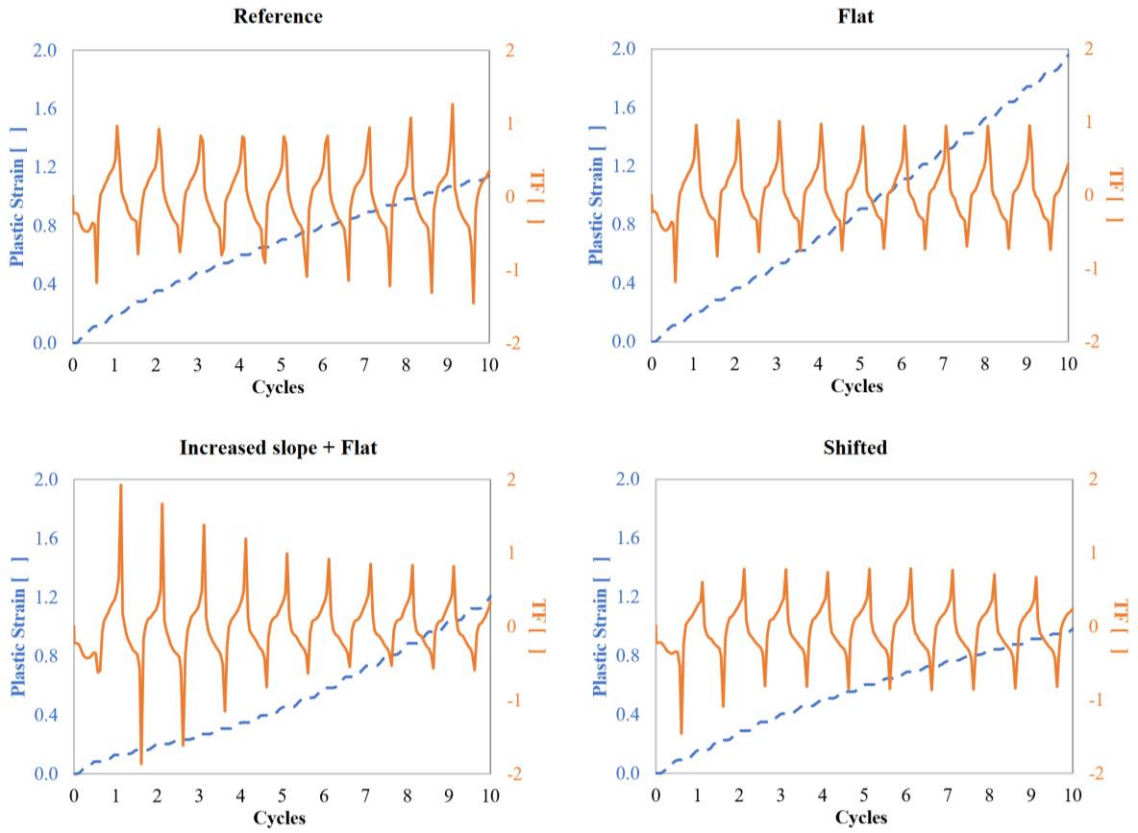


Figure 41: Histories of plastic strain and TF in the critical point of solder considering different solder constitutive curves.

Figure 42 shows the TF vs plastic strain histories in the critical points of solder, copper, and polyimide modelling different solder constitutive curves. Such graphs are meaningful because, as a general reference concept, when TF is greater than zero, the area under the TF vs plastic strain curve is strictly related with the ductile damage that accumulates in the material.

The results indicate that the levels of plastic deformation may vary greatly between different materials, depending on the solder's flow curve parameters. For instance, the Flat curve in the solder tends to increase the deformation in polyimide and reducing it in copper, while increasing it in the solder itself. Conversely, the Shifted curve does exactly the opposite. It is worth noting that in the solder material, low or negative TF values may justify the very high strain observed, which may be tolerated without damage.

Then, the study shows that the solder's constitutive curve has a profound influence on the strain distribution across all materials, demonstrating how the mechanical behavior of one material may affect another within the same package. Then, the interdependence observed between the different materials emphasizes the need for a holistic approach to the material selection, package design and the importance of having an accurate characterization of the mechanical behavior of the materials involved in the package, including their plastic behavior.

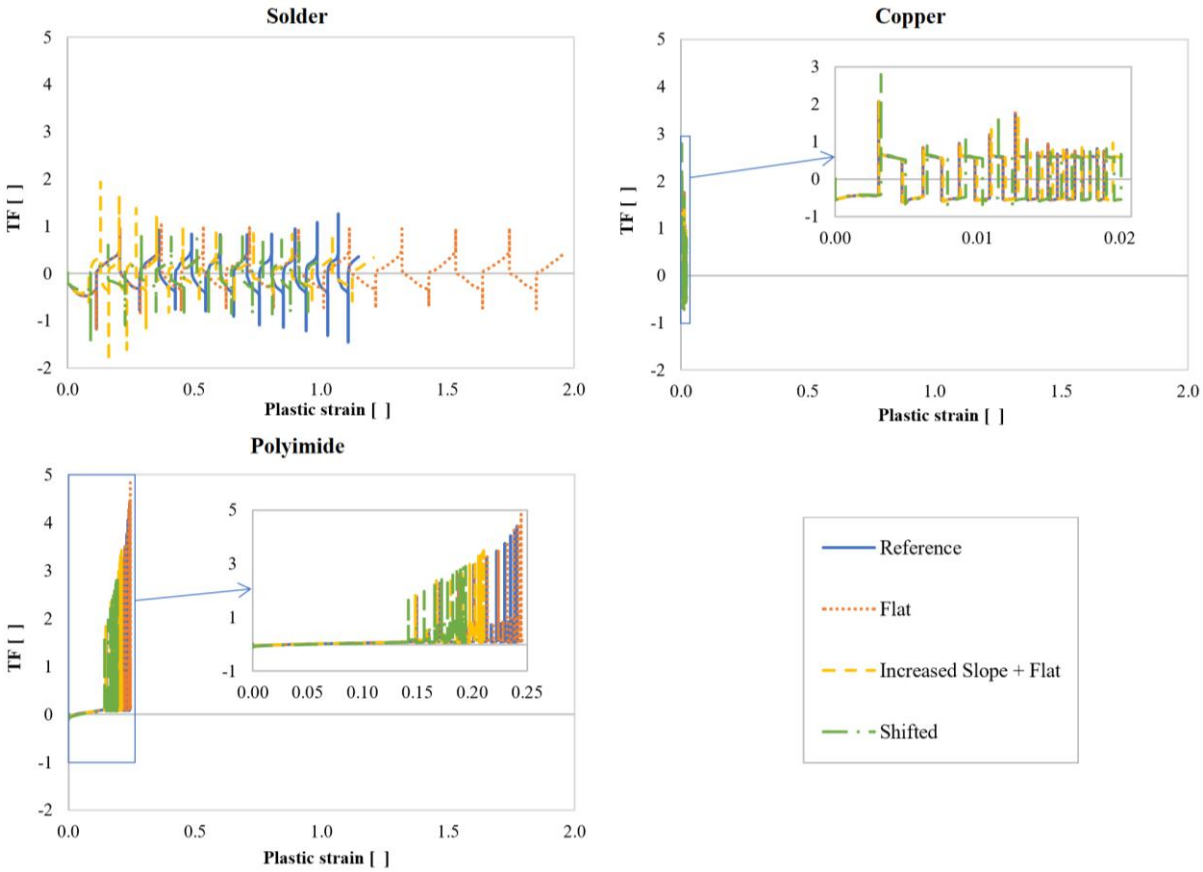


Figure 42: TF vs plastic strain histories in the critical points of solder, copper, and polyimide considering different solder constitutive curves.

4.4.2 Brittle damage of elastic layers

The present study now focuses on the modeling of elastic damage of the resin within the power electronics package, specifically utilizing and comparing the Modified Tresca (MT) criterion and the Cohesive Zone Model (CZM). As already pointed out, resin is taken as a reference for a general damageable elastic material; the same approach can be followed for the other elastic materials (e.g., TEOS, SiC, and Si_3N_4 layers).

Starting with the MT criterion, two calibration parameters are involved: the shape parameter μ and the size parameter τ_{cr} of the fracture locus. The shape parameter was determined by minimizing the approximation error with respect to all experimental data available in the literature, namely those reported by Morelle et al. [68] and Hu et al. [67]. In this procedure, the experimental stresses were normalized by their respective τ_{cr} values. The resulting optimized value of μ is -0.275, as listed in Table 11.

For the size parameter, τ_{cr}, the initial value proposed by Hu et al. was adopted, namely τ_{cr} = 43.5 MPa, associated with a corresponding σ_{cr} = 73.5 MPa. The resulting fracture locus is illustrated in Figure 43, together with those obtained by Morelle et al. [68] and Hu et al. [67].

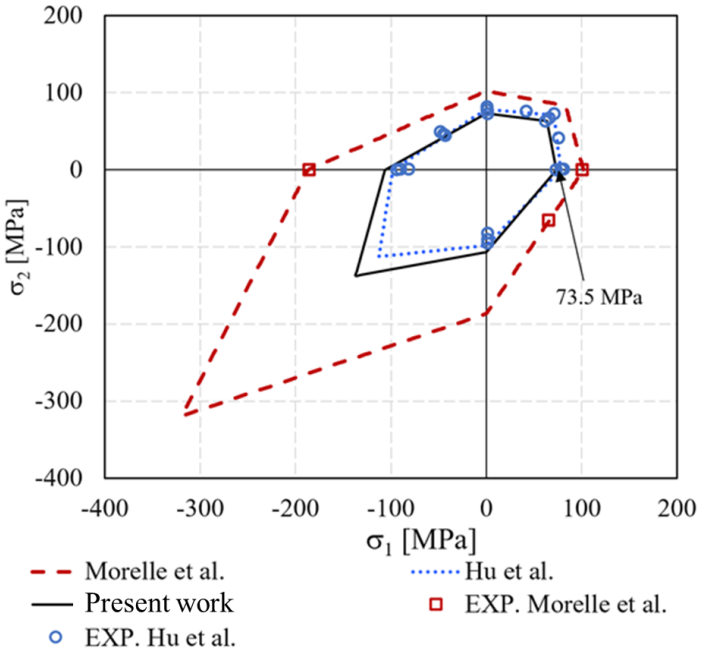


Figure 43: Fracture data: experimental fracture data from Morelle et al. (red squares) and Hu et al. (blue circles); MT criterion fracture locus according to Morelle et al. (dashed red line), Hu et al. (blue dotted line), and the present work (black solid line).

Considering the path shown in the left part of Figure 44, the obtained damage path plot at the end of the first cycle is shown in the right part of Figure 44. The damage variable is calculated normalizing the actual shear stress from eq. (*9*) with respect to the critical shear stress τ_{cr} = 43.5 MPa previously discussed. Therefore, the material failure is achieved for values of damage equal or greater than 1. As shown in the figure, considering the calibration parameters featured before, resin failure occurs after a single thermal cycle, but only around the corners corresponding to the changes of interfaces. It should be noted that the resin body mesh is not highly refined around these corners, unlike the TEOS, Si_3N_4, and polyimide meshes. Therefore, a mesh dependency issue may be present other than the usual critical aspect of modelling sharp edges and materials discontinuities, as discussed in the previous chapters.

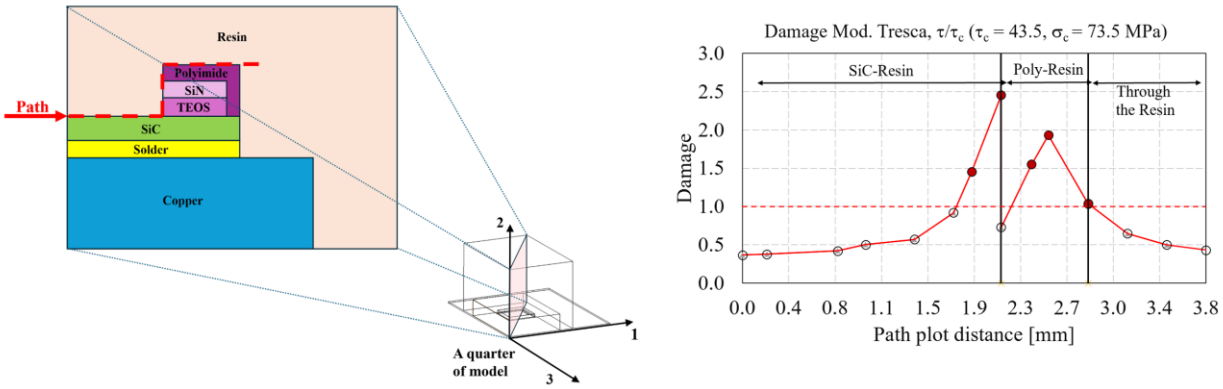


Figure 44: MT Criterion with τ_{cr}=43.5 MPa, σ_{cr}=73.5 MPa: Path plot of the damage value after one cycle.

Another useful exercise for the design of the encapsulation of power modules is the determination of the value σ_{cr} that the resin should assume, i.e., which size should be the resin's fracture locus, to prevent its failing after one cycle, equivalently meaning that the damage variable does not reach one at any node. For this purpose, Figure 45 shows the history plots of damage in four different nodes of the resin located in the previously identified critical area, varying σ_{cr}. It can be observed that, for all points and all σ_{cr} values, the damage increases only during the heating phase of the first cycle and then remains constant at that value as the cycles increase. Furthermore, a critical sigma value of 181 MPa can be identified, as for this value, the most critical point reaches a damage value exactly equal to one. This information could be useful for the manufacturers and the designers, as it would indicate the minimum critical stress needed to prevent the resin from breaking in this type of application.

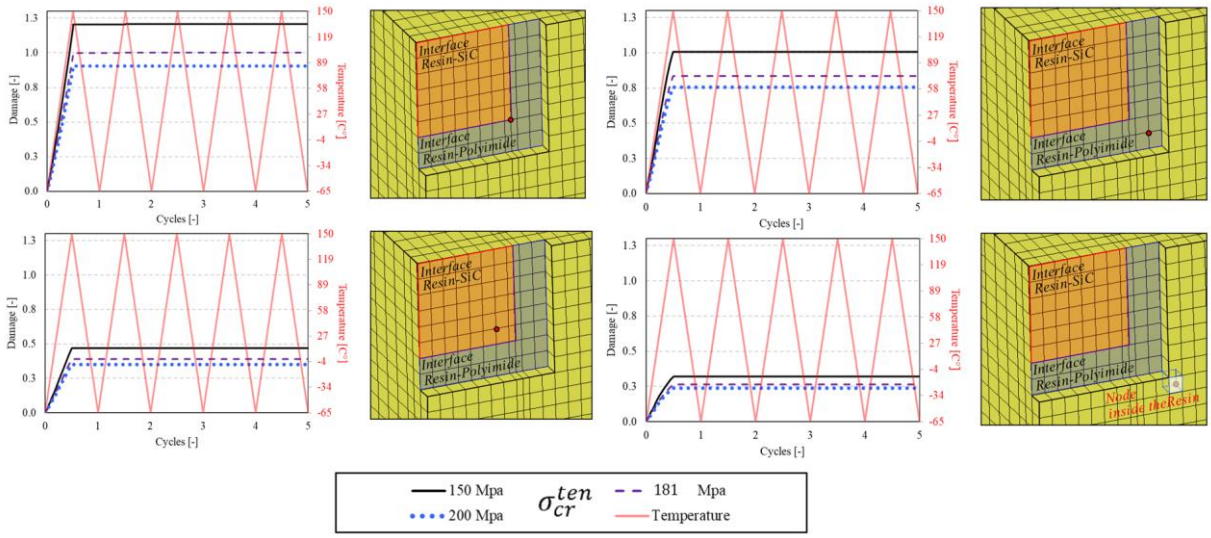


Figure 45: MT Criterion with different σ_{cr}: history plots of damage in four different nodes of the resin located in the critical area.

Having identified the σ_{cr} limit value related to the MT criterion, the comparison between this brittle damage model and the Cohesive Zone Model is discussed. The CZM was applied to the interface between the resin and the rest of the package, and calibrated according to Krieger et al [66], as mentioned previously.

Figure 46 shows the comparison between the two approaches in terms of damage contour plots at the end of the first heating and at the end of the first cycle in both elastic and elastoplastic simulations. Analyzing the figure, it can be observed that with both models, and in both elastic and elastoplastic simulations, there are no substantial differences between the contour plots at the end of the first heating phase and the end of the first cycle, suggesting that most of the damage occurs during the initial heating. On the other hand, the two models yield qualitatively different results in two aspects. First, in the case of the MT criterion, a higher damage value is reached in the elastoplastic simulation compared to the elastic one, contrary to the results obtained with the CZM. Additionally, it can be noted that the location of maximum damage differs between the two cases. Quantitatively, the differences are evident, with the maximum damage values being 0.875/1 for the MT criterion and 0.02/0 for the CZM in the elastic/elastoplastic simulations.

When commenting on these differences in results, it is important to consider that the two models were calibrated independently of each other, even if done realistically, and not with respect to the same experimental references. Moreover, as previously mentioned, using the CZM requires the insertion of a layer of interface elements between the resin and the rest of the package. Consequently, the mesh used to implement the two different models is not exactly the same. Despite this, the differences in the results are evident both qualitatively and quantitatively, highlighting the critical challenges related to simulating damage phenomena in these particularly complex applications. The results are strongly influenced by the modeling choices made. Therefore, to determine the approach that most closely aligns with reality for a given application, it would be necessary to have experimental data that is as detailed as possible.

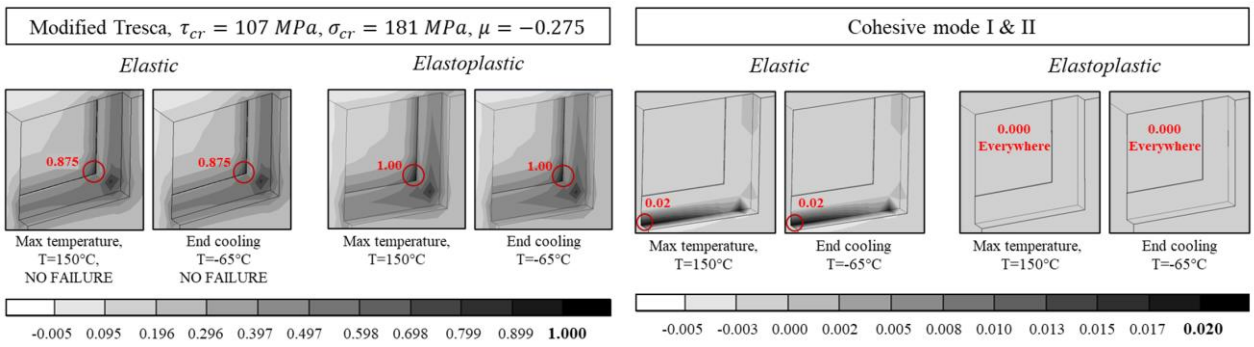


Figure 46: MT Criterion with σ_{cr}=181 MPa vs CZM: Damage contour plots at the end of the first heating and at the end of the first cycle in the elastic and elastoplastic simulations.

In order to analyze the damage evolution, however small, in the simulations with the CZM, Figure 47 shows the history plots of damage in two critical points of the resin in both the elastic and elastoplastic simulations. Analyzing the figure, it can be seen that in the elastic analysis, the damage remains exactly zero in both points, which is supposed to be slightly unrealistic.

In the case of the elastoplastic analysis, at the point previously identified as the most critical, the damage reaches a value of around 0.02, which is still very low but more physically meaningful. It is noteworthy that after the first heating cycle, the damage value already reaches approximately 0.015, once again demonstrating that, with this approach, as in the case of the MT criterion, the damage occurs almost entirely during the first heating cycle.

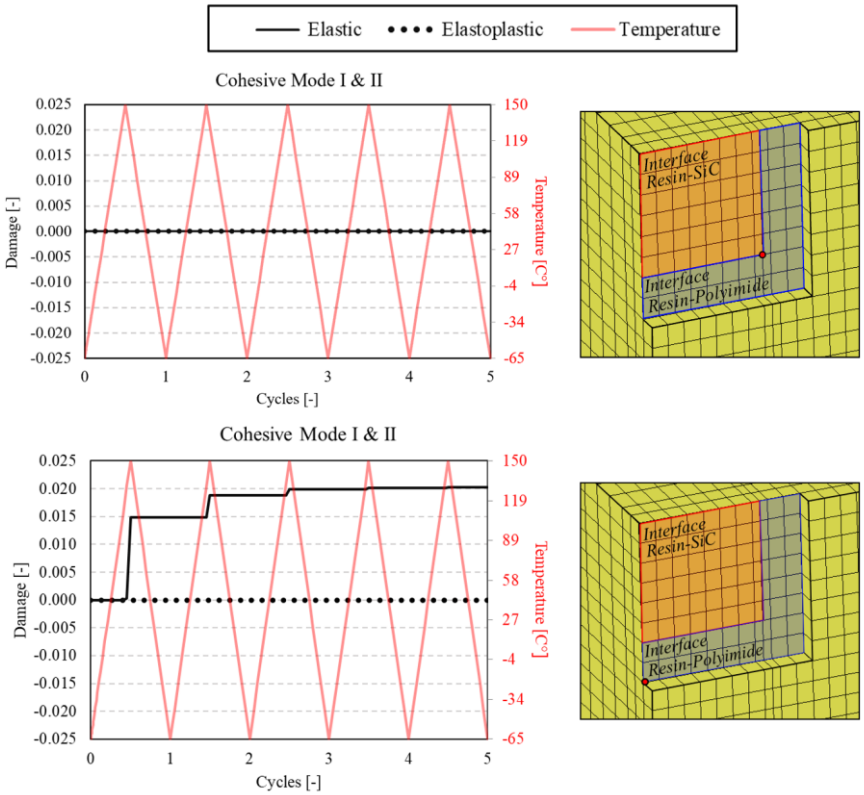


Figure 47: CZM: history plots of damage in two different nodes of the resin located in critical area. Comparison between elastic and elastoplastic simulations.

4.5 Sensitivity analysis of the Cohesive Zone parameters for the modelling of delamination in SiC-based power modules

In this final paragraph, a study on the sensitivity analysis of the cohesive parameters used in the previously described bi-linear Cohesive Zone Model (CZM) is presented. Indeed, per se, this proposed tool for the prediction of damage initiation in the SiC-based power modules is among the commonly used solutions for these kinds of applications, and its implementation is already valuable from a technical applicative point of view. As mentioned before, the Cohesive Zone Models typically used for simulating delamination are calibrated through semi-inverse procedures to replicate experimental results [43,69,70]. However, there is no universally accepted methodology for this purpose. Therefore, there is a need for valuable information to comprehensively understand the functioning of these modeling tools, enabling their conscious calibration, with regard to the specific application.

Without lack of generality, starting from the package model presented in the paragraph 1.1 (which is a simplified version of a package, not considering the layer of polyimide), its delamination behavior under a linear temperature–time law is herein simulated and it is taken into account for the sensitivity analysis proposed for this study.

For the presented analysis, the modelling approach combines the Global-Local FEM and the utilization of cohesive elements to model one of the package's critical interfaces. The model used as global domain is the same described in the paragraph 1.1, while the local domain has the same dimensions of the model described in the paragraph 2.4.

These two domains were modeled with the commercial software for finite elements MSC Marc Mentat 2015®. As reported in the paragraph 2.1, the study of the local delamination problem should require a strong refinement of the mesh in the areas of interest. Moreover, as mentioned multiple times before, the various layers involved in the package exhibit very different thicknesses and plan dimensions. Therefore, given the large number of simulations to be run, a single comprehensive model with a sufficiently dense mesh would have required a great computational effort. Thus, a GL approach was adopted. Firstly, a global analysis was performed under a linear temperature–time law on a comprehensive model with a sufficiently refined mesh to accurately describe the global deformation of the system. Then, a local sub-model encompassing a representative lamination-wise critical volume with a denser mesh was created. The nodal displacements, forces, and temperatures calculated from the global model were imposed on the nodes lying on the local

domain's frontier. The CZM was implemented in the local model to describe one of the most critical interfaces of the package, according to the results presented in paragraph 1.2: the resin/Si_3N_4 interface. Figure 48 shows both the global and local models with their relationship and details.

In both models, all materials were considered to be elastic, linear, and isotropic. Their properties are shown in Table 1. The large deformations option was activated in order to take into account geometric non-linearities.

In the global model, given the micrometric thickness of the TEOS and Si_3N_4 layers compared to their much greater plan dimensions and to the other layers' thicknesses, planar elements with thick shell formulation (Quad4-75 in Marc) were considered for the thinner layers, while solid elements are used for the remaining layers. In particular, the resin encapsulation was modeled with tetrahedral elements having four nodes (Tetra4-134 in Marc). The remaining layers were modeled with hexahedral elements with 8 nodes (Hexa8-7 in Marc). Rigid contact was implemented at all interfaces between different materials. Glued contact was implemented for the hexa/hexa and the hexa/quad interfaces, while rigid links were used to connect the shell/shell interface since planar elements do not support the glued contact on both of their faces. The structural constraints modeled a planar frictionless support, simulating that the package is placed over the bench of a climatic chamber and is subjected to the prescribed temperature histories, permitting the free expansion and warpage of the overall system. Specifically, one hinge and two mutually perpendicular slides on the x–y plane were imposed on three of the four lower vertex base points of the package.

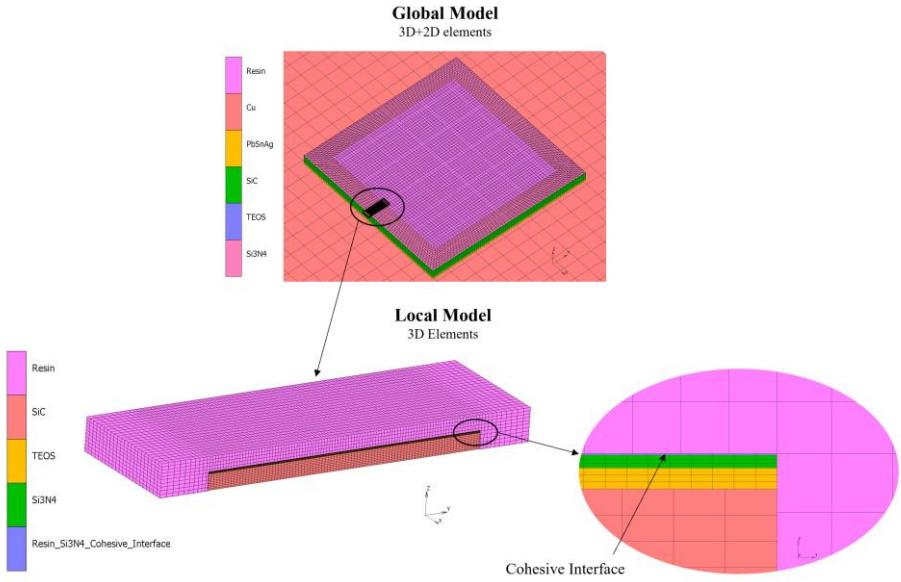


Figure 48: Global and local models used for the present analysis.

In the local model, the geometry was finely discretized, paying particular attention to the interfaces between the layers. Cohesive solid elements were implemented to describe one of the most critical interfaces of the package in terms of delamination, i.e., the resin/Si3N4 interface. Indeed, cohesive elements were specifically designed to capture the mechanical behavior of the interfaces and provide an accurate representation of the initiation and propagation of damage. Despite being a comparative study, a mesh-dependency analysis was carried out in order to guarantee the accuracy of the CZM simulation results. An evaluation was conducted regarding the maximum dimensions of the cohesive elements below which the numerical differences in the results compared to a very fine mesh were found to be below 1% in terms of the delaminated area.

The imposed boundary condition on both global and local model was an uniform heating between -65 °C and 150 °C, as well as done in the previous paragraph 1.1. Numerous simulations on the local model were carried out, changing the parameters of the cohesive elements at the resin/Si_3N_4 interface, in order to evaluate the influence of the single cohesive variables on the delamination phenomenon.

It is essential to emphasize that this study serves solely as a comparative analysis rather than providing absolute results, given the highly mesh-dependent nature of the phenomenon under investigation. Therefore, the objective is to evaluate how different cohesive elements behave based on their specific parameters under realistic thermomechanical conditions relevant to power electronics applications.

In the local simulations, the damage variable is computed at each step for every cohesive element, determined by the displacement of its corresponding nodes. When the damage variable reaches unity, the element is deactivated. The influence of the cohesive elements' properties on the package's reliability is assessed by measuring the percentage of delaminated elements at the simulation's conclusion. Figure 49 illustrates an example of the local model’s output, displaying the damage variable as a contour plot. Fully damaged cohesive elements are automatically eliminated, while the current crack front at the given analysis step is represented by the remaining cohesive elements -those not yet removed- showing damage values near one (visible as a yellow band).

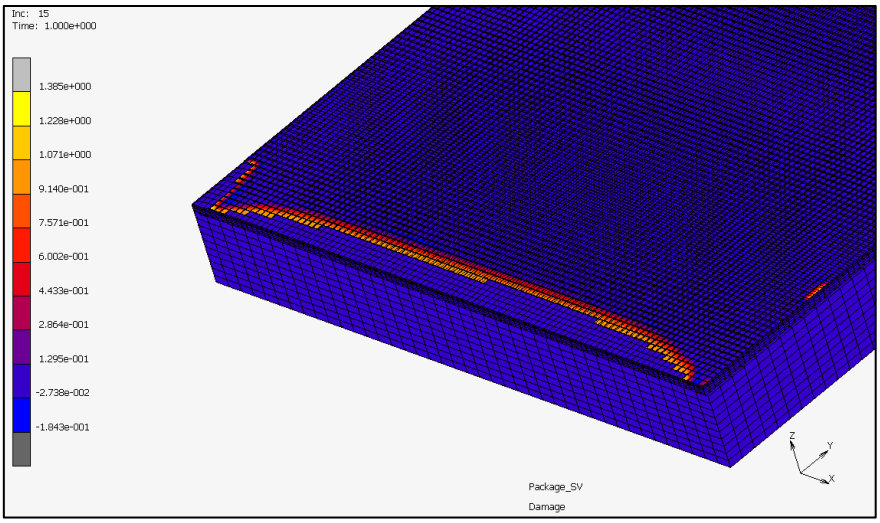


Figure 49: Example of simulation output with delaminated elements and damage plot.

The three characterizing parameters of the cohesive elements which have been varied between the different local simulations are the MOD, the COD, and the Gc. The value sets of these parameters used in this comparative sensitivity analysis are reported in Table 12, together with the consequent maximum traction σ_{max}.

		Gc [J/mm²]									
		0.0015	0.003	0.006	0.01	0.015	0.02	0.03	0.06	0.09	
MOD [µm]	0.01	0.005 300	0.005 600	0.005 1200	0.005 2000						*COD [µm]* σ_{max}[N/mm²]
	0.05	0.025 60	0.025 120	0.025 240	0.025 400						
	0.1	0.05 30	0.05 60	0.05 120	0.05 200	0.05 300	0.05 400				
	0.2	0.05 15	0.05/0.15 30/30	0.05 60	0.05 100	0.05 150		0.05 300	0.05 600		
	0.3	0.05 10	0.001/0.05/0.1/0.25/0.29 20/20/20/20/20	0.05 40	0.05 66.67			0.05 200	0.05 400	0.05 600	
	0.4		0.05 15								
	0.5		0.05 12								

Table 12: Cohesive Zone parameter sets: MOD, COD, Gc, and σ_{max}, used for the sensitivity analysis.

4.5.1 Results and discussion

Looking at the simulations results, Figure 50 shows the influence of the ratio of COD/MOD on the delaminated area (percent over the total contact area) at the end of the prescribed load case (accomplished temperature variation from −65 to 150 °C). In all of these simulations, the cohesive elements are characterized by the same Gc value of 0.003 J/mm^2. The curves are parametrized with the MOD. Thus, a single curve of the graph refers to cohesive traction-separation triangles with the same area (energy Gc) and height (maximum traction σ_{max}), but different positions of the upper vertex along to the base of the triangle. It is possible to see that the %COD/MOD has an almost negligible effect on the delamination. Indeed, the percentage of delaminated elements only slightly decreases with the COD converging to the MOD, i.e., with the hardening recoverable part of the cohesive law growing with respect to the softening irreversible part. As expected, curves characterized by higher values of MOD induced a lower delamination because a greater relative displacement was needed to obtain the unit damage value of the cohesive elements.

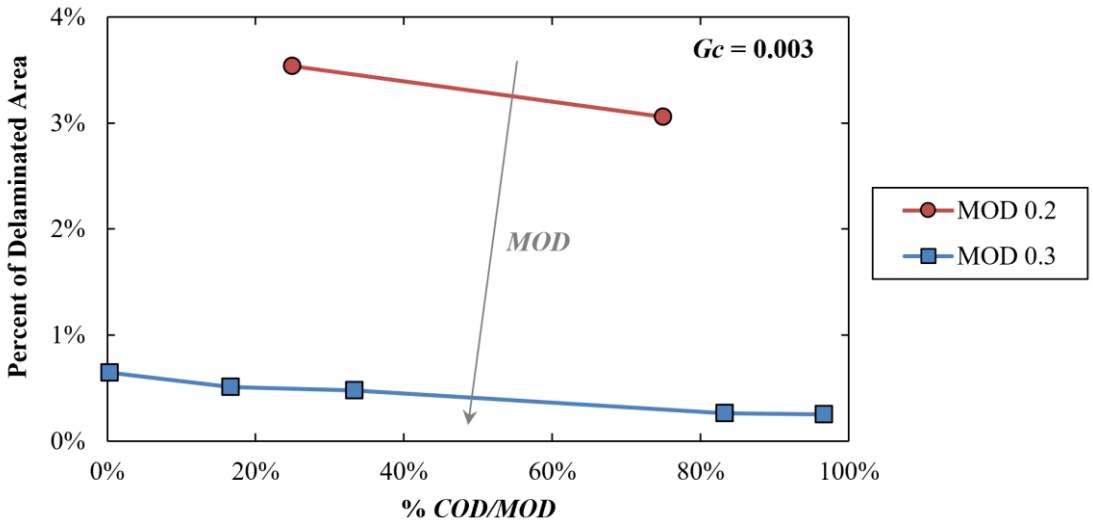


Figure 50: Local simulations results: percentage of delaminated area versus %COD/MOD with the curves parametrized with the MOD. Gc is equal to 0.003 in all simulations.

Figure 51 shows the influence of the MOD on the delaminated area. Given its negligible influence, COD is set between 0.005 µm and 0.050 µm in all simulations. The curves, parametrized with Gc, are characterized by a somehow common trend with a peak of delamination for MOD around 0.1 µm and a progressively extinguishing delamination as the MOD approaches 0.3 µm. Instead, the delaminated area at very low values of MOD exhibits certain differences depending on the specific

energy Gc. Moreover, for a given value of MOD, the delaminated percent area increases with decreasing Gc.

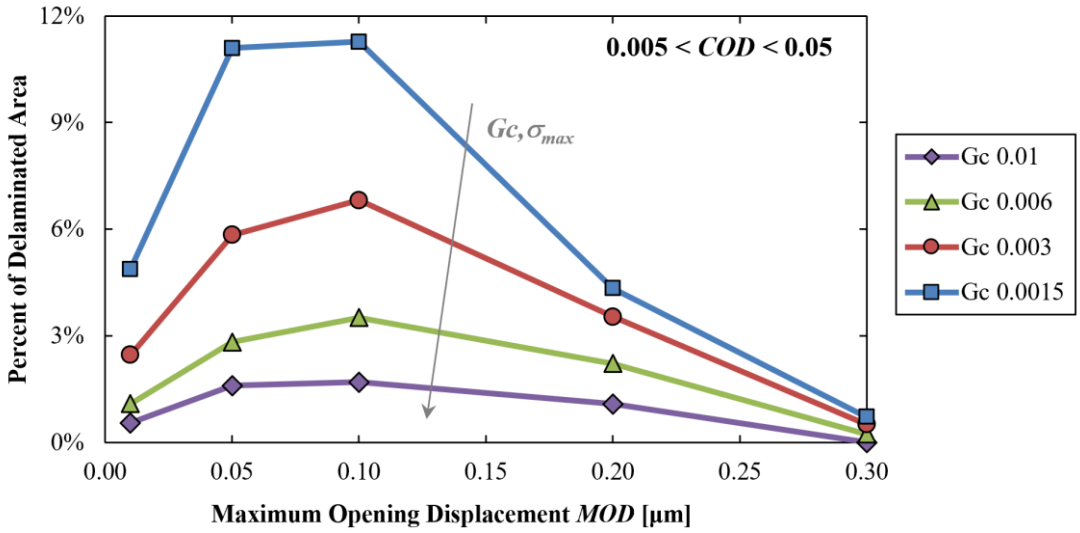


Figure 51: Local simulations results: percentage of delaminated area versus MOD with the curves parametrized with the Gc. COD is between 0.005 and 0.05 in all simulations.

Going from the highest to lowest values of MOD, it is clear that the percentage of the delaminated area increases, since a lower relative displacement between the nodes is necessary to reach complete damage of the element. On the other hand, approaching values of MOD closer to zero, the counter-intuitive trend inversion which occurs for a value of approximately 0.10 µm is explained by the fact that, having fixed the value of the other variables, the lower the MOD value, the higher the cohesive triangle will be (greater maximum traction σ_{max}). Thus, below a certain value of MOD, the traction produced by the cohesive elements becomes relevant in limiting the deformation of the elements themselves and, in turn, reducing the percentage of delamination.

In other words, at MOD values below 0.1 µm, the delamination is mostly force-driven, while at higher MOD values, it progressively becomes mostly displacement-driven.

The fracture of fragile interfaces (failing at smaller MOD values) is also driven by local forces and thus by the cohesive energy (fracture directly affected by the whole set of cohesive parameters and curves quite different from each other at MOD values below 0.1 µm); in contrast, the fracture of compliant interfaces (failing at large MOD values) is mainly displacement-driven as it only depends on the local opening value and is mostly unaffected by the other cohesive parameters (curves progressively overlapping to each other as MOD values tend to 0.3 µm).

Due to the thermomechanical deformation mode of interest (warpage due to temperature variation), the overall structural stiffness of the package may also affect the failure for a given set of

cohesive parameters. In fact, for very stiff structures (low local displacements with forces at the interface limited by the cohesive layer), the local displacements hardly reach the MOD value necessary for the delamination (right end of the diagram in Figure 51), poor or not delamination at all, independent of the other cohesive parameters σ_{max} and Gc).

Instead, intermediate-stiffness structures (lower forces and larger local displacements at the interfaces) can easily induce local displacements comparable to the MOD value with forces comparable to σ_{max}: in this case, the delaminated area increases (peak zones in Figure 51) and greatly depends on the other cohesive parameters σ_{max} and Gc as well.

If the structure becomes too compliant (too low forces for inducing the displacements comparable to the MOD), then the amount of delamination decreases again because the local forces are lower than the cohesive traction σ_{max}, and thus the damage cannot even initiate (left side of Figure 51). In addition, in this case, the amount of delaminated area depends on both MOD and σ_{max}.

Finally, Figure 52 shows the influence of Gc on the delamination. COD is set to 0.05 µm in all simulations. The curves parametrized by the MOD exhibit a common monotonic trend. Indeed, the greater the Gc, the lower the delamination. Moreover, curves with a lower MOD induce a greater delaminated area.

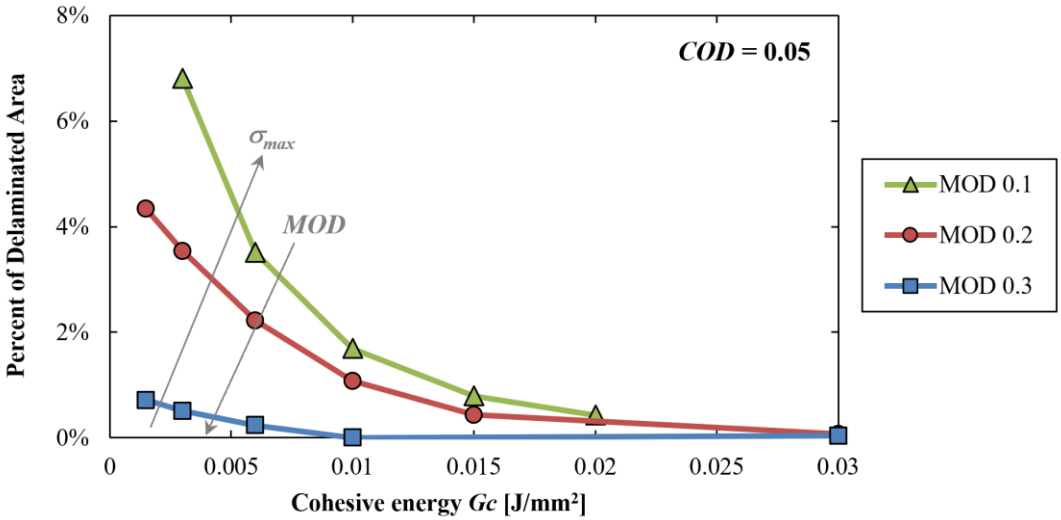


Figure 52: Local simulations results: percentage of delaminated area versus Gc with the curves parametrized with the MOD. COD is equal to 0.05 in all simulations.

The general descending trend of the curves with the Gc is easily explained by the fact that, as already seen before, with the other variables fixed, the greater the Gc, the higher the cohesive triangle will be and, in turn, the greater the produced limiting delamination traction will be. However, in this case, it is possible to see that when approaching very low values of Gc, the parametrized curves do

not tend to the same value. Indeed, even if the Gc becomes very low, in order to induce delamination in an element, it is still necessary that the local displacements reach the value of the MOD.

Summarizing the obtained results, for relatively compliant interfaces, the maximum opening displacement (MOD) is definitely the main parameter directly influencing the separation-driven delamination, while for stiffer and more fragile interfaces, the fracture-promoting energy Gc largely controls the traction-driven delamination process. The transition parameter between reversible and irreversible cohesive responses, triggered by the COD parameter, has modest effects on the delamination which only slightly decreases as the above transition is delayed (increasing COD/MOD values).

The given comprehensive description of this advanced modeling approach, including a global–local approach and the implementation of CZM, provides a complete and accurate solution for the FE simulation of delamination in power electronics and similar applications. Moreover, the modeling tools used for delamination simulations are typically calibrated through reverse procedures to replicate experimental results and there is no unique accepted methodology for this purpose; thus, an accurate explanation of the model's functioning and an analysis of the conducted parametric study and sensitivity analysis provides, given a target experimental result, fundamental reference points and guidelines for a conscious calibration of the constitutive parameters of the model, with regard to the specific application.

4.6 Conclusions

In the present chapter, the modeling procedures of damage phenomena in power modules have been discussed, with specific reference to ductile damage in elastoplastic materials, brittle damage in the encapsulating resin, and delamination at critical interfaces. Prior to the damage modeling analyses, a comparative study was carried out between a purely elastic package (all materials modeled as linear elastic) and an elasto-plastic package (e.g., Copper, Solder, Polyimide modeled as elastoplastic). From this comparative study, it was observed and confirmed that in a purely elastic package stresses can be overestimated at the maximum temperature of the thermal cycle, and no residual stresses or plastic deformations are present—features that are, however, fundamental for explaining phenomena such as warpage or thermomechanical fatigue damage of metallic layers.

Regarding ductile damage, the histories of triaxiality factor and accumulated plastic strain were evaluated as a function of the number of cycles. The analysis highlighted that solder is the

material particularly prone to accumulate plastic strain (and, consequently, more susceptible to thermomechanical fatigue damage). For the encapsulating resin, a pressure-dependent brittle damage model, referred to as the modified Tresca (MT), was calibrated on the basis of experimental data from the literature concerning two types of thermosetting resins. From the MT damage model, it was found that the critical stress level below which the resin does not undergo damage before 10 cycles is approximately 180 MPa.

Finally, by employing literature data for the parameters of a bilinear Cohesive Zone Model (CZM), the resin–die interface was modeled. However, this interface did not exhibit particularly significant values of the damage variable (i.e., only a limited stiffness degradation) during the imposed thermal cycles.

Chapter 5: Modelling of the mechanical behavior of a SiC-based power module subjected to spatial thermal gradients

In the sections discussed before, it has been assumed that the electronic package is subjected to quasi-static thermal loading conditions, typical of passive reliability tests carried out in a climatic chamber. In these tests, the power module is placed inside temperature-controlled chambers and is cyclically heated and cooled over time intervals on the order of several tens of minutes.

In addition to passive tests, power modules are also subjected to active power cycling reliability tests, characterized by faster thermal cycles. In this case, the package is mounted on dedicated test benches, where a DC or AC power supply imposes controlled power cycles on the electronic device. For each power cycle, the module responds with a thermal transient.

The diagram shown in Figure 53, taken from the standard [16], qualitatively illustrates the temperature history measured at the hottest point of the package, i.e., inside the semiconductor die (junction temperature). It is within the die that the greatest amount of electrical power is dissipated through Joule heating, leading to heat transfer from the interior to the exterior of the module.

According to reliability testing standards, in addition to the junction temperature -typically estimated via direct voltage and/or current measurements within the die- two other temperatures are often monitored: the so-called case temperature (Tc) and sink temperature (Ts). The case temperature is measured during tests in which the power module includes the copper baseplate, with the sensor placed at a specific point on this element. The sink temperature is measured in configurations where the module is also equipped with a heat exchanger, either air- or liquid-cooled, with the sensor placed near the finned surface.

The temperature difference between Tj and Tc provides valuable information about the spatial thermal gradient between the die and the baseplate. This gradient depends, as expected, on the thermal conductivity of the intermediate layers and their geometry, particularly their thickness.

Spatial temperature gradients contribute to the generation of thermomechanical stresses within the package, since hotter regions tend to expand more than cooler ones, resulting in constrained thermal deformation.

In this section, the thermomechanical response of a SiC-based package to a spatial temperature gradient will be discussed. Two cases will be considered: first, a time-independent temperature field; second, a more general case involving a time-dependent temperature distribution.

For the sake of simplicity, the modeled spatial temperature distribution has been assumed to be spherical.

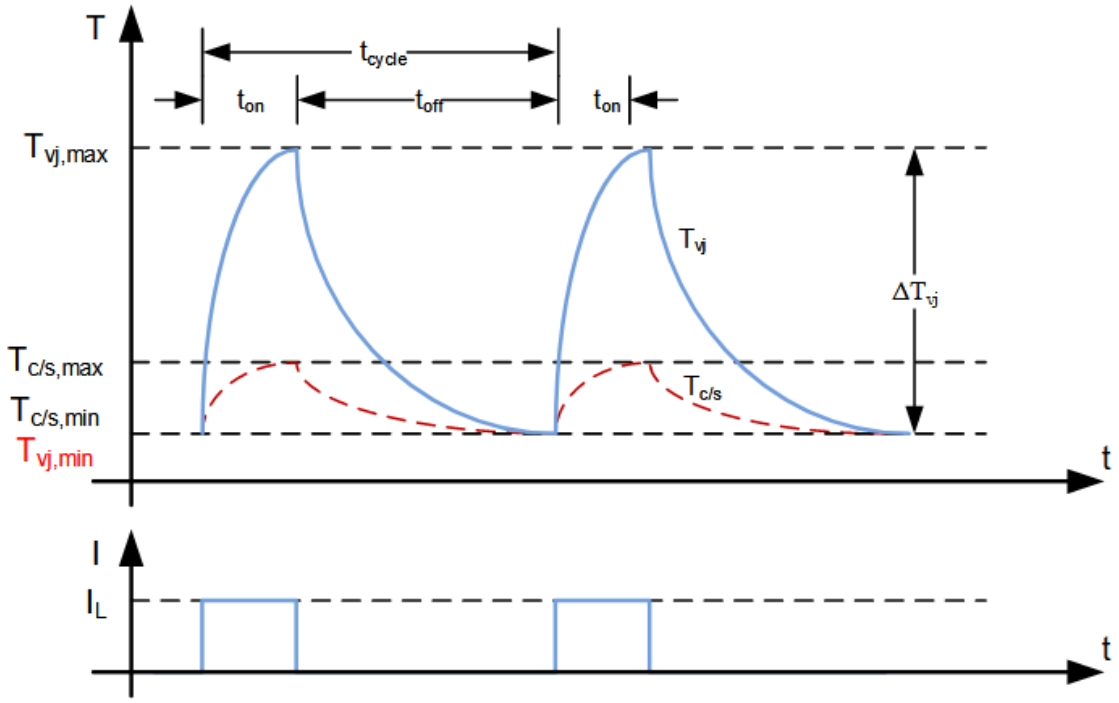


Figure 53: Thermal histories measured at specific locations (up) and current cycles (down) imposed on a power module, during an active thermal cycle.(Image taken from [16])

5.1 Modelling procedure

Let us consider the package model described in the paragraph 3.2. The modeled geometry corresponds to one quarter of the full package, exploiting two symmetry planes: x–y and z–y.

Materials have been modeled under the assumption of linear elasticity, except for the copper, solder, and polyimide layers, which have been considered as elastoplastic materials, with their respective flow curves defined by equations ((5). The table containing the linear thermo-mechanical properties is the Table 8.

The novelty introduced in the present analysis lies in the different modeling of the initial conditions and boundary conditions applied to the system. The following two cases are distinguished.

5.1.1 Spatial gradients constant with time

Let us assume that the modeled package is subjected to one active heating/cooling thermal cycle with a total duration of τ = 100 s. Suppose that the hottest point within the die, located at coordinates (x_0, y_0, z_0), follows a triangular time–temperature profile ranging between T_{min} and T_{max}. An effective way to express such a thermal cycle in analytical form is the following:

(11) $T(x_0, y_0, z_0, t) = T_{min}(x_0, y_0, z_0) + \frac{2}{\pi}[T_{max}(x_0, y_0, z_0) - T_{min}(x_0, y_0, z_0)]|arcsin\,(sin(\omega t))|; t \in [0, \tau]$

The absolute value in the equation is used to rectify the triangular waveform, which would otherwise consist of a positive and a negative half-wave of period equal to 2τ. With this consideration, the angular frequency ω of the thermal cycle is given by: $\omega = 2\pi/2\tau = \pi/\tau = 0.0314$ rad/s. Let us consider the following scalar field, defined on a parallelepiped undeformed domain having the dimensions a x b x c (eq. (12)):

(12) $T: [0, a]x[0, b]x[0, c]x[0, \tau] \rightarrow \mathbb{R} \quad T(x, y, z, t) = T(x_0, y_0, z_0, t) - k\,\rho^2(x, y, z)$

where $T(x_0, y_0, z_0, t)$ is the function reported in the equation (11), ρ is the distance between the generic point P(x, y, z), belonging to the spatial domain, and the hottest point of the package (x_0, y_0, z_0); k is the real parameter which regulates the temperature gradient along the radial coordinate ρ. It is straightforward to observe that, according to eq. (12), all points equidistant from the hottest point of the die have the same temperature (spherical distribution). If the parameter k does not have a dependency of time, then the spatial gradient of temperature is, consequently, time independent.

To determine the value of *k*, a temperature gradient must be imposed at a fixed time instant. It should be noted that, physically, at t = 0 s all points in the package should be at the same temperature, T = 25 °C. However, this would result in a zero value of *k*.

Therefore, consider $t = \tau/2$ = 50 s, which corresponds to the maximum temperature. The condition to be imposed is that the temperature difference ΔT between the point *(x_0, y_0, z_0)* and the point at the maximum distance from it, *(a, b, c)*, is 60 °C. The calculation is then the following:

$(x_0, y_0, z_0) = (0, 1.35, 0)\ [mm] \quad and\ (a, b, c) = (5, 5, 7.5)[mm] \rightarrow \quad \rho^*$

$= \sqrt{(5-0)^2 + (5-1.35)^2 + (7.5-0)^2} = 9.725\ mm$

$k = -\frac{\left(T_{(a,b,c)} - T_{(x_0,y_0,z_0)}\right)}{\rho^{*2}} = 0.634\ \frac{°C}{mm^2}$

Once the value of *k* is fixed (or a time-independent spatial ΔT is imposed), it becomes evident that if the initial temperature of the SiC is assumed to be 25 °C, at t = 0 s, then -at the furthest point from the SiC hotspot- the temperature predicted by the present model would be −35 °C.

This clearly demonstrates that, in order to accurately model time-varying spatial temperature gradients within the package, *k* must be treated as a function of time.

Nevertheless, for the purpose of maintaining a constant-gradient model, it has been assumed that at t = 0 s the temperature at point *(a, b, c)* is 25 °C (corresponding to 85 °C at the SiC hotspot), and at t = 50 s, the maximum temperature reaches 160 °C (with 100 °C at the point furthest from the hotspot).

5.1.2 Spatial gradient varying with time

Let us now consider the temperature field defined by equation (12). The physical phenomenon to be simulated is a temperature difference (ΔT) between the SiC hotspot and the point located at the maximum distance from it, which starts from zero at t = 0 s, increases linearly over time up to 60 °C at $t = \tau/2$, and then returns to zero.

For this purpose, the triangular waveform previously introduced in equation (11) can be recalled and employed as follows:

$$k(t) = k_{max}\frac{2}{\pi}|\arcsin(\sin(\omega t))| = -\frac{T(x,y,z,t) - T(x_0,y_0,z_0,t)}{\rho(x,y,z)^2}$$

Considering that the function $T(x_0, y_0, z_0, t)$ is the one given in equation (11), the temperature field with a linearly time-varying gradient is expressed by the following equation:

(13) $$T(x,y,z,t) = T_{min}(x_0,y_0,z_0) + \frac{2}{\pi}|arcsin\,(sin(\omega t))|[T_{max}(x_0,y_0,z_0) - T_{min}(x_0,y_0,z_0) - k_{max}\,\rho^2(x,y,z)]$$

5.2 Results and discussion

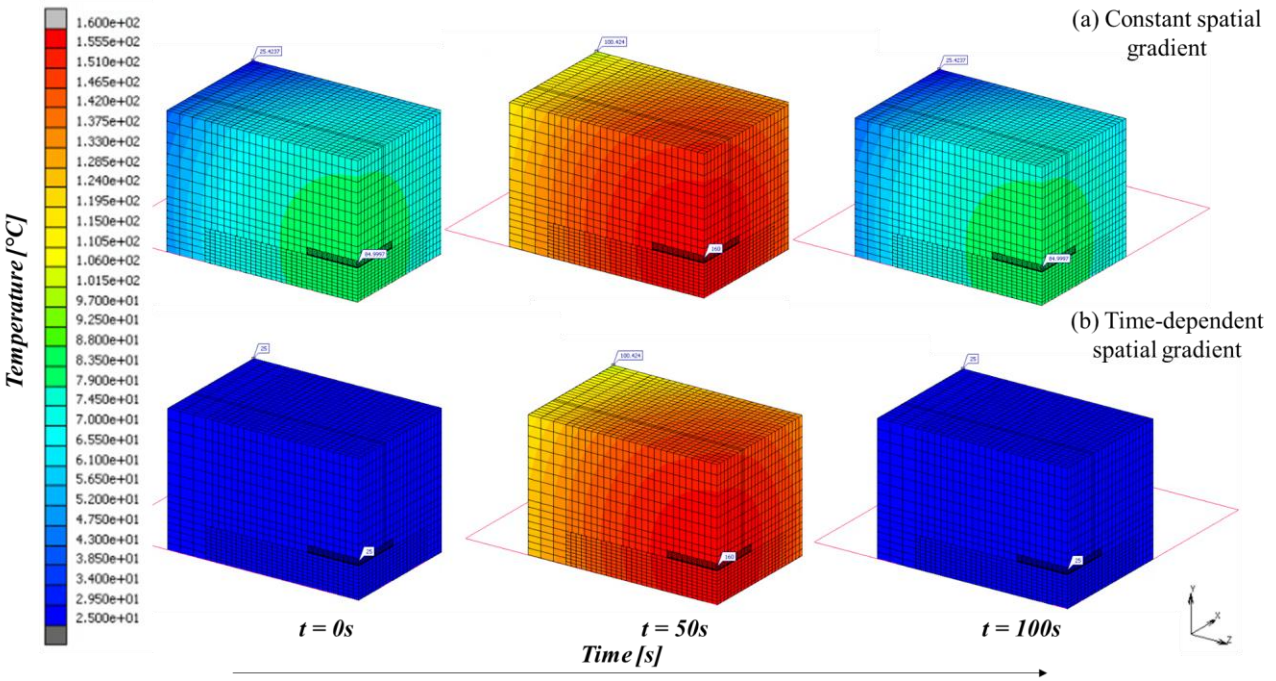


Figure 54: Spatial distribution of temperature in the two modeled cases: a) Constant spatial gradient; b) Time-dependent spatial gradient.

As already done in Chapter 3, the stress distributions were analyzed at two specific time points during the thermal cycle applied to the package: at the peak temperature (t = 50 s, corresponding to the mid-cycle) and at the end of the cooling phase (t = 100 s). At these two instants of time, the components of stress tensor were plotted along six interfaces of the package (it should be noted that the origin of each path lies on the package's axis of symmetry, i.e., the y-axis):

- **Interface 1**: copper/solder in the first segment of the path; copper/resin in the second segment;
- **Interface 2**: solder/SiC;
- **Interface 3**: SiC/resin in the initial segment; SiC/TEOS in the final segment where the contact with the passivating frame begins;
- **Interface 4**: TEOS/Si_3N_4 (and a short section of TEOS/polyimide near the edge of the double passivation);
- **Interface 5**: Si_3N_4/polyimide;
- **Interface 6**: polyimide/resin;

All the paths and their respective interfaces are reported in the following Figure 55. The stress distribution plots were organized into three columns. The first column contains the stress components that are continuous across the interface, namely the normal component to the interface and the two interlaminar shear stress components. The second and third columns contain, respectively, the stress components that are discontinuous when transitioning from material A to material B across the interface: two in-plane normal stress components and one in-plane shear stress component.

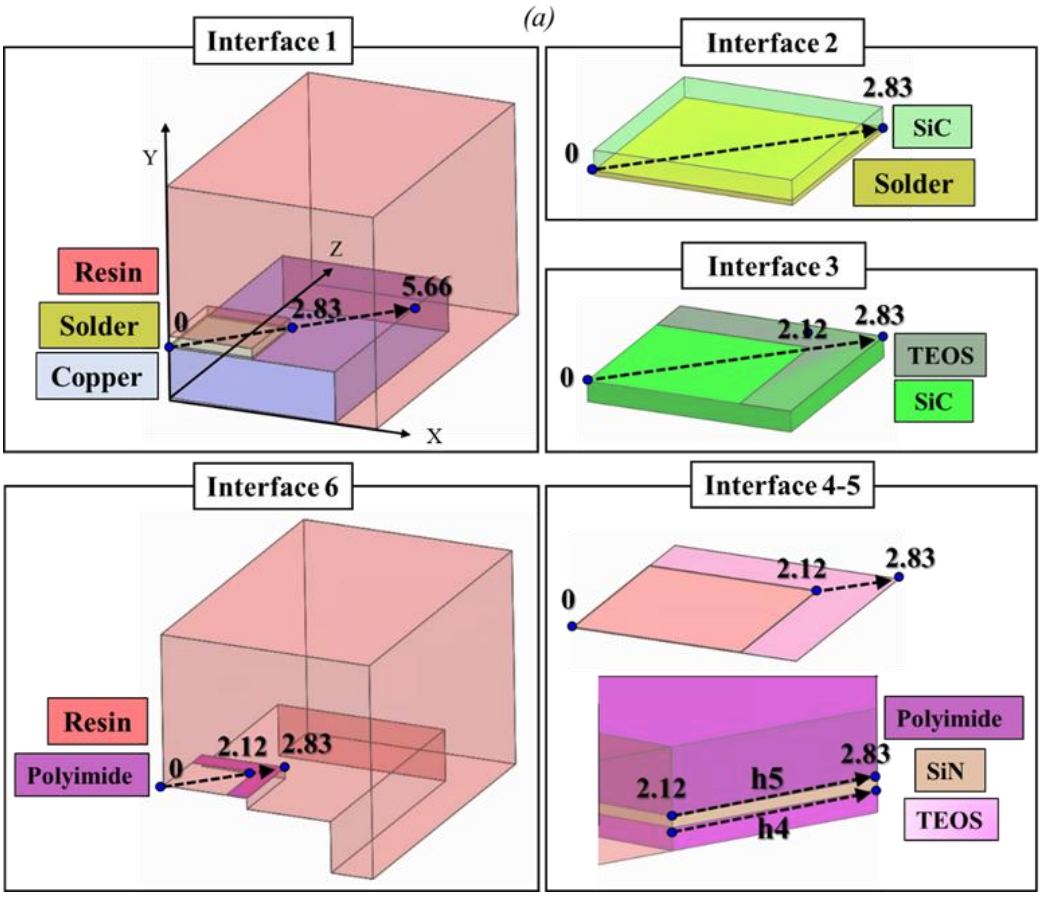


Figure 55: Paths and interfaces where stress components were extracted.

5.2.1 First case: spatial gradient of temperature constant with time

5.2.1.1 Stress components at mid-cycle (t=50 s)/maximum temperature

At interface 1 (copper/solder and copper/resin), the interfacial stress components exhibit strong local variations near material transitions: in particular, the interfacial normal stress σ_{22} changes from a plateau value of 10 MPa, at the interface with solder, to a plateau value of almost zero, in the region of contact with the resin. At the same time, the interlaminar shear components are nearly equal to each other (in terms of absolute value) and exhibit a monotonic increasing trend from zero up to 20 MPa in the transition region. In both copper side and solder (or resin) side, the in-plane shear stress

is approximately negligible in the regions of the path undisturbed from the transition zone. The copper is mainly in a compression stress state ($\sigma_{11}=\sigma_{33}$=-20 MPa out of the transition zone), as well as the solder ($\sigma_{11}=\sigma_{33}$=-10 MPa). Instead, the resin side is mainly in tension ($\sigma_{11}=\sigma_{33}$=10 MPa out of the transition zone).

At interface 2 (solder/SiC), the stress components in the SiC layer reach higher values: σ_{11} and σ_{33} assume approximately a peak value 210 MPa at the center of the layer, progressively decreasing -towards the boundary of the die- to 30 MPa.

Regarding the passivating frame, the in-plane normal stresses are approximately equal to 40 MPa and 120 MPa, respectively, in the TEOS and Si_3N_4 region, confirming the relevant gradient of stresses through the thickness.

5.2.1.2 Stress components at the end of thermal cycle (t=100 s)

As shown in the Figure 57, at the end of the thermal cycle applied to the package, almost all six considered interfaces are unstressed. This can be explained by the fact that the ductile layers accumulate negligible plastic strains along the thermal history modeled in this specific case. In fact, as already discussed in Chapter 4, if all layers were modeled as purely elastic materials, then the entire package, at the end of the cooling phase, would return to its initial mechanical state (undeformed and stress-free). In the case of elasto-plastic layers, if the plastic strains are "small", then after just one thermal cycle the residual stresses are also negligible. The only interface that shows significant internal stresses is the copper/solder interface. On the copper side, there is a distribution of in-plane normal stresses reaching a peak of about 30 MPa (at the center of the package), which decrease progressively toward the copper/resin interface, where they completely vanish. This observation can be confirmed posing the focus on the distributions of plastic strains accumulated in the following layers: copper, solder and polyimide.

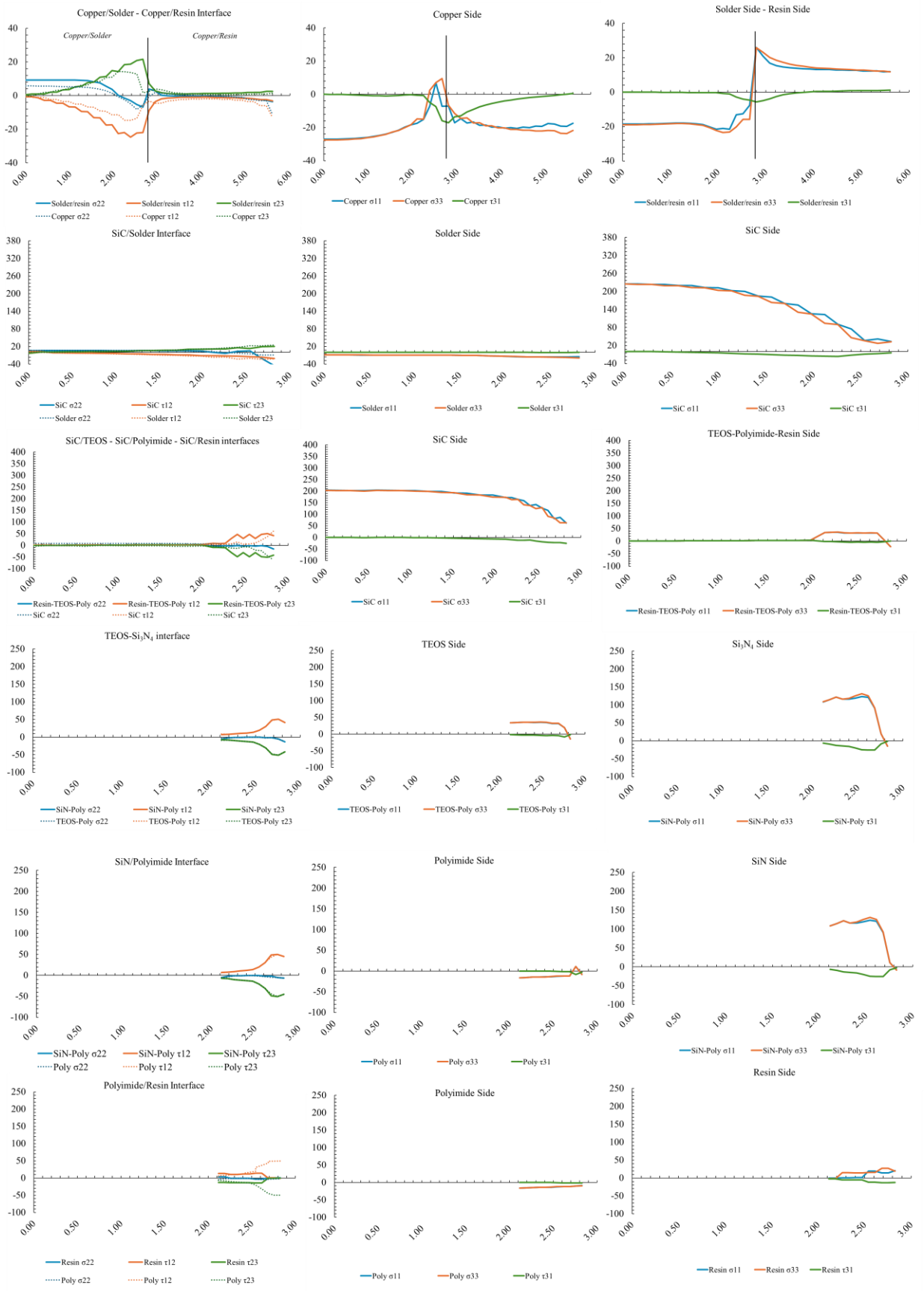


Figure 56: First case of spatial thermal gradient: stress components (y-axis) plotted along the interfaces (arc length in x-axis) considered in figure Figure 55, at t=50 s (mid-cycle).

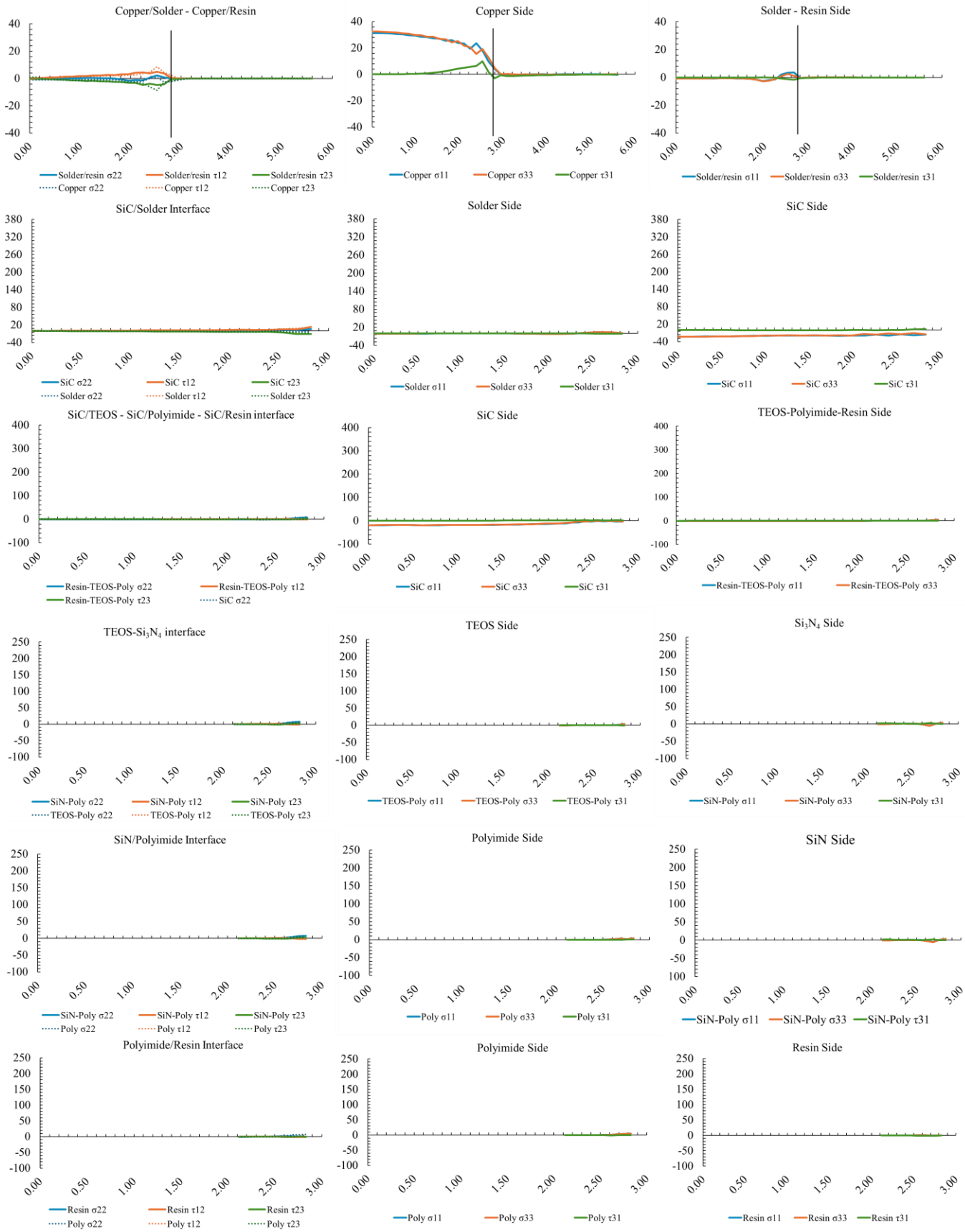


Figure 57: First case of spatial thermal gradient: stress components (y-axis) plotted along the interfaces (arc length in x-axis) considered in Figure 55, at t=100 s (end of cooling cycle).

5.2.1.3 Distributions of plastic strains in ductile layers at t=50 s (mid-cycle), and t=100 s (end of cooling phase)

As shown in the following Figure 58, the residual strains accumulated at the end of the thermal cycle at interfaces involving elastoplastic materials remain below 1%. The peak in accumulated plastic strain is observed in the solder at the interface with the SiC, near the sharp corner edge, where a stress concentration or amplification is certainly present. At the copper/solder interfaces, on the copper side, the plastic strain distribution is approximately uniform toward the central region of the package (around 0.05%) and increases rapidly toward the transition zone with the resin, reaching approximately 0.15%. At the interfaces involving the polyimide at the edge of the passivation layers (TEOS and Si_3N_4), plastic strains are maximum at the outer sharp edge of the frame and reach values on the order of a few ten-thousandths. Relatively higher plastic strains are found in the polyimide frame at the interface with the resin, reaching values of about 0.5%. It is worth noting that these values are likely influenced by the mesh refinement level in the vicinity of the sharp corner, which may affect the accuracy of the local strain estimation.

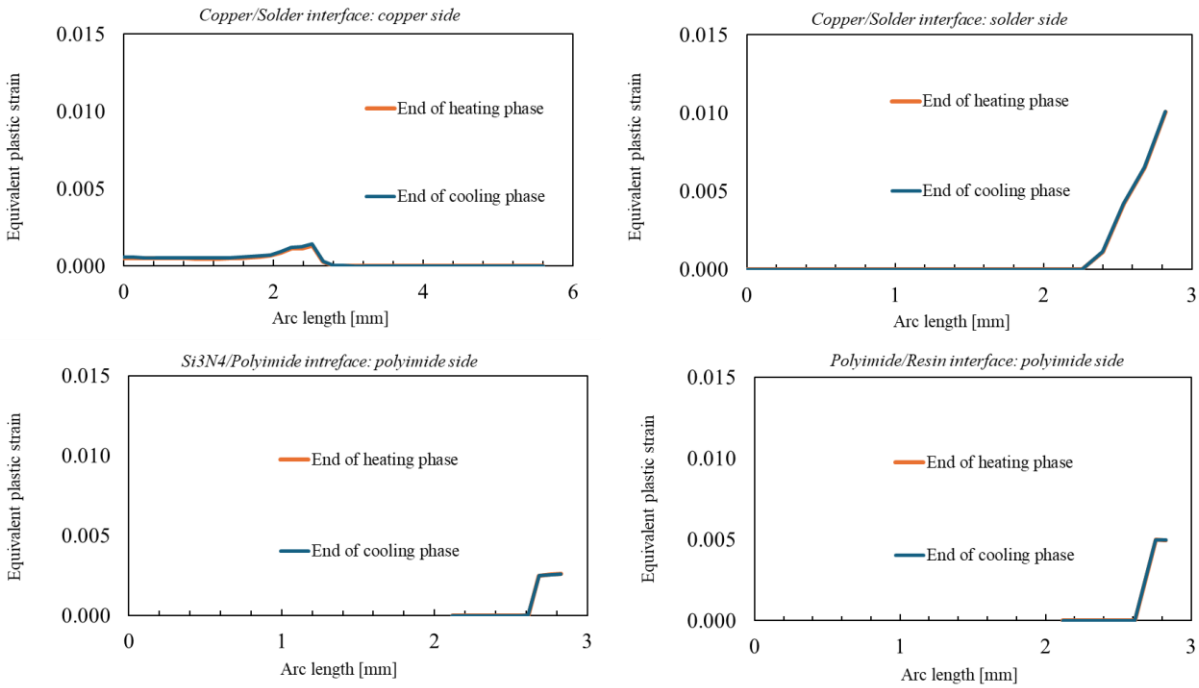


Figure 58: Distributions of equivalent plastic stains, along four elastoplastic interfaces, at mid-cycle (t=50s) and at the end of cooling phase.

5.2.2 Second case: spatial gradient of temperature varying with time

5.2.2.1 Stress components at mid-cycle (t=50 s)/maximum temperature

In the second case, characterized by a time-dependent spatial temperature gradient model, it is clearly observed that the hottest point of the package (within the die) undergoes a greater thermal excursion compared to the case with a temporally constant temperature gradient. Specifically, at this location, the temperature variation (ΔT) at peak heating in Case 1 was 75 °C, whereas in Case 2 the same point experiences a ΔT of 135 °C at mid-cycle. It is therefore expected that the layers surrounding the die in Case 2 are subjected to higher mechanical stresses than in Case 1.

As shown in Figure 59, at the copper/solder interface, the normal stress component perpendicular to the interface is approximately uniform and positive (tensile), with a magnitude of about 10 MPa. This value progressively decreases, eventually changing sign, towards the transition zone near the copper/resin interface, where it becomes nearly zero. The interlaminar shear stresses along the copper/solder interface increase in absolute value from zero at the center of the package, reaching a peak of approximately 20 MPa in the transition region close to the copper/resin interface. Along the latter interface, these shear stresses tend to vanish.

The in-plane normal stresses within the copper layer follow an approximately parabolic trend, ranging from –30 MPa (compressive) at the center of the package, to around 15 MPa near the copper/resin transition, and returning to –30 MPa in the copper region in direct contact with the resin. On the other side of the interface, the in-plane normal stresses within the solder layer are about –20 MPa (compressive), transitioning to an average of 15 MPa within the resin layer. The in-plane shear stresses can be reasonably considered negligible.

As in the previous case, at the SiC/solder interface, the most critical stresses (or the most critical stress gradients) are the in-plane normal components within the SiC layer. It is clearly observed that at the center of the SiC, the in-plane normal stress reaches a peak value of approximately 300 MPa, decreasing progressively to about 30 MPa towards the outer edge of the layer. In the previous case, the peak stress was approximately 220 MPa.

The in-plane normal stresses within the TEOS layer reach a plateau value of about 50 MPa along the diagonal of the frame, which is 10 MPa higher than in the previous case. In the Si_3N_4 layer, these stresses exhibit a plateau of approximately 180 MPa along the same path, representing an increase of 55 MPa compared to Case 1.

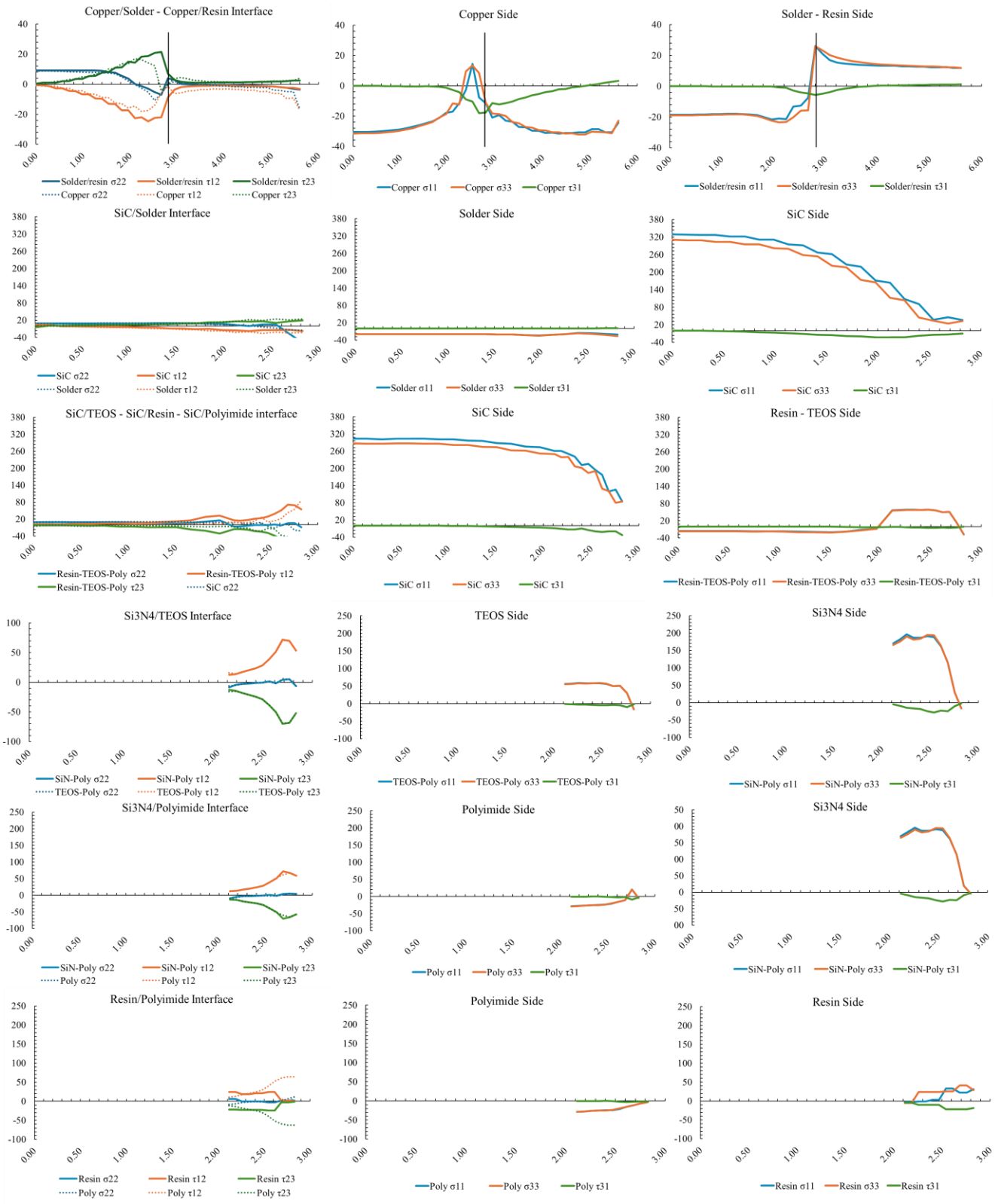


Figure 59: Second case of spatial thermal gradient: stress components (y-axis) plotted along the interfaces (arc length in x-axis) considered in Figure 55, at t=50 s (mid-cycle).

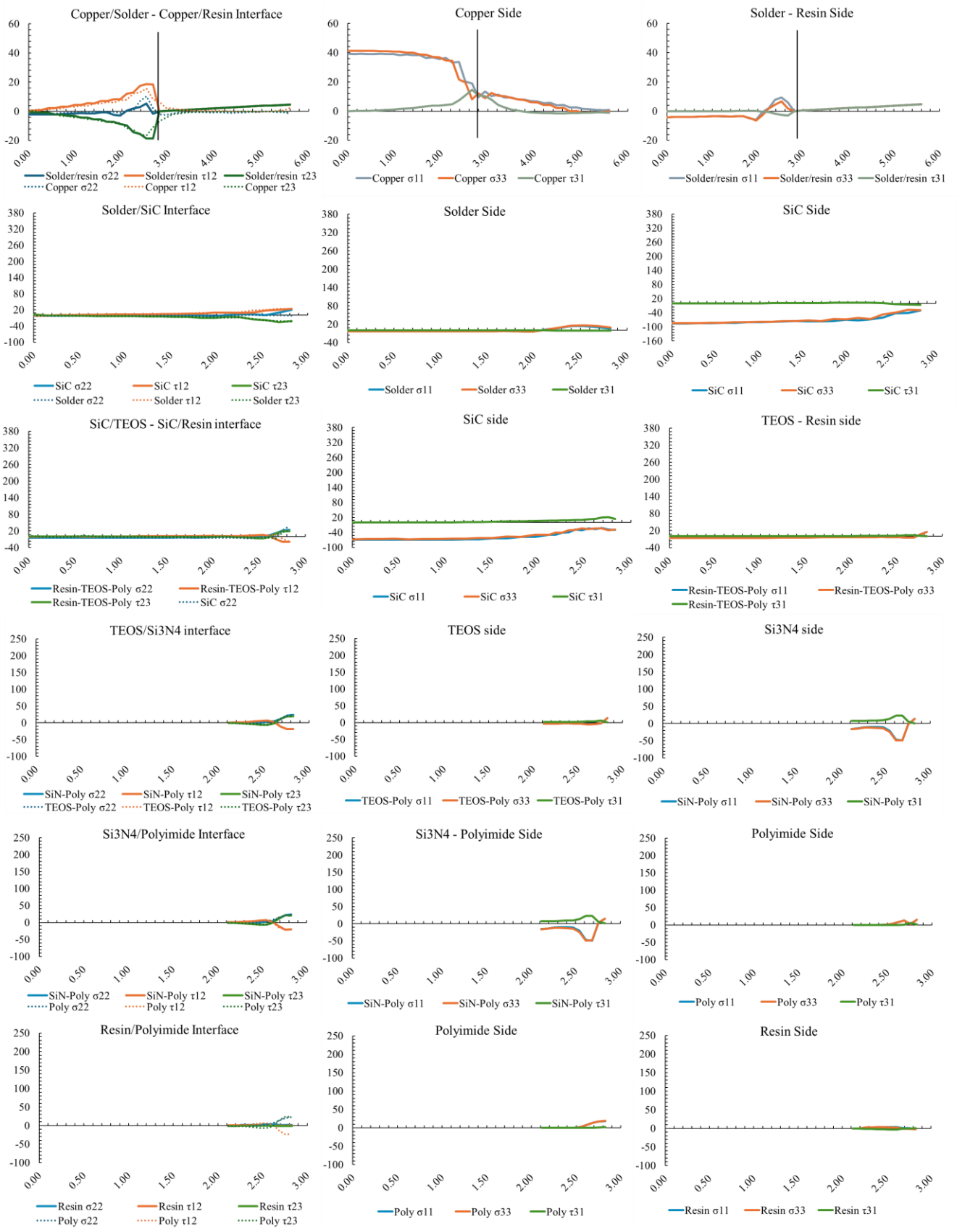


Figure 60: Second case of spatial thermal gradient: stress components (y-axis) plotted along the interfaces (arc length in x-axis) considered in Figure 55, at t=100 s (end of cooling).

5.2.2.2 Stress components at the end of cooling phase (t=100 s)

As shown in Figure 60, also in this second case, some material interfaces become stress-free at the end of the thermal cycle, while those involving elastoplastic materials that have undergone plastic deformation exhibit residual stresses. At the copper/solder interface, residual interlaminar shear stresses of approximately 20 MPa are observed in the transition zone toward the copper/resin interface. On the copper side, at the end of the heating phase, the residual in-plane normal stresses are relatively uniform toward the center of the package, reaching values of approximately 40 MPa in tension, and progressively decreasing toward the resin-adjacent regions.

At the SiC/solder interface (SiC side), the in-plane normal stresses are compressive and range from –85 MPa at the center of the package to –20 MPa at the outer edge of the SiC. If Case 1 had been considered, these latter stresses—at the end of the thermal cycle—would have been nearly negligible (Figure 60). This clearly demonstrates that the modeling approach adopted for the time-dependent spatial thermal gradients has a significant influence on the resulting stress distributions.

Finally, at the Si_3N_4/polyimide interface, both the residual interfacial stresses and the in-plane normal and shear stresses are more concentrated in the transition zone between the two passivation frames. The Si_3N_4 frame is laterally surrounded by polyimide, a material that undergoes extensive plastic deformation. As a result, plastic deformation is localized in this region. At the polyimide/Si_3N_4 interface, interfacial stresses peak at the outer edge of the polyimide frame, all reaching approximately 25 MPa in absolute value. In-plane normal stresses on the silicon nitride side reach a compressive peak of –35 MPa in the transition zone toward the polyimide frame, while the in-plane shear stress component reaches a maximum of about 25 MPa at the same location.

5.2.2.3 Distributions of plastic strains in ductile layers at t=50 s (mid-cycle), and t=100 s (end of cooling phase)

As shown in Figure 61, the trends of the plastic strain distributions, both at the end of the heating phase and at the end of the thermal cycle, are similar to those observed in Case 1, but with higher peak values, as expected. At the copper/solder interface, the copper continues to accumulate plastic strain even after reaching the maximum temperature. The plastic deformation is uniformly distributed across the central regions of the package, with an average value of approximately 2.3 ‰ along the initial segment of the path at the end of the thermal cycle. The peak plastic strain at the end of the cycle reaches approximately 3.8 ‰ in the transition zone near the copper/resin interface.

The solder undergoes an additional 1% of plastic strain during the cooling phase, increasing from a maximum of 4% up to 5% at the most stressed location, namely the sharp corner edge.

Polyimide is the only layer that does not exhibit any further accumulation of plastic strain during the second part of the cycle. The maximum plastic strain in this layer is localized at the interface with the encapsulant resin, close to the outer edge. In this region, the plastic strain at the end of the thermal cycle is approximately 4%.

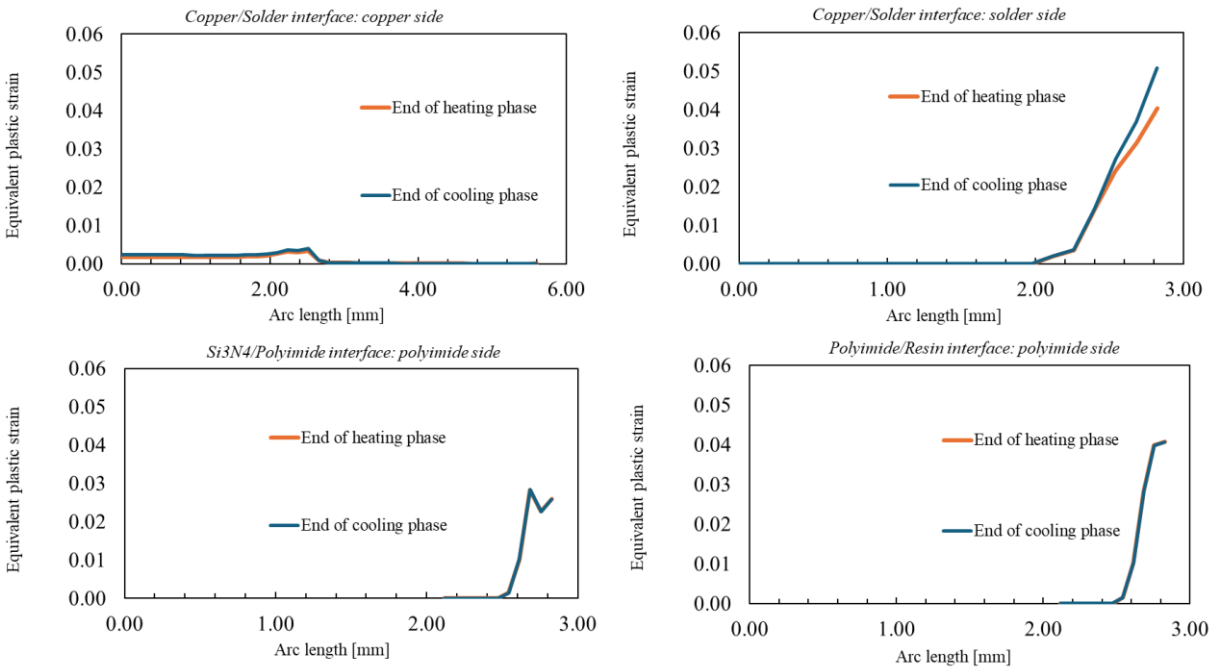


Figure 61: Distributions of equivalent plastic stains, along four elastoplastic interfaces, at mid-cycle (t=50s) and at the end of cooling phase.

5.3 Conclusions

In his chapter, the thermo-mechanical response of a SiC-based power module subjected to spatial thermal gradients has been investigated, simulating the typical condition of an active power cycle. Unlike passive thermal cycling, active power cycling induces faster temperature fluctuations and more localized thermal gradients, especially at the die level, where power is dissipated through Joule heating.

To simulate this behavior, two different spatial temperature field scenarios were analyzed: one assuming a time-invariant spatial gradient, and the other introducing a time-dependent temperature distribution. A spherical temperature profile was assumed in both cases, with the highest temperature located at the SiC hotspot and decreasing radially. In the first case, a fixed temperature difference

between the hotspot and the external boundary was imposed throughout the cycle, while in the second, the gradient evolved in time, reaching its peak at mid-cycle and returning to zero at the end.

The mechanical response of the package was evaluated in terms of interfacial stress distributions and plastic strain accumulation. Results revealed that during the heating phase (mid-cycle), substantial thermal stresses developed, particularly along the SiC/solder and passivation interfaces.

At the end of a thermal cycle, the maximum observed plastic strain is on the order of 5%, localized on a stress concentration point, at the SiC/solder interface.

Consequently, residual stress distributions at the end of the cooling phase were “minimal” but not negligible. This confirms that a single thermal cycle, under the assumed conditions, induces limited irreversible mechanical damage, although repeated cycles would likely lead to fatigue accumulation over time.

From the results observed so far, it can be inferred that the solder remains the layer most prone to thermal fatigue damage, while the die and its passivation layers are subject to delamination phenomena due to the high normal and shear stress gradients across the thickness.

In summary, the results underline the critical role of temperature gradients -not only in magnitude but also in their temporal evolution- in determining stress distributions within power electronic packages. The developed modeling approach allows to capture the primary effects of non-uniform and transient thermal fields, laying the groundwork for future fatigue life predictions and reliability assessments under realistic power cycling conditions.

Chapter 6: Quasi-static tensile response of Polycarbonate

Polycarbonate (PC) is an amorphous thermoplastic polymer widely used in engineering applications due to its unique combination of mechanical, optical, and thermal properties. Its high impact resistance, transparency, dimensional stability, and ease of processing make it suitable for various structural and safety-related components across automotive, aerospace, consumer electronics, and protective equipment industries. Applications include transparent armor, safety visors, optical lenses, machine guards, and structural glazing, where both mechanical reliability and visual clarity are essential. The mechanical behavior of Polycarbonate, however, is considerably more complex than that of traditional structural metals, especially under uniaxial tensile loading. Unlike metallic materials, where plastic deformation typically localizes and leads quickly to fracture following necking, Polycarbonate exhibits a peculiar deformation mechanism characterized by strain localization followed by strain propagation along the gauge length. This unique behavior introduces significant challenges in the interpretation of experimental results, the identification of the constitutive behavior, and the modeling of its deformation in numerical simulations. The tensile behavior of Polycarbonate has been the subject of extensive research over the last few decades. When subjected to uniaxial tensile loading, the material initially deforms uniformly across the gauge length. Upon reaching the maximum load, the specimen undergoes necking, characterized by localized plastic deformation and a reduction in cross-sectional area. While in ductile metals necking typically leads to rapid fracture due to continued strain localization, in Polycarbonate the localization gradually relaxes, and the deformation begins to propagate along the specimen. This phase is characterized by a plateau in the load-displacement curve, indicating a pseudo-stable propagation of the neck under nearly constant load. The first systematic observation of this strain propagation phenomenon in polymers was reported by Miklowitz [71], and subsequent works by G'Sell and Jonas [72] and G'Sell et al. [73] provided fundamental insights into the mechanics of necking and its transition into propagation. By employing area-based measurements and high-speed photography, they attempted to reconstruct the true stress–strain curve and to infer the material's constitutive response. Their work also emphasized the necessity of accounting for triaxial stress states in the necked region, following Bridgman's correction approach, in order to correctly derive the flow curve from the true stress–strain response. Buisson and Ravi-Chandar [74] further advanced the understanding of the neck propagation in PC by using a grid technique to capture the heterogeneous strain field during tensile loading. They attempted to extract the constitutive behavior of the material through photoelastic analysis, revealing the difficulties in interpreting experimental data due to strain gradients and stress triaxiality. Neale

and Tugcu [75] explored this complex behavior through finite element simulations, proposing that the observed neck propagation in polymers is analogous, in some respects, to Lüders band propagation in metals. Hutchinson and Neale [76] provided a theoretical framework for the analysis of neck propagation based on nonlinear elasticity and inelastic flow theories, underscoring both the similarities and the key differences between polymers and metallic materials.

Due to the complexity of its deformation mechanisms, Polycarbonate (PC) requires characterization approaches distinct from those typically used for metals [77–79]. Moreover, the intrinsic rate and temperature sensitivity of Polycarbonate adds further complexity, as the material exhibits significant viscoelastic and viscoplastic behavior that must be accounted for in any realistic modeling framework. To address these challenges, several researchers have proposed continuum-level constitutive models for glassy polymers. Sarva and Boyce [80], for instance, developed a three-dimensional constitutive framework based on intermolecular resistance, capturing both static and dynamic responses of PC. Mulliken and Boyce [81] and Richeton et al. [82] proposed rheological models incorporating temperature, pressure, and rate dependencies. Bergström [83] introduced a micromechanical model for large-strain viscoplastic behavior in amorphous polymers, which has been successfully applied to various polymeric systems including PC. Other efforts, such as those by Safari et al. [84], focused on high-rate response modeling through rheological formulations, while Cao and co-authors [85] proposed viscoelastic and elastoplastic constitutive models to capture the tensile response of PC under different thermal and loading conditions. These studies collectively confirm that PC's mechanical response is governed by a complex interplay of strain rate, temperature, and molecular dynamics. Despite the richness of proposed models, a fundamental problem persists: accurately capturing the post-necking behavior and deriving the constitutive curve from experimental data. Many studies either neglect the correction for triaxiality or rely on empirical assumptions, which leads to inaccuracies in numerical simulations and prevents the reliable extrapolation of material behavior under different loading regimes. Recent advancements in optical measurement techniques have opened new avenues for characterizing the mechanical behavior of PC. Digital Image Correlation (DIC), in particular, has emerged as a powerful tool for measuring full-field strain distributions in polymer specimens. By tracking the surface displacement of speckled patterns during deformation, DIC provides spatially resolved strain maps, making it possible to study localization phenomena and to reconstruct true stress–strain curves based on local cross-sectional area reductions. Several researchers have applied DIC to study Polycarbonate. Tzibula et al. [86] performed quasi-static and dynamic tensile tests on round specimens and identified different stages of necking and propagation, proposing a piecewise four-point approximation of the material flow curve. Zhang et al.

[87] investigated local strain rate evolution during dynamic necking, showing that the local strain rate can be two or three times greater than the nominal value. Their models attempted to simulate the dynamic response either by amplifying the static curve or by applying a thermally activated yield formulation. Foster et al. [88] and Mirone et al. [89] further analyzed the mechanical behavior of PC using DIC technique. Sato et al. [90] extended the study to shock regimes, proposing empirical relationships to fit the experimental curves at low strains. Xu et al. [91] proposed a hardening function coupled with a damage evolution law, aimed at capturing the dual-phase nature of the softening and hardening responses observed in PC during tensile loading. Mirone et al. [89] proposed a "General-neck" approach for rectangular specimens, where the area-based true curve is derived from "general" cross sections undergoing deformation under constant load as the first necking section propagates along the gage length. This "general neck" true stress strain curve was corrected for triaxiality by a function based on six experimental parameters and three material parameters.

Despite the numerous studies available in the literature, a complete and widely accepted methodology to extract the flow curve of PC, particularly in the post-necking regime, is still lacking. The unique deformation pattern of Polycarbonate, including diffuse and localized necking, strain propagation, and the gradual transition from high to low triaxial stress states, makes traditional correction methods ineffective or inaccurate. The primary aim of this work is to contribute to the characterization and modeling of Polycarbonate's tensile behavior across static and dynamic loading conditions. The focus is on identifying an effective and physically grounded methodology to derive the material flow curve from experimental data, accounting for the effects of triaxiality and strain localization. Experimental tensile tests are performed on both round and flat PC specimens at quasi-static and dynamic strain rates. Two experimental-numerical approaches were developed in order to correct the area-based true stress–strain curve, eliminating the influence of triaxial stress states and obtaining the equivalent stress-strain curve (or flow curve), expressing the constitutive relationship for the plasticity of the given material. The resulting flow curves were validated by comparing experimental and simulated stress–strain behaviors, both in terms of global responses (load-displacement) and local strain distributions. The dynamic amplification of flow stress was evaluated and discussed in the context of strain rate-dependent behavior, as well as the temperature effect on the softening exhibited by the material. Through this integrated experimental–numerical approach, the present work aims to clarify several open questions in the mechanical characterization of Polycarbonate, while also providing a practical methodology for its implementation in advanced FEM simulations.

6.1 Classical Methodologies for obtaining the tensile stress-strain curve of Polycarbonate round specimens

Polycarbonate is a thermoplastic polymer capable of exhibiting extensive plastic strains. Its mechanical response under tensile loading is characterized by distinct phases: an initial pre-necking hardening phase, followed by a softening phase immediately after neck initiation, and subsequently a second hardening stage leading up to failure. The tensile mechanical characterization of this material is of fundamental importance for the analysis of applications involving permanent deformations, such as impact protection devices (helmet visors, riot shields, protective glasses, and windshields).

Assuming the material behaves as isotropic, governed by J2 (Von Mises) plasticity with isotropic hardening, the relationship between the equivalent stress and the equivalent strain defines the so-called *elasto-plastic material* curve or *flow curve*, which describes the evolution of the yield surface throughout the deformation history of the material.

Considering the principal Cauchy stress tensor $\boldsymbol{\sigma} = [\sigma_1, \sigma_2, \sigma_3]$, any second-order stress tensor can be decomposed into a hydrostatic (spherical) component: $\boldsymbol{\sigma}_h = 1/3\ \mathrm{trace}(\boldsymbol{\sigma})\ \mathbf{I}$ and a deviatoric component: $\boldsymbol{s} = \boldsymbol{\sigma} - \boldsymbol{\sigma}_h$, where $\mathbf{I}$ is the identity tensor. The *equivalent Von Mises Stress* is defined as follow ((14):

$$\sigma_{eq} = \sqrt{\frac{3}{2}\,\boldsymbol{s} : \boldsymbol{s}} = \sqrt{\frac{1}{2}\left[(\sigma_1 - \sigma_2)^2 + (\sigma_1 - \sigma_3)^2 + (\sigma_2 - \sigma_3)^2\right]} \tag{14}$$

Let us now consider the principal strain tensor $\boldsymbol{\varepsilon} = [\varepsilon_1, \varepsilon_2, \varepsilon_3]$. Under the assumption of additive elasto-plasticity, it can be decomposed into an elastic component $\boldsymbol{\varepsilon}^e$ and a plastic component $\boldsymbol{\varepsilon}^p$, such that:

$$\boldsymbol{\varepsilon} = \boldsymbol{\varepsilon}^e + \boldsymbol{\varepsilon}^p \tag{15}$$

Under the *hypothesis of incompressibility*, which expresses the condition such that plastic strains does not lead any changing in the material's volume at local scale, then the trace of the plastic strain tensor is zero:

$$trace(\boldsymbol{\varepsilon}^p) = 0 \tag{16}$$

The *equivalent plastic strain* is defined as the following scalar quantity:

$$\varepsilon_{eq}^p = \sqrt{\frac{2}{3}\,\boldsymbol{\varepsilon^p} : \boldsymbol{\varepsilon^p}} = \sqrt{\frac{2}{3}(\varepsilon_1^2 + \varepsilon_2^2 + \varepsilon_3^2)} \tag{17}$$

Considering all the assumptions mentioned above, the yield function assumed for Polycarbonate is given by:

$$(18) \quad f(\boldsymbol{\sigma}) = \sigma_{eq} - R\left(\varepsilon_{eq}^{p}\right) - \sigma_{y0} = 0$$

where R is the isotropic hardening function, and σ_{y0} is the first yield. The relationship between the equivalent Von Mises stress and the equivalent plastic strain, expressed by the equation (18), is the material's flow curve mentioned above. This curve, representing a material's property in the plastic regime, is then the target of the tensile characterization. In the following section, the experimental and numerical methodologies of the Polycarbonate characterization will be described.

6.1.1 The uniaxial tensile test of Polycarbonate round specimens

The simplest way to obtain the flow curve of a material is to perform a uniaxial tensile test on a smooth cylindrical or flat specimen. In the following paragraph, the discussion will specifically refer to cylindrical specimens, although it can be easily extended to flat specimens.

During a quasi-static displacement-controlled tensile test, a dogbone specimen is loaded in tension — using a testing machine — at a controlled elongation rate. The load cell of the testing machine instantaneously measures the applied force. By means of optical measurement techniques, which will be described in detail later, it is possible to acquire both the elongation of the specimen's gauge section and its instantaneous diameter (or the resistant cross-section).

In the large displacement regime — that is, for plastic deformations exceeding approximately 2% — the well-known engineering approach for measuring longitudinal stress and strain becomes inaccurate. For this reason, the logarithmic measure of longitudinal strain (also called *true strain*), defined as follow, is adopted:

$$(19) \quad \varepsilon_{True} = \int_{L_0}^{L} \frac{dL}{L} = ln\left(\frac{L}{L_0}\right)$$

while the measure of the longitudinal stress -in the large displacement regime- is the *true stress*, which express the ratio between the instantaneous load F and the current resistant cross-section A:

$$(20) \quad \sigma_{True} = \frac{F}{A}$$

before the onset of necking, the stress and strain distributions remain uniform along the entire gage length. Recalling the hypothesis of incompressibility expressed by (16), extended to the whole volume of the gage section, then $AL=A_0L_0$. The equations (19) and (20) can also be expressed as:

$$\varepsilon_{True} = ln\left(\frac{L}{L_0}\right) = ln\left(\frac{A_0}{A}\right) \quad and \quad \sigma_{True} = \frac{F}{A} = \frac{F}{A_0}\frac{L}{L_0}$$

basing on the the acquisition of the instantaneous elongation and the instantaneous area reduction, then we can distinguish between these two approximations of the *true stress-true strain curve:*

Elongation-based true stress-strain curve $\begin{cases} \varepsilon_{TrueL} = \ln\left(\frac{L}{L_0}\right) \\ \sigma_{TrueL} = \frac{F}{A_0}\frac{L}{L_0} \end{cases}$

Area-based true stress-strain curve $\begin{cases} \varepsilon_{TrueA} = \ln\left(\frac{A_0}{A}\right) \\ \sigma_{TrueA} = \frac{F}{A} \end{cases}$

Then, under the conditions of uniaxiality, uniformity and volume conservation, during the pre-necking phase of tensile test, the two formulations of stress and strain coincide and deliver the material's flow curve:

$\sigma_{eq} = \sigma_z = \sigma_{True}\ and\ \varepsilon_{eq} = \varepsilon_z = \varepsilon_{True}$

Once the necking initiates — corresponding to the point at which the load applied to the specimen reaches its maximum value — the specimen's geometry progressively evolves from cylindrical to hourglass-shaped. During necking, the principal strains become highly non-uniform and localize around the minimum cross-section. On the other hand, the stress state is no longer uniaxial throughout the gage length: it becomes highly triaxial at the necked region, while remaining progressively closer to uniaxial in the undisturbed sections of the specimen. In this case, the hypothesis of volume conservation of the entire gage section is no longer applicable, remaining valid only considering infinitesimal slices of the specimen.

The elongation-based true curve becomes useless during the necking localization because it underestimates the amount of local axial plastic strain in the minimum cross-section. Instead, the area-based approach represents the most accurate measurement of the stress and strain at semi-local scale since they express the averaged value of these two quantities across the necking section:

$$\sigma_{z_{AVG}} = \frac{1}{A}\iint_A \sigma_z\, dA = \frac{F}{A} = \sigma_{True_A}$$

$$\varepsilon_{z_{AVG}} = \frac{1}{A}\iint_A \varepsilon_z \, dA = \ln\left(\frac{A_0}{A}\right) = \varepsilon_{True_A}$$

In any case, the true area-based curve in the post-necking regime does not represent the material's flow curve due to the triaxial stress state developing in the necked section. In the following paragraphs, both direct and inverse methods will be discussed to relate area-based true quantities to the equivalent stress and strain. The two approximations introduced so far generally can be generally applied for tensile tests on isotropic materials, such as metals and polymers. However, unlike most structural metals, Polycarbonate exhibits peculiar deformation and hardening mechanisms, which will be directly analyzed starting from the experimental results obtained from quasi-static tensile tests on cylindrical specimens.

Quasi-static tensile tests were conducted on Polycarbonate[11] round bars machined on a lathe at the INATECH laboratories of the University of Freiburg. The tests were performed using an electromechanical testing machine Zwick Z100 (load cell with a maximum capacity of 100 kN). The tests were carried out on cylindrical specimens with a nominal gage length of 8.5 mm and a nominal diameter of 6 mm. Tensile tests were displacement-controlled, imposing a crosshead speed of 5 mm/min which corresponds to a nominal strain rate of 0.01 s^{-1}. Three repetitions were performed for each nominal strain rate.

Two optical measurement techniques were employed for strain evaluation. Instantaneous diameter measurements were acquired using an optical system based on an LED transmitter and a CMOS receiver sensor equipped with telecentric lenses (commercial Keyence TM-X5000), providing a measurement accuracy of ±1 µm. The acquisition rate of the TM-X5000 was set to 1.428 frames per second (interframe time 0.7 s), in order to obtain approximately 300 useful frames up to fracture. The recorded frames were processed using the TM-X Navigator software.

For the measurement of the elongation of the gauge length, a Basler acA4112-20 um high-resolution camera (4096 × 3000 pixels) was used, framing the specimen to capture approximately 620 pixels over the initial diameter. The frame rate set for the Basler camera was 0.5 frames per second (approximately 150 useful frames acquired by the camera). Instantaneous elongation was obtained via Digital Image Correlation (DIC), applying a typical speckle pattern to the specimen using an airbrush to control the speckle size distribution (speckle sizes ranging between 5 and 10 pixels). The frames acquired by the camera were processed using the commercial DIC software GOM Correlate, employing facets of 30 px in size and a point spacing of 15 px.

[11] Makroclear™, Arla Plast, Sweden.

For the strain measurements obtained via DIC, two gage lengths were defined: a "global" gauge length of 8 mm, and a "semi-local" gauge length of 4 mm. In addition, a "pointwise" strain measurement, referred to as ε_{zDIC}, was extracted by taking as reference the central point of the necking section.

However, two important aspects must be highlighted. First, the pointwise axial strain obtained in this way is still an average strain over the facet size. Theoretically, infinitesimal facets would be required to obtain a truly local strain measurement. Second, the strains measured by DIC refer to the specimen's outer surface, and therefore do not account for internal strain gradients that develop during necking localization.

In cylindrical specimens, in particular, the axial strain distribution along the necking section typically reaches its maximum at the specimen's center and decreases towards the outer surface. As a consequence, the surface strain ε_{zDIC} is generally lower than the strain estimated from diameter measurements (ε_{TrueA}), since the latter represents the longitudinal strain averaged over the entire minimum cross-section of the specimen. Assuming that the true area-based strain can be approximated by the DIC strain, then the DIC-based true stress can then be approximated as follows:

DIC-based true stress-strain curve

$$\begin{cases} A \cong A_0 e^{-\varepsilon_{Z_{DIC}}} \\ \sigma_{Z_{DIC}} = \frac{F}{A_0}\, e^{\varepsilon_{Z_{DIC}}} \end{cases}$$

For the three data sets: (time machine, Force); (time TM-X, Diameter); (time camera, Gage Global, Gage Semi-Local, ε_z DIC), the time axes were automatically synchronized at time t = 0 s by means of two triggers (one for the TM-X5000 and one for the camera), using a signal sent by the testing machine once a load threshold of 50 N was exceeded. The TM-X and camera data sets were linearly interpolated using the machine time as reference time base. Supposing an additive

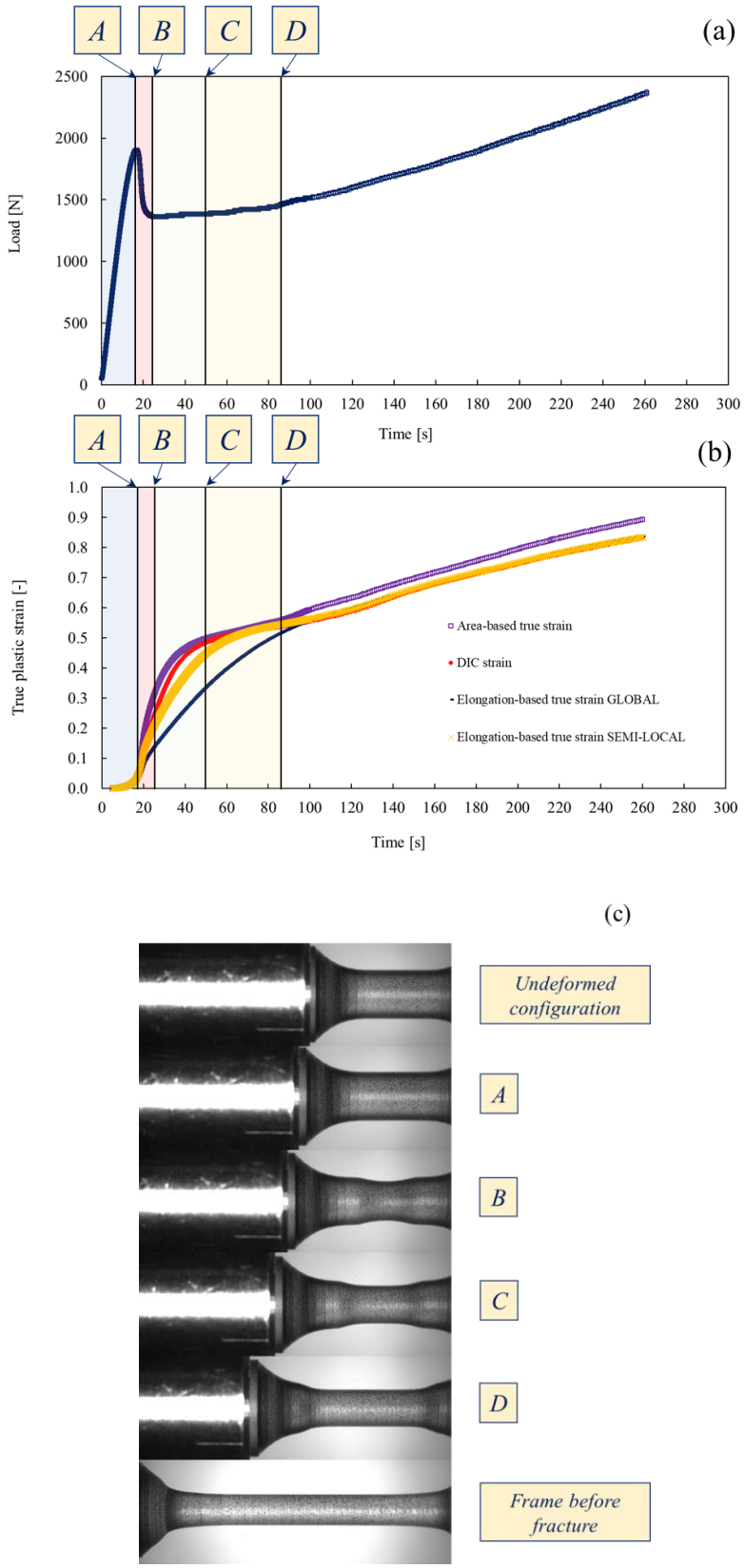


Figure 62: (a) Load-Time diagram from a quasi-static tensile test on Polycarbonate round specimen; (b) Plastic strain-Time history from the same test; (c) Frames taken from the recording of the tensile test.

decomposition of the total strains, the plastic strains were evaluated by subtracting the elastic component, according to these equations:

$$(21) \qquad \varepsilon^{p}_{True_{L_i}} = ln\left(\frac{L_i}{L_{0_i}}\right) - \frac{\sigma_{True_{L_i}}}{E} \qquad \varepsilon^{p}_{True_A} = ln\left(\frac{A_0}{A}\right) - \frac{2\nu\sigma_{True_A}}{E} \qquad \varepsilon^{p}_{Z_{DIC}} = \varepsilon_{Z_{DIC}} - \frac{\sigma_{DIC}}{E}$$

where E is the Young's Modulus, here assumed equal to 2400 MPa, and ν is the Poisson's Ratio assumed to be equal to 0.33. As shown in the Figure 62 (a) and (b), the Polycarbonate at hand exhibits these following deformation mechanisms:

I. *Pre-necking* (before the peak load at instant A). Uniform deformation takes place in the entire gauge length, firstly elastic (until the yield load at 1380 N) and then plastic. All the measured strains coincide and increase together at the same speed.
II. *Necking and strain localization* (between instants A and B). Once the peak of load is reached, the diffuse necking incepts and the localization of the deformation begins, with the progressive reduction of the specimen's diameter over a short part of the gauge length. The necking strain value is very low and approximately equal to 0.033. During the diffuse necking localization, the specimen assumes an hourglass-like shape and the stress state at the minimum cross section becomes triaxial with three principal components of the stress tensor: the longitudinal stress σ_z, the radial stress σ_r and the hoop stress σ_θ. The distributions of the stress components across the necking section are decreasing from the center to the external surface. During the necking localization, the specimen's curvature increases until it reaches a maximum value approximately at the instant B. The rate of growth of the area-based true strain is higher than the global length-based one. This stage is accompanied by a load decreasing due to these two main reasons. The first is related to the onset of tensile geometric instability (necking), which causes a rapid reduction in the minimum resistant cross-section and, consequently, lowers the force required to further elongate the specimen. The second reason lies in a peculiar intrinsic material instability, occurring during necking: polymer chains progressively disentangle from their initial spaghetti-like configuration and begin to 'flow' in the vicinity of the necked region, gradually aligning along the loading direction. The load reduction tends to stabilize around a plateau value at the instant B.
III. *Transition between localization and propagation* (between instants B and C). The localization of the deformation around the neck section undergoes a trend reversal. Indeed, the further diameter reduction in the necking zone proceeds at a decreasing speed and the hourglass region of the

specimen begins propagating along the gage length. Then, the slope of the ε_{true_A} vs. $\varepsilon_{true_{L-global}}$ curve continues progressively decreasing.

IV. *Strain propagation* (between instants C and D). The cross section where the neck initially started nearly stops contracting while the necking propagates at a nearly constant load. During the propagation stage, it is noteworthy that all the cross-sections reached by the necking front undergo plastic deformation under a constant load. This phenomenon can be described as 'continuous necking' and it will be mathematically described soon. As a result, the entangled polymer chains located in the straight (undisturbed) region of the specimen's gage length progressively uncoil.

V. *Post-propagation* (between instant D and fracture). The propagation of the necked region ceases once the necking fronts -moving in both directions- have traversed the entire gage length. As a consequence, the duration of the constant-load phase depends on the specimen length: the longer the specimen, the more time is required for completing propagation, and the longer the load remains at its plateau level. Once propagation is complete, the specimen totally recovers its cylindrical shape, and the assumptions of uniaxial stress and strain uniformity along the gage length become valid again. During the post-propagation phase, a new increasing in load is observed, which can even exceed the local maximum load previously reached at the onset of necking. The diameter-based strain continues to evolve at an approximately constant rate (i.e., strain linear with respect to time). A particularly interesting feature that characterizes this stage - distinguishing it from the initial pre-necking stage- is the emergence of a shift between the strain evolution measured via cross-sectional area reduction and that obtained from elongation-based measurements, regardless of the initial gage length. It is worth recalling that the equality between the true strain computed from the cross-section area and that from elongation implies global volume conservation of the gage length throughout the deformation history. The observed deviation from this equivalence seemingly violates the condition of plastic incompressibility, as expressed by equation (*16*). This may suggest that: 1) Polycarbonate exhibits volumetric plastic strains at large deformations; or 2) the estimated plastic strains, obtained by subtracting the elastic component from the total measured strain, are affected by an error in the estimation of the elastic strain components. In particular, both the elastic modulus and Poisson's ratio were assumed to remain constant throughout the deformation process, but they could change after the material experience the post-necking instability.

The hypothesis regarding possible volumetric plastic deformations appears to be refuted by density measurements performed on four Polycarbonate specimens before tensile testing and after fracture. If volumetric plastic deformations (i.e., a permanent change in the specimen's volume) were present, a significant variation in the material's density would be expected between the initial and final states. The density measurements were conducted at the University of Catania, in collaboration with the Materials Science group, by performing two weight measurements using an analytical balance: one in air and one in water. The analytical balance measures the apparent weight of the specimen, which is the sum of the weight force and the Archimede's force, the latter depending on the fluid in which the balance pan containing the specimen is immersed. The equation used to determine the unknown density of the material is as follows:

$$\rho_{specimen} = \rho_{air} + (\rho_{water} - \rho_{air}) \left(\frac{m_{air}}{m_{air} - m_{water}} \right) \quad (22)$$

m_{air} and m_{water} are the apparent mass measurements of the specimen in air and in water, respectively, while ρ_{air} and ρ_{water} represent the densities of air and water at ambient temperature (in this case, the recorded temperature was 24.5 °C). In the undeformed condition, the average density measured related to the 4 specimens was 1175.76 kg/m³, whereas after fracture the average measured density was 1179.64 kg/m³. These density values are consistent with those reported in the literature, which are approximately 1200 kg/m³. The variation in density between the undeformed and fractured specimens is about 0.4%, indicating that any volumetric plastic deformations are not significant and therefore do not justify the shift observed in the area strain vs. elongation strain plot in the post-propagation phase. It remains to be verified, then, the second hypothesis: that the elastic properties of Polycarbonate (the elastic modulus and Poisson's ratio) may not remain constant throughout the test. These two elastic constants should be measured through static loading-unloading tests at different levels of plastic strain.

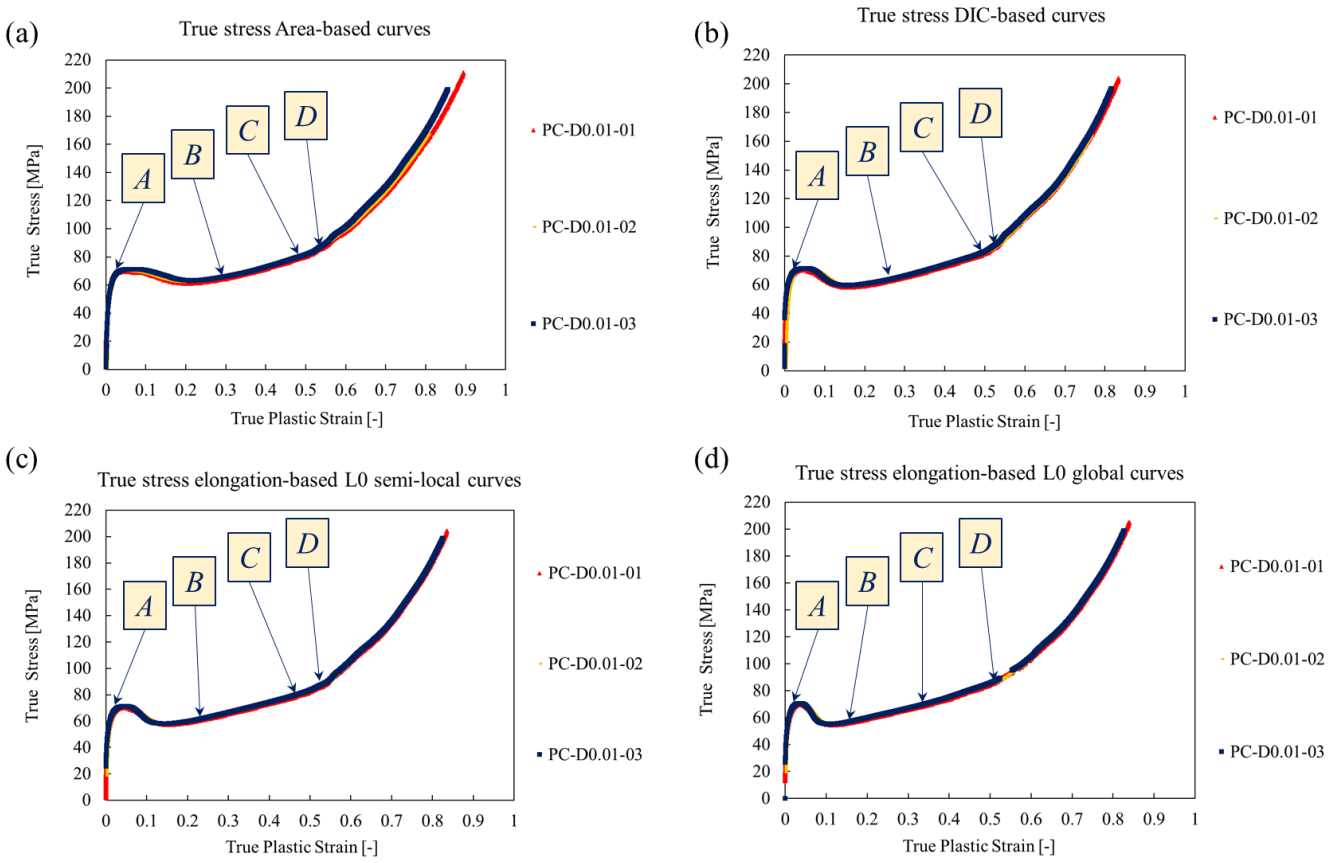


Figure 63: Quasi-static (0.01 s^{-1}) tensile stress-strain curves for Polycarbonate round specimens, obtained from four different methodologies. The capital letters from A to D identify the instants of the test captured in Figure 62 c).

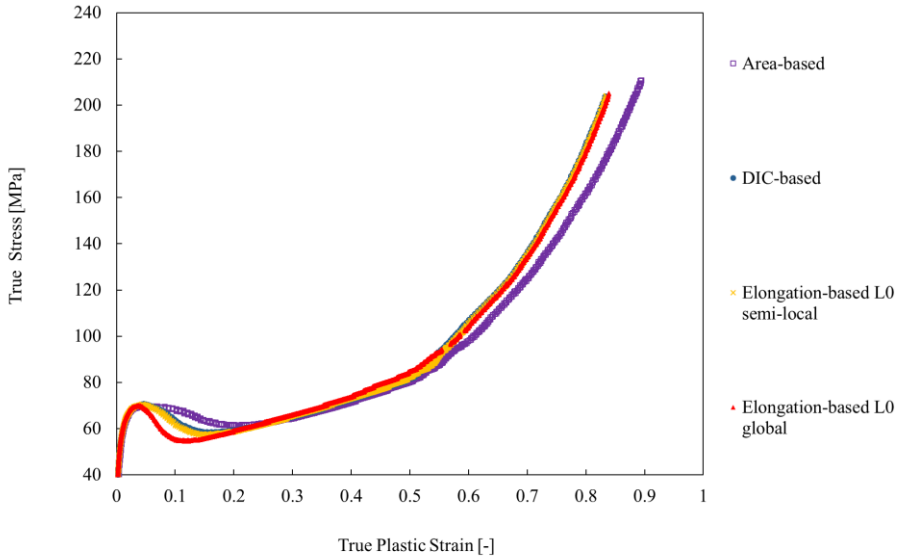


Figure 64: Summary of the Polycarbonate round specimen stress-strain curves at 0.01 s^{-1}.

As shown in Figure 63 and Figure 64, the material begins to yield at a stress of approximately 48.5 MPa, while preserving both the uniaxiality and uniformity of the strain field up to a plastic strain of about 0.033. Within the plastic strain range from 0 to 0.033, the true stress-strain curves are coincident and exhibit a monotonically increasing trend (hardening phase). At a strain of 0.033, the load -as previously commented- reaches a local maximum, which corresponds to the onset of the geometric tensile instability known as *necking*. Mathematically, the condition for necking is expressed by the *Considère criterion*, reported below:

(23) $\frac{d\sigma}{d\varepsilon} = \sigma$

Proof: The local maximum of the load satisfies the equation $\frac{dF}{d\varepsilon} = 0$ with $F = \sigma A$, then $\frac{d(\sigma A)}{d\varepsilon} = 0 \rightarrow \frac{d\sigma}{d\varepsilon}A + \frac{\sigma dA}{d\varepsilon} = 0$. By the definition of $\varepsilon = \ln\left(\frac{A_0}{A}\right)$, then $A = A_0 e^{-\varepsilon} \rightarrow \frac{dA}{d\varepsilon} = -A_0 e^{-\varepsilon} = -A \rightarrow \frac{d\sigma}{d\varepsilon} = \sigma$. □

Therefore, the onset of necking in the true stress-strain curves is identified *before* the stress reaches its maximum value, specifically at the point where the derivative of the true stress curve equals the true stress itself. From this point onward, all true curves continue to increase for a very short interval until they reach a local maximum and then begin to bifurcate. This behavior is characteristic of Polycarbonate and distinguishes it from the typical response observed in metals.

At the local maximum of the true curve, its derivative becomes zero, marking the onset of the material's intrinsic instability, which is attributed to the disentanglement of polymer chains. Once this instability begins—along with the progressive localization of the necking—the highest of all true curves is the area-based one, which accounts for the effect of mean triaxiality within the necked section. Conversely, the global elongation-based curve is the least affected by this phenomenon, for reasons previously discussed. It can be observed that, beyond a certain point, all true curves tend to converge toward a single curve that can be mathematically described by an exponential function. This behavior reflects a typical phenomenon in this material, known as *continuous necking* or *necking propagation*. The phenomenon of *continuous necking* can be described through a generalization of the Considère criterion previously introduced. In particular:

if $\frac{dF}{d\varepsilon} = 0 \; \forall \varepsilon \in [\varepsilon_1, \varepsilon_2]$, then $\sigma_{True} = k e^{\varepsilon} \; \forall \varepsilon \in [\varepsilon_1, \varepsilon_2]$

The proof is trivial if we consider that the condition expressed in (23) is extendable as a differential equation defined in the interval [ε_1, ε_2], where the load remains constant. This equation is simply integrable as follow:

$\frac{dF}{d\varepsilon} = 0 \quad \forall \varepsilon \in [\varepsilon_1, \varepsilon_2] \quad \leftrightarrow \quad \frac{d\sigma_{True}}{d\varepsilon} = \sigma_{True} \quad \forall \varepsilon \in [\varepsilon_1, \varepsilon_2] \rightarrow \int \frac{d\sigma_{True}}{\sigma_{True}} = \int d\varepsilon \quad \leftrightarrow \ln(\sigma_{True}) = \varepsilon +$

$+c \; \forall \varepsilon \in [\varepsilon_1, \varepsilon_2] \rightarrow \; \sigma_{True} = ke^{\varepsilon} \quad \forall \varepsilon \in [\varepsilon_1, \varepsilon_2].$

Recalling, for example, the definition of true area − based curve, then $\sigma_{True} = \frac{F}{A} = \frac{F_{plateau}}{A_0} e^{\varepsilon}$.

By observing that the plateau load is approximately equal to the first yield load, then $\sigma_{True} = \sigma_{y0} e^{\varepsilon}$.□

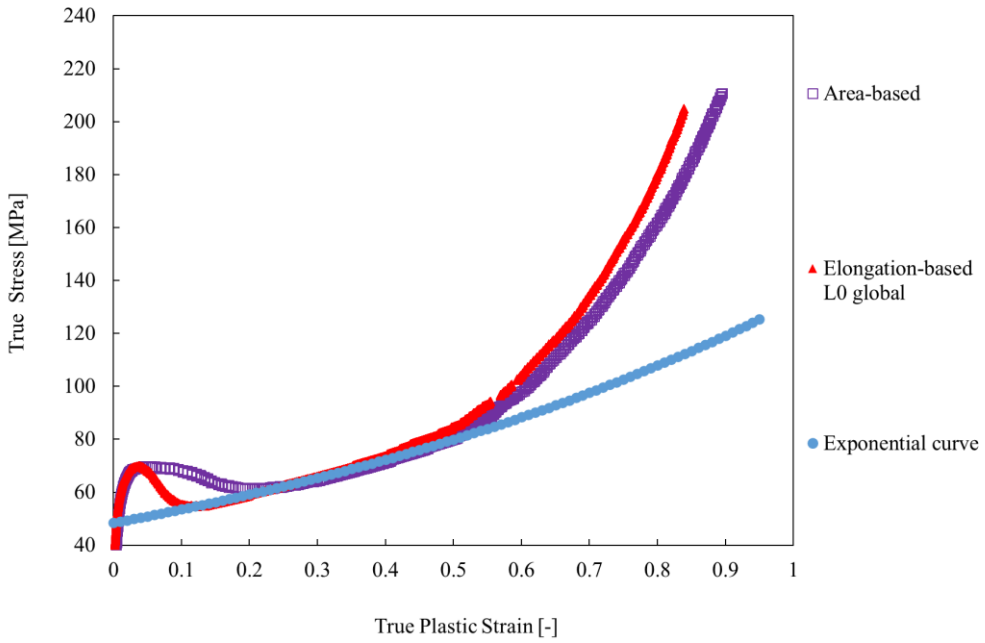


Figure 65: Comparison between the true stress-strain curves from elongation and area measurements, and the fitting exponential curve 48.5 exp(ε).

The area-based true stress curve exhibits an exponential trend within a strain range approximately between 0.3 and 0.55, whereas the global elongation-based true curve follows this behavior in the range between 0.15 and 0.55 (Figure 65).

Once the necking propagation is complete and the load starts increasing monotonically again until final fracture, the true curves also exhibit this increasing trend, which is more than exponential. The curve with empty purple squares (area-based) is shifted to the right with respect to the elongation-based true curves. This reflects the fact that, according to the plastic strain estimates discussed so far,

at a given global elongation strain in the post-propagation phase, the corresponding area-based strain is higher, in apparent violation of global volume conservation.

These observations can be more intuitively captured by examining a diagram where the global elongation strain is plotted on the x-axis and the cross-sectional strain on the y-axis (Figure 66). The bisector of this diagram represents the line for which $\varepsilon_{TrueA}=\varepsilon_{TrueL}$, i.e., the condition of volume conservation. The deviation of the curve from this line, more pronounced as the initial gauge length L0 used for measuring elongation increases, is related to the strains non-uniformities that develop throughout the deformation history within the gauge length. This diagram allows one to clearly identify the key deformation mechanisms of the specimen, which have been previously described.

Once the experimental true stress-strain curves have been determined and their relation to the material's flow curve has been discussed, it becomes necessary to define a method to extract the latter. As previously mentioned, the area-based true curve relates the average axial stress over the cross-section to the average axial strain on the same section, and thus provides the closest approximation to the material's actual flow curve. In the following section, Bridgman's theory will be introduced as a means to derive the material flow curve starting from the area-based true curve.

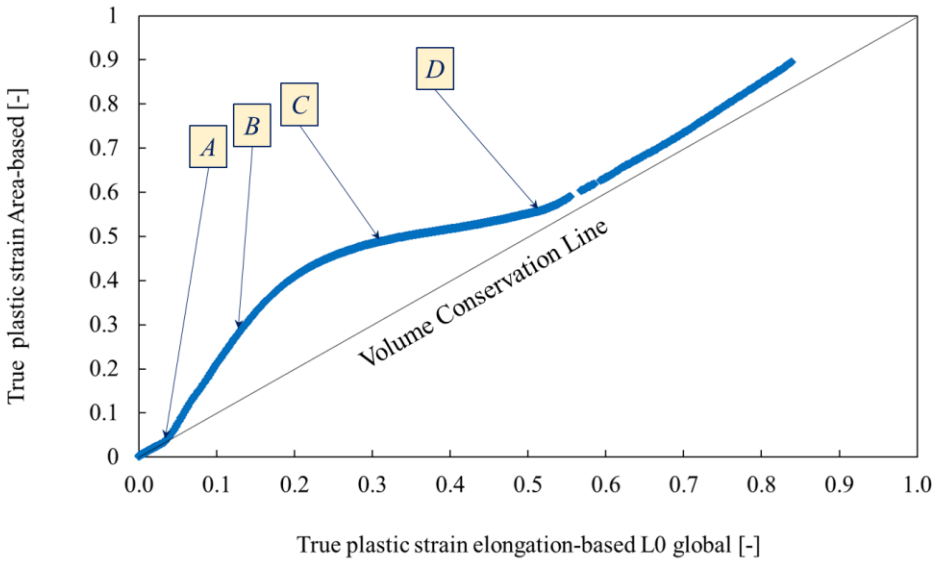


Figure 66: Area strain vs Global elongation strain for Polycarbonate round specimen at 0.01 s^{-1}. The capital letters from A to D identify the instants of the test captured in Figure 62 c).

6.2 Bridgman's Theory for correcting the true stress area-based curve into the material's flow curve

In 1964, Nobel prize in Physics P.W. Bridgman published in his book *Studies in Large Plastic Flow and Fracture* [92] a theory for determining the stress state within the necked section during a tensile test on axisymmetric specimens.

Let us consider a specimen with a typical hourglass shape, at a given point of its deformation history and let us focus on a material element with cylindrical symmetry subjected to axial, radial, and circumferential normal stresses, as well as tangential shear stresses. The equilibrium of the forces acting on this material element in the radial direction leads the following equation:

$$\frac{\partial \sigma_r}{\partial r} + \frac{\partial \tau_{r\theta}}{\partial z} + \frac{\sigma_r - \sigma_\theta}{r} = 0 \quad (24)$$

From the condition of cylindrical symmetry, applied to the conservation of plastic strains, it follows that:

$$\varepsilon_r = \varepsilon_\theta \; and \; \varepsilon_r + \varepsilon_\theta + \varepsilon_z = 0 \rightarrow \; \varepsilon_r = -\frac{1}{2}\varepsilon_z \quad (25)$$

According to the definition of equivalent plastic strain given in (17), by the result expressed from (25), it follows that

$$\varepsilon_{eq} = \varepsilon_z \quad (26)$$

The incremental form of the plastic strain tensor is expressed by the *flow rule*:

$$d\boldsymbol{\varepsilon_{pl}} = \frac{\partial g(\boldsymbol{\sigma})}{\partial \boldsymbol{\sigma}} d\lambda \quad (27)$$

where g($\boldsymbol{\sigma}$) is the plastic potential (equal to the yield function f($\boldsymbol{\sigma}$) under the hypothesis of associative plasticity) and λ is a scalar value defined as *plastic multiplier*. It is possible to demonstrate that in case of J2 (Von Mises) plasticity, the plastic multiplier coincides with the equivalent plastic strain. Therefore, under J2 plasticity theory, the partial derivatives of the Mises yield function with respect to each component of the principal stress tensor give:

$$(28)\quad \begin{cases} d\varepsilon_r^{pl} = \frac{3}{2}\frac{s_r}{\sigma_{eq}} d\varepsilon_{eq} \\ d\varepsilon_\theta^{pl} = \frac{3}{2}\frac{s_\theta}{\sigma_{eq}} d\varepsilon_{eq} \\ d\varepsilon_z^{pl} = \frac{3}{2}\frac{s_z}{\sigma_{eq}} d\varepsilon_{eq} \end{cases}$$

From (25), (26), and (28), the radial and hoop deviatoric part of stress tensor results equal to each other as well as the radial and hoop stress (axisymmetric stress state). The radial deviatoric part of the stress tensor results -1/3 of the equivalent Von Mises stress. By remembering that the hydrostatic stress is the 1/3 of the trace of the stress tensor, in this case:

$$(29)\quad \sigma_{hydro} = \frac{\sigma_r+\sigma_\theta+\sigma_z}{3} = \frac{2\sigma_r+\sigma_z}{3}$$

$$s_r = \sigma_r - \sigma_{hydro} = -\frac{1}{3}\sigma_{eq} \rightarrow \sigma_r - \sigma_z = -\sigma_{eq} \rightarrow \sigma_r = \sigma_z - \sigma_{eq}$$

These latter observations, combined to the equation (24), give:

$$(30)\quad \frac{\partial(\sigma_z-\sigma_{eq})}{\partial r} + \frac{\partial\tau_{r\theta}}{\partial z} = 0$$

By using simple considerations with the Mohr's Circle, it is possible to calculate the shear stress $\tau_{r\theta}$ as follows:

$$(31)\quad \tau_{r\theta} = \tan(\psi(z))(\sigma_z - \sigma_r) \cong \psi(z)\sigma_{eq}$$

Where ψ(z) is the local inclination of the flux line at coordinate z or, in other words, it is the derivative of the flux line ψ(z)=df(z)/dz. Therefore,

$$\frac{\partial(\sigma_z - \sigma_{eq})}{\partial r} + \frac{\partial\left(\psi(z)\sigma_{eq}\right)}{\partial z} = 0.$$

At the necking section z=0. Supposing that the radial distribution of the equivalent Von Mises stress is uniform, then we can finally write this following equilibrium equation:

$$(32) \quad \frac{\partial \sigma_z}{\partial r} + \left(\frac{\partial \left(f'(z) \right)}{\partial z} \right)_{z=0} \sigma_{eq} = 0 \quad \leftrightarrow \quad \frac{\partial \sigma_z}{\partial r} + f''(0)\sigma_{eq} = 0$$

The second derivative of the generic flux line at z=0 corresponds approximately to its curvature (or the inverse of the curvature radius) evaluated at the minimum cross section. Bridgman calculated the curvature radius of the flux line at the necking section, in function of the radial coordinate, starting from some geometric observations:

$$(33) \quad \rho(r) = \frac{a^2 - r^2 + 2aR}{2r} \qquad \textit{Curvature radius calculation according to Bridgman}$$

In the manuscript of Siebel [93], he gave an approximation of the calculation of the curvature radius reported by Bridgman, according to this formula:

$$(34) \quad \rho(r) = \frac{aR}{r} \qquad \textit{Curvature radius approximation according to Siebel}$$

where *a* is the instantaneous radius of the necking section, *R* is the curvature radius of the necking section calculated at the external surface, and r is the radial coordinate. Just for simplicity, without lack of generality, I'll show the integrations of (32) using the Siebel's approximation.

$$\frac{\partial \sigma_z}{\partial r} = -\frac{\sigma_{eq} r}{aR} \rightarrow \sigma_z(r) = \int -\frac{\sigma_{eq} r}{aR} dr = -\frac{\sigma_{eq} r^2}{2aR} + c$$

The boundary condition, imposed at the external radius, is that the radial stress must be equal to zero. Therefore

$$\sigma_r(r = a) = 0 \rightarrow \sigma_z(r = a) = \sigma_{eq} \rightarrow -\frac{\sigma_{eq} a^2}{2aR} + c = \sigma_{eq} \rightarrow c = \sigma_{eq}\left(1 + \frac{a}{2R}\right).$$

Thus, the triaxial stress state of the necking section, at a certain instant of the deformation history is totally determined:

$$(35)\quad \begin{cases} \sigma_z(r) = \sigma_{eq} + \sigma_{eq}\left(-\frac{r^2}{2aR} + \frac{a}{2R}\right) = \sigma_{eq}\left[1 + \frac{a}{2R}\left(1 - \left(\frac{r}{a}\right)^2\right)\right] \\ \sigma_r(r) = \sigma_\theta = \sigma_{eq}\left(-\frac{r^2}{2aR} + \frac{a}{2R}\right) = \sigma_{eq}\left[\frac{a}{2R}\left(1 - \left(\frac{r}{a}\right)^2\right)\right] \end{cases}$$

As said before, the true area-based stress is the axial stress averaged across the minimum cross section, then

$$(36)\quad \sigma_{True_A} = \frac{1}{A}\iint_A \sigma_z\, dA = \frac{1}{\pi a^2}\, 2\pi \int_0^a \left(\sigma_{eq} + \sigma_{eq}\left(-\frac{r^2}{2aR} + \frac{a}{2R}\right)\right) r dr = \sigma_{eq}\left(1 + \frac{a}{4R}\right)$$

The factor 1+ a/4R is the Siebel's correction function of the true stress, which establishes that the flow stress is directly related to the area-based true stress by a function depending on the necking curvature or, in other words, on the specimen's shape during the localization. This theory represents a powerful tool for correcting the experimental true stress curve and it is noteworthy that no particular hypotheses have been made on the material's plastic behavior, excepting for its Von Mises-like yielding surface, allowing its potential application for extracting a complex material's flow curve like that of Polycarbonate.

6.2.1 Experimental measurements of the necking curvature during the quasi-static tensile test

From the measurements performed using the telecentric lens system TM-X5000, we obtained a sufficient number of frames of the axisymmetric specimen during the post-necking phase, from the onset of localization to the end of propagation. In order to apply Siebel's direct correction, the following procedure can be adopted.

At a given time instant *t*, corresponding to a measured instantaneous diameter *D*, the coordinates of the points along the necked profile of the specimen were manually extracted using the image processing software *ImageJ* (freely available online) (Figure 67).

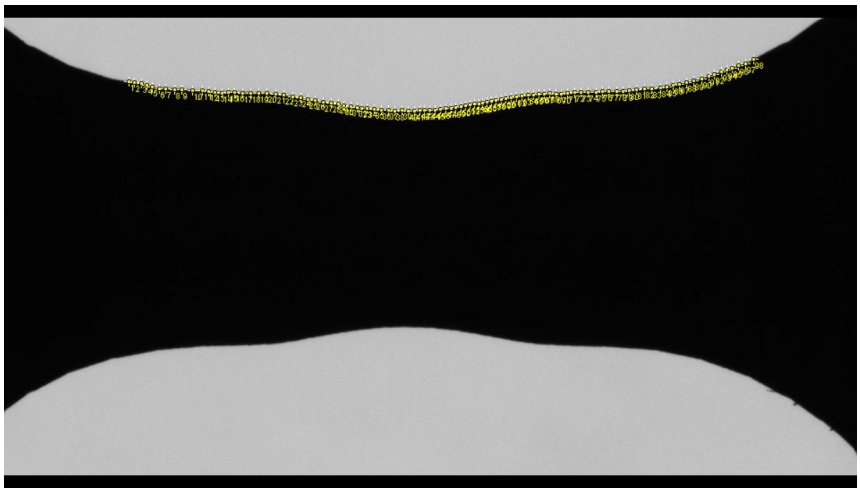


Figure 67: Quasi-static tensile test on round specimen. Frame taken at total area-based strain of 0.46. The coordinates of the yellow points were manually extracted by the ImageJ software.

The representative points of the specimen's contour were fitted using a sixth-order polynomial function (Figure 68), whose second derivative was evaluated at the point $z = 0$. This second derivative is approximately equal to the curvature (i.e., the inverse of the curvature radius R) of the specimen's surface at the minimum necking section.

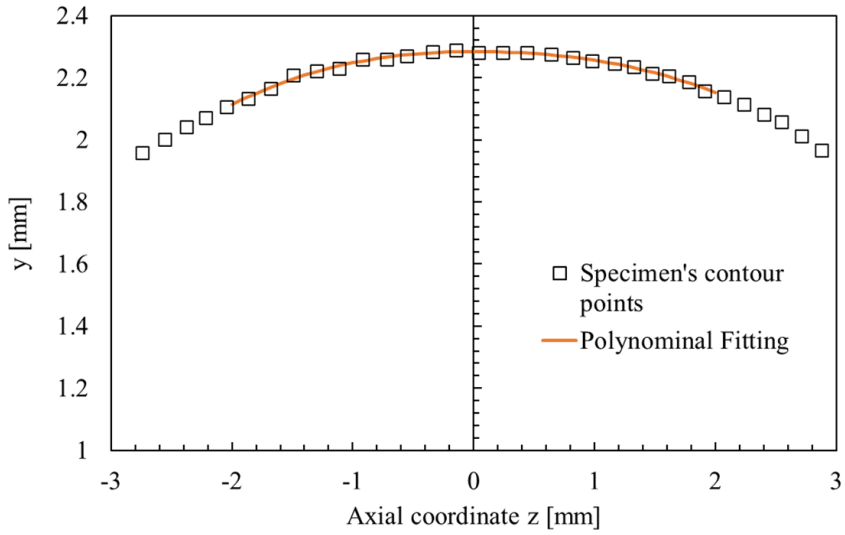


Figure 68: Specimen's contour points and their fitting with a polynomial function, taken at true strain area-based of 0.46.

This simple, but also time-consuming, procedure is repeated for a selected number of frames within the post-necking phase and for each quasi-static test performed, in order to obtain a statistically meaningful set of measurements. The results in terms of curvature radius vs area-based plastic strain and a/R vs area-based plastic strain are reported below (Figure 69).

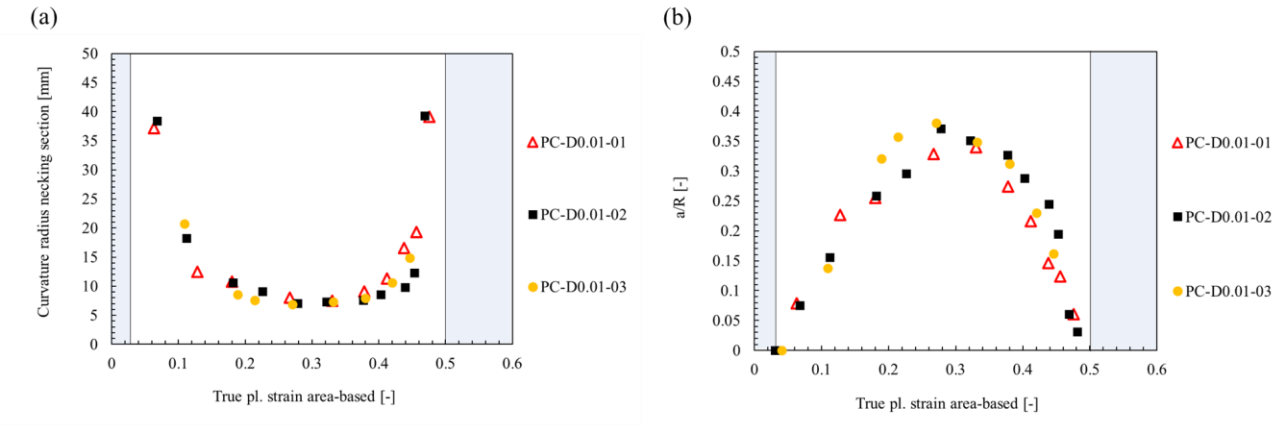


Figure 69: a) Curvature radius vs plastic strain area-based diagram; b) a/R vs plastic strain area-based diagram.

From the experimental measurements of the curvature radius, it is clearly observed that this quantity tends to diverge asymptotically at the necking strain (straight profile, $R \rightarrow \infty$), decreases during the necking localization phase reaching a local minimum at approximately $\varepsilon \approx 0.30$, and then the trend reverses (a clear indication of the transition from localization to propagation), rapidly tending to diverge again asymptotically at a strain of about $\varepsilon \approx 0.48$, where the specimen profile becomes locally straight again. This trend appears reversed when considering the diagram in which the vertical axis reports the *a/R* ratio, which is the key variable underlying the Siebel (or Bridgman) correction factor. At the onset of necking, the curvature of the minimum cross-section is zero; it increases during the localization phase and reaches a local maximum at approximately $\varepsilon \approx 0.27$–0.28. This value does not coincide with $\varepsilon \approx 0.30$ observed previously, as in the *a/R* variable, both *a* and *R* vary with the true strain, causing a shift in the local maximum. After this point, *a/R* decreases and returns to zero at $\varepsilon \approx 0.49$.

By defining the value $\varepsilon = 0.49$ as the *propagation strain* and $\varepsilon = 0.033$ as the *necking strain*, it is possible to construct a normalized variable $\chi = (\varepsilon - \varepsilon_{neck})/(\varepsilon_{prop} - \varepsilon_{neck})$ which therefore varies between 0 and 1. The experimental measurements of *a/R* were fitted using the following fourth-order polynomial, constrained to pass through the points (0,0) and (1,0) (Figure 70):

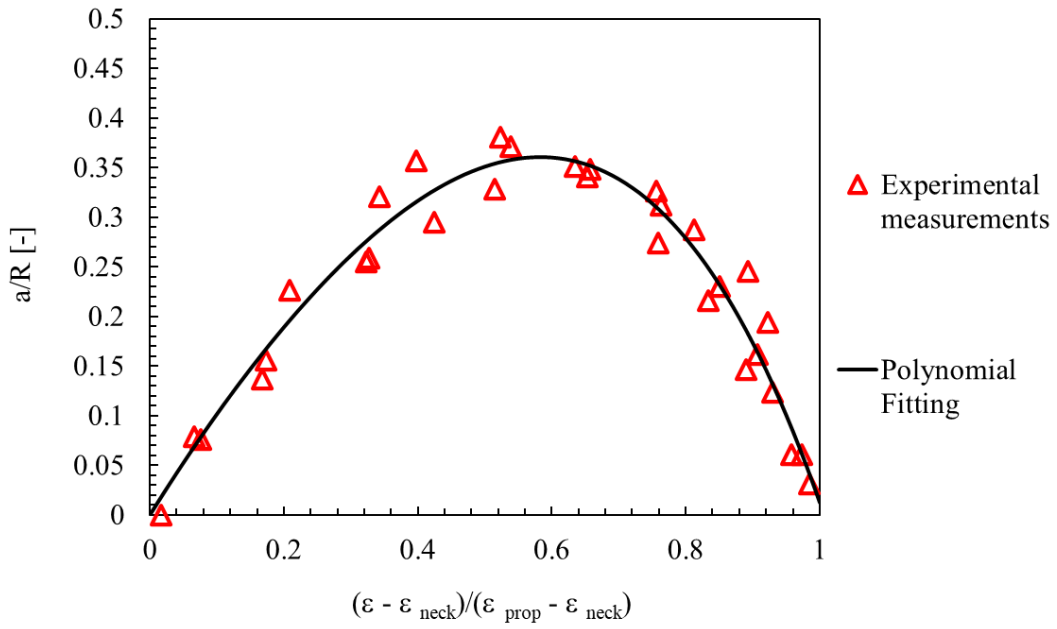


Figure 70: Experimental measurements of a/R vs normalized true strain variable.

(37) $$\frac{a}{R} = 1.0856\chi - 0.7092\chi^2 + 0.1269\chi^3 - 0.4907\chi^4$$

By combining equations (36) and (37), a closed-form expression allows to calculate the Von Mises stress, for each value of area-based strain, through the direct correction of the true stress.

(38) $$\sigma_{eq} = \begin{cases} \sigma_{true_A} \; if \; \varepsilon_{True_A} \in [0, \varepsilon_{neck}[\\ \frac{\sigma_{true_A}}{1+\frac{1a}{4R}} \; if \; \varepsilon_{True_A} \in [\varepsilon_{neck}, \varepsilon_{prop}[\\ \sigma_{true_A} if \; \varepsilon_{True_A} \in [\varepsilon_{prop}, \varepsilon_{fracture}] \end{cases}$$

The material's flow curve obtained applying this methodology and the correspondent true stress-strain curve area-based area are reported below:

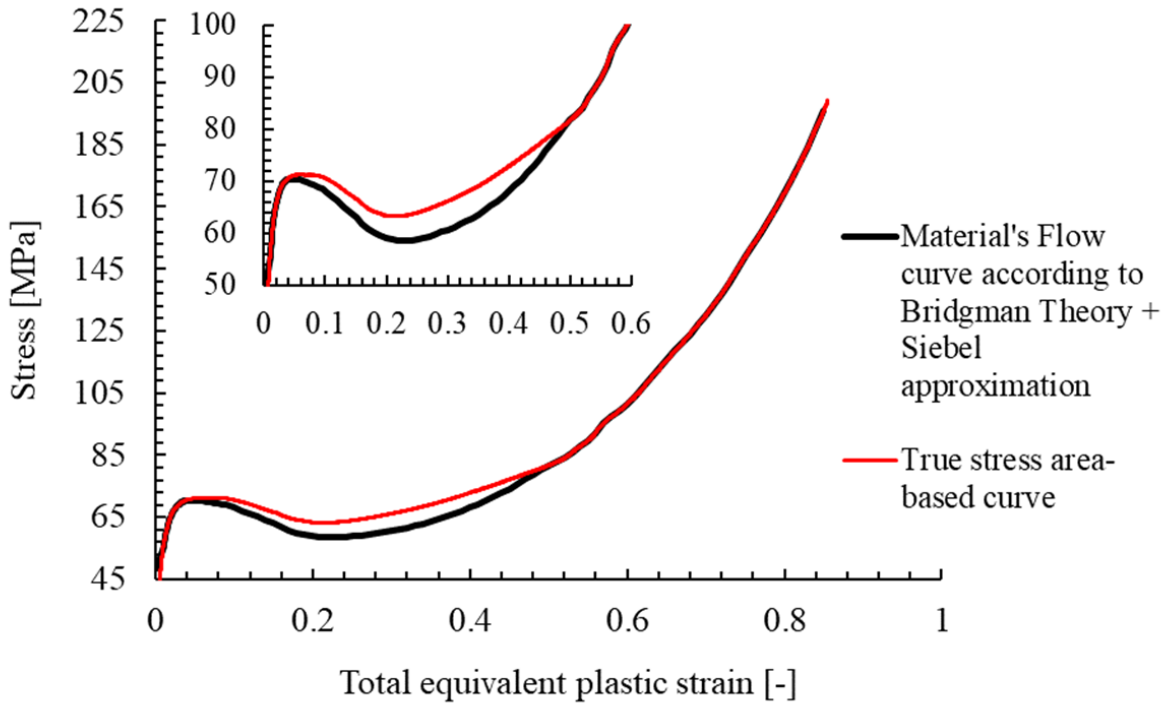


Figure 71: Polycarbonate's material curve at 0.01 s^{-1} and its relative true stress curve from tensile test on round specimens.

6.3 Finite Element Modelling of the tensile response of Polycarbonate at quasi-static rate

The validation of the quasi-static material curve obtained through Bridgman's theory was carried out by means of finite element modelling of the cylindrical tensile specimen. The simulation was performed using the FEM software MSC Marc Mentat® v2023.4. Given the symmetry of the geometry, a quarter of an axisymmetric specimen was modelled. The gage region was discretized using 34 elements along the radial direction and 80 elements along half of the gage length**.** A bias factor was applied to the mesh in order to achieve a finer resolution in the gauge region, where plastic deformation localizes, and a coarser discretization near the shoulder of the specimen, where the strain remains purely elastic.

The material model implemented in the FEM code corresponds to an elastic–plastic formulation, assuming linear elasticity (Poisson's ratio equal to 0.33 and Young's modulus equal to 2400 MPa, as adopted during the analysis of the experimental results) and J2 plasticity (Von Mises

criterion) with isotropic hardening. The material flow curve was provided in tabulated form, using a selected subset of data points extracted from the curve shown in Figure 71.

The following constraints were applied to all the nodes lying along the specimen's axis of symmetry: the radial displacement and the rotation around the axis orthogonal to the plane containing the section must be equal to zero.

(39) $u_r = 0,\ \phi_r = 0 \quad \text{for each point belonging to the specimen's axis}$

The following constraints were applied to all the nodes lying on the mid-length cross-section of the specimen: the axial displacement of these nodes, as well as the rotation of the cross-sections around the axis orthogonal to the section plane, were set to zero.

(40) $u_z = 0,\ \phi_r = 0 \quad \text{for each point belonging to the mid} - \text{length section}$

A master node was used to simulate the displacement of the testing machine crosshead and to apply a rigid axial displacement to all the nodes on the shoulder of the specimen through 1-to-N structural links. A displacement of 10 mm, corresponding to half of the total elongation expected at the end of the test, was prescribed to the master node. The analysis was conducted under static conditions, and all inertial effects and strain rate dependencies were neglected.

The simulation was performed by enabling the "large strain" option, combined with the "Updated Lagrangian" formulation for the computation of each element's stiffness matrix, allowing the model to account for geometric non-linearities due to large displacements. The numerical analysis was carried out using the implicit solver.

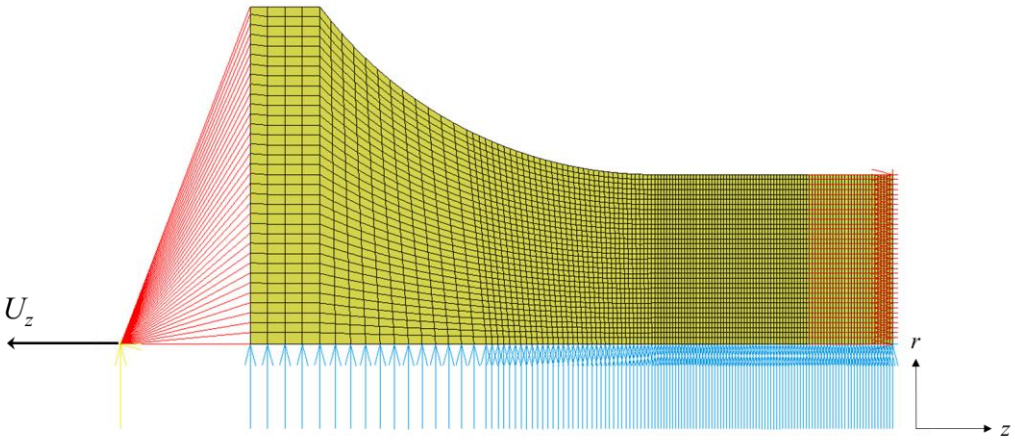


Figure 72: FEM Modelling of the quasi-static response of Polycarbonate round specimen: meshed axisymmetric model and prescribed boundary condition.

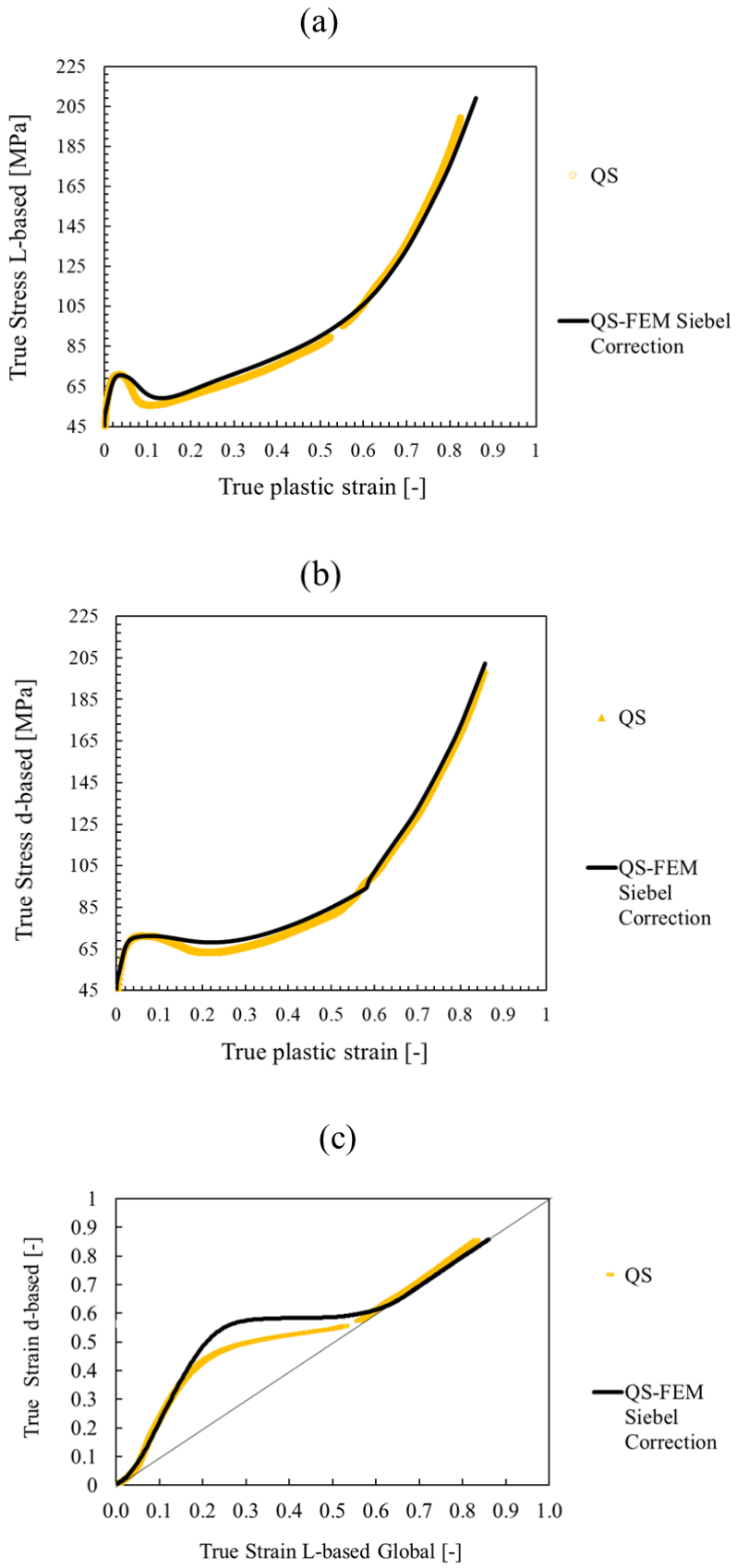


Figure 73: Finite Element Modelling of the elasto-plastic response of Polycarbonate at static rate: comparison between experimental data (yellow dots) and FEM results (black line). a) True stress

global elongation-based curve; b) True stress area-based curve; c) Area strain vs Elongation strain diagram.

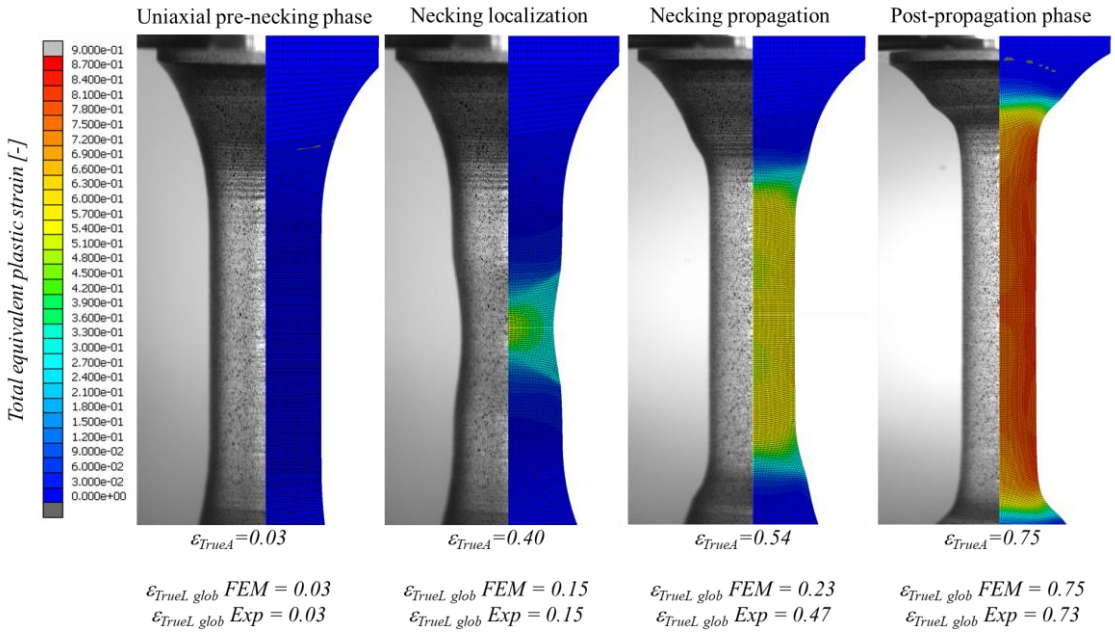


Figure 74: Qualitative comparison between quasi-static experiments and FEM results at four relevant instants.

From the graphs in Figure 73, it can be observed that the adopted methodology to convert the true stress–strain curve into the corresponding constitutive curve is quite effective in capturing the overall mechanical response of Polycarbonate in the elasto-plastic regime. The area-based true stress curve obtained from the FEM simulation exactly matches the experimental counterpart in the strain intervals [0, 0.035] and from 0.58 up to failure. A deviation of slightly less than 8% between FEM and experimental data is observed at a strain of 0.20. In the exponential hardening region, the error between FEM and experimental curves is approximately 3.8% at a strain of 0.45.

The largest discrepancy appears in the area strain versus elongation strain diagram, specifically in the region that physically corresponds to the transition between necking localization and its propagation. In the FEM model, beyond a true area strain of 0.4, the specimen appears to localize at a higher rate compared to the experimental observations. As a result, the strain-versus-strain curve exhibits a sharper knee in the FEM simulation, whereas in the experimental case, the transition toward propagation occurs in a much more gradual manner.

It can therefore be concluded that the flow curve approximated using Bridgman's theory provides an excellent first tentative estimation of the actual elastoplastic response of the material, taking in consideration that it was derived based on the assumptions outlined in the previous section. The proposed methodology confirms that it is indeed possible to estimate the elastoplastic behavior

of Polycarbonate in tension directly from simple uniaxial tensile tests. Additional physical phenomena may, of course, be considered and properly modeled, such as the time dependence of the elastic modulus and Poisson's ratio or, in other words, all dissipative and irreversible time-dependent effects that are not strictly related to plastic deformation, such as viscous phenomena. In the following sections, the dynamic behavior of Polycarbonate will also be investigated, including the effects of strain rate and temperature. The percentage difference between the experimental true stress–strain curve and the one obtained from the FEM analysis, when the initial trial flow curve is used as input, provides a quantitative measure of how much the latter needs to be "scaled down" in order to yield the best approximation of the experimental true curve. In other words, since the Siebel correction underestimates the average stress triaxiality over the cross-section (leading to a FEM-predicted true curve that lies above the experimental one), the Siebel correction factor was modified by introducing an additional term that accounts for the percentage error between the initial FEM-predicted true curve and the experimental true curve.

$$(41)\quad \frac{\sigma_{eq_{AVG}}^{II\ Approx}}{\sigma_{True_A}^{Exp}} = \frac{1}{1+\frac{1a}{4R}} - \left| \frac{\sigma_{\mathrm{True}_A}^{FEM\ I\ Approx} - \sigma_{True_A}^{Exp}}{\sigma_{True_A}^{Exp}} \right| = Modified\ Siebel\ Correction(\varepsilon_{eq})$$

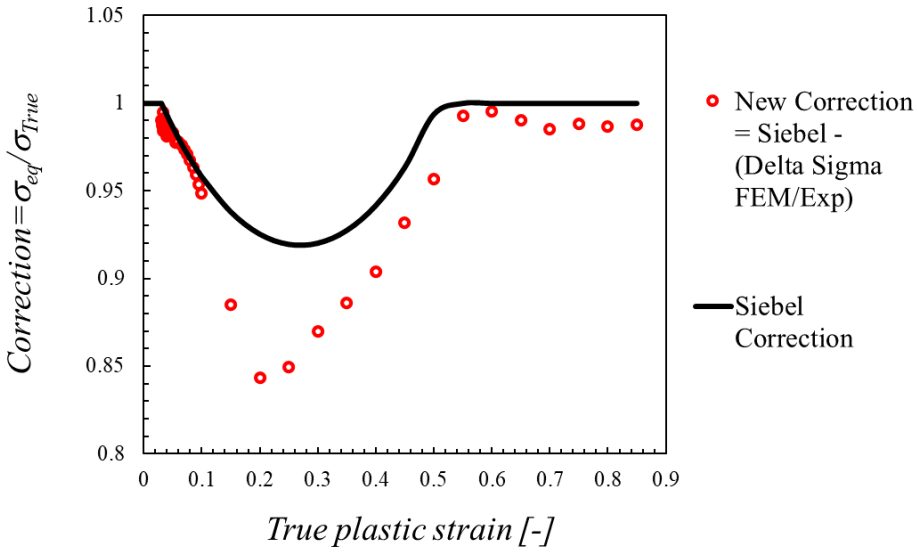


Figure 75: Siebel correction vs New approximated correction of the true curve. The difference between the black line and the red dots represents the percentage difference between the first approximation (Siebel) true curve and the experimental one.

This additional refinement step of the material flow curve can be considered as a semi-inverse technique. The key aspect behind this approach lies in the use of a direct correction derived from analytical calculations to estimate the average stress triaxiality over the necking cross-section, which

provides a first approximation of the flow curve. Subsequent approximations of the flow curve can be performed by adding a correction term to the factor depending on *a/R*, in order to minimize the error between the FEM-predicted true stress–strain curve (from cross-sectional area) and the experimental one. A single additional iteration is sufficient to achieve this goal. The results are shown in the following Figure 76:

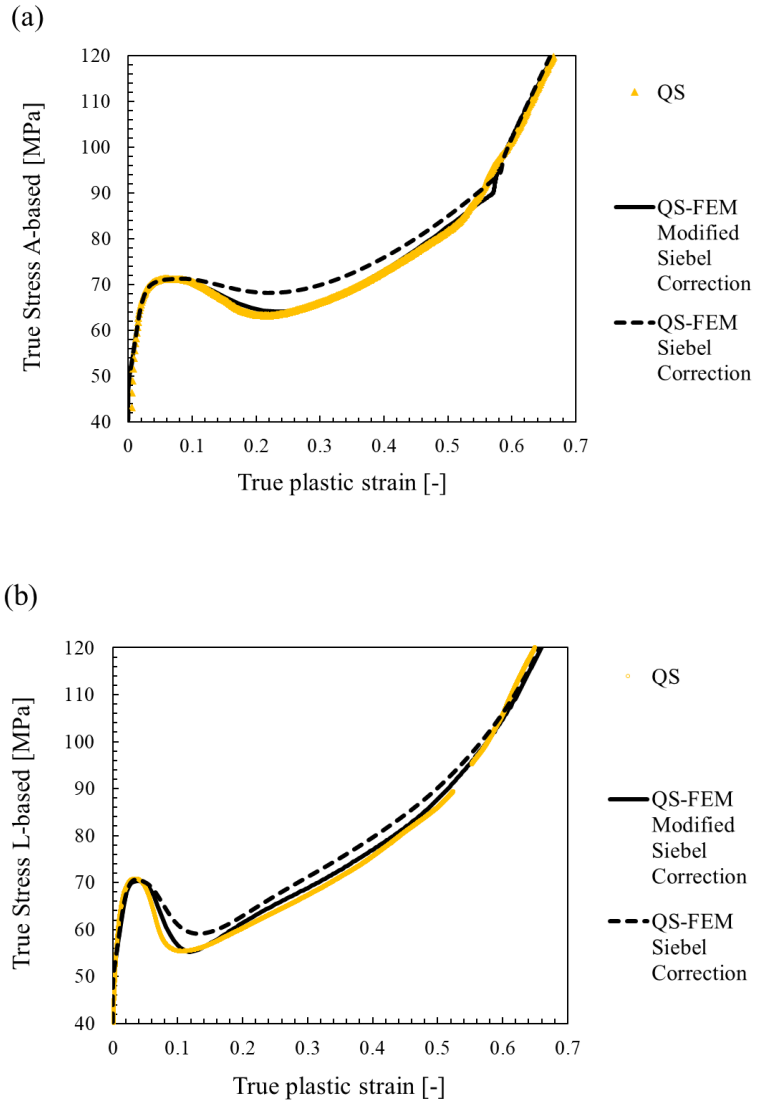


Figure 76: Comparison between the Finite Element results (black lines) and experimental data (yellow dots). The black solid line and the dashed one indicate, respectively, the results in output from the second approximation and the first approximation of the material's flow curve.

The flow curve defined at the nominal strain rate of 0.01 s^{-1} for this Polycarbonate is shown in the following Figure 77. It can be observed that the strain hardening phase (SH) of this flow curve (from a strain of 0.25 up to fracture) is accurately described by the following equation (42):

(42) $\sigma_{eq}^{SH}(\varepsilon_{eq}) = \sigma_{y0}\exp(c_1\varepsilon_{eq}^{c_2}) \qquad \forall\varepsilon_{eq} \in [0.25, \varepsilon_{fracture}]$

The flow curve defined at the nominal strain rate of 0.01 s^{-1} for this Polycarbonate is shown in the following Figure 77. It can be observed that the strain hardening phase of this flow curve (from a strain of 0.25 up to fracture) is accurately described by the following equation, where c_1 and c_2 are two fitting parameters obtained by minimizing the L_2 error norm the equivalent stress predicted by the fitting equation and the equivalent stress derived from the FEM analysis:

$$L_2(c_1, c_2) = \sqrt{\sum_{i=1}^{N}\left(\frac{\sigma_{eq}^{SH}(\varepsilon_i)}{\sigma_{eq}^{FEM}(\varepsilon_i)} - 1\right)^2} \rightarrow minimization\ of\ L_2 \rightarrow c_1, c_2$$

The minimization of the L_2 norm was carried out in an Excel spreadsheet using the GRG (Generalized Reduced Gradient) solver for nonlinear optimization problems. The solution of this problem is the following: c_1= 1.967; c_2 = 1.976. A similar expression of the equation (42) was used by G' Sell et al. [72] for describing the material flow curve of glassy polymers like PVC and HDPE.

To capture the more complex behavior of Polycarbonate (hardening–softening–hardening), a function representing a bell-shaped trend, having 3 parameters, was multiplied by equation (42). In summary, the quasi-static flow curve of Polycarbonate, obtained through the semi-inverse approach, is fully described by the following equation:

(43) $\sigma_{eq}(\varepsilon_{eq}) = \sigma_{y0}\exp(c_1\varepsilon_{eq}^{c_2})\,[1 + c_3\varepsilon_{eq}^{c_4}\exp(-c_5\varepsilon_{eq})]$

The parameters c_i for i = *3, 4, 5* were also obtained by minimizing the L_2 norm, as previously described. Their values are summarized in the following table (Table 13):

c_1	c_2	c_3	c_4	c_5
1.967	1.976	98.207	1.326	27.137

Table 13: Polycarbonate material's constant for the equation (43).

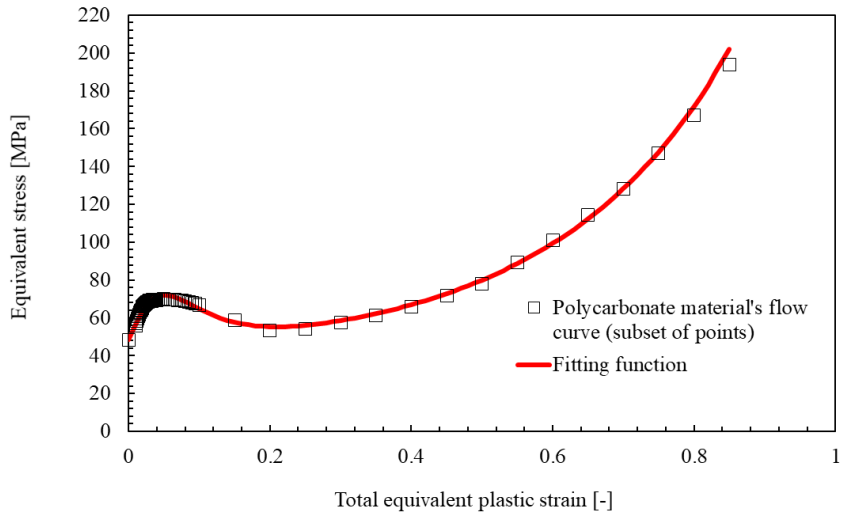


Figure 77: Polycarbonate definitive flow curve and its approximation by fitting function (43).

6.4 Uniaxial tensile test of Polycarbonate flat specimens

In the previous section, the quasi-static tensile behavior of a Polycarbonate material was fully investigated using cylindrical specimens. In practical applications, especially in protective equipment, armor systems, and windshields, Polycarbonate is typically manufactured through extrusion into uniform-thickness plates, which are then cut using techniques that minimize local heating of the material, such as the water-jet cutting. From these plates, rectangular or square cross-section specimens can be obtained.

The literature reports numerous studies focused on the static and dynamic characterization of Polycarbonate using prismatic specimens. While the material behavior in terms of its elastoplastic constitutive law is, by definition, independent of specimen's geometry, the shape of the true (local) stress-strain curve, obtained from cross-sectional area measurements, could be significantly affected by the stress triaxiality at the minimum cross-section section, which is, instead, geometry-dependent.

Consequently, the methodology previously presented, based on the direct correction of the area-based true stress-strain curve using the Bridgman's theory, must be revised to account for the effect of prismatic geometry on the average triaxiality within the necked region.

In flat specimens, for instance, necking localization typically occurs via the formation of shear bands, whose inclination also depends on the stress state (i.e., plane stress or plane strain). This feature implies a deformation mechanism that differs from that observed in cylindrical specimens.

In the following paragraphs, the deformation mechanisms observed in flat Polycarbonate specimens subjected to quasi-static tensile testing are discussed. The corresponding true tensile curves obtained using some of the approaches discussed in the previous section (based on elongation and minimum cross-sectional area measurements) will be presented. Finally, two novel methodologies for material characterization will be introduced: a fully advanced inverse procedure and a semi-inverse characterization method involving three parameters to be identified through successive iterations.

Static tensile test at room temperature were carried out on Polycarbonate dog bone flat specimens with two geometries: the first one is the *large* geometry, characterized by a width of 10 mm, a thickness of 4 mm, and a gage length of 60 mm; the second geometry named *small* have the following dimensions: width 6 mm, thickness 4 mm, and gage length 30 mm. Then, the width/thickness aspect ratio of the large geometry is 2.5, while for the small one is 1.5. The specimens' geometry is shown in the following Figure 78. A nominal strain rate of 0.0007 s^{-1} has been imposed to the specimens in order to avoid strain rate effects and to guarantee isothermal conditions.

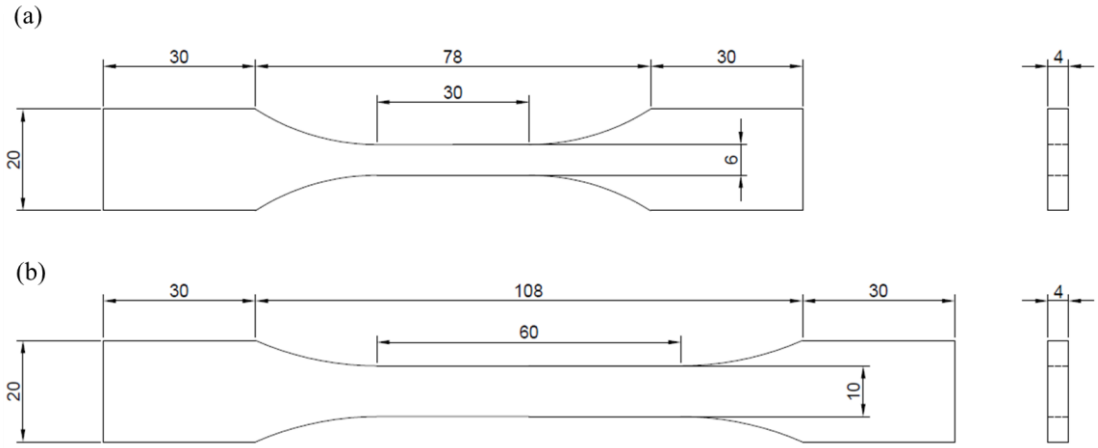


Figure 78: Polycarbonate dog bone specimens with rectangular cross section: a) Flat Small specimen; b) Flat Large specimen.

The tensile tests were carried out at the University of Catania, by the universal testing machine Zwick-Roell Z100 with a 100 kN load cell and the strain measurements were acquired using a high-resolution video recording of the deforming specimen. The camera used for the acquisitions were an ethernet camera The Imaging Source® DMK23G445 with a resolution of 1280 x 960 pixels. The frame rate was set at 0.5 fps. The specimens were marked with vertical signs every 10 mm in order to have fixed reference sections. A speckle pattern strip was applied to the central region of the

specimens using white paint and black spray in order to enable the acquisition of the instantaneous elongation of the gage length through the Digital Image Correlation (DIC) technique. Moreover, from the video recording, it was acquired the minimum width *w* of the specimen, by means of pixels count technique.

It was assumed that the material's behavior remains isotropic during the tests, which implies that the reduction of the thickness t can be considered proportional to the reduction of the width w during the test. Indeed, analyzing the broken specimen, it was verified that the ratio between the thickness and the width of the cross-section remained constant up to fracture. From this consideration, it is possible to estimate the current thickness as $t = t_0/w_0 \cdot w$, where t_0 and w_0 are the initial thickness and width respectively. Then, the current minimum cross-section area of the specimen is $A = t \cdot w$.

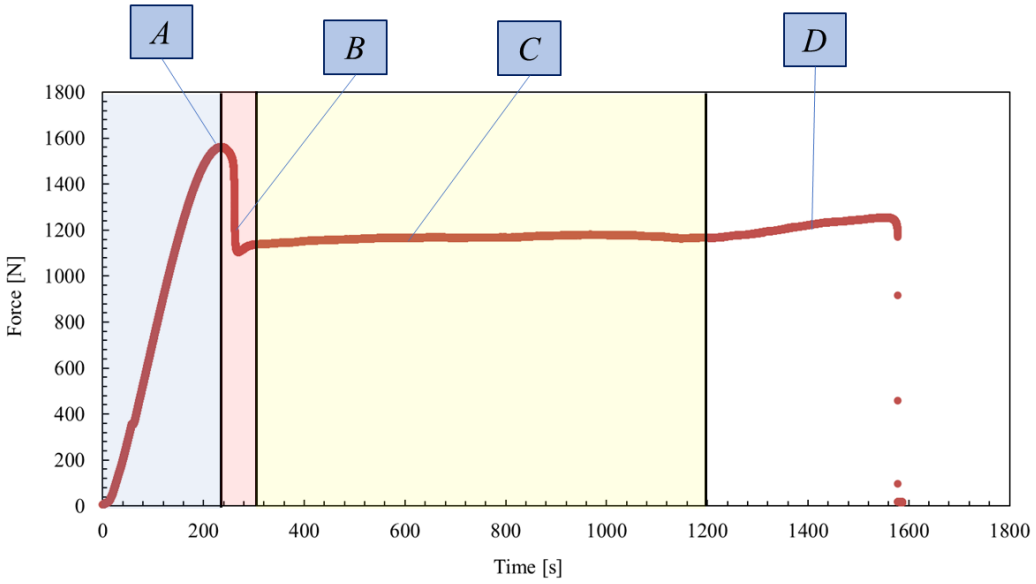
After the synchronization of the load F with the instantaneous global gage length *L* and the width *w*, it is possible to evaluate the true stress σ_{true} and the true strain ε_{true} according to the length-based approach and the cross-section area approach, as shown in eqs. (44) and (45). The total true strains were depurated from the elastic part by assuming a constant Young modulus of 2300 MPa and Poisson's ratio of 0.33.

$$(44) \quad \begin{cases} \varepsilon_{True_L} = \ln\left(\frac{L}{L_0}\right) \\ \sigma_{True_L} = \frac{F}{A_0}\left(\frac{L}{L_0}\right) \end{cases}$$

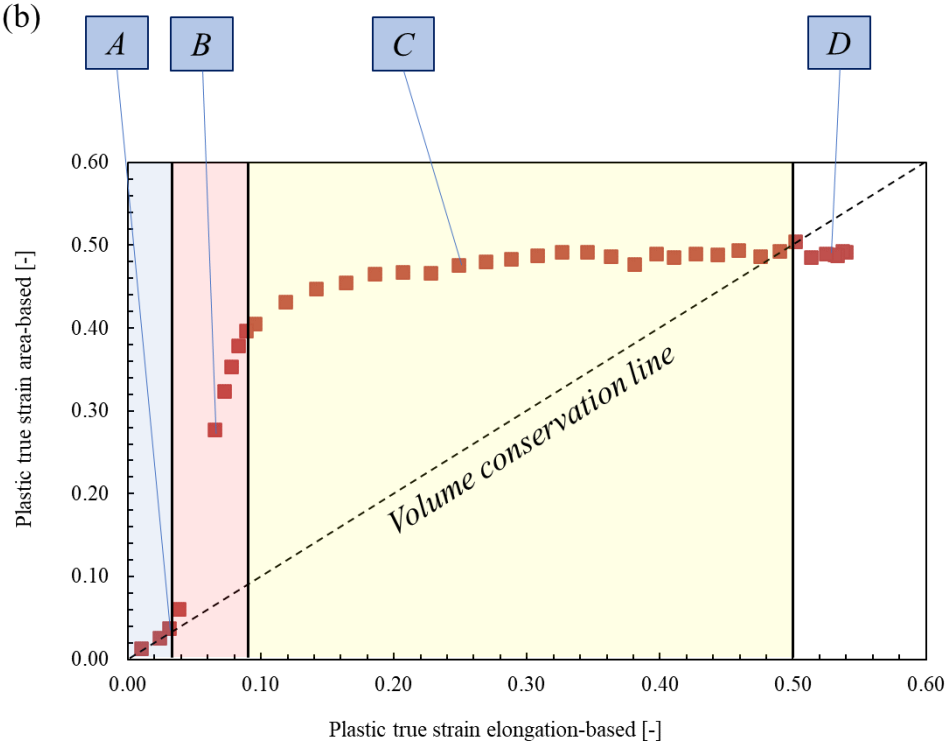
$$(45) \quad \begin{cases} \varepsilon_{True_A} = \ln\left(\frac{A_0}{A}\right) = \ln\left(\frac{w_0 t_0}{wt}\right) = \ln\left(\frac{w_0^2}{w^2}\right) = 2\ln\left(\frac{w_0}{w}\right) \\ \sigma_{True_A} = \frac{F}{A} \end{cases}$$

Figure 79 a) shows the load-time history of the test conducted on the flat *small* geometry, with four significant instants indicated by capital letters. The four distinct test phases are highlighted with different colors. Figure 79 c) shows the frames of the specimen corresponding to the significant instants indicated in Figure 79 a). The load evolves according to the typical trend of Polycarbonate observed before and in the literature, exhibiting an initial peak just after the first yield, a sudden drop, a subsequent nearly constant plateau and, finally, an increasing of the load corresponding to the post-propagation phase. Figure 79 b) presents the history of the area-based true strain ε_{true_A} against the length-based global true strain calculated considering the entire 30 mm gage length ε_{true_L}.

(a)


A
B
C
D
Force [N]
Time [s]
0
200
400
600
800
1000
1200
1400
1600
1800

(b)


A
B
C
D
Volume conservation line
Plastic true strain area-based [-]
Plastic true strain elongation-based [-]
0.00
0.10
0.20
0.30
0.40
0.50
0.60

(c)

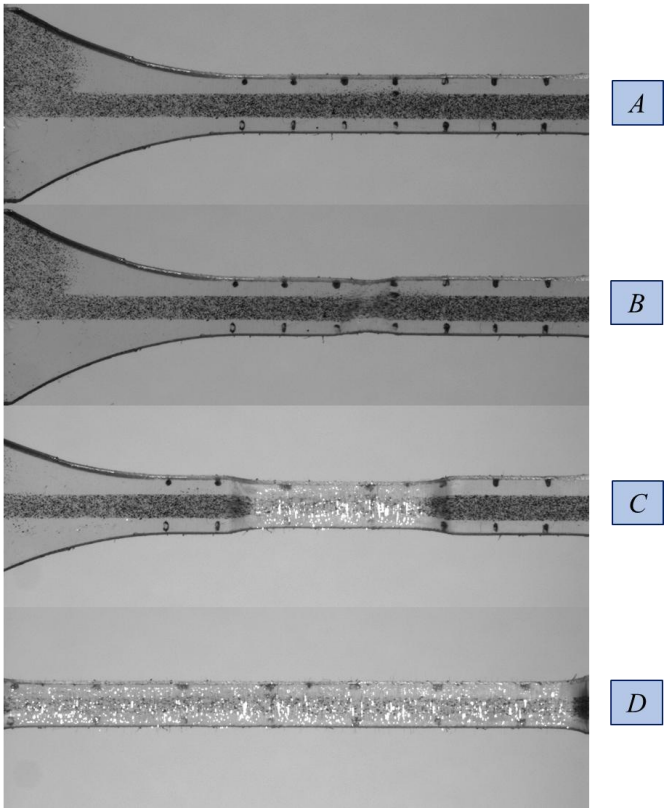


Figure 79: Static tensile test of Polycarbonate flat (small) specimen: a) Load vs time diagram; b) area-based strain vs elongation-based strain diagram; c) frames taken from the video recording of the test.

The different phases characterizing the deformation mechanism and the material's hardening are discussed below:

I. *Pre-necking* (area-based strain between 0 and 0.035). In the pre-necking phase, the distributions of axial stress and strain are uniform along the entire gage length. As a consequence of volume conservation, the strain evaluated from the elongation and that derived from the cross-sectional area reduction coincide at each instant (volume conservation line in Figure 79 b)), as do the true stress-strain curves obtained through these two approximations.
II. *Increasing strain localization* (area-based strain between 0.035 and 0.40). At the peak of load, the necking incepts (point A) and the localization of the deformation begins, with the progressive reduction of the width of the specimen over a very short part of the gauge length. Shortly afterwards, as soon as the slope of the load decreases further, localized necking is also triggered. This stage marks the beginning of the appearance of a transversal band inclined with respect to the specimen axis. There is a slight sliding of the specimen around this band and, as the localized necking evolves, the profile of the specimen becomes increasingly distorted (point B).

III. *Propagation phase* (area-based strain between 0.40 and 0.48). The localization of the deformation around the neck section undergoes a trend reversal. Indeed, instead of further distorting in the necking zone, the geometry of the specimen begins to relax, i.e., the axial portion of the specimen affected by the necking gradually becomes longer, while the minimum section continues to contract but gradually more and more slowly. Once the global elongation reaches a value of 0.20, the cross section where the neck initially started nearly stops contracting while the deformation proceeds propagating to the rest of the gauge length that had remained (point C).

IV. *Post-propagation phase* (elongation-based strain greater than 0.50). If failure does not occur during the propagation phase and the necking fronts are able to reach the specimen shoulders, a post-propagation stage begins, analogous to what is observed in cylindrical specimens, in which the axial strain distribution becomes reasonably uniform along the newly formed constant cross-section region, and the stress state is uniaxial. Under these conditions, even for flat specimens, global prismatic volume conservation should be maintained ($AL = A_0L_0$), and the strain diagram based on cross-sectional area versus that based on elongation is expected to once again follow the volume conservation line. However, as it can be observed from Figure 80, the experimental data points intersect the bisector of the quadrant at an elongation-based strain of 0.50 and subsequently remain below this line. To explain this behavior, it is important to consider that the true strain derived from cross-sectional area has been estimated under the assumption that the minimum section remains rectangular throughout the deformation history, without in-plane distortion. In reality, as evident from the post-fracture images of the specimens, its shape does not remain rectangular. Indeed, due to necking localization, it progressively deforms by bending inward toward the center. As a result, the effective resistant area is smaller than the one estimated, and consequently, the "real" area-based true strain is higher. This implies that, if the area-based true strain were accurately evaluated, the nearly plateau segment, corresponding to the propagation phase would shift upward, bringing the strain vs. strain diagram above or approximately onto the 45° line.

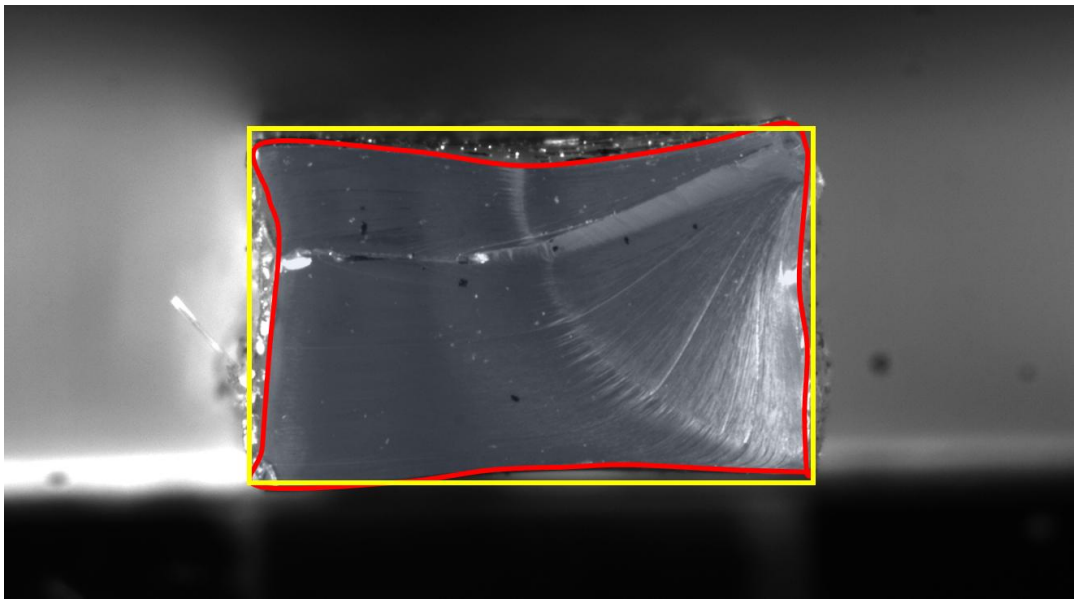


Figure 80: Polycarbonate flat (small) specimen tested at quasi-static rates: post-fracture image of the specimen. It is interesting to observe that the minimum resistant cross-section is smaller (red boundary) than the one estimated by assuming a rectangular shape (yellow boundary).

By comparing the deformed shapes of the specimens across the three tested geometries (Figure 81), it can be clearly observed that, for equal elongation, necking tends to be diffuse in the case of cylindrical geometry; mixed localized-diffuse, with the presence of a shear band, in the case of flat specimens with an almost square cross-section (*Flat Small*, aspect ratio 1.5); and fully localized with a shear band in the case of rectangular cross-section geometry (*Flat Large*, aspect ratio 2.5). The higher the cross-sectional aspect ratio, the stronger the tendency of the specimen to exhibit a shear-dominant response during necking localization. In the case of rectangular geometries, the true stress-strain curve derived from cross-sectional area tends to reflect a tension-shear response. The cross-sectional reduction in the presence of localized necking is caused by the local sliding of the two parts of the specimen, along the direction of maximum shear stress. Furthermore, the localization of strain in increasingly smaller regions of the specimen tends to promote earlier fracture. In *Flat Large* specimens, the area-based true strain at fracture is around 0.47; in *Flat Small* specimens, approximately 0.49; while in *Round* specimens it can reach up to 0.90. Notably, Flat Large specimens fractured even before the necking fronts could propagate, whereas Flat Small specimens were able to exceed this phase. In order to investigate the large-strain regime of the material (i.e., local strain greater than 0.5), it is advisable to test square or cylindrical specimens (where necking is more diffuse rather than localized with shear bands), using the shortest possible gage length (gage length-to-width ratio between 2 and 3), so as to allow the specimen to complete the propagation stage without failing during it.

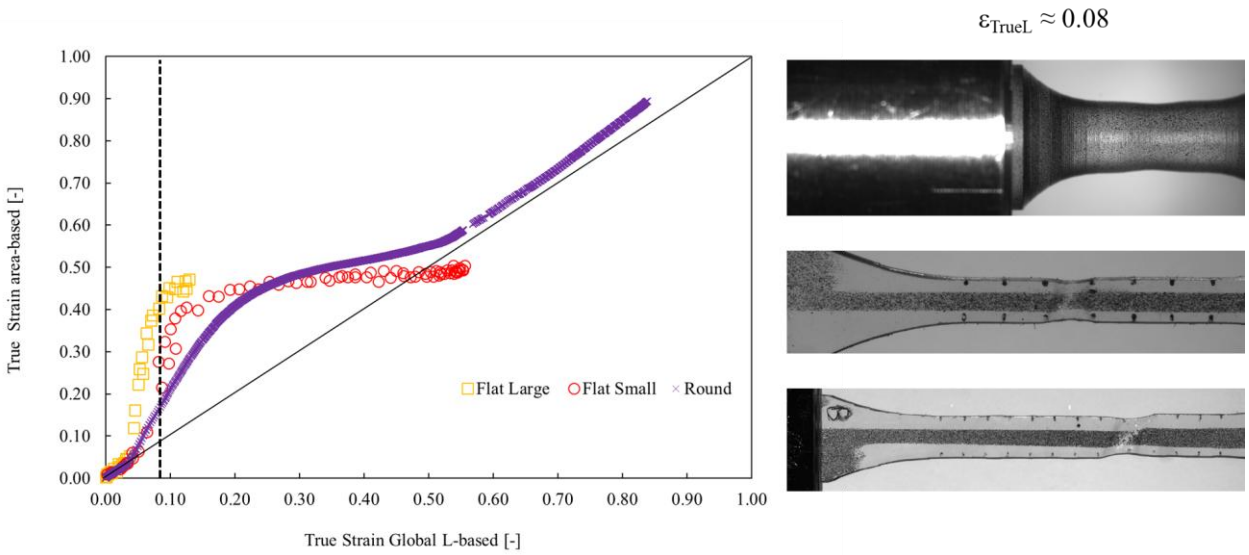


Figure 81: Comparison of the strain vs strain diagram for three different geometries: Flat Large (rectangular section with aspect ratio 2.5); Flat Small (rectangular section with aspect ratio 1.5); Round specimen.

Figure 82 shows the true stress-strain curve calculated based on the width reduction (area-based), and length-based for the three tested geometries.

As expected, the different approaches give equal curves until the necking inception (strain approximately equal to 0.035) and then they diverge after the peak stress of around 69 MPa. It is observed that, despite the two tested Polycarbonate batches originating from different lots, processed using two distinct manufacturing techniques and tested at different strain rates, 0.01 s^{-1} for the cylindrical geometry and 0.0007 s^{-1} for the flat geometries, the mechanical response in tension is identical in both cases. For area-based strains between 0.23 and 0.5, the true stress-area curves are perfectly described by the exponential law $48.5 \cdot \exp(\varepsilon_{True})$, indicating that all specimens have the same yield stress. The true stress-strain curves based on elongation, for all three geometries, converge onto the same exponential curve starting from a strain of approximately 0.10. In the two flat geometries, the drop in the elongation-based true stress curves occurs more rapidly than in the cylindrical geometry, as the gage length of the rectangular specimens is significantly longer than that of the cylindrical ones, and necking localization occurs with only a small overall elongation of the specimen.

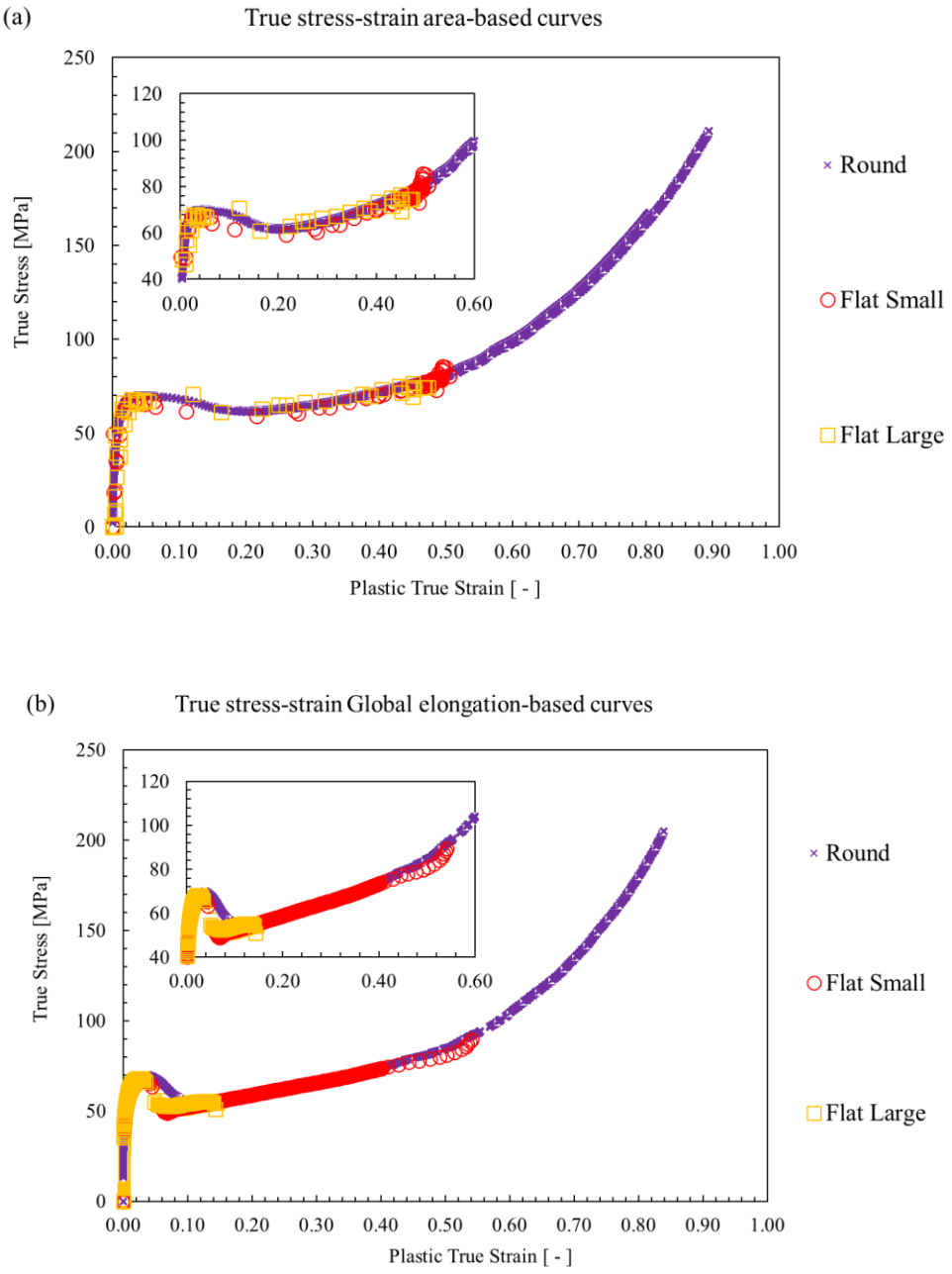


Figure 82: Quasi-static tensile true stress-strain curves for Polycarbonate round and flat specimens: a) Area-based true curves; b) Elongation-based true curves.

6.4.1 First necking and Generalized necking in Polycarbonate

An interesting observation in the case of polymers exhibiting necking propagation is that a generic section of the gage length that is 'undisturbed'—i.e., located far from both the region where necking firstly initiates and the specimen shoulders—undergoes a different loading and deformation history compared to the minimum section where strain localization first occurs. I will refer to such an undisturbed section of the gage length as a *generalized necking section*.

It is important to highlight that, in order for at least one generalized necking section to exist, the gage length must be 'sufficiently long' so that there is a region in the specimen that remains under uniaxial stress when the condition for the first necking is triggered.

With these premises, let us analyze a generic undisturbed section of the gage length during a tensile test. As the specimen begins to deform—first elastically, then plastically—as already mentioned multiple times, before necking occurs, the entire gage length is in a state of uniaxial stress and strain uniformity. Any cross section within the constant-area region responds identically in the pre-necking phase.

Once the necking condition (here referred to as *first necking*) arises at a certain section N1 of the specimen, the load applied to the specimen begins to drop rapidly due to the combined effect of geometric and material instabilities. A generic undisturbed section (denoted Ng), being unloaded, remains 'frozen' at the plastic strain corresponding to necking initiation (estimated at 0.035), while gradually recovering part of the elastic strain as the applied force decreases. In simple terms, the Ng section undergoes an uncontrolled elastic unloading.

At the end of this unloading phase, when section N1 transitions from localization to propagation, the mechanical state of section Ng is characterized by a plastic true strain of 0.035 and a true stress of $\sigma = 48.5 \cdot \exp(\varepsilon_{necking}) = 50.2$ MPa. During the propagation of N1, the true stress-strain curve of Ng remains fixed at this point until one of the two propagation fronts reaches it.

Once Ng is reached by the propagation front, the prismatic volume of material ahead of the front is forced to progressively deform (as plastic deformations are isochoric, the volume changes shape but remains constant over time), thinning and elongating until it becomes prismatic again once behind the front. Meanwhile, the Ng section, which thus deforms plastically under constant load, follows the exponential true stress curve from 0.035 up to approximately 0.47 (the strain associated with propagation end), and then becomes 'frozen' again in this mechanical state until all other sections of the gage length experience the same deformation history (strain equal to 0.53), whereas the latter stage of such straining (roughly from 0.47 to 0.53) occurs under almost-uniform straining all over the specimen which, by then, is returned to be again a nearly-straight parallelepiped, obviously thinner and longer than the undeformed one, subjected to a uniform and uniaxial tensile stress state.

The propagation phase can be completed all over the gage length without premature failure only in case of round specimens and of cleanly machined flat specimens with nearly-square cross sections, whereas flat specimens with width/thickness ratio exceeding 1.5 are too prone to localized necking and the shear bands originate failure initiation before the propagation can extend to the entire specimen,

If the propagation is completed without failure, then the specimen is again under uniform uniaxial stress state as aforementioned, therefore the true curves calculated over whatever cross section (including N1 and Ng) return to be identical to each other; such common post-propagation true curve, after the strain of around 0.53 exhibits a C1 discontinuity in the form of a rather sharp bend upward, and since then further evolves with greater slopes than those of the previous exponential true curve.

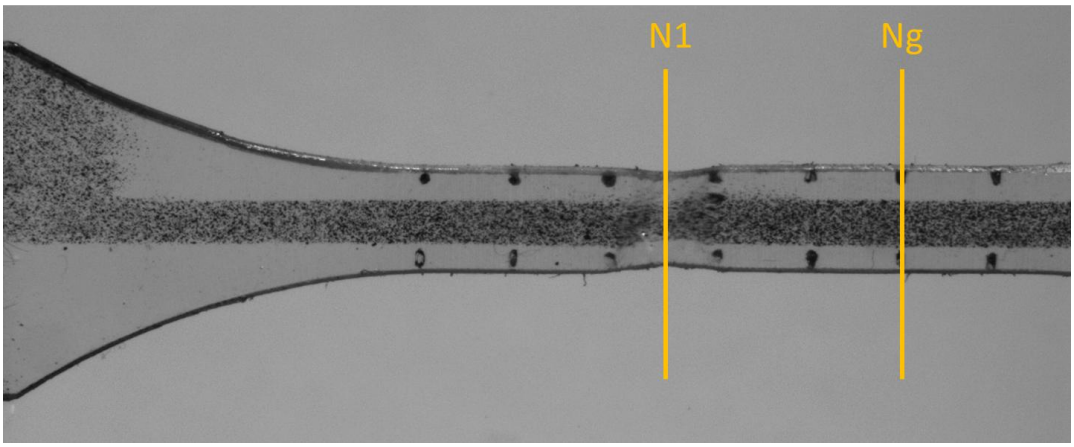


Figure 83: First necking section (N1) and generalized one (Ng) during a quasi-static tensile test of Polycarbonate flat specimen.

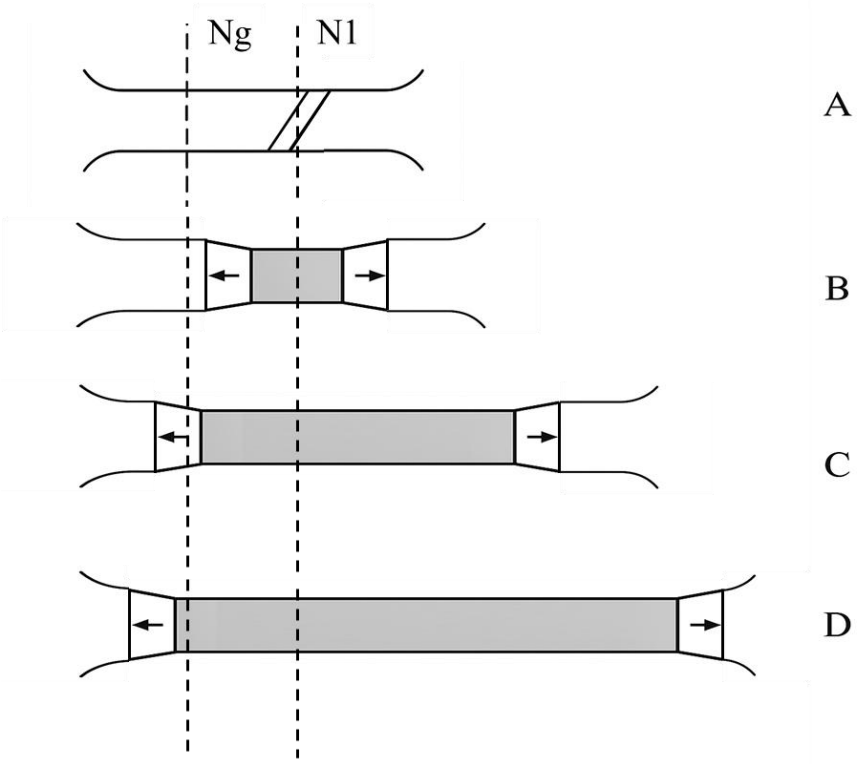


Figure 84: Stages of deformation history experienced by the first necking (N1) and generalized necking section (Ng).

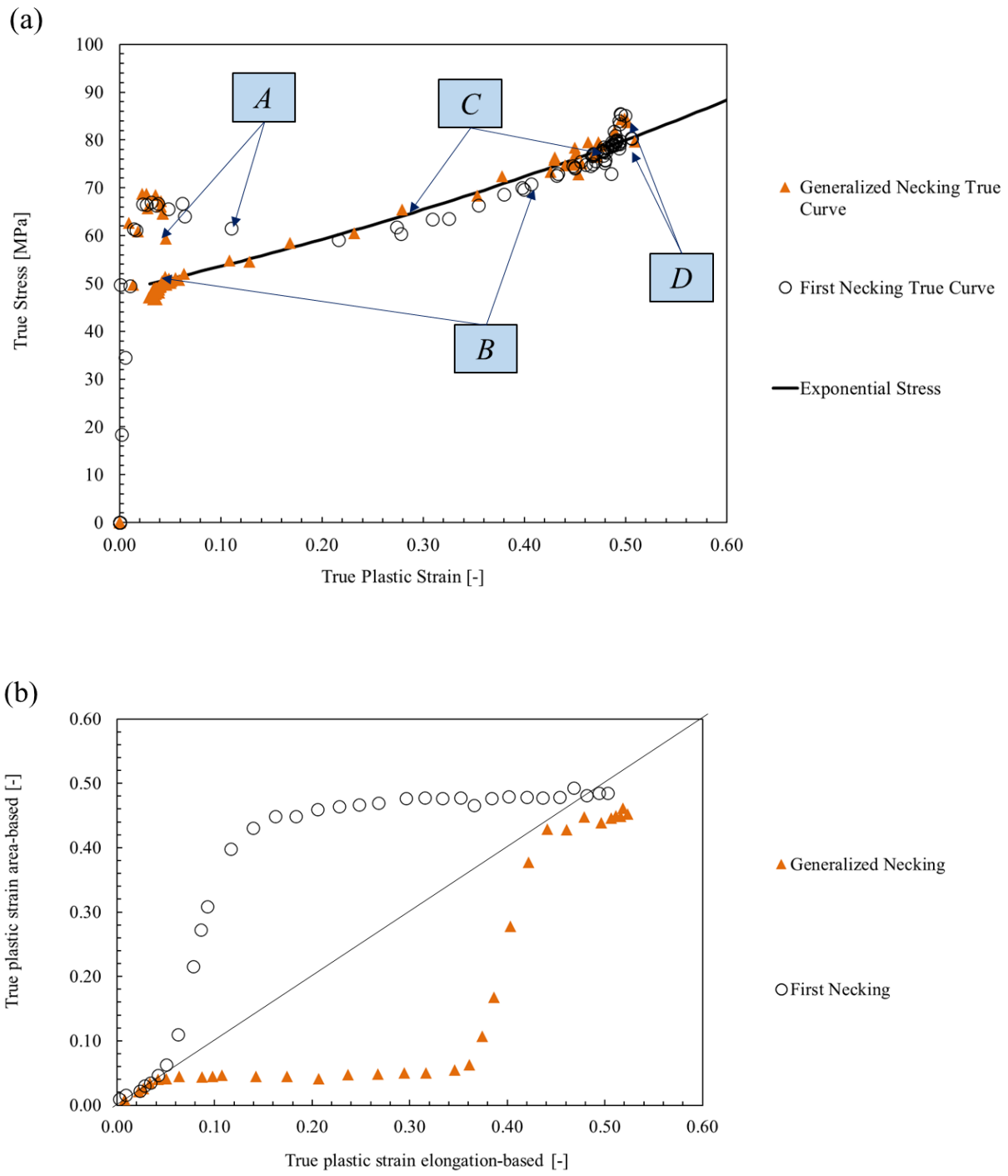


Figure 85: a) True stress-strain area-based from first necking and generalized necking. The instants A, B, C, D are referred to Figure 84; b) Strain vs Strain diagram from first necking and generalized necking.

6.5 Polycarbonate's material flow curve from the correction of Generalized Neck True curve

In the pre-necking strain range the smooth specimen is perfectly straight, then the stress state is uniform and uniaxial, and the true curve is identical to the flow curve.

After necking initiation, the specimen progressively develops a distorted profile due to the formation of the shear bands, inducing stress triaxiality and non-uniformity and causing the deviation between the flow and the true curve.

At the end of the shear band localization, the shape of the necking region tends to become less distorted and more similar to a diffuse necking, characterized by a symmetric curved profile. The profile originated at the first necking section, then, splits in two halves which start moving in opposite directions along the specimen axis.

As the propagating front approaches a general "undisturbed" cross section, the first part of the curved profile reaching such section exhibits an outward convexity (Figure 86 *b)*).

As the propagation proceeds and the curved profile further moves along the specimen, the generalized neck section experiences the progressive transition between the convex (Figure 86 *c)*) and the concave part of the front of propagation (Figure 86 *d)*). Finally, as the propagation is passed beyond, the local curvature of the generalized necking section returns to be again zero (local straight profile) Figure 86 *e)*.

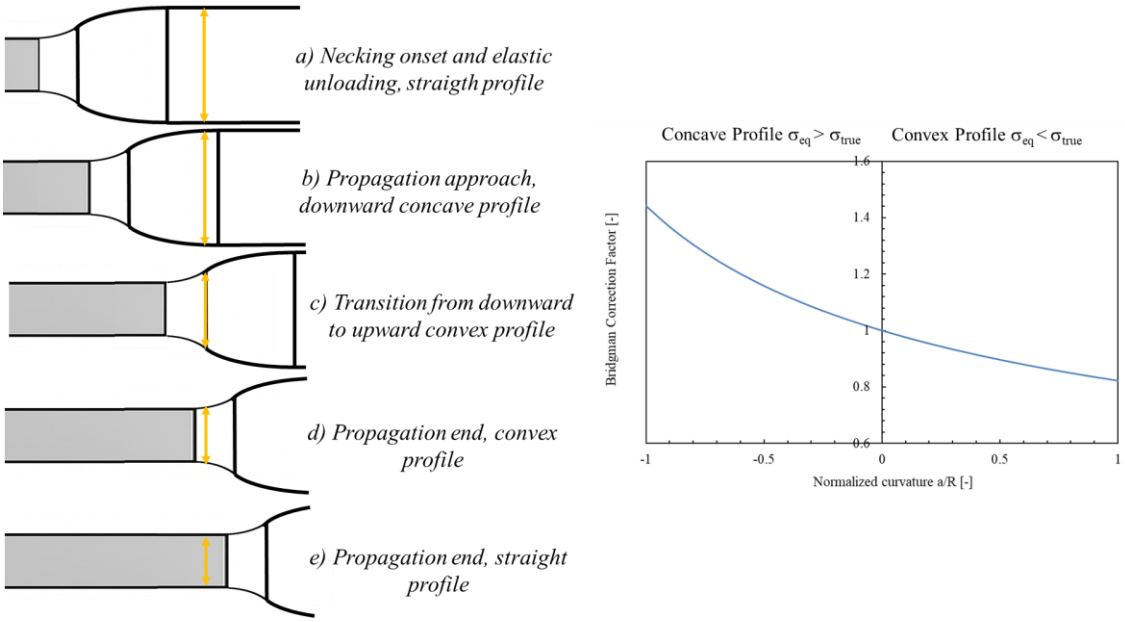


Figure 86 : Schematic representation of the moving front of propagation during its approach with the generalized necking section (orange double arrow) (on the left); Bridgman correction factor vs. normalized curvature of the generalized necking section (on the right).

As widely discussed in the paragraph 6.2, curved necking profiles in tensile specimens are known to generate stress triaxialities. The relationship between the Equivalent Stress and the True Stress was established under the analytical calculations of the Bridgman's Theory. That theory is strictly valid for axisymmetric specimens, but I can try to extend some considerations to the flat rectangular geometry. In Figure 86, the known Bridgman factor is reported for positive and negative values of the normalized curvature *a/R*.

The Bridgman formula was referred to the neck section of axisymmetric tensile specimens with monotonically increasing localization of the strain, therefore the actual relationship between the True stress and the Equivalent stress, for flat specimens of Polycarbonate undergoing both strain localizations from diffuse and localized necking, together with interacting localization-propagation mechanisms, may differ. However, the known correspondence between convex-concave neck profiles and the evolution of the average triaxiality experienced by the generalized necking section is assumed to remain valid, as also indicated by G' Sell et al. [73].

According to such considerations, a preliminary qualitative relationship between true curve and flow curve is proposed in Figure 87, where the difference between the unknown equivalent stress (red) and the known true curve at generalized neck (black) defines an additive correction function as reported in the following equation (46).

$$\sigma_{eq}(\varepsilon_{eq}) = \sigma_{True_{Gen.\ Neck}} + Corr(\varepsilon_{eq}) \quad (46)$$

As the first necking section is subjected to strain localization, the generalized one experiences the elastic unloading and remains at the same plastic strain (the strain at necking) until the propagation front reaches it. As the moving curved profile reaches the generalized neck section and firstly "touches" it with the convex end, such general cross section is restressed (following the unloading path) up to the yield stress level at necking, according to the fact that the outward convexity of the specimen profile makes the equivalent stress greater than the true stress.

This means that the correction function must begin with a positive value, whose magnitude for ensuring the C0 continuity of the flow curve, is equal to the stress drop at the elastic unloading.

As the necking profile further moves along the specimen axis and across the generalized section at hand, its convexity at the monitored cross section progressively reduces, also reducing the magnitude of the positive correction function (Figure 87, qualitative strain range 0.05 – 0.15).

Then an inversion point is reached, so the necking profile becomes concave with increasing curvature (Figure 86, c) to d)) and the correction becomes negative, with increasing magnitude (qualitative strain range 0.15 – 0.25 in Figure 87).

As the front of propagation further moves across the generalized necking section at hand, also the concave curvature reaches a maximum and then progressively decreases, tending to low-negligible curvature as the propagation is nearly complete and the profile returns to be locally straight (Figure 86, d) to e)). Correspondingly, also the negative values of the correction function decrease their magnitude and progressively tend to zero (Figure 87, qualitative strain range beyond 0.25).

According to the above considerations, the corrective function defined in equation (46) was approximated with a piecewise function made of three parts, as depicted in

Figure *88* a).

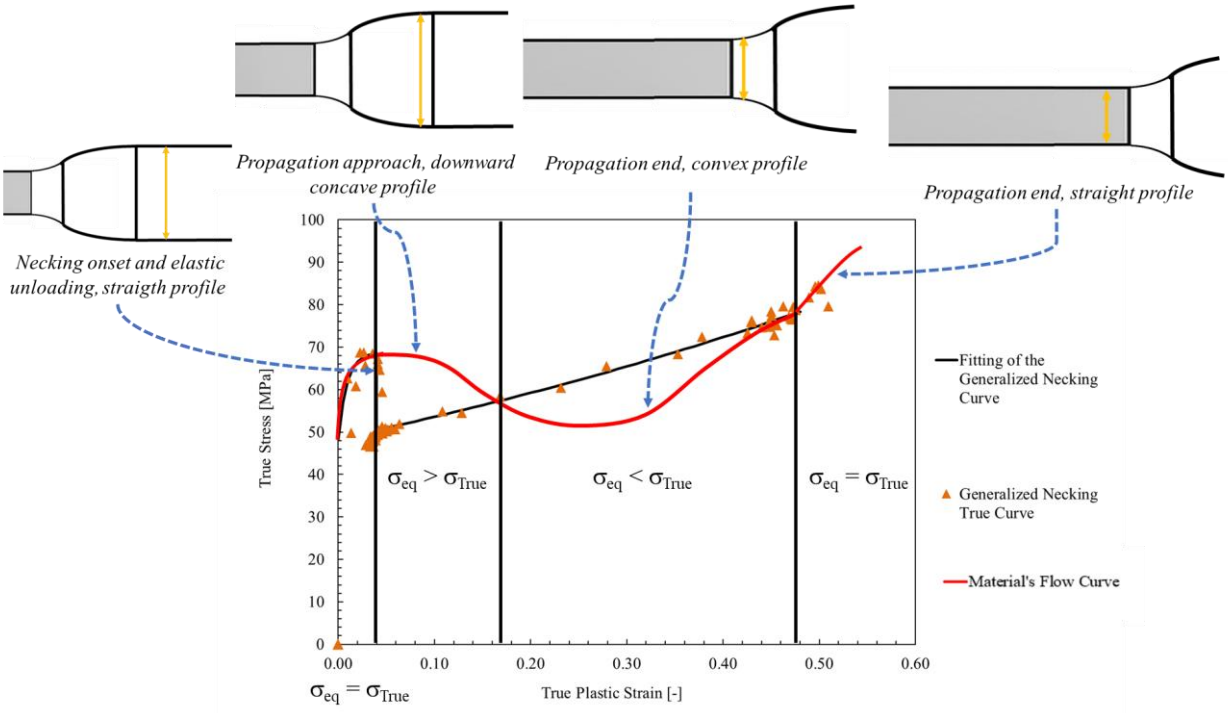


Figure 87 : Qualitative differences between flow curve and true curve.

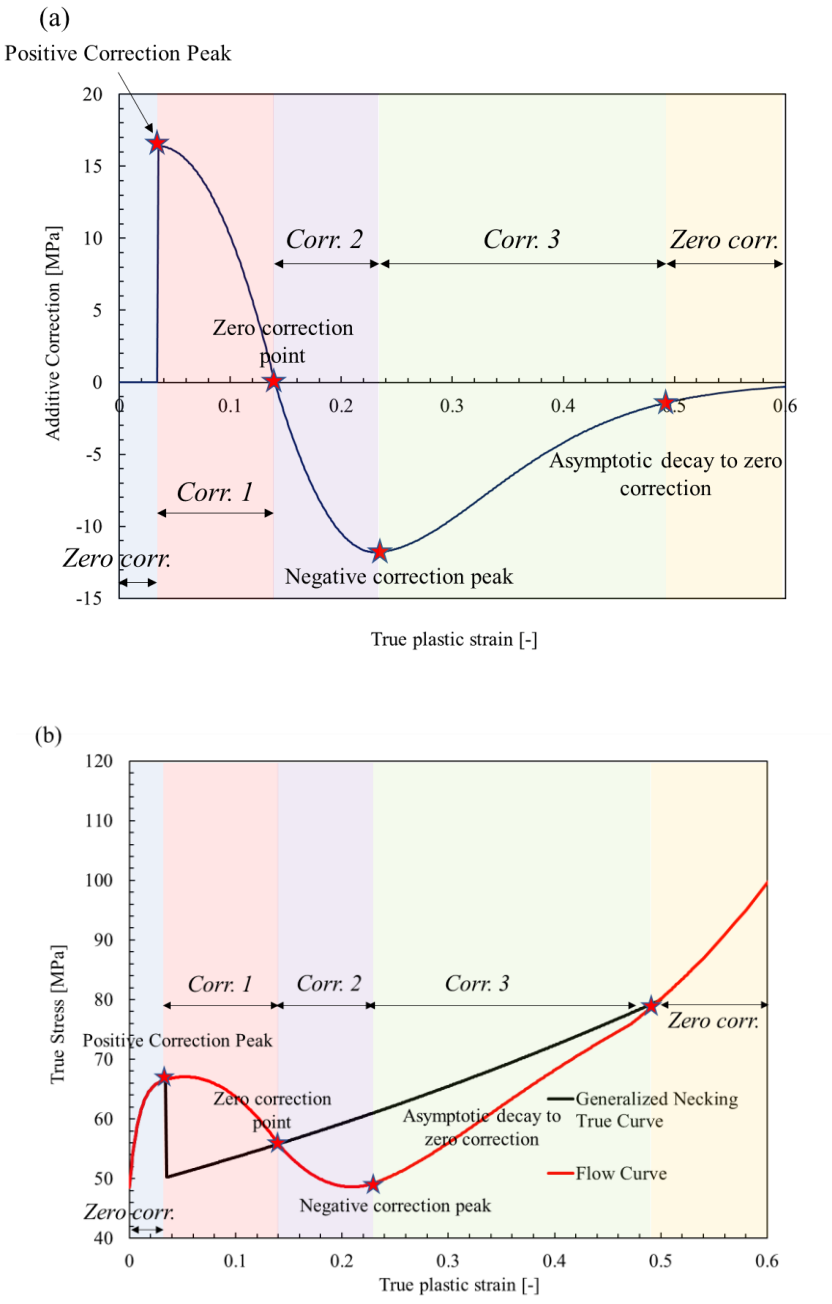


Figure 88 : a) Polycarbonate's additive correction function; b) Gen. Neck true curve and flow curve of Polycarbonate at static rates.

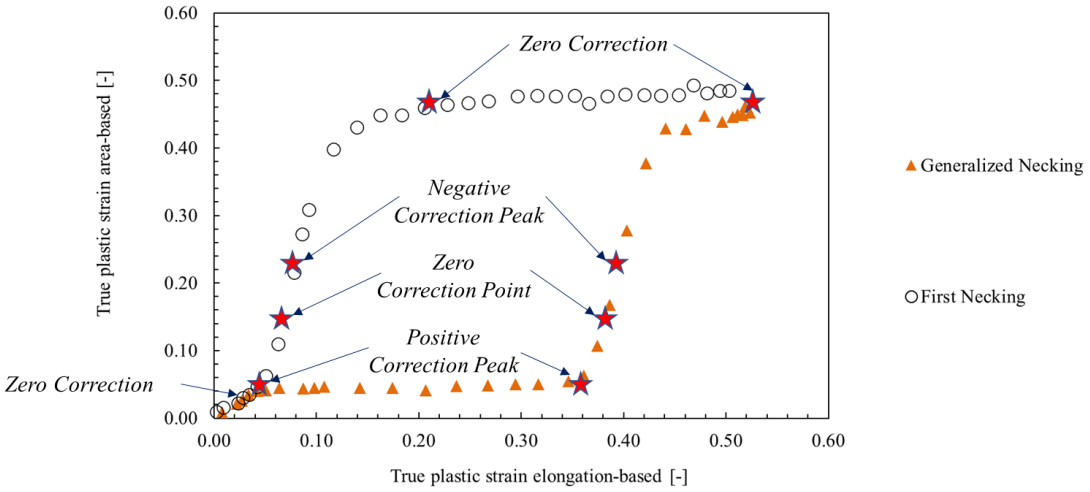


Figure 89: Area-based strain vs Elongation-based strain for the assessment of the relevanrt points of the additive correction.

The first branch of the proposed function begins with a *positive correction peak (PCP)* at the corresponding strain ε_{PCP}, very close to the necking strain, $\varepsilon_{PCP} \approx 0.035$, where the strain localization initiates and begins evolving together with the increasing slope $d\varepsilon_{GenNeck}/d\varepsilon_{TrueL}$ (first star mark in Figure *88* and Figure 89).

The first piece of the correction function ends at the test stage where the correction reverses from positive to negative and passes through the *zero-correction* (ZC) at which $\sigma_{eq}=\sigma_{True}$, associated here to the strain level ε_{ZC} where the localization-elongation ratio becomes fully established so that $d\varepsilon_{GenNeck}/d\varepsilon_{TrueL}$ quits increasing and becomes nearly constant (second star mark of Figure *88* and Figure 89), $\varepsilon_{ZC} \approx 0.15$.

The first piece of the correction function (named $Corr_1$) between such fixed extremities is simply approximated by a quadratic polynomial of the post-necking strain $\varepsilon_{eq} - \varepsilon_{Neck}$ (eq. 47)

47) $$Corr_1 = a_0 + a_1(\varepsilon - \varepsilon_N) + a_2(\varepsilon - \varepsilon_N)^2 \quad for\ \varepsilon_{PCP} \leq \varepsilon < \varepsilon_{ZC}$$

where a_0 expresses the difference between the stress at necking onset and the stress and the end of the elastic unloading of the general neck section, while a_1 and a_2 are constrained to the condition that the correction must nullify at the zero-correction strain ε_{ZC}. Therefore, the function is fully determined at its ends and two parameters are related to each other (i.e., $a_2=a_2(a_1)$) so that just the single parameter a_1, determined by the slope of the polynomial at necking onset, remains free and available for calibration.

The second part (named *Corr₂*) of the additive correction extends from the ZC point described above, up to a *negative correction peak* (NCP) at the strain ε_{NCP}, where the propagation progressively becomes predominant over the localization; such strain is associated to the test stage where the curve slope $d\varepsilon_{GenNeck}/d\varepsilon_{TrueL}$ of Figure 89 quits being constant and starts to decrease (third star mark in Figure *88* and Figure 89, $\varepsilon_{NCP} \approx 0.23$).

Similarly to what was done for the first part of the correction function, also for the second piece (named *Corr₂*), a simple quadratic approximation is proposed here, according to eq. (48)

48) $$Corr_2 = b_0 + b_1(\varepsilon - \varepsilon_{ZC}) + b_2(\varepsilon - \varepsilon_{ZC})^2 \quad for\ \varepsilon_{ZC} \le \varepsilon \le \varepsilon_{NCP}$$

The two conditions imposed to this second part of the function are: 1) the passage for the zero point at ZC strain; 2) the slope of the function must be zero at the negative correction peak strain. Then, it is trivial to prove that $b_0=0$, $b_1= -2\, b_2\, (\varepsilon_{NCP} - \varepsilon_{ZC})$, and $b_2= -\, Corr_2(\varepsilon_{NCP})/(\varepsilon_{NCP} - \varepsilon_{ZC})^2$. Only the amplitude of the delta stress at NCP remains undetermined from the experiments and needs to be find by successive iterations.

The last piece of the additive correction (named *Corr₃*) extends from the NCP point defined above up to failure or, in case of propagating specimens, up to complete propagation all over the specimen. This function starts from a negative triaxiality value at the NCP point and tends asymptotically to zero as the strain tends to the strain at propagation end. A mixed power-exponential function with three parameters is adopted to approximate such trend, according to eq. (49).

49) $$Corr_3 = c_0 * \left(\frac{\varepsilon}{\varepsilon_{NCP}}\right)^{c_1} \exp\left(c_2\, (\varepsilon_{eq} - \varepsilon_{NCP})\right) \quad for\ \varepsilon_{NCP} < \varepsilon$$

Two conditions can be imposed to determine two parameters of the correction (i.e., c_0 and c_1) by imposing the continuity of the function and its derivative between *Corr₂* and *Corr₃* at NCP point. The third parameter c_2, regulating the rate of decay of the correction, remains free.

In summary, the proposed piecewise correction function of the generalized necking true curve has nine constants to determine: four of these (i.e., ε_{PCP} , ε_{ZC}, ε_{NCP}, PCP) are directly related to the deformed shape of the front of propagation and are determinable by the experiments; two parameters derive from the condition imposed at zero-correction and at positive correction peak; finally, only three parameters remain to be determined by inverse calibration with the aim of Finite Element simulations.

6.5.1 Finite Element Simulation of the mechanical response of Polycarbonate flat specimens and inverse calibration of the material's flow curve

Finite elements simulations of the static tensile tests on Polycarbonate flat specimens were run with the Hexagon software MSC Marc Mentat® v2023.4. The two flat geometries (Large and Small) have been simulated.

After a preliminary check on mesh sensitivity, the flat small geometry has been divided into 120 division along the gage length, 20 along the width, and 15 through the thickness; instead, the flat large one has been discretized into 100 parts along the gage, 20 elements along the width, and 12 elements through the thickness. The fillets between gage length and specimen shoulders are also modelled, with a progressively coarser mesh.

The entire specimen is modelled without exploiting its geometrical symmetry, to avoid spoiling the output of local displacements and strains distributions during the diffuse-localized necking and during the successive peculiar stage of strain propagation.

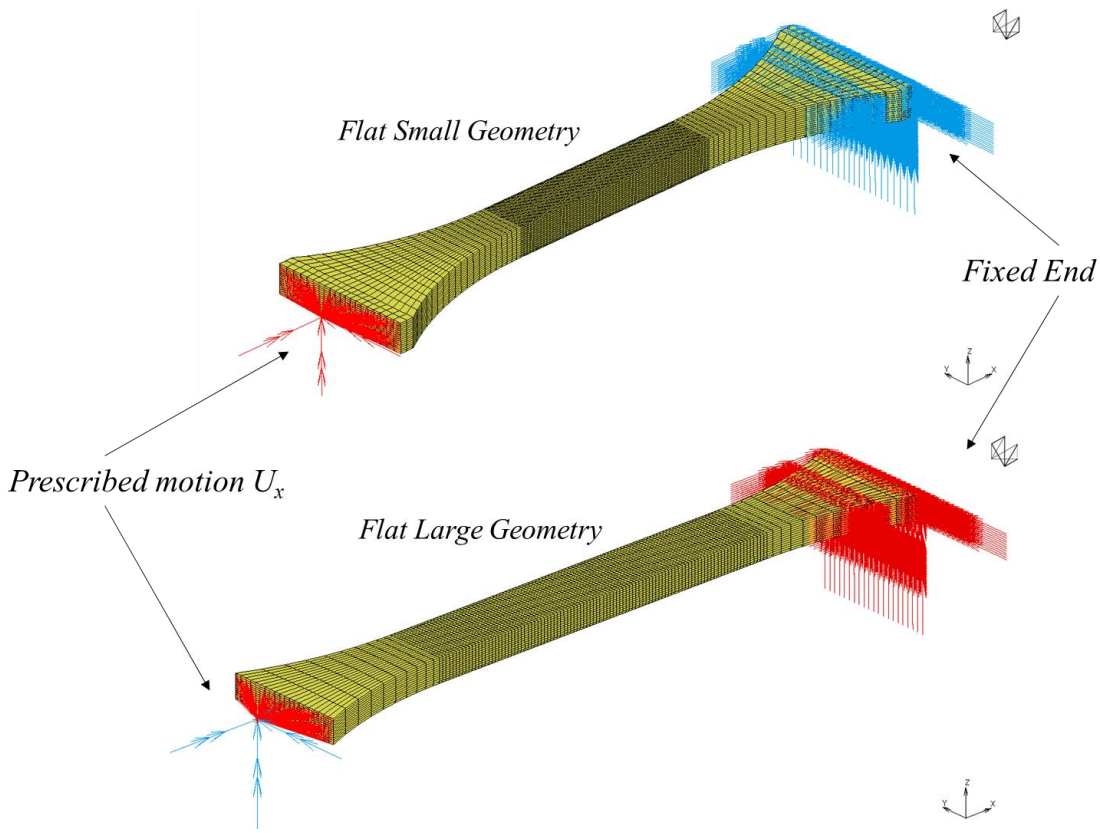


Figure 90: Meshed specimens used for the present work: Flat Small and Flat Large.

The boundary conditions include fixed nodes at a specimen end and prescribed axial motion to a set of nodes at the other specimen end.

The elasto-plastic response of Polycarbonate has been modelled by isotropic J2-plasticity with isotropic hardening. The elastic constants have been supposed as follow: Young Modulus of 2400 MPa and Poisson's ratio equal to 0.33. The material's flow curve was determined by successive iterations (trial and error or reverse engineering approach), varying the three calibration parameters of the correction function and comparing the results from the Finite Element simulations in terms of area-based true stress, global elongation-based true stress and strain vs strain diagram, both at first necking and generalized necking section.

The additive correction was applied to the Generalized Necking true curve derived from the experimental data shown in Figure 85, and fitted by the following piece-wise function (eq. 50):

$$50)\quad \sigma_{True_{GEN.NECK}} = \begin{cases} 48.5 + 18.5\,[1 - \exp(-110\varepsilon_{True})] & if\ \varepsilon_{True} < \varepsilon_{Neck} \\ 48.5\exp(\varepsilon_{True}) & if\ \varepsilon_{Neck} \leq \varepsilon_{True} < 0.49 \\ 48.5\exp(1.967\ \varepsilon_{True}^{1.976}) & if\ \varepsilon_{True} > 0.49 \end{cases}$$

After numerous simulations employing input curves obtained through a trial-and-error procedure and guided by the observations reported in the article of Barbagallo et al. [94], the flow curve delivering an acceptable agreement between FEM results and experimental data combination of parameters for the additive correction proposed herein that minimizes the error between is reported in the following Table 14:

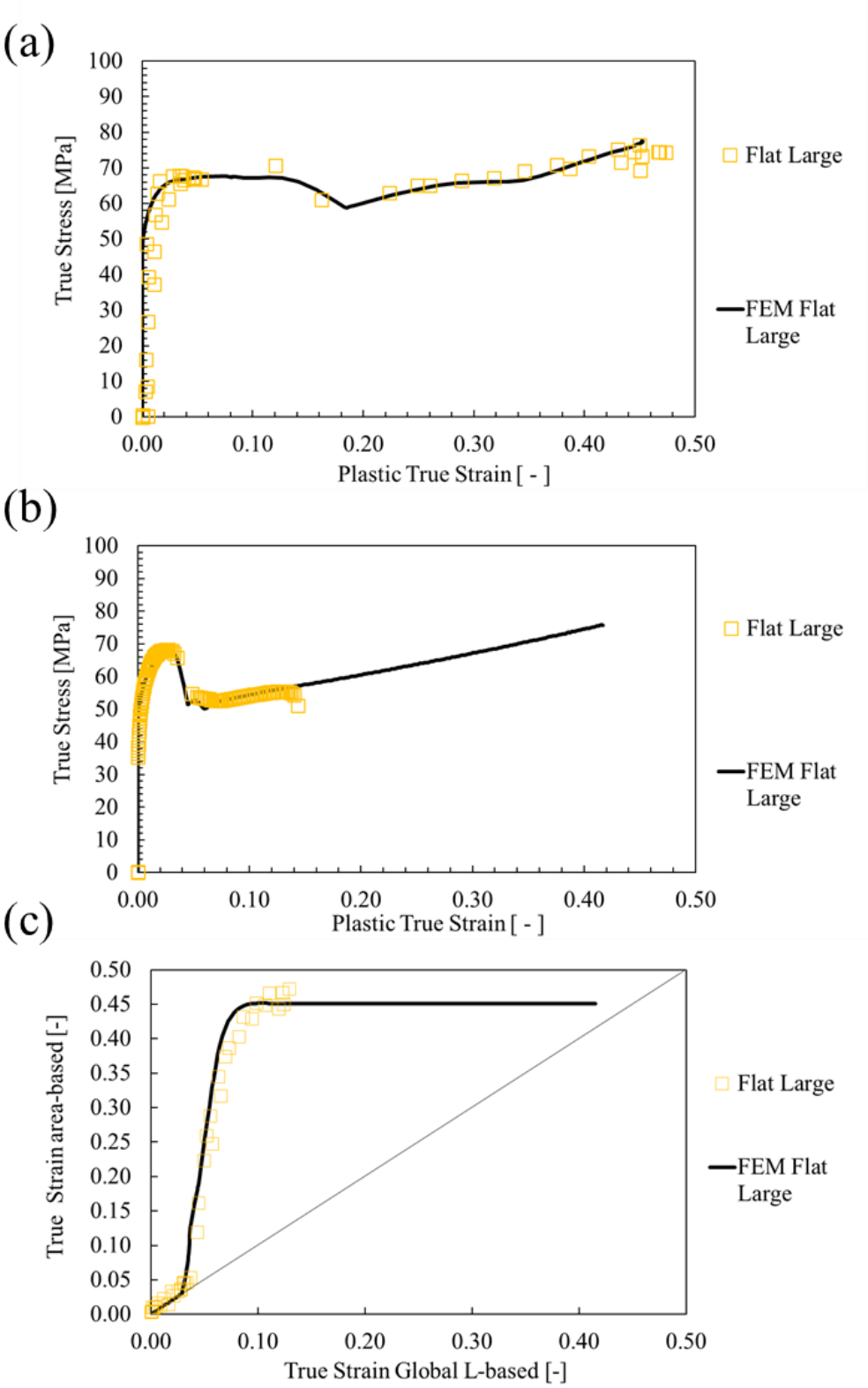
Additive Correction Parameters								
a_0	a_1	a_2	b_0	b_1	b_2	c_0	c_1	c_2
16.4	0	-1487.53	0	-262.22	1456.79	-11.8	5.5	-24

Table 14: Additive Correction parameters used for the determination of the material's flow curve.

The outcome of the simulated tension test with the calibrated parameters is reported below against the experimental results.

Figure 91 prove that the derived flow curve allows to correctly reproduce all the features of the quasistatic tensile experiments and, more generally, also demonstrate the suitability of the

proposed procedure for thoroughly characterizing the plasticity of Polycarbonate plates, up to large strains exceeding the transition between localizing-propagating stages.



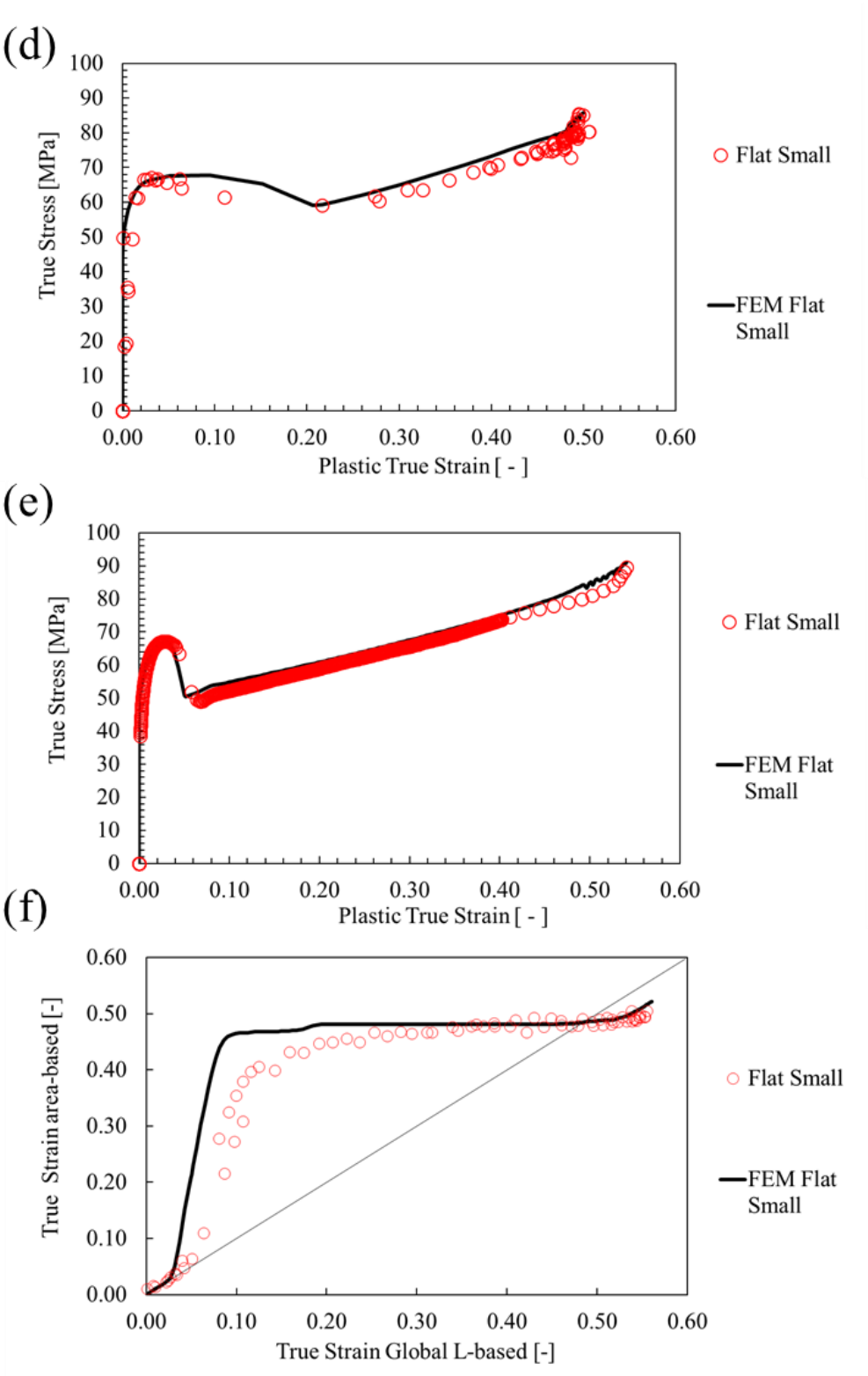


Figure 91: Quasi-static tensile test of Polycarbonate flat specimens: comparison between FEM results (black line) and experimental data (yellow and red dots). Results related to the Flat Large geometry: a) True area-based curve; b) True elongation-based curve; c) Area strain vs elongation strain. Results related to the Flat Small geometry: c) True area-based curve; d) True elongation-based curve; e) Area strain vs elongation strain.

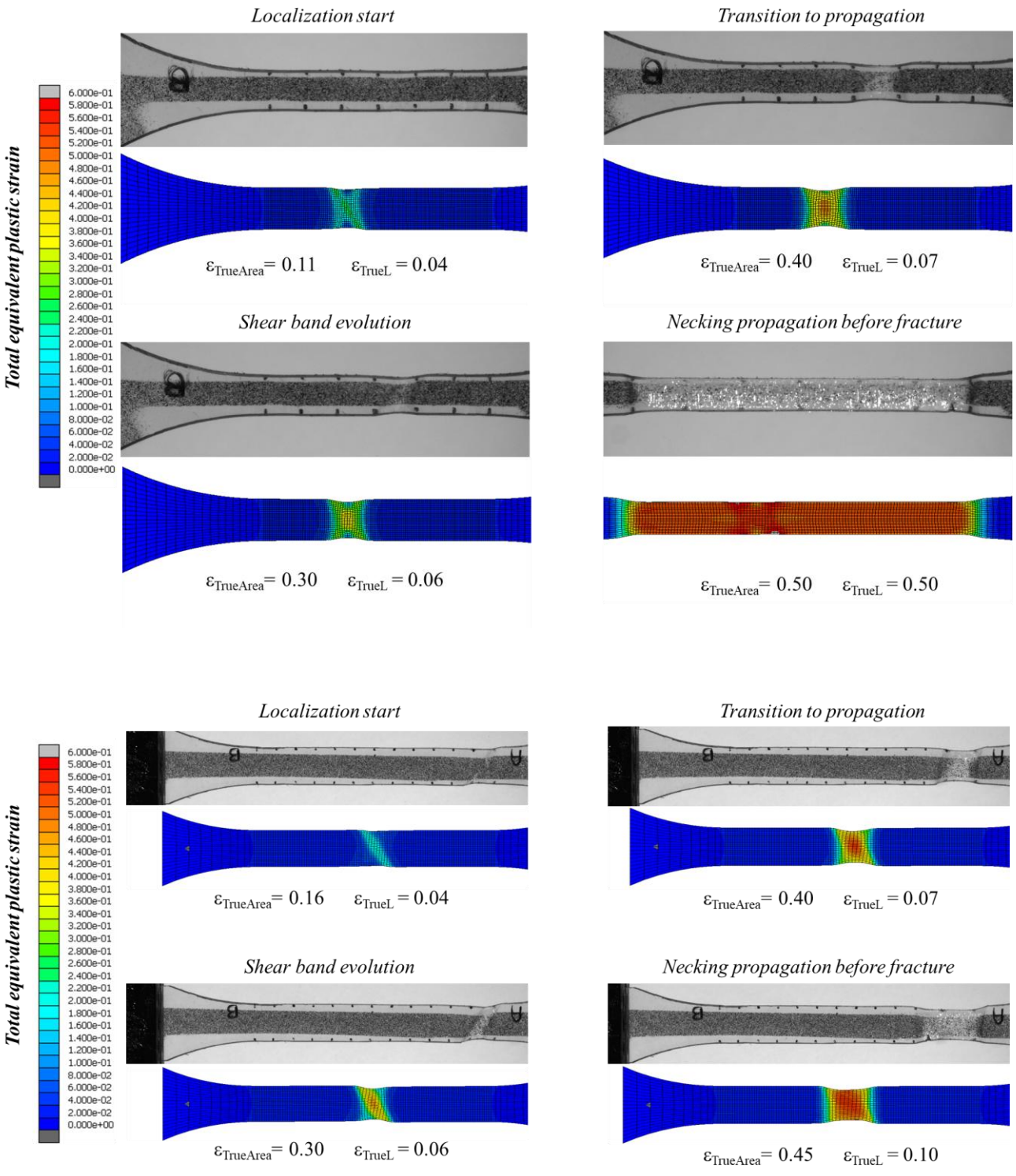


Figure 92: Comparison between the specimen's shape predicted by the Finite Element simulation and the experimental profile in the two tested geometries: Flat Small (top); Flat Large (bottom).

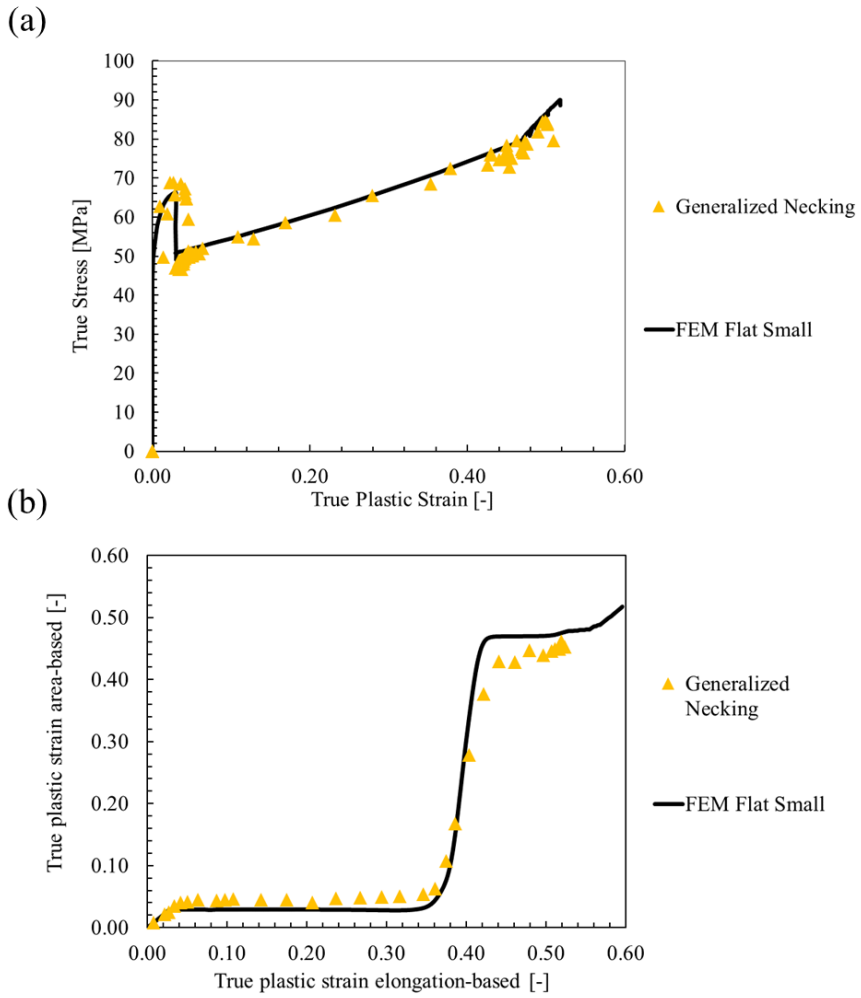


Figure 93: Comparison between experimental data (yellow dots) and FEM results (black line) for the quasi-static tensile test on Polycarbonate Flat Small specimen (Generalized Necking): a) Generalized Necking true stress strain curve; b) Area-based strain vs Elongation-based strain (Gen. necking).

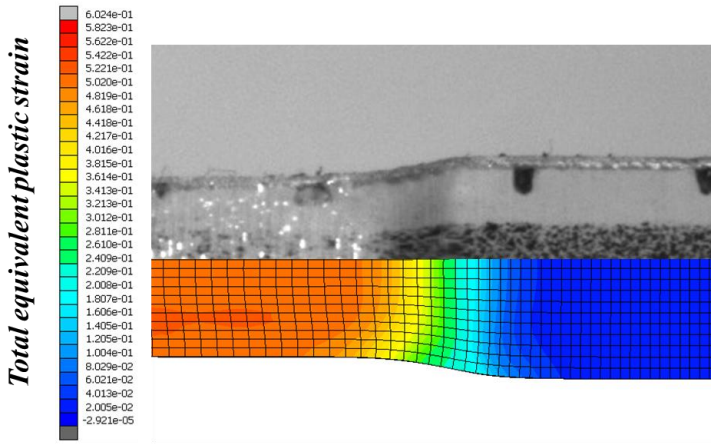


Figure 94: Specimen's profile during the propagation phase compared with the profile from FE simulation.

6.6 Conclusions

In the present chapter, the tensile response of Polycarbonate under quasi-static conditions was investigated. The study focused on three specimen geometries: round, flat-small (approximately square cross-section), and flat-large (rectangular cross-section). The deformation mechanisms of the material were analyzed in detail, namely: pre-necking, necking localization, propagation, and post-propagation (the latter occurring only if fracture does not take place before the necking fully propagates along the gage length). By examining the deformation mechanisms in both round and flat geometries, two methodologies were proposed for the material characterization, aimed at correcting the true stress–strain curve derived from area reduction into the corresponding material flow curve.

For round specimens, starting from the experimental measurements of the curvature of the necking section, a direct Bridgman-type correction methodology was applied, including a numerical iteration to refine the flow curve.

For flat specimens, instead, a semi-inverse correction methodology of the area-based true curve was proposed, relying on the *Generalized Necking* approach. The Generalized Necking true curve was not derived at the location of the first strain localization at necking, but rather on an "undisturbed" section, away from this region, which deforms under constant load during the propagation of the initial necking section. The additive Generalized Necking correction requires several numerical iterations (trial-and-error procedure) to determine three parameters which, at present, cannot be directly obtained from experimental measurements.

Both procedures were validated by comparing the experimental data with the outputs of numerical simulations. Although the Generalized Necking procedure has the advantage of being applicable to a true curve composed of a pre-necking segment and an exponential post-necking segment, and is therefore not affected by the complex triaxiality induced by the shear band, the procedure requires that the specimens be sufficiently long (gage length-to-diameter or width ratio greater than 5) and that necking propagation be extended enough to allow the identification of an undisturbed section deforming under constant load.

Chapter 7: Dynamic tensile behavior of Polycarbonate

Polycarbonate is well known for being highly sensitive to both strain rate and temperature effects. In general, for both metals and polymers, the strain rate effect tends to increase the material's strength: at a given strain level, the dynamic equivalent stress is higher than its static counterpart. Conversely, the influence of temperature acts in the opposite direction, softening the material: at temperatures above ambient conditions and for any given strain, the equivalent stress decreases.

This dual behavior is commonly described by stating that strain rate leads to a Dynamic Amplification of the flow curve, while temperature increase results in Thermal Softening. These two phenomena are generally not decoupled.

It is possible, for instance, to perform quasi-static tensile tests at various temperatures in order to assess the material's sensitivity to thermal softening. Conversely, during dynamic tests conducted at constant nominal strain rate, the material tends to self-heat due to the conversion of plastic work into heat. If the strain rate is sufficiently high such that the duration of the deformation process is shorter than the characteristic time required for the specimen to dissipate heat via conduction, convection, and radiation, a fraction of the plastic work per unit volume, defined as the integral of the equivalent stress over the strain history, is converted into sensible heat. This localized heating leads to a temperature rise in the plastically deforming regions of the specimen.

In the present work, the mechanical response of Polycarbonate specimens, both cylindrical and flat, under low, intermediate, and high strain rates is investigated.

For the cylindrical specimens tested at the INATECH laboratories in Freiburg, an extensive experimental campaign was carried out, comprising tensile tests at nominal strain rates of 0.1 s^{-1}, 7 s^{-1}, and 1000 s^{-1}, performed using different experimental setups.

As for the dynamic tests on flat specimens conducted in Catania, tensile experiments were carried out at a nominal strain rate of 7 s^{-1}.

A methodology will be proposed, previously applied by Mirone et al. [95] to an AISI 304 stainless steel, to decouple the two competing phenomena of Dynamic Amplification and Thermal Softening in Polycarbonate. This approach integrates experimental data available in the literature concerning the thermal softening effect, particularly the results reported by G' Sell et al [96].

7.1 Dynamic tensile tests on Polycarbonate round specimens

The dynamic tensile tests were performed at low (0.1 s^{-1}), intermediate (7 s^{-1}) and high strain rates (1000 s^{-1}). The tested specimens had the same geometry of the quasi-static tests (nominal gage length of 8.5 mm, nominal diameter of 6 mm). Three repetitions were run for each nominal strain rate. The gage length chosen for all the dynamic tests was 4 mm, corresponding to the "semi-local gage length" of the quasi-static tests. The tensile tests at 0.1 s^{-1} were carried out in the electromechanical testing machine Zwick Z100 used for the quasi-static tests. The tests at intermediate strain rate were run on a custom-made desktop testing machine developed at INATECH laboratories: the so-called *Quickdrive* machine. Finally, the tests at high strain rates were run on a Split Hopkinson Tension Bar (SHTB). In this section, I will describe the experimental setup implemented for the tests at 0.1 s^{-1} and 7s^{-1}, leaving the description of the SHTB facility in another sub-section.

Low-dynamic strain rate (0.1 s^{-1}): Experimental Setup

The tensile tests at 0.1 s^{-1} were carried out on a universal testing machine Zwick Z100 (loadcell of maximum 100 kN). The crosshead speed was imposed at 50 mm/min, which delivers a nominal strain rate of approximately 0.1 s^{-1}. The specimens were painted with black dots applied with an airbrush, in order to use the Digital Image Correlation to measure the elongation. The instantaneous minimum diameter was measured by the optical telecentric system TMx-5000. The elongation was tracked by using the Basler acA4112-20 um high-resolution camera (4096 × 3000 pixels). The frame rate was set as 10 fps for the TM-X5000 (approximately 200 frames before fracture), and 5 fps for the high-resolution camera (approximately 100 frames before fracture). For these tests, an infrared camera Micro-Epsilon® TIM 640 was used to measure the instantaneous self-heating of the specimen. This infrared camera has a resolution of 640 x 180 pixels and a frame rate of 32 Hz. The measurable temperature range was set between 0 °C and 250 °C. The camera is auto calibrated at ambient temperature (25 °C).

Intermediate-dynamic strain rate (7 s^{-1}): Experimental Setup

The experimental setup used for the dynamic tests at 7 s^{-1}, referred to as the *Quickdrive testing machine*, was developed and built at the INATECH laboratories of the University of Freiburg. It consists of a benchtop skew-driven machine equipped with two stepper motors powered at 48 V. The

system is controlled via G-code language, as in conventional CNC machines. The software employed to control the motors is the *Universal G-Code Sender*.

The force was measured using a load cell with a maximum capacity of 10 kN, calibrated before the tests. The voltage output signal from the load cell was amplified using a signal amplifier with a gain of 100 and acquired by a digital oscilloscope (Picoscope 6®). Load cell data were filtered using a 1 kHz low-pass filter and sampled at approximately 18 MS/s. Each test was recorded over a time window of 500 ms, with a pre-trigger time of 5 ms.

The trigger signal was provided by the pulse train sent from the controller to the stepper motor. Specifically, to move the screw by 1 mm, the controller sends 800 pulses at 4.5 V to the motor. These control pulses, which govern the motor displacement, were also acquired in order to track the relative displacement of the grips.

To measure strain, it was only possible to use the telecentric lens system TM-X5000, due to the difficulty of integrating an additional camera into the experimental setup. The true curves derived from dynamic tests at low and intermediate strain rates are shown in the following figures: Figure 96 and Figure 97.

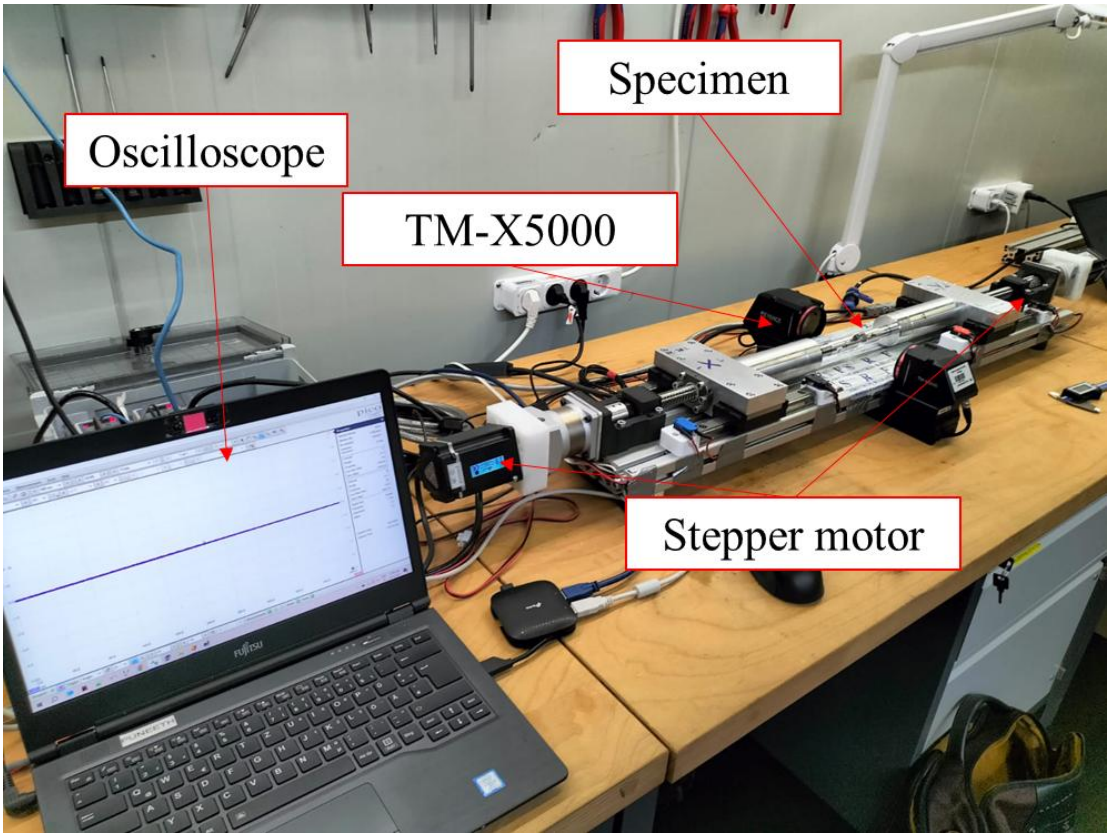


Figure 95: Experimental setup for the tests at intermediate strain rate (7 s^{-1}).

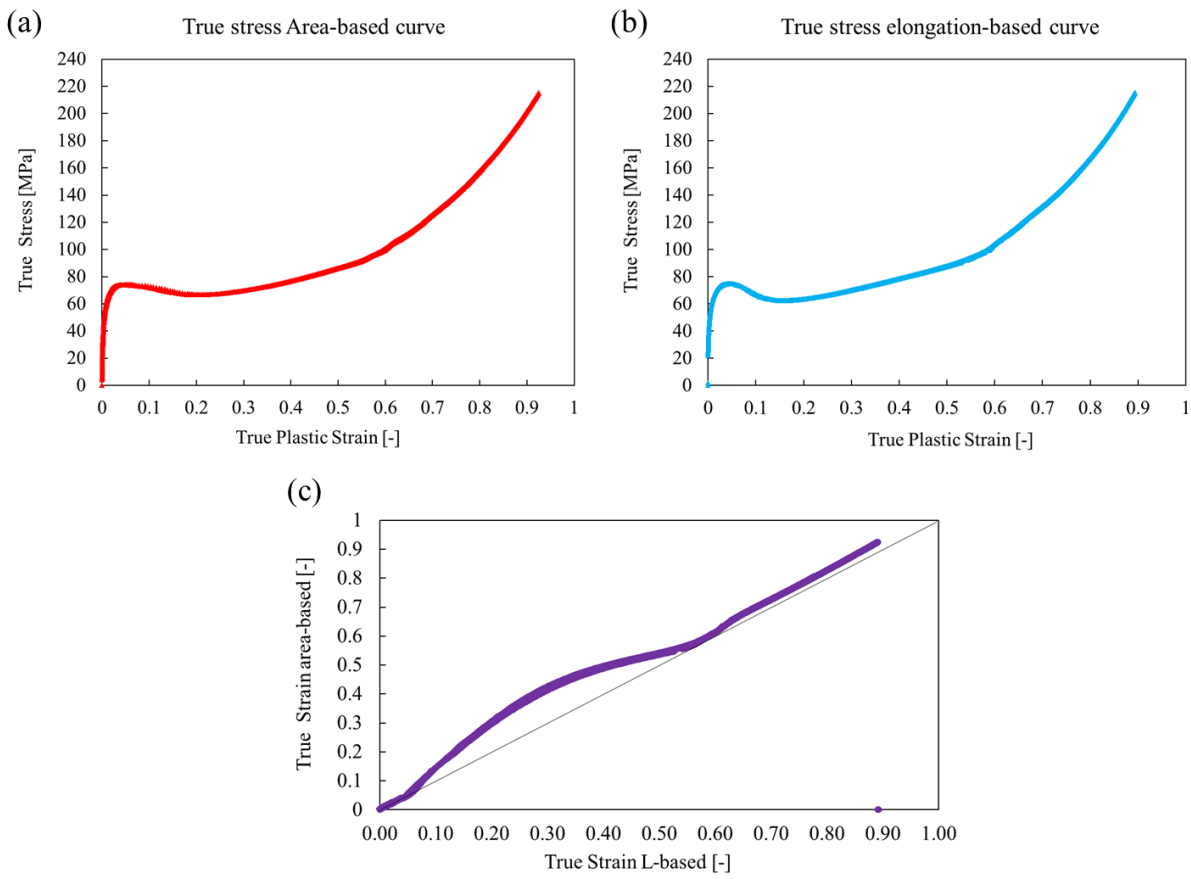


Figure 96: Tensile tests of Polycarbonate at 0.1 s^{-1}: a) true stress area-based curve; b) true stress elongation-based curve; c) area-based strain vs elongation-based strain.

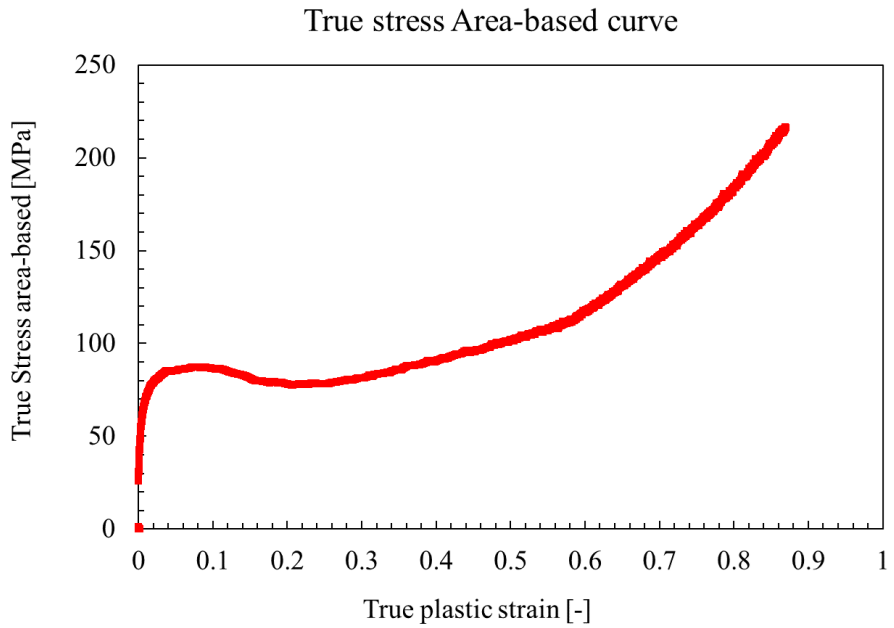


Figure 97: Tensile tests of Polycarbonate at 7 s^{-1}: true stress area-based curve.

7.1.1 The Split Hopkinson Tension Bar (SHTB) apparatus

To test materials under high strain rates (typically in the range between 10^2 and 10^4 s^{-1}), the experimental apparatus most commonly employed in laboratories is the Split Hopkinson Tension Bar (SHTB). Although this device may feature specific architectural variations, its working principle is generally based on a two-bar system, an *input bar* and an *output bar*, usually made of metal, although polymeric materials may be used in specific cases. The specimen to be dynamically tested is positioned between these two bars.

A portion of the input bar is dedicated to the generation of a strain wave, which propagates along it at the speed of sound in the material. In order to generate an ideal square-shaped strain pulse, various designs can be adopted for the input bar system. In one widely used configuration, a segment of the input bar is inserted into a cylindrical barrel, inside which a hollow striker, typically made of polyoxymethylene (POM), is placed. The inner diameter of the striker matches the nominal diameter of the input bar, while its outer diameter matches the inner diameter of the barrel. The striker is pushed by a compressed air system in the direction of the left end of the input bar, where a transfer flange is located.

Upon impact with the flange, the striker's kinetic energy is converted into elastic potential energy within the input bar segment, which propagates toward the specimen and the output bar at the speed of sound. The elastic strain wave generated in the input bar, commonly known as *incident wave*, reaches the first specimen-bar interface and, due to energy conservation, is partially reflected back into the input bar (*reflected wave*) and partially transmitted through the specimen (*transmitted wave*).

When the transmitted wave reaches the second interface between the specimen and the output bar, it is again partially reflected back and partially transmitted into the output bar. The strain waves traveling in both the input and output bars are recorded using strain gauges mounted on their surfaces.

The position of the strain gauge on the input bar is crucial to ensure that the incident and reflected strain waves are recorded without temporal overlap. Let t_0 denote the time at which the incident wave reaches the input strain gauge. If the speed of sound in the bar material is c_0, and the wavelength of the pulse is λ, then the duration of the incident wave is given by $t_1 - t_0 = \lambda/c_0$.

If x is the distance between the input strain gauge and the interface between the input bar and the specimen, the time required for the incident wave to travel to the interface and return as a reflected wave is $\Delta t^* = 2x/c0$. A necessary condition for the incident and reflected waves to be recorded separately (i.e., without overlapping) is that $2x/c_0 > \lambda/c_0$, which simplifies to: $x > \lambda/2$. It will be shown later that the incident wave wavelength λ is equal to twice the length of the striker.

To investigate the phenomenon of elastic wave propagation along a cylindrical bar, the following considerations are made. Let us consider an infinitesimal element of the bar, having density ρ, with circular cross-section area A and length d*x*. Assuming that only longitudinal strain waves propagate along the bar, the element is subjected to normal stresses (taken as positive in tension) acting on the two circular faces located at positions *x* and *x+dx*, as well as to inertia force.

The dynamic equilibrium of these forces leads to the following equation:

51) $$-\sigma_x(x,t)A + \sigma_x(x+dx,t)A = \rho A dx \frac{\partial^2 u_x(x,t)}{\partial t^2} \rightarrow \frac{\partial \sigma_x}{\partial x} A dx = \rho A dx \frac{\partial^2 u_x(x,t)}{\partial t^2} \rightarrow \frac{\partial \sigma_x}{\partial x} = \rho \frac{\partial^2 u_x(x,t)}{\partial t^2}$$

For linear elastic materials, the normal stress is related to the axial strain by the Hooke's law $\sigma_x = E \varepsilon_x$, and the axial strain is the spatial derivative of the axial displacement u_x. Then, the equation (51) becomes:

52) $$\frac{\partial}{\partial x}\left(\frac{E \partial u_x(x,t)}{\partial x}\right) = \rho \frac{\partial^2 u_x(x,t)}{\partial t^2} \rightarrow E \frac{\partial^2 u_x(x,t)}{\partial x^2} = \rho \frac{\partial^2 u_x(x,t)}{\partial t^2} \rightarrow \frac{\partial^2 u_x(x,t)}{\partial x^2} = \frac{\rho}{E} \frac{\partial^2 u_x(x,t)}{\partial t^2}$$

Equation (52) is the one-dimensional form of the wave equation, where the ratio E/ρ represents the square of the speed of sound for longitudinal waves propagating in a solid medium c_0.

53) $$c_0 = \sqrt{\frac{E}{\rho}}$$

It can be shown that one of the general solutions to the wave equation can be expressed as the sum of two functions, $f(x-c_0t)$ and $g(x+c_0t)$ known as the *traveling wave solution*. Physically, these functions represent two disturbances propagating at speed c_0 in opposite directions along the bar: f travels in the positive x-direction ($x > 0$), while g travels in the negative x-direction.

54) $$u_x(x,t) = f(x - c_0 t) + g(x + c_0 t)$$

As said before, the axial strain is the spatial derivative of the displacement function u_x.

55) $$\varepsilon_{input}(x,t) = \frac{\partial u_x}{\partial x} = \frac{\partial f(x-c_0t)}{\partial (x-c_0t)} \frac{\partial (x-c_0t)}{\partial x} + \frac{\partial g(x+c_0t)}{\partial (x+c_0t)} \frac{\partial (x+c_0t)}{\partial x} = \varepsilon_i(x,t) + \varepsilon_r(x,t)$$

From the traveling wave solution, it follows that the strain wave propagating in the input bar can be interpreted as the superposition of an incident wave (propagating forward) and a reflected wave (traveling backward).

The time derivative of the displacement of the bar section at position x is defined as the *particle velocity*, and it physically represents the local velocity of an infinitesimal volume element of the solid through which the elastic wave is propagating.

56) $$v_{x_{input}}(x,t) = \frac{\partial u_x}{\partial t} = \frac{\partial f(x-c_0t)}{\partial (x-c_0t)}\frac{\partial (x-c_0t)}{\partial t} + \frac{\partial g(x+c_0t)}{\partial (x+c_0t)}\frac{\partial (x+c_0t)}{\partial t} = -c_0\varepsilon_i(x,t) + c_0\varepsilon_r(x,t)$$

Analogous considerations can be extended to the output bar, where only the forward-traveling wave component is taken into account. Then:

57) $$u_{x_{output}}(x,t) = h(x-c_0t)$$

The transmitted wave is:

58) $$\varepsilon_{x_{output}}(x,t) = \frac{\partial h(x-c_0t)}{\partial (x-c_0t)}\frac{\partial (x-c_0t)}{\partial x} = \varepsilon_t(x,t)$$

and the particle velocity along the output bar is:

59) $$v_{output}(x,t) = \frac{\partial h(x-c_0t)}{\partial (x-c_0t)}\frac{\partial (x-c_0t)}{\partial t} = -c_0\,\varepsilon_t(x,t)$$

The particle velocity at a generic section of the input bar, at time t, is the sum of an incident component and a reflected component. The incident particle velocity is:

60) $$v_i(x,t) = -c_0\varepsilon_i(x,t)$$

Recalling the Hooke's law, it is possible to express the incident stress wave as function of the incident particle velocity as follow:

61) $$\varepsilon_i(x,t) = -\frac{1}{c_0}v_i(x,t) \rightarrow \sigma_i(x,t) = -\frac{E}{c_0}v_i(x,t) = -\rho c_0 v_i(x,t)$$

The term ρc_0 is called *specific mechanical impedance*. From equation (61), we can also define the relationship between the input force wave (travelling forward or backward) and the particle velocity as follow:

62) $$F_i(x,t) = -\rho_{in} c_{0_{in}} A_{in} v_i(x,t)$$

By extending these considerations also to the reflected and transmitted component of the particle velocity, then the reflected and transmitted force waves are:

63) $$F_r(x,t) = \rho_{in} c_{0_{in}} A_{in} v_r(x,t) \quad and \quad F_t(x,t) = -\rho_{out} c_{0_{out}} A_{out} v_t(x,t)$$

where $\rho c_0 A = Z$ is the mechanical impedance of the bar. In general, if the bars are made by different materials and/or have different cross section, then the fraction of the incident wave that is partially reflected and transmitted at the interface between two cylindrical bars, depends on the mismatch between the mechanical impedances of the two bars.

Let consider two cylindrical bars, A (input) and B (output), made of different materials and with different cross-section areas, placed in contact. At each instant, the interface between A and B must satisfy the conditions of zero relative velocity, i.e., $v_{input} - v_{output} = 0$, and force equilibrium, i.e., $F_{input} = F_{output}$. Then,

64) $$\begin{cases} v_i(x^*,t) + v_r(x^*,t) = v_t(x^*,t) \\ -Z_A v_i(x^*,t) + Z_A v_r(x^*,t) = -Z_B v_t(x^*,t) \end{cases}$$

From the system of equations (64), two ratios can be determined: the ratio between the transmitted and the incident particle velocity (*transmission coefficient*), and the ratio between the reflected and the incident particle velocity (*reflection coefficient*):

65) $$\begin{cases} \frac{v_r}{v_i} = R = \frac{Z_A - Z_B}{Z_A + Z_B} \\ \frac{v_t}{v_i} = T = 2\frac{Z_A}{Z_A + Z_B} \end{cases}$$

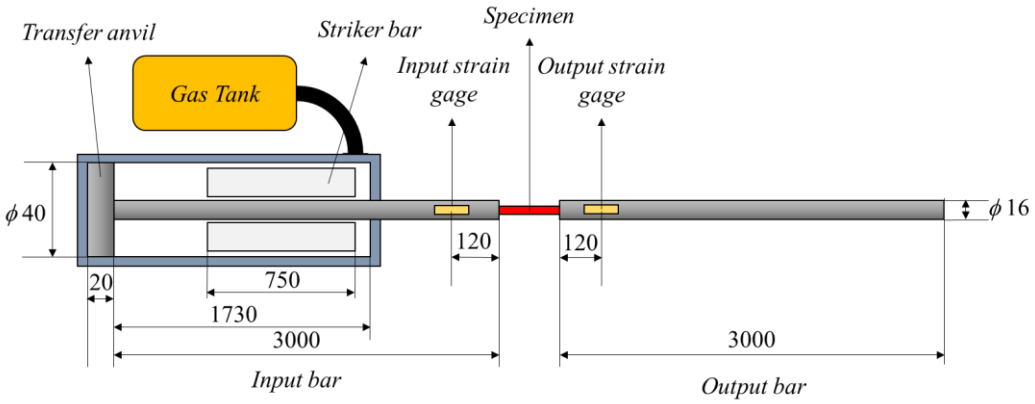


Figure 98: Scheme of the Split Hopkinson Tension Bar used for the present work, at the INATECH laboratories (University of Freiburg).

The generation of an incident deformation wave, in a system such as the one previously described and illustrated in the Figure 98 occurs when the striker impacts the transfer flange of the input bar. When a striker impacts a cylindrical bar, assuming they have the same cross-section, a compressive wave is generated and travels within the striker at the speed of sound. Once it reaches the free end of the striker, it is reflected as a tensile wave. For the Hopkinson bar configuration shown in the Figure 98, the particle velocity imparted to the input bar is approximately equal to half the velocity of the striker. The resulting wave in the input bar has a wavelength equal to twice the length of the striker.

7.1.2 Dynamic tensile tests at high strain rates: experimental setup

The experimental setup shown in Figure 98 was used to test Polycarbonate specimens at high strain rates. The specimens used are shown in Figure 99, with a nominal gage length of 8.5 mm and a diameter of 6 mm. Given the engineering strain rate targeted for the test, the choice of the gage length L_0 must be made considering that the larger this dimension is, the higher the required striker velocity (and consequently the tank pressure) for achieving the engineering strain rate. Then, the nominal gage length of the specimens was set as small as possible in order to ensure a pre-necking uniaxial stress state and to operate with tank pressures on the order of a few bar.

The specimens were machined with M8 threaded shoulders to allow them to be screwed into the bars.



Figure 99: M8 Threaded Polycarbonate specimen used for dynamic tests.

The bars used in the present work are made of Ergal aluminum (Aluminum 7075-T6), with an elastic modulus of 71700 MPa and a density of 2810 kg/m³. The speed of sound in the material is therefore equal to 5051 m/s.

The striker is made of polyoxymethylene (POM), with an approximate density of 1400 kg/m³ and an elastic modulus of 3200 MPa. The speed of longitudinal waves in this material is approximately 1500 m/s. Given the striker length of 750 mm, and based on the considerations discussed so far, the duration of the incident wave traveling along the input bar is equal to:

66) $$\tau_{incident} = \frac{\lambda}{c_{0_{striker}}} = \frac{2L_{striker}}{c_{0_{striker}}} \cong 1\ ms$$

If a test is conducted at a strain rate of 1000 s^{-1}, knowing that the specimens tested under quasi-static conditions exhibit an engineering fracture strain of approximately 1.5, the duration of a tensile test on this material would be:

67) $$\Delta t_{experiment} = \frac{elongation\ at\ break}{nominal\ strain\ rate} = \frac{1.5}{1000} s = 1.5\ ms > \tau_{incident}$$

The estimated duration of a complete experiment (up to fracture) at a strain rate of 1000 s^{-1} is therefore longer than the duration of the incident wave. The maximum engineering strain achievable with this experimental setup at this strain rate is approximately 100% (corresponding to a maximum logarithmic strain of 0.7). Equivalently, in order to fracture the specimen, strain rates greater than 1500 s^{-1} would be required.

The nominal strain rate to be imposed on the specimen is equal to the relative particle velocity between the specimen shoulders divided by its gage length L_0:

68) $$\frac{d\varepsilon_{nom}}{dt} = \frac{v_{in} - v_{out}}{L_0} = \frac{c_{0_{bar}}}{L_0}(-\varepsilon_i + \varepsilon_r + \varepsilon_t)$$

To set the maximum nominal strain rate achievable during the test, one can, as a first approximation, neglect v_{out} and adjust v_{in} based on the impact velocity of the striker, which in turn depends on the gas pressure inside the tank. This assessment was performed through a series of tests (*plain pulse tests*) in which the two bars were connected by a threaded aluminum rod, 260 mm in length and 16 mm in diameter. The output bar was clamped at its right end, and the striker was launched against the transfer flange at different gas pressure levels.

At each impact, the force wave (in theory, entirely incident) propagating along the bar assembly was measured using two strain gauges placed respectively on the incident and transmitted bars (see Figure 98). As shown in the graph in Figure 100, the incident wave is partially reflected and transmitted due to the presence of the intermediate aluminum rod.

Although, in theory, there should be no impedance mismatch at the bar/bar interface, the threaded connection induces local mechanical impedance mismatches that cause this phenomenon.

The strain gauge mounted on the input bar, located 120 mm from the interface with the specimen (or with the additional rod in this case), records the superposition of the incident and reflected waves. The strain gauge on the output bar, also located 120 mm from its interface with the specimen, records the transmitted wave.

When the forces acting on the left and right ends of the specimen (or added bar segment) are balanced, the sum of the incident and reflected waves equals the transmitted wave.

Therefore, during a *plain pulse test*, the pressure reached inside the tank for pushing the striker can be correlated with the peak amplitude of the transmitted force wave. According to the eqs. (62) and (63), the amplitude of the force wave is related to the particle velocity by the mechanical impedance. Then, there is a direct relationship between the gas pressure, the particle velocity and -then- the nominal strain rate.

The results of the plain pulse tests area reported in the following Table 15:

Test Number	*Tank pressure [bar]*	Force Amplitude [N]	Particle velocity [m/s]	Striker velocity [m/s]	*Estimated maximum nominal strain rate [s-1]*
1	0.5	6000	2.10	4.20	247
2	0.5	6500	2.28	4.56	268
3	0.7	9200	3.22	6.44	379
4	0.7	9050	3.17	6.34	373
5	1	12500	4.38	8.76	515
6	1	12900	4.52	9.04	531

Table 15: Experimental results of the plain pulse tests.

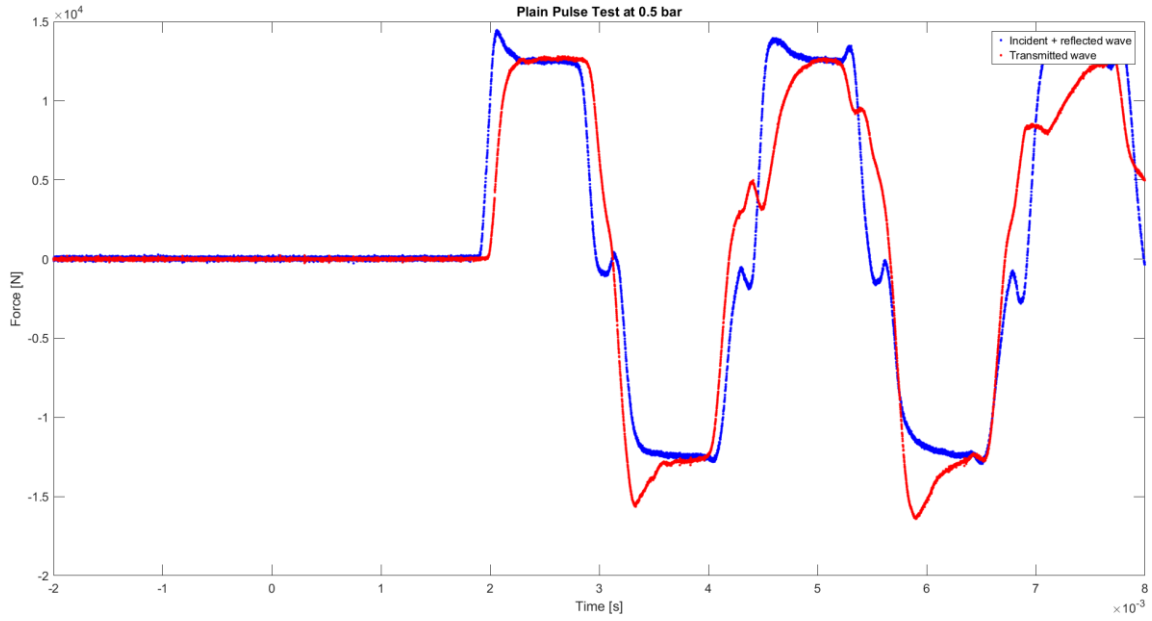


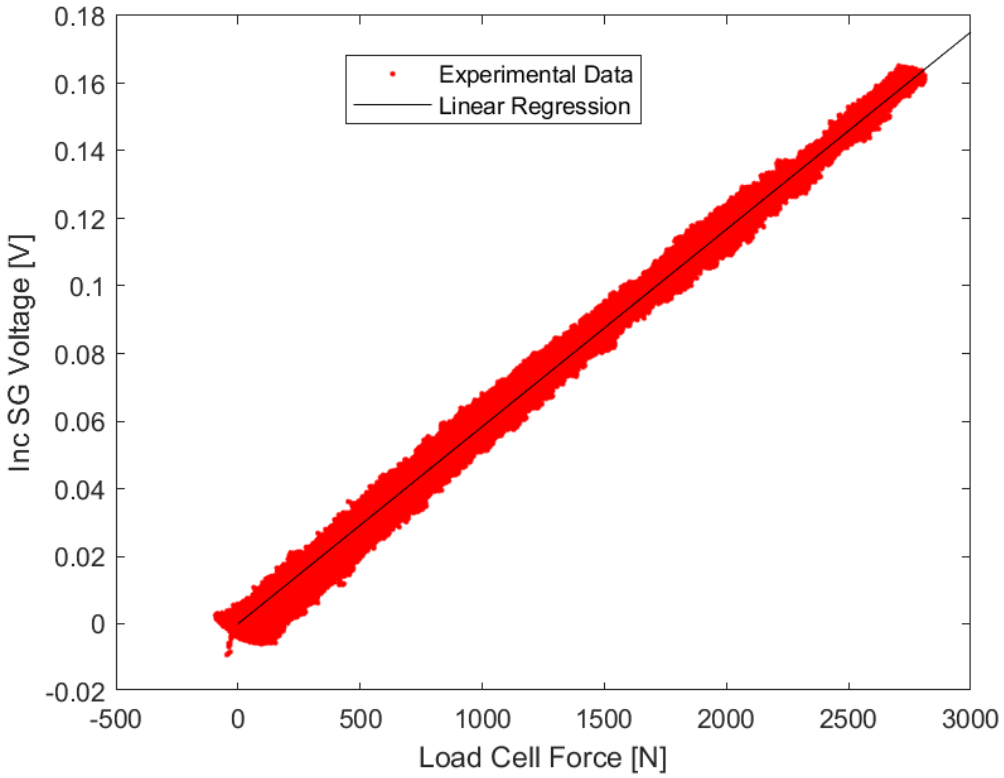
Figure 100: Force waves measurements during a plain pulse test.

From the plain pulse test, it is possible to derive the relationship (in this case, linear) between the maximum strain rate achievable during the test and the pressure to be set in the tank. With this system, it is possible to vary the pressure up to a maximum of 2 bar (corresponding to a maximum strain rate of 1000 s^{-1}). The tests were conducted at a nominal pressure of approximately 1.8 bar, corresponding to a nominal strain rate of about 900 s^{-1}.

As previously mentioned, the elastic deformation waves traveling in the input and output bars were acquired using strain gauges. To measure the strain on a specific section of the bar, a pair of

strain gauges must be placed in a diagonal arrangement on a Wheatstone bridge in order to cancel out axial strain measurements caused by bending.

The strain gauges were attached to the bar surfaces, after careful cleaning, using a cyanoacrylate adhesive. Once installed, quasi-static loading tests were carried out on the bars to determine their sensitivity factor in mV/N. The bars were connected in series through a 10 kN load cell, and both the force signal and the amplified electrical signals from the strain gauges were recorded. By plotting the amplified electrical signal of each strain gauge as a function of the force reading from the reference load cell, the calibration curve of the strain gauges was obtained. If the calibration curve is linear, its slope represents the sensitivity factor K of each strain gauge.



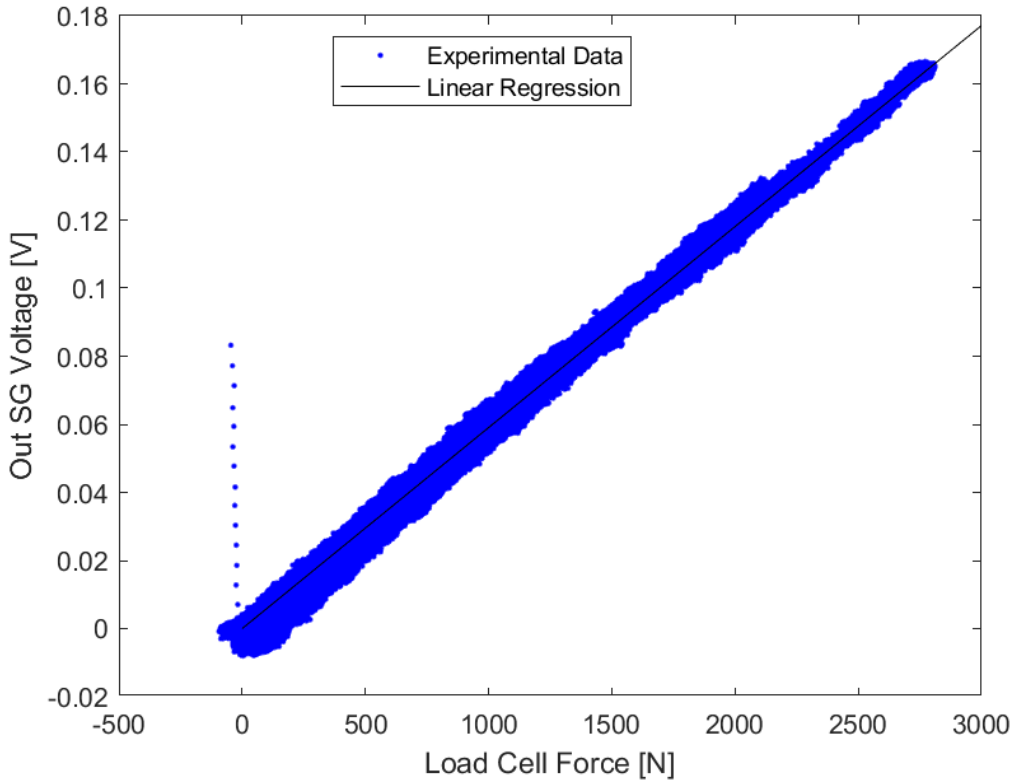


Figure 101: Calibration curves of the strain gages: Input strain gage (on the top); Output strain gage (on the bottom).

For the input strain gage, the K factor is K_{inc}= 6.158 x 10^{-5} V/N = 0.06158 mV/N, while for the output strain gage, I obtained a value of K equal to K_{out}= 6.228 x 10^{-5} V/N = 0.06228 mV/N.

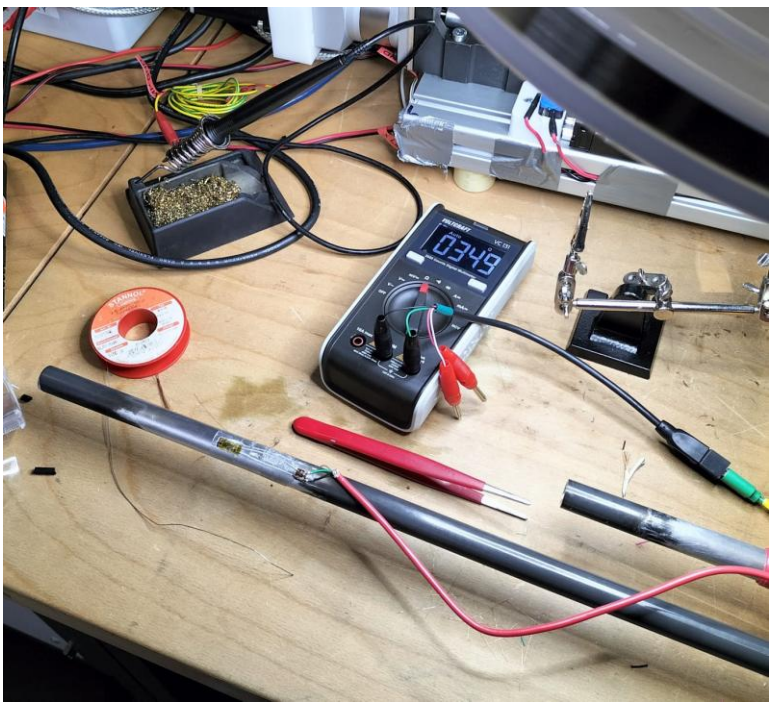


Figure 102: Installation procedure of the strain gages on the bars. Note that the multimeter measures a nominal resistance of the strain gage of 350 Ω.

During the Hopkinson bar tests, both the instantaneous minimum diameter of the specimen and the elongation of the gage length were recorded using a high-speed camera Photron® Fastcam SA-Z.

Two points were marked along the gage length using a marker, spaced approximately 4 mm apart, in order to measure the elongation. The high-speed camera operated with a resolution of 768 × 184 pixels and a frame rate of 120000 fps, with an exposure time of approximately 6.5 µs.

The field of view was adjusted such that, in the undeformed configuration of the specimen, the diameter was represented by approximately 160 pixels. The recordings from the camera and strain gages were triggered by a signal emitted from a photocell activated by the passage of the striker along the cylindrical barrel.

The strain gage acquisition had a duration of 10 ms, with a pre-trigger time of 2 ms. Strain gage data were sampled at a frequency of 10 MHz.

As previously stated, the strain gauges can record the sum of the incident and reflected waves on the input bar and the transmitted wave on the output bar. The instantaneous strain, on the other hand, is acquired directly on the specimen. These two sets of signals must therefore be synchronized by temporally shifting the incident + reflected wave and the transmitted wave so that they are referenced to the specimen.

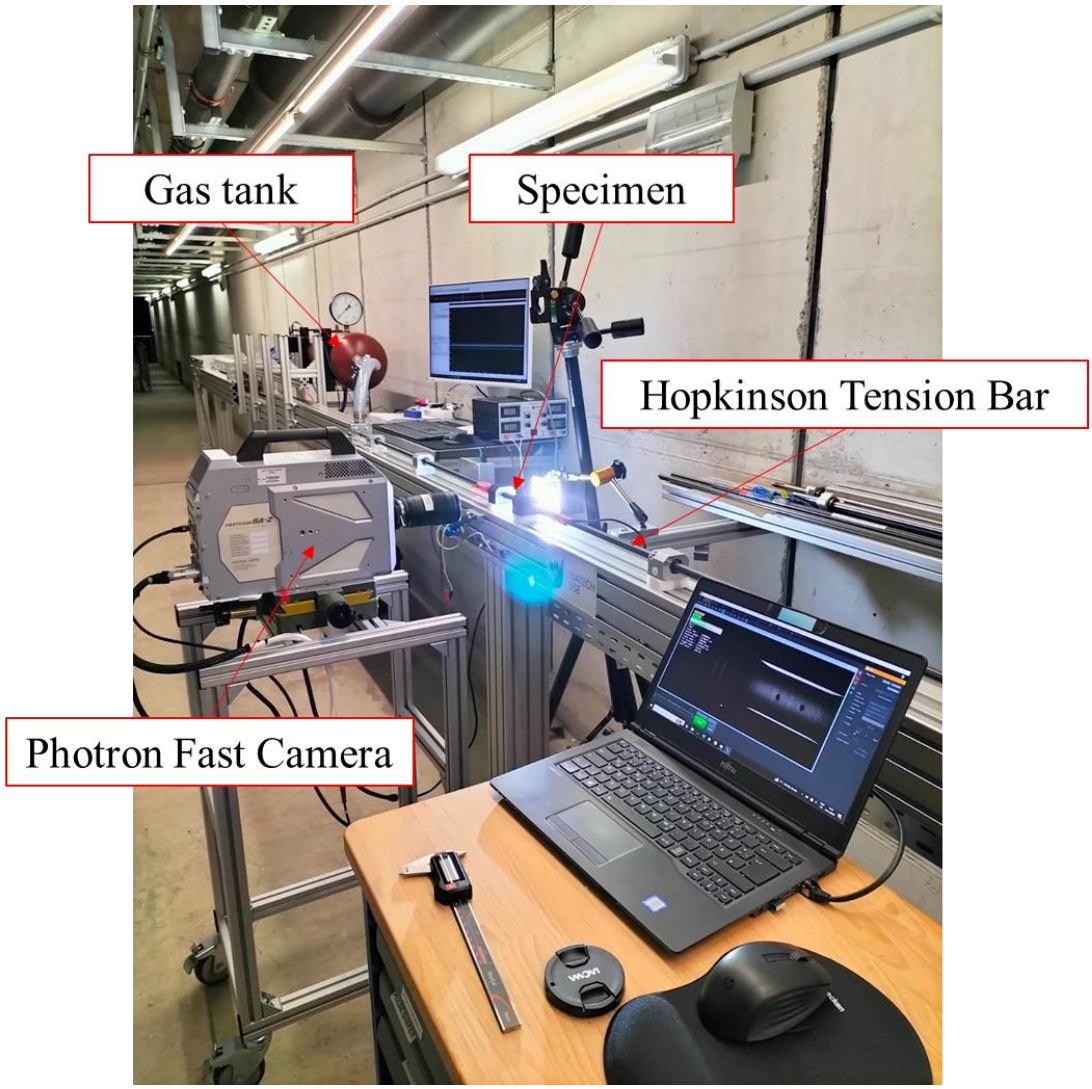


Figure 103: Experimental setup for the high strain rate dynamic tests at 1000 s^{-1}.

The sum of the incident and reflected waves must be shifted by:

$$\Delta t_{i+r} = +\frac{120\ mm}{5051\ \frac{m}{s}} = +23.76\ \mu s$$

while the transmitted wave must be shifted by

$$\Delta t_t = -23.76\ \mu s$$

After this operation, two forces act on the specimen: the input force (also called *2-waves*) and the output one (known as *1-wave*).

69) $F_{in}(t) = E_{bar}A_{bar}(\varepsilon_i(t) + \varepsilon_r(t))$

70) $F_{out}(t) = E_{bar}A_{bar}\varepsilon_t(t)$

The force acting on the center of the specimen (*3-waves*) is assumed to be the mean value of these ones:

$$71) \quad F(t) = \frac{F_{in}(t)+F_{out}(t)}{2} = E_{bar}A_{bar}\frac{\varepsilon_i(t)+\varepsilon_r(t)+\varepsilon_t(t)}{2}$$

When the inertia force acting on the specimen becomes negligible (typically beyond the elastic regime), a condition of dynamic equilibrium is reached in which the input and output forces become equal or, equivalently, the sum of the incident and reflected waves equals the transmitted wave.

As can be seen from the following Figure 104, the dynamic equilibrium of the three waves is reached just after yielding (at approximately 200 µs). As expected, the duration of the incident wave is about 1 ms (970 µs). In the time interval between 200 µs and 970 µs, the three-wave superposition can be considered as the force acting on all sections of the specimen. Similarly, to what was done for quasi-static and intermediate-rate tests, the true stress-strain curves at a nominal strain rate of approximately 1000 s^{-1} are obtained using equations (19) and (20). Three repetitions were done at this strain rate. To reduce noise in the force vs. time data, a centered moving average filter with a window of 10 data points was applied using an Excel spreadsheet. The resulting true curves of the dynamic tests at high strain rate are shown in Figure 105.

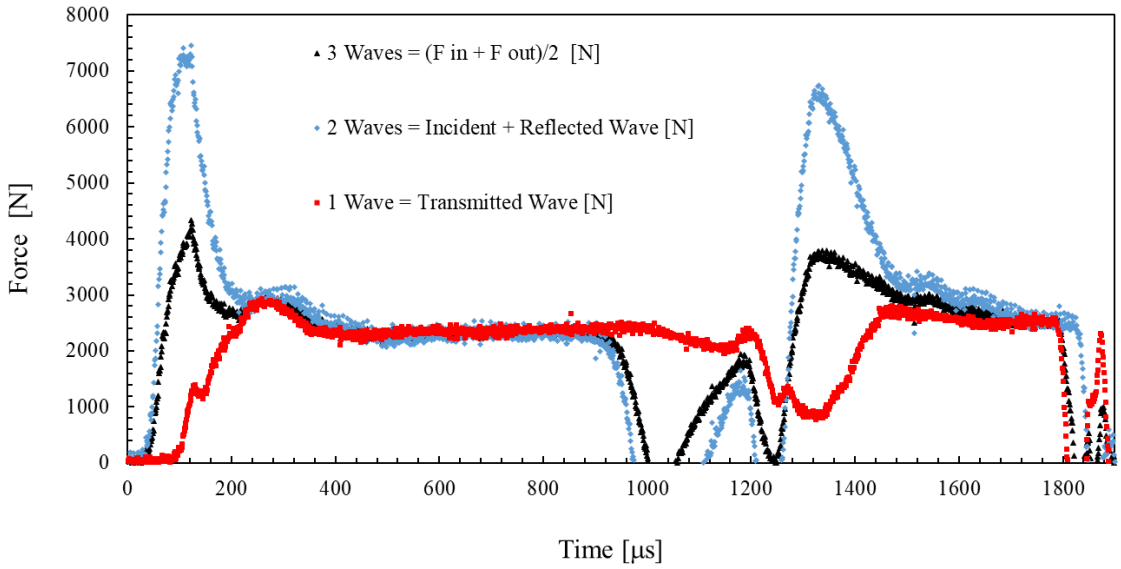


Figure 104: Forces vs time diagram during a tensile test on Polycarbonate round specimen with the Hopkinson bar apparatus.

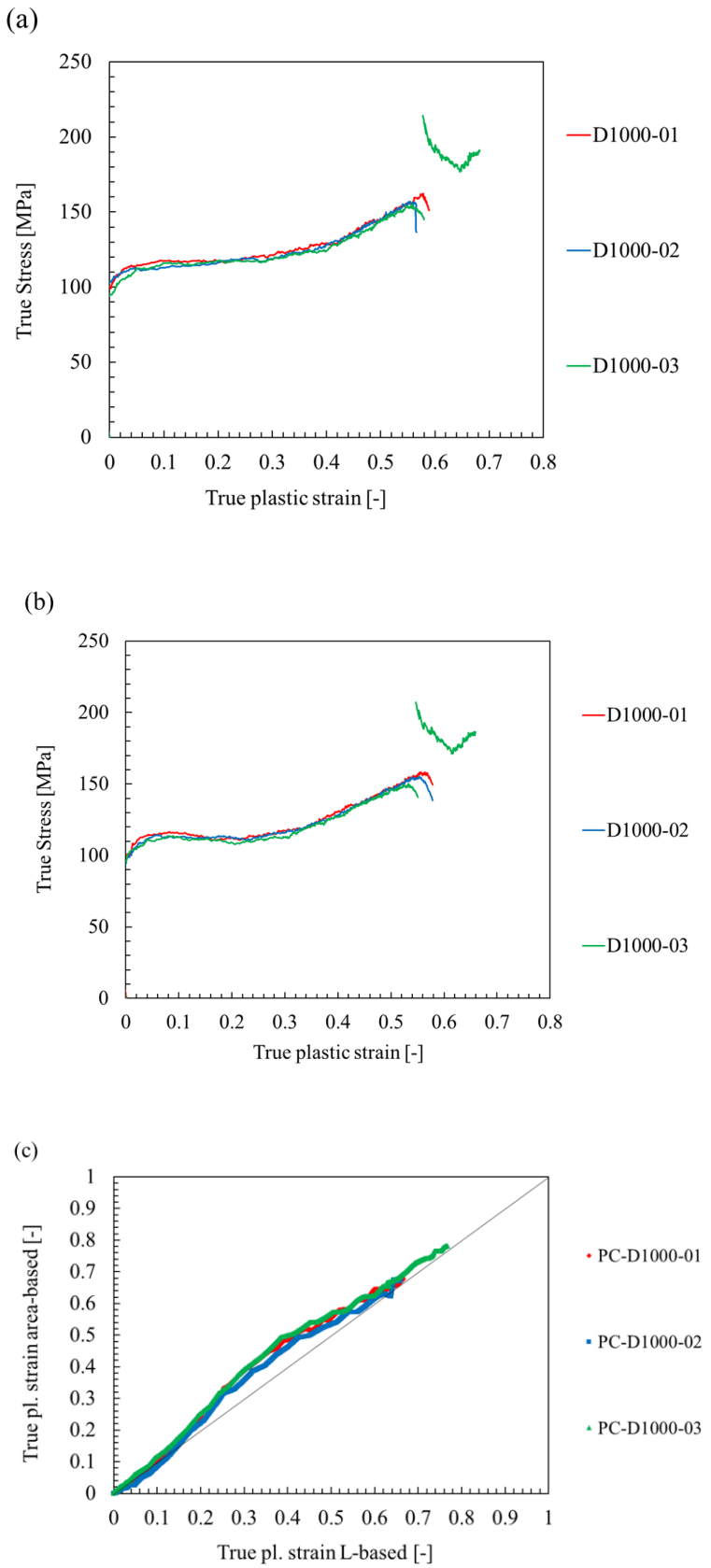


Figure 105: True stress-strain curves for Polycarbonate round specimens at 1000 s^{-1}. a) True stress area-based curve; b) True stress elongation-based curve; c) area-strain vs elongation strain diagram.

7.1.3 Results and discussion

As it is possible to observe from the Figure 106, the mechanical response of Polycarbonate is clearly sensitive to the strain rate effect. At each strain level, the material strength is higher during the dynamic tests compared to the quasi-static one, excepting for the experiments at 0.1 s^{-1}. Indeed, at this nominal strain rate, both the two formulations of the true curve intersect the quasi-static curves at a plastic strain of 0.58, remaining below them up to fracture. Behind this behavior, there could be the effect of thermal softening induced by the material self-heating during the plastic strain history.

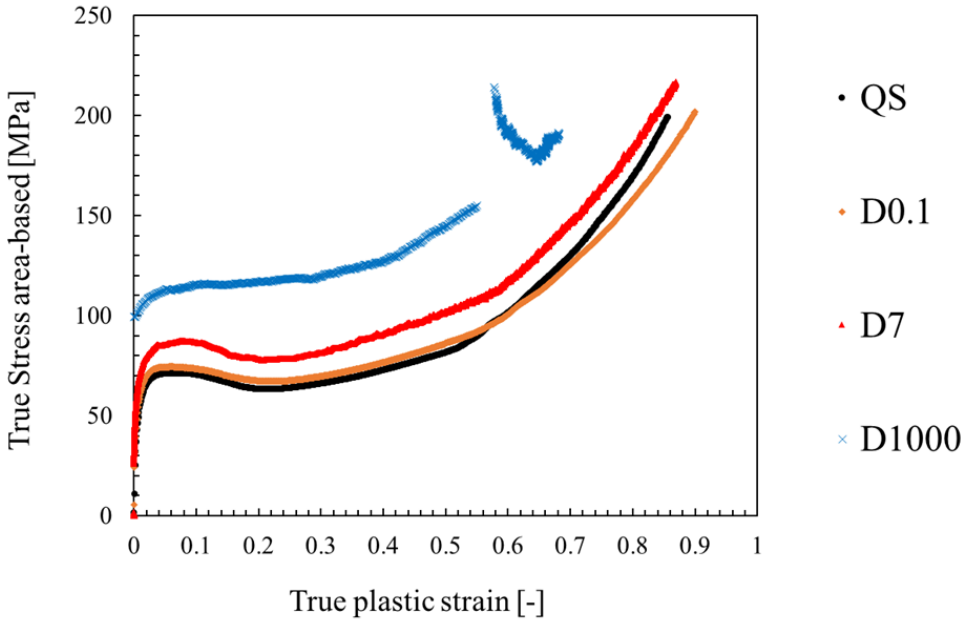
From the temperature measurements performed with the IR camera at 0.1 s^{-1} (see Figure 107), a temperature variation of approximately 35 °C (plastic strain 0.9) is observed at fracture. These results are consistent with those reported in the literature by Mulliken [97] and Song et al. [98]. It should be noted that, in these studies, the temperature measurements were carried out during compression tests on Polycarbonate. In Mulliken's work, measurements were performed using an infrared radiation detector system. On the other hand, the data plotted in the work by Song et al. were obtained from measurements using thermocouples embedded in the compression specimens, at a strain rate higher than 0.1 s^{-1} but of the same order of magnitude. Assuming that the response of Polycarbonate in compression (in terms of the material constitutive curve) is approximately the same as in tension, then the comparison among these three data sets is meaningful. A temperature increasing of 35 °C in this material could explain why, although in the strain range between 0.6 and 0.9 the strain rate of the 0.1 s^{-1} test is constant and higher than that of the quasi-static test (see Figure 108), the fact that the true stress curve at 0.1 s^{-1} lies below the corresponding quasi-static must be attributed to the phenomenon of thermal softening.

At the onset of necking (defined by the condition $d\sigma/d\varepsilon = \sigma$), the stress values at different nominal strain rates are: 70.16 MPa (0.01 s^{-1}); 73.8 MPa (0.1 s^{-1}); 85.1 MPa (7 s^{-1}); and 110.9 MPa (1000 s^{-1}). The corresponding strain values at necking are: 0.035 (0.01 s^{-1}); 0.038 (0.1 s^{-1}); 0.040 (7 s^{-1}); and 0.048 (1000 s^{-1}). It is, therefore, observed that the higher is the strain rate, the greater is the strain at which necking initiates. This phenomenon was already observed and explained in the work of Mirone et al. [95] with reference to a structural steel AISI 304.

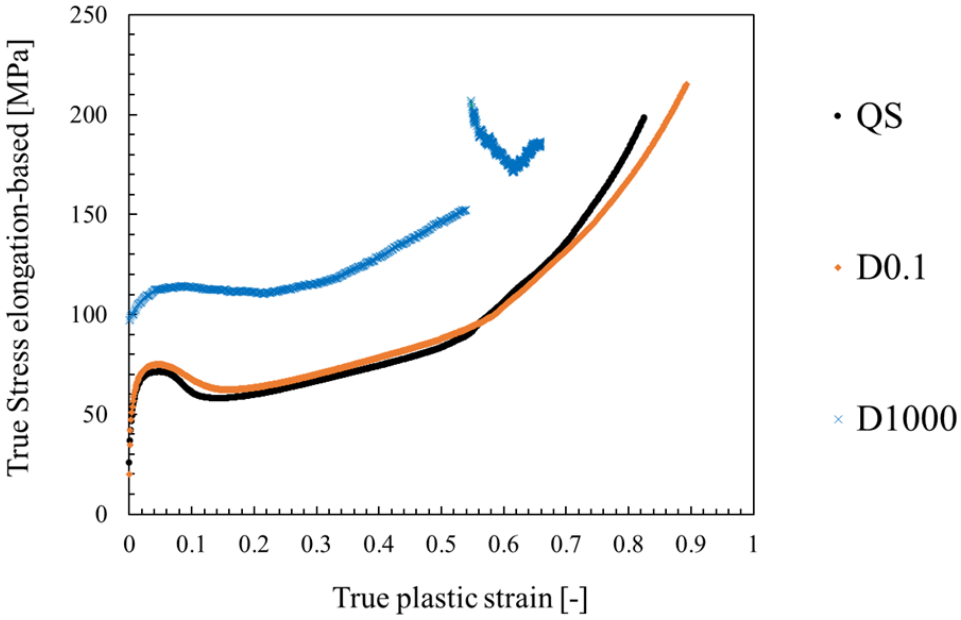
In the area-based true curve at 1000 s^{-1}, it can be seen that the post-necking softening is nearly absent. This phenomenon may be related to the fact that at high strain rates the polymeric chains do not have sufficient time to relax during necking localization. For the third tests at 1000 s^{-1}, the true curves are extended beyond 0.6 plastic strain (Figure 105). Indeed, in this particular test, after the incident wave ended, a compressive wave reached the specimen but did not further plasticize it,

followed by a second tensile reverberation wave that increased the specimen elongation. In the other two tests, instead, the compressive wave that arrived after the incident tensile wave was strong enough to induce buckling instability, causing the bending of the specimen.

(a)



(b)



(c)

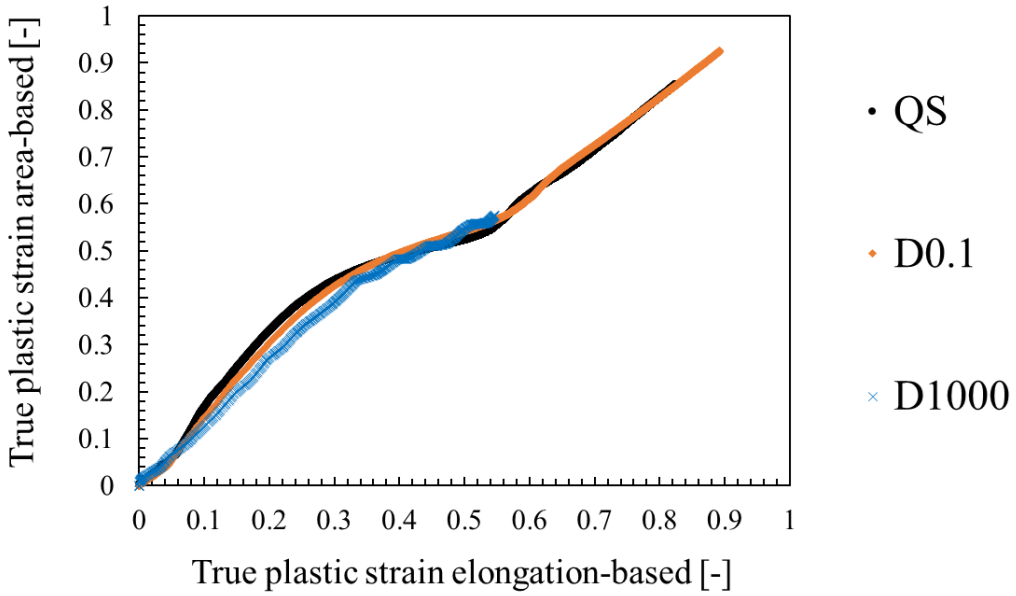


Figure 106: Quasi-static and dynamic response of Polycarbonate: a) true stress area-based curve; b) true stress elongation-based curve; c) area-based strain vs elongation-based strain.

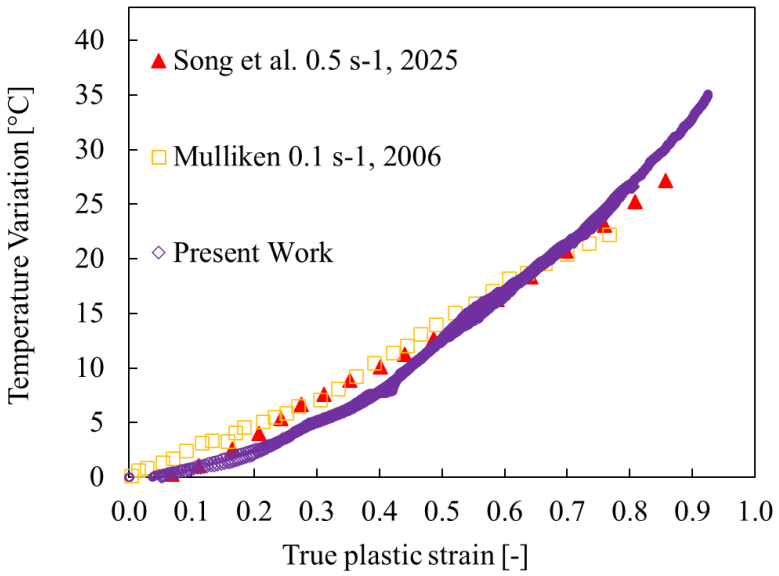


Figure 107: Temperature rising during the tensile tests at nominal strain rate of 0.1 s^{-1}. Comparison with other experimental data derived from compression tests on Polycarbonate.

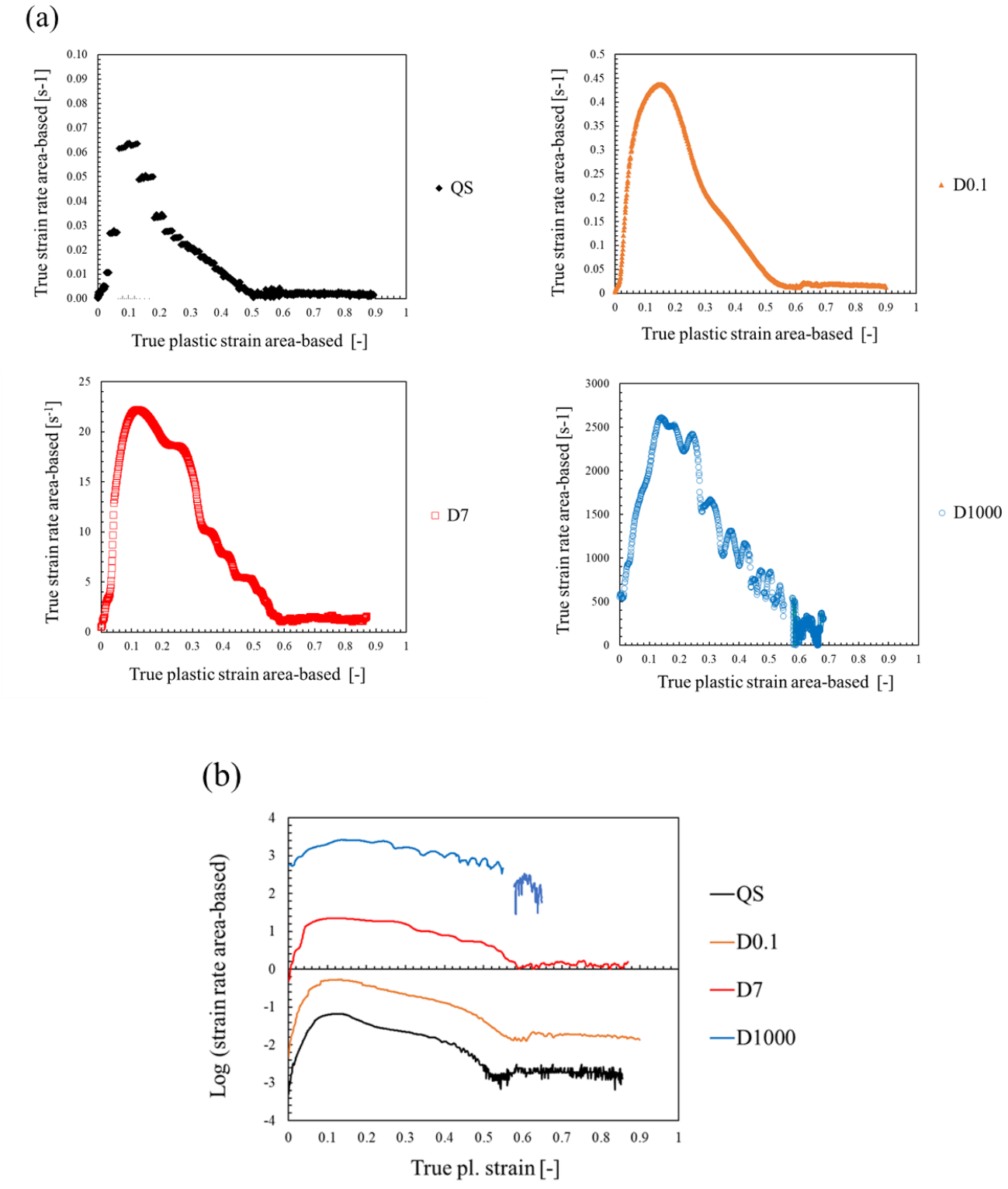


Figure 108: Area-based strain rate histories: linear scale a) and logarithmic scale b) for each tensile test.

From the area-strain vs. elongation-strain plot shown in Figure 106 c), it is clearly observed that, as the nominal strain rate increases, the tendency of the material to localize during necking decreases for the same elongation. For instance, at an elongation strain of 0.20, the corresponding area strain is

approximately 0.33 at a nominal strain rate of 0.01 s^{-1}, 0.30 at 0.1 s^{-1}, and 0.27 at 1000 s^{-1}. This trend is further confirmed by the measurement, at each strain level, of the ratio between the diameter of the necked section and the local radius of curvature of the specimen evaluated at the minimum cross-section, across different nominal strain rates, as shown in Figure 109. The maximum value of the a/R ratio, at a post-necking strain of approximately 0.25, is 0.37 at 0.01 s^{-1}; 0.31 at 7 s^{-1}, and 0.18 at 1000 s^{-1}.

Another important observation is that the strain rate history does not remain constant nor equal to the nominal strain rate imposed to the machine through the crosshead speed control. By evaluating the strain rate measurements derived from the area reduction, it becomes evident that -despite a fixed nominal strain rate set on the testing machine- the local strain rate varies significantly throughout the test. By adopting a base-10 logarithmic scale for the strain rate and constructing a strain rate (area-based) vs. strain (area-based) diagram, a distinctive trend in this parameter can be observed during a tensile test.

Specifically, the local strain rate increases monotonically during the pre-necking phase, reaching approximately the nominal value at the necking strain, indicating that the rise time of the elongation waves is comparable to the time necessary for the specimen to achieve the necking strain. Subsequently, as expected, it continues to increase during the initial stage of strain localization, reaching a peak at strain levels ranging from approximately 0.12 (in the quasi-static test) to 0.17 (in the high-rate D1000 test). Once this peak is reached, the local strain rate begins to decrease and eventually stabilizes around the strain level corresponding to the propagation phase. For strain values exceeding 0.60, the strain rate can be considered stabilized and nearly constant in all tests up to failure.

Interestingly, the stabilized strain rate value in the final phase corresponds to approximately one-fifth of the nominal strain rate. That is, 0.002 s^{-1} for the 0.01 s^{-1} test, 0.02 s^{-1} for the 0.1 s^{-1} test, 1.4 s^{-1} for the 7 s^{-1} test, and 180 s^{-1} for the 1000 s^{-1} test. The maximum local strain rate reached in each test is as follows: 0.065 s^{-1} (quasi-static test), 0.50 s^{-1} (D0.1), 22.4 s^{-1} (D7), and 2500 s^{-1} (D1000).

Therefore, the ratio between the peak local strain rate and the nominal imposed strain rate decreases as the test speed increases. In the quasi-static test, the local strain rate reaches a value approximately seven times greater than the nominal one, whereas in the D1000 test, the peak strain rate is only 2.5 times the nominal value. This observation, combined with the previously discussed findings on the area-strain vs. elongation-strain diagram and curvature measurements, confirms that the visco-plastic behavior of Polycarbonate at high strain rates tends to delay the onset of necking, while also reducing and slowing down its localization.

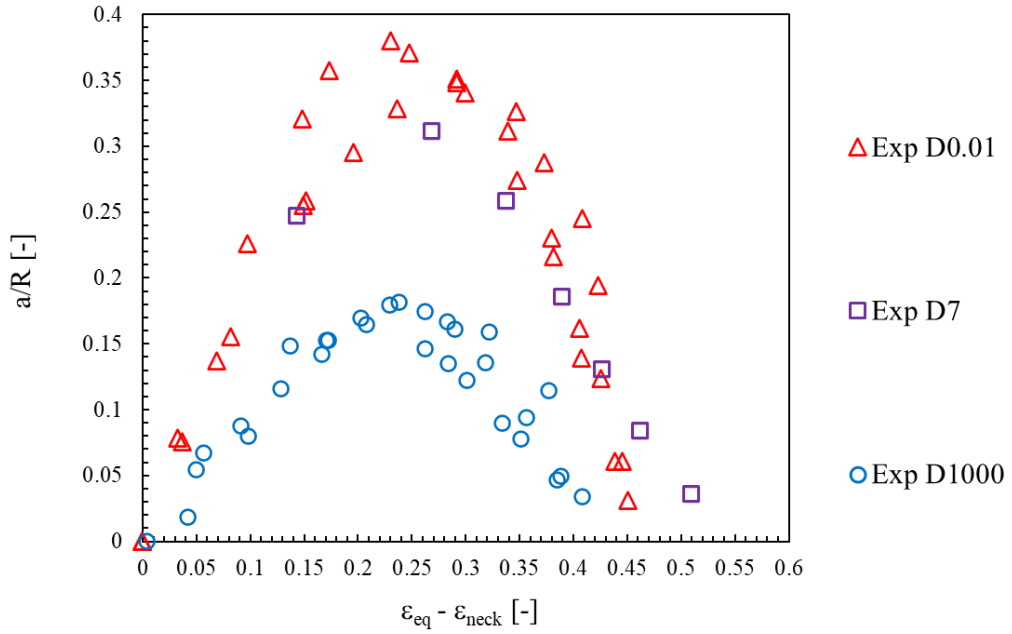


Figure 109: Measurements of the ratio diameter/necking radius of curvature in the post-necking regime, at different nominal strain rates.

7.2 Conclusions

In the present chapter, the experimental results of dynamic tensile tests on round Polycarbonate specimens, at low (0.1 s^{-1}), intermediate (7 s^{-1}), and high (1000 s^{-1}) strain rates, were presented. From the true stress–strain curves obtained from area-based and elongation-based measurements, it was observed that the material is strain-rate sensitive, exhibiting an increase in strength with increasing strain rate. By comparing the two true stress–strain curves derived from area reduction at 0.1 s^{-1} and under quasi-static conditions, it was found that, in the post-necking propagation stage (strains greater than approximately 0.55), the former curve intersects and remains below the latter, despite the higher applied strain rate. This phenomenon is associated with the temperature rising inside the specimen due to the dissipation of plastic work into heat.

Temperature measurements performed by means of an infrared (IR) camera, at a nominal strain rate of 0.1 s^{-1}, revealed a heating of approximately 35 °C before failure. These results highlight the combined influence of temperature and strain rate on the tensile response of Polycarbonate. Increasing the strain rate tends to strengthen the material, delaying its softening after necking, whereas the adiabatic heating effect tends to soften the material at large plastic strains.

Another important observation arising from this study is that, although the nominal strain rate (elongation-rate) was controlled and constant for all tests, the local strain rate (derived from diameter measurements) was found to vary significantly with plastic strain during the test. The local strain rate initially increases during the early stage of plastic deformation. At the onset of necking, it reaches a value close to the nominal strain rate, after which it continues to grow until reaching a maximum at approximately 0.15–0.18 plastic strain. Subsequently, although the necking section continues to contract, the localization rate slows down and stabilizes at a value about one-fifth of the nominal elongation-rate during the post-necking propagation stage. This latter stage of the material's lifetime can therefore be regarded as occurring at an approximately constant strain rate.

From the strain-rate measurements, the area-based strain vs. elongation-based strain diagram, and from the curvature analyses of the necking section, it was also observed that the material tends to localize less during necking as the strain rate increases. This phenomenon is most likely related to the shorter time available for the polymer chains to relax and uncoil during the softening phase of the material.

Chapter 8: Mechanical characterization of Polycarbonate at low, intermediate, and high strain rates: combined rate-temperature effect on the post-necking plasticity

To characterize the mechanical response of Polycarbonate at low, intermediate, and high strain rates, the methodology proposed by Mirone et al. in their work [95] was adopted. As previously discussed, the experimental true stress-strain curves of Polycarbonate are affected by a combined effect of strain rate and temperature. Nevertheless, for each nominal strain rate, it is theoretically possible to depurate the effect of the average stress triaxiality across the minimum cross-section from the true stress area-based curves, in order to obtain the corresponding dynamic flow curves, according to eq. (72).

$$72) \quad \sigma_{eq}\left(\varepsilon_{True}, \frac{d\varepsilon_{True}}{dt}, T\right) = \sigma_{True}\left(\varepsilon_{True}, \frac{d\varepsilon_{True}}{dt}, T\right) * Correction(\varepsilon_{True} - \varepsilon_{Neck})$$

Starting from the curvature measurements of the necking section performed for each test, and by applying Bridgman's theory (with Siebel's correction for simplicity), the experimental true curves from dynamic tests can be corrected in the post-necking regime. The resulting "fixed" flow curves are associated to the nominal strain rate of the corresponding test, although such flow curves actually correspond to complex strain rate and temperature histories taking place in the specimen, for the reasons already discussed before. The "fixed" dynamic flow curves are firstly validated here through dynamic FEM simulations where the flow stress is only made dependent on the plastic strain, with no dependence on the strain rate variability nor on the temperature histories actually occurring during tensile tests.

Regardless of the strain rate and temperature history, before the onset of necking and after the completion of neck propagation, the specimen has a straight cylindrical shape, with a uniaxial stress state within the gage length and uniform strain distributions. This implies that, for each nominal strain rate, the experimental true curve coincides with the flow curve for strain values below approximately 0.05 (before necking onset) and above 0.55 (after complete propagation). Within the strain range between these two regions the two curves deviate to each other, with a gap that depends on the evolution of average triaxiality across the section throughout the deformation history.

The "fixed" dynamic flow curves, from the depuration of the triaxiality effect, are shown in the following figure and compared with the corresponding experimental true curves.

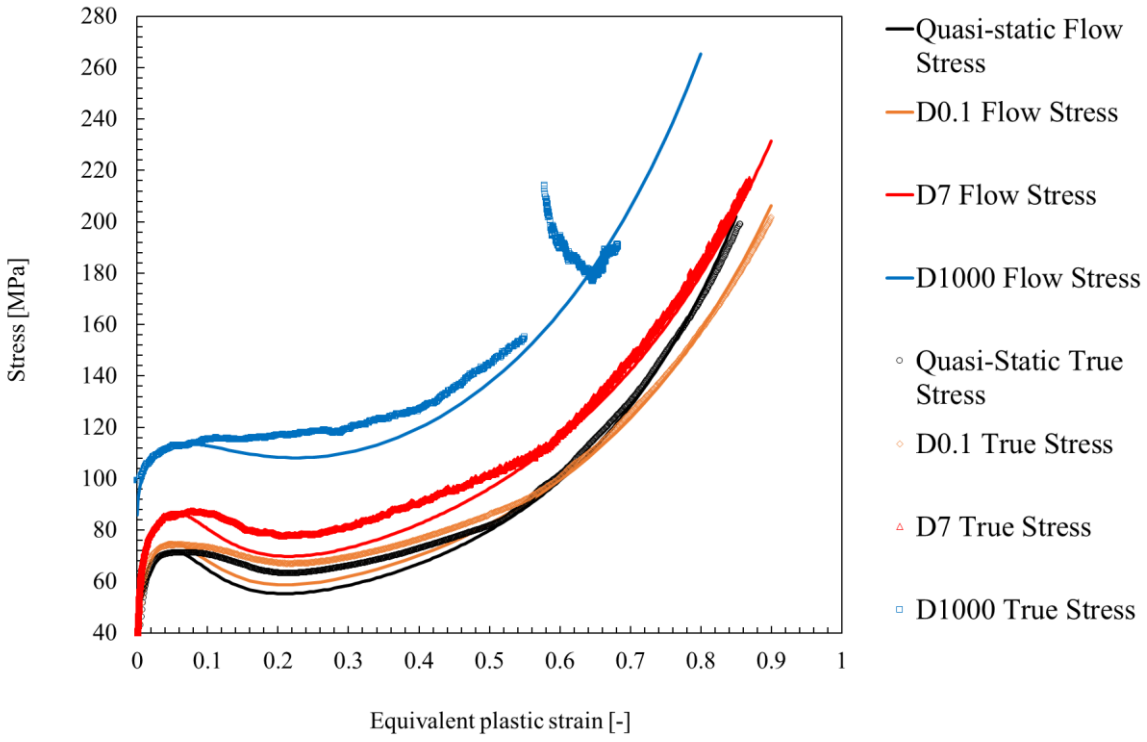


Figure 110: Static and dynamic "fixed" flow stress curves of Polycarbonate compared with the corresponding true stress curves.

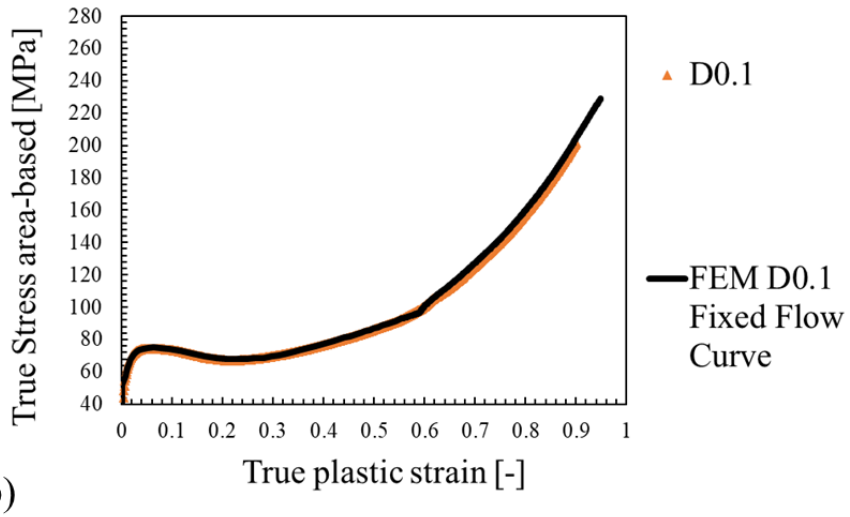
It is worth noting that, due to the gage length-to-diameter ratio close to 1.5 of the round specimens discussed here, the generalized necking correction approach for obtaining the post-necking flow curve (equations 47), 48), and 49)) from a perfectly exponential true curve cannot be used because there is not an "undisturbed" cross section out of the first necking region.

Therefore the flow curves, for each nominal strain rate, are fitted here by the five-parameters equation (43), whose parameters are reported in the following Table 16.

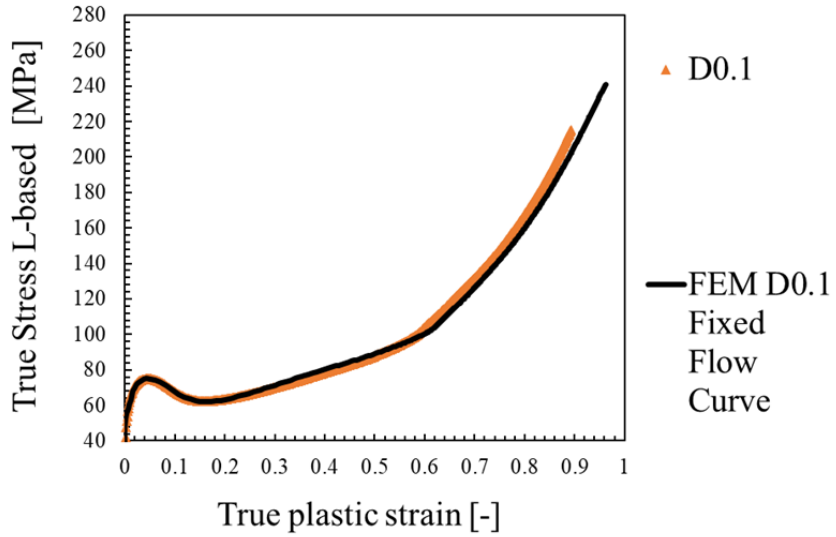
Nominal strain rate [1/s]	*First yield [MPa]*	c_1	c_2	c_3	c_4	c_5
0.1	50.6	1.6995	1.8033	53.2941	1.1617	24.7636
7	59.5	1.6366	1.7659	52.2838	1.1942	23.5806
1000	86	1.7386	1.9509	2.352	0.5286	8.9221

Table 16: Polycarbonate flow curves' parameters for the equation (43), at each nominal strain rate.

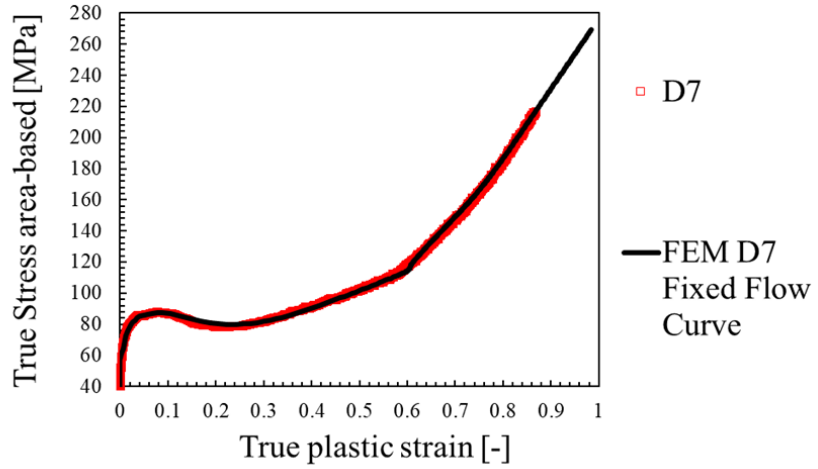
(a)


True Stress area-based [MPa]
280
260
240
220
200
180
160
140
120
100
80
60
40
0
0.1
0.2
0.3
0.4
0.5
0.6
0.7
0.8
0.9
1
True plastic strain [-]
D0.1
FEM D0.1 Fixed Flow Curve

(b)


True Stress L-based [MPa]
280
260
240
220
200
180
160
140
120
100
80
60
40
0
0.1
0.2
0.3
0.4
0.5
0.6
0.7
0.8
0.9
1
True plastic strain [-]
D0.1
FEM D0.1 Fixed Flow Curve

(c)


True Stress area-based [MPa]
280
260
240
220
200
180
160
140
120
100
80
60
40
0
0.1
0.2
0.3
0.4
0.5
0.6
0.7
0.8
0.9
1
True plastic strain [-]
D7
FEM D7 Fixed Flow Curve

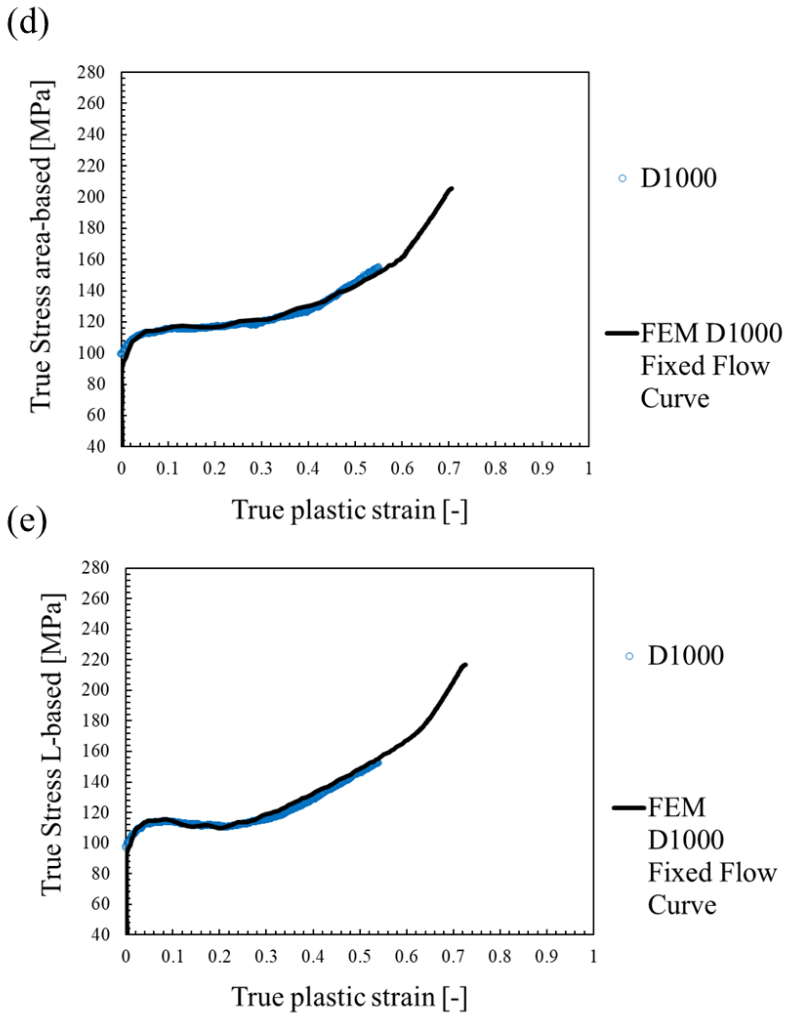


Figure 111: Tensile response of Polycarbonate at low, intermediate, and dynamic strain rates: comparison between the results from FE simulation (black line) with fixed flow curves and experimental data (orange, red, and blue dots).

As visible above, the fixed flow curves already deliver satisfactory results in simulating the experimental tests. However, a further advancement is attempted by identifying the dependence of the flow stress on the single variables strain, strain rate and temperature.

The aim of this section of the thesis is then to decouple the effects of temperature and strain rate, in order to construct a material model valid over the strain rate range from 0.01 s^{-1} to 1000 s^{-1}, fast enough that the temperature histories from the self-heating are assumed to result from adiabatic conversion of plastic work.

A multiplicative material model is considered, according which the flow curve is expressed as the product of three functions: the function describing the quasi-static flow curve at a reference room temperature T_0 (see quasi-static flow curve of Figure 77), a function S accounting for thermal softening, and a function A describing the dynamic amplification.

The function S should not be considered explicitly as a function of temperature T alone, but more generally as a function also of the equivalent plastic strain and strain rate. Indeed, as previously mentioned, the self-heating effect -caused by the conversion of a fraction of the plastic work into heat- is closely related to both of these variables. Thermal softening and strain rate sensitivity are, in general, not uncoupled phenomena.

73) $$\sigma_{eq}(\varepsilon_{True}, \dot{\varepsilon}_{True}, T) = \sigma_{eq}{}_{S,T_0}(\varepsilon_{True})\, S(\varepsilon_{True}, \dot{\varepsilon}_{True}, T)\, A(\varepsilon_{True}, \dot{\varepsilon}_{True})$$

The thermal softening function can be expressed as the sum of two contributions: a static thermal softening S_{stat} and a dynamic one S_{dyn}. The function S_{stat} expresses the ratio between the equivalent stress at temperature $T > T_0$ and that at reference temperature T_0, under the condition of a constant strain rate equal to zero.

To determine S_{stat}, a campaign of quasi-static tensile tests at different temperatures would be required. In the work by G' Sell et al. [96], the authors provide a set of constitutive curves at a fixed strain rate of 10^{-4} s^{-1} and at different prescribed temperatures: 25 °C, 40 °C, 80 °C, 120 °C, and 135 °C (see Figure 112). Polycarbonate exhibits a glass transition temperature of approximately 150 °C, thus it is necessary to remain below this threshold in order to stay within the glassy state of the polymer.

74) $$\sigma_{eq}(\varepsilon_{True}, 0, T) = \sigma_{eq}{}_{S,T_0}(\varepsilon_{True})\, S_{stat}(\varepsilon_{True}, T) \rightarrow S_{stat}(\varepsilon_{True}, T) = \frac{\sigma_{eq}(\varepsilon_{True}, 0, T)}{\sigma_{eq}{}_{S,T_0}(\varepsilon_{True})}$$

From Figure 112, it is clearly observed that, at each strain level, the equivalent stress of the material at $T > T_0$ is lower than that at room temperature T_0. It can also be noted that the strain corresponding to the peak flow stress, as well as the strain at necking, occurs earlier as the imposed temperature increases.

At temperatures higher than T_0, the width of the peak in the true stress-strain curve becomes narrower, in contrast to the effect induced by strain rate on the softening phase.

As also discussed in the work by Mirone et al. [95], earlier onset of necking at higher temperatures is easily demonstrated to be the indicator that thermal softening depends on temperature and plastic strain coupled together, e.g. at high temperature a further dependence on plastic strain arises, which is not present at room temperature.

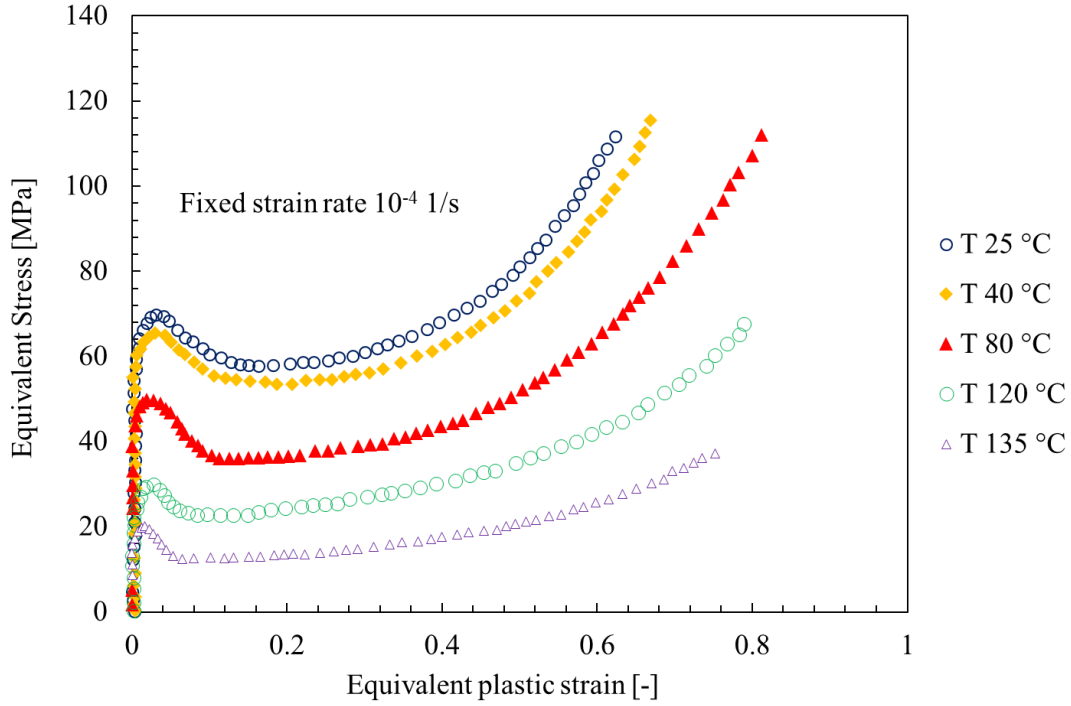


Figure 112: Polycarbonate's material static flow curves at different fixed temperatures (G. Sell et al. [99]*).*

To determine the strain corresponding to the onset of necking, the following Considère's criterion must be recalled:

$$\sigma_{eq}(\varepsilon_{True},0,T) - \frac{d\sigma_{eq}(\varepsilon_{True},0,T)}{d\varepsilon_{eq}} = \sigma_{eq}(\varepsilon_{True},0,T) - \frac{\partial \sigma_{eq_{S,T_0}}(\varepsilon_{True})}{\partial \varepsilon_{eq}} S_{stat}(\varepsilon_{True},T) +$$

$$\sigma_{eq_{S,T_0}}(\varepsilon_{True}) \frac{\partial S(\varepsilon_{True},T)}{\partial \varepsilon_{True}} = 0 \quad \leftrightarrow \quad \frac{1}{\sigma_{eq_{S,T_0}}(\varepsilon_{True})} \frac{\partial \sigma_{eq_{S,T_0}}(\varepsilon_{True})}{\partial \varepsilon_{eq}} + \frac{1}{S_{stat}(\varepsilon_{True},T)} \frac{\partial S(\varepsilon_{True},T)}{\partial \varepsilon_{True}} = 1$$

The ratio between the derivative of the static flow curve at room temperature and the corresponding flow stress is equal to 1 at the room temperature necking strain.

If the static thermal softening function is strictly decreasing with respect to the equivalent strain (i.e., it has a negative partial derivative), then the term $\partial S/\partial \varepsilon$ tends to shift the ratio $\partial \sigma_{s,T0}/\partial \varepsilon$ downward, leading to an earlier onset of the strain corresponding to the necking condition.

The ratios between the flow curves at temperature $T > T_0$ and the corresponding flow curve at room temperature are plotted in the following Figure 113.

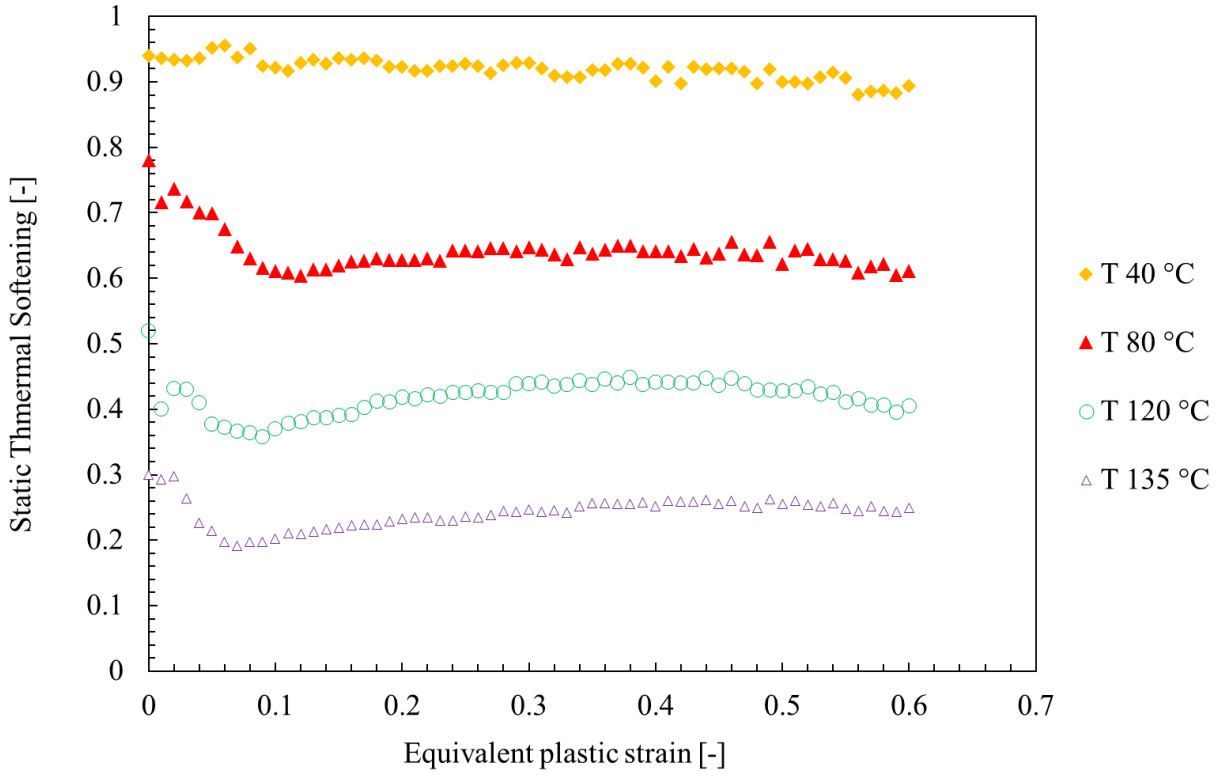


Figure 113: Static thermal softening functions of Polycarbonate at four fixed temperatures (from G' Sell et al. [99]*).*

The dataset shown in Figure 113 clearly demonstrates that thermal softening is, in general, a strain and temperature-dependent phenomenon and behaves as a roughly decreasing function of strain for a given test temperature. It can be observed that between first yield and plastic strains of approximately 0.10 the thermal softening function decreases down to a plateau that then persists up to specimen failure. A two-variables function that can approximate this trend is proposed below:

$$75) \quad S_{stat}(\varepsilon_{True}, T) = S_{\infty}(T) + \left(S_0(T) - S_{\infty}(T)\right) \exp\left(-k(T)\, \varepsilon_{True}\right) \qquad T > 25\ °C$$

where S_∞ is the value of the softening only depending on the temperature, expressed by the fitting law: $S_\infty(T) = 1.1688 - 0.0067\ T$; S_0 is the thermal softening at first yield depending on the temperature alone, too: $S_0(T) = 0.9872 + 0.001\ T - 4\ 10^{-5}\ T^2$, and k is the decay factor temperature-dependent to realize the coupling between strain and temperature effects, expressed by $k(T) = -8.8216 + 0.3503\ T$.

It is noteworthy that the thermal softening due to the adiabatic self-heating in dynamic tests, where temperatures in the range 40-80 °C develop at higher strains than approximately 0.10, can be

approximated by the asymptotic part of the above function, temperature-alone dependent, as summarized below:

76) $$S_{stat}(\varepsilon_{True}, T) \approx S_{\infty}(T) \qquad for \;\; T > 25\,°C, \;\; \varepsilon_{True} > 0.12$$

The initial transitory phase of each dynamic test, roughly ranging from first yield to plastic strain around 0.1, in principle would require the strain-temperature coupling to be modeled too, in order to capture remarkable variations in the whole thermal softening function at constant temperature, and to reproduce the phenomena of necking onset anticipation at higher temperatures. However, at such strain levels the self-heating is still at its earlier stages, so that temperatures are still close to T_0 and the thermal softening functions remains close to unity.

The function expressed by equation (76) is the one generally used in the literature to model the effect of temperature on Polycarbonate. It represents a particular case of a Johnson–Cook like thermal softening function.

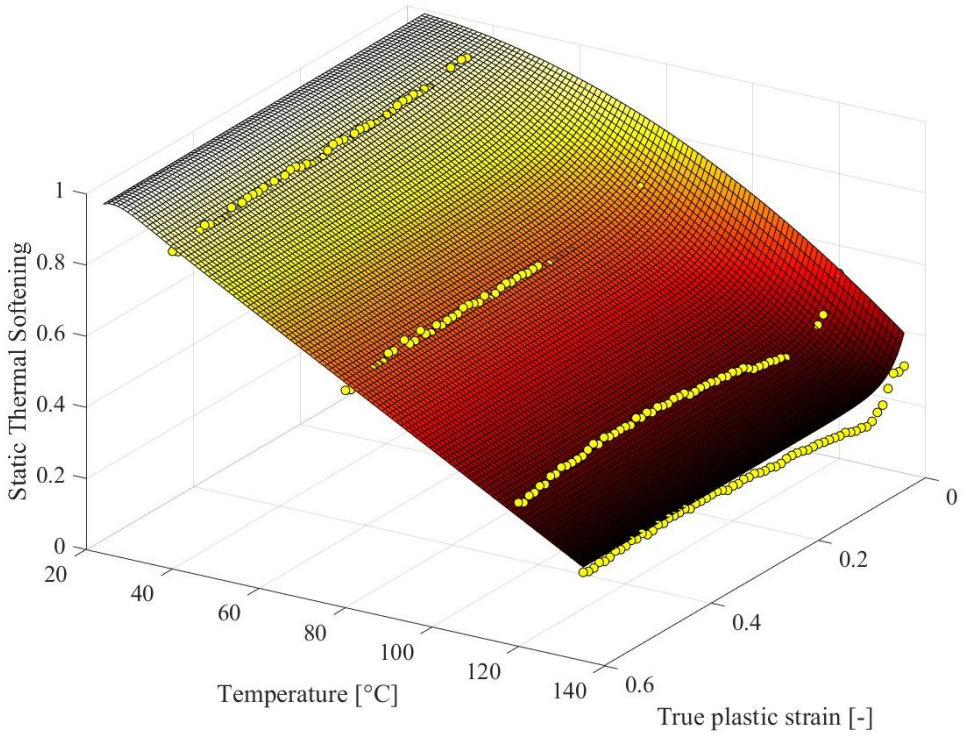


Figure 114: Static thermal softening fitting surface and originating experimental data (yellow dots).

In addition to the static thermal softening, as previously discussed, there may also be a thermal softening component explicitly dependent on both strain rate and temperature, here referred to as

Dynamic Thermal Softening. In fact, the effect of a fixed temperature T on the material's response at a strain rate higher than quasi-static may, in general, differ from the effect of the same temperature under quasi-static conditions. To derive a proper dynamic thermal softening function, one would require tensile tests conducted at a prescribed temperature $T > T_0$, with a true strain rate $d\varepsilon/dt > 10^{-4}$ 1/s held constant throughout the entire experiment.

As already noted, even when the nominal strain rate imposed on the specimen (e.g. the elongation rate) is constant all over a test, the local strain rate history varies significantly, except for the post-propagation strain range (plastic strains between 0.55 and fracture). Since, to the best of the author's knowledge, no flow stress data are currently available in the literature regarding dynamic tensile tests performed at elevated temperatures, the contribution of dynamic thermal softening has been neglected in the present work.

By knowing the effect of temperature on the material's flow curve and by estimating the temperature variation occurring during the tensile tests, it is possible to correct the previously obtained "fixed" flow curves (see Figure 110) from the effect of static thermal softening. This correction allows to reconstruct of the so-called *isothermal flow curves*. These curves represent the material's flow stress, still dependent on the strain rate history, at a constant reference temperature.

To estimate the local temperature rise during a tensile test due to the phenomenon of adiabatic self-heating, it is assumed that a fraction of the plastic work per unit volume is converted into sensible heat:

$$77) \quad \Delta T(\varepsilon_{True}) = \frac{\beta}{\rho c_v} \int_0^{\varepsilon_{True}} \sigma_{eq}\left(\varepsilon_{eq}, \dot{\varepsilon}_{eq}, T\right) d\varepsilon_{eq}$$

where ρ is the material's density assumed 1170 kg/m^3, c_v is the specific heat at constant volume assumed equal to 1300 J/kg K, and β is the Taylor-Quinney coefficient (also known as integral form of TQ coefficient).

The experimental measurement of the Taylor-Quinney coefficient is very challenging, as it requires an accurate determination of the local temperature variation in the specimen during the deformation history.

Temperature measurements are often performed using infrared thermography, since thermocouples would need to be placed directly in contact with the specimen section undergoing necking [100]. For Polycarbonate, available estimates of the Taylor-Quinney coefficient reported in the literature are generally derived from compression tests carried out over a strain rate range between

0.1 s^{-1} and 10^3 s^{-1}. The works of Song et al. [98], Lambros et al. [101], and Shao et al. [102] consistently report that, within this strain rate range, the average Taylor-Quinney coefficient for Polycarbonate falls within the interval 0.50 to 0.60.

The very large difference between the Taylor-Quinney coefficients of metals (TQ close to 1 [100,103]) and Polycarbonate (TQ close to 0.5), might be the expression of the large additional dissipative phenomena occurring in the plastic straining of latter materials, namely the rearrangement-uncoiling-motion of long polymeric chains and the viscoelastic relaxation corresponding to the decreasing phase of the area-based true curve.

From the temperature measurements conducted for this thesis, it was confirmed that the Taylor-Quinney coefficient measured at a nominal strain rate of 0.1 s^{-1} is approximately 0.60. For the modeling of the Polycarbonate behavior at low, medium, and high strain rates developed in this work, a fixed average Taylor-Quinney coefficient of 0.55 was adopted.

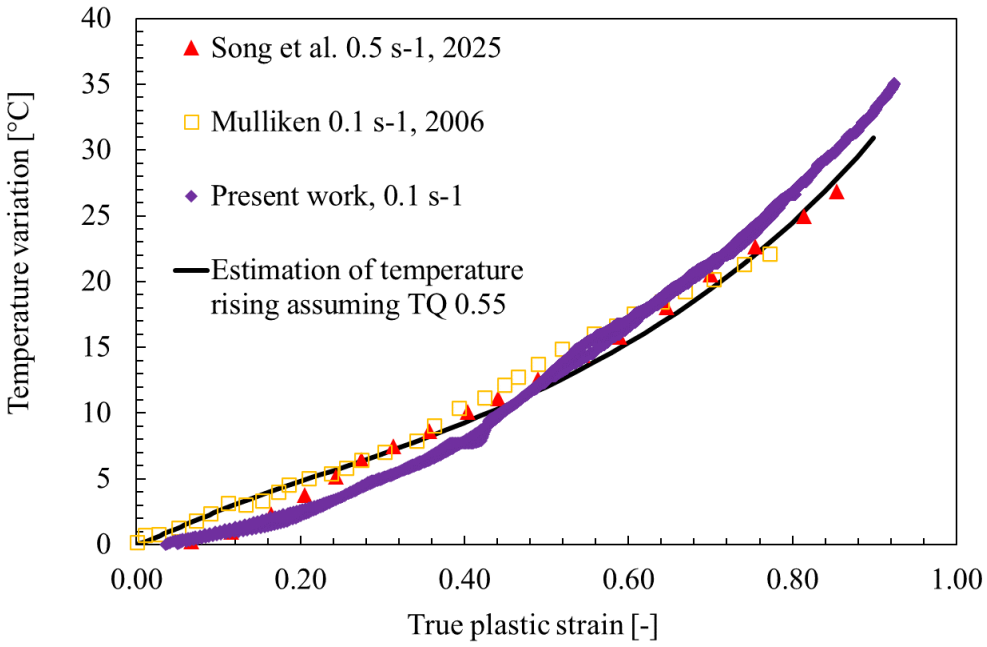


Figure 115: Comparison between the estimation of temperature rising using fixed TQ coefficient of 0.55 and experimental data.

Taking into account the temperature history due to self-heating during each tensile test at a given nominal strain rate, the isothermal flow curves can be derived as follows:

78) $$\sigma_{eq}{}_{T_0}(\varepsilon_{True}, \dot{\varepsilon}_{True}) = \frac{\sigma_{eq}(\varepsilon_{True}, \dot{\varepsilon}_{True}, T)}{S(\varepsilon_{True}, \dot{\varepsilon}_{True}, T)} = \sigma_{eq}{}_{S,T_0}(\varepsilon_{True})\ A(\varepsilon_{True}, \dot{\varepsilon}_{True})$$

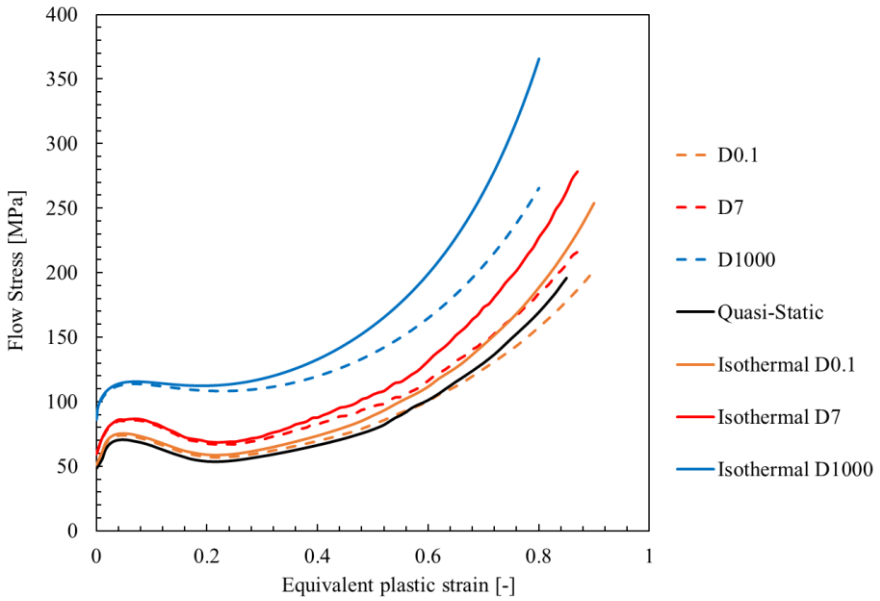


Figure 116: Flow curves at fixed nominal strain rate (dashed lines) and Isothermal flow curves.

The results of the isothermal flow curves, compared with the "fixed" flow curves, are shown in the following graph (Figure 116). From the curves shown, it can be observed that the effect of thermal softening, both at low and high strain rates, becomes significant after a strain of approximately 0.20.

At this stage, for each test at a given nominal strain rate, the local strain rate history as a function of the local strain is known. This allows us to compute the ratio between the dynamic isothermal curve and the corresponding static curve, thus finally obtaining the dynamic amplification function as a function of both strain rate and strain.

By plotting this ratio on a graph where the horizontal axis is the strain rate in logarithmic scale, a very interesting trend emerges. When the strain rate increases during the test (in the strain range between 0 and approximately 0.15), the material experiences the strain rate sensitivity, and the hardening increases progressively with it. The data relative to the dynamic amplification during the increasing of the strain rate follow the trend shown by the solid line in the graph of Figure 117.

When the strain rate decreases (from about 0.15 plastic strain to failure), it is clearly observed that the dynamic curves of Polycarbonate remain amplified, with a constant amplification level approximately equal to that reached at the maximum strain rate.

Such counterintuitive behavior, defined “freezing of the strain rate effect” was already observed for structural metals by Mirone et al. [95,104].

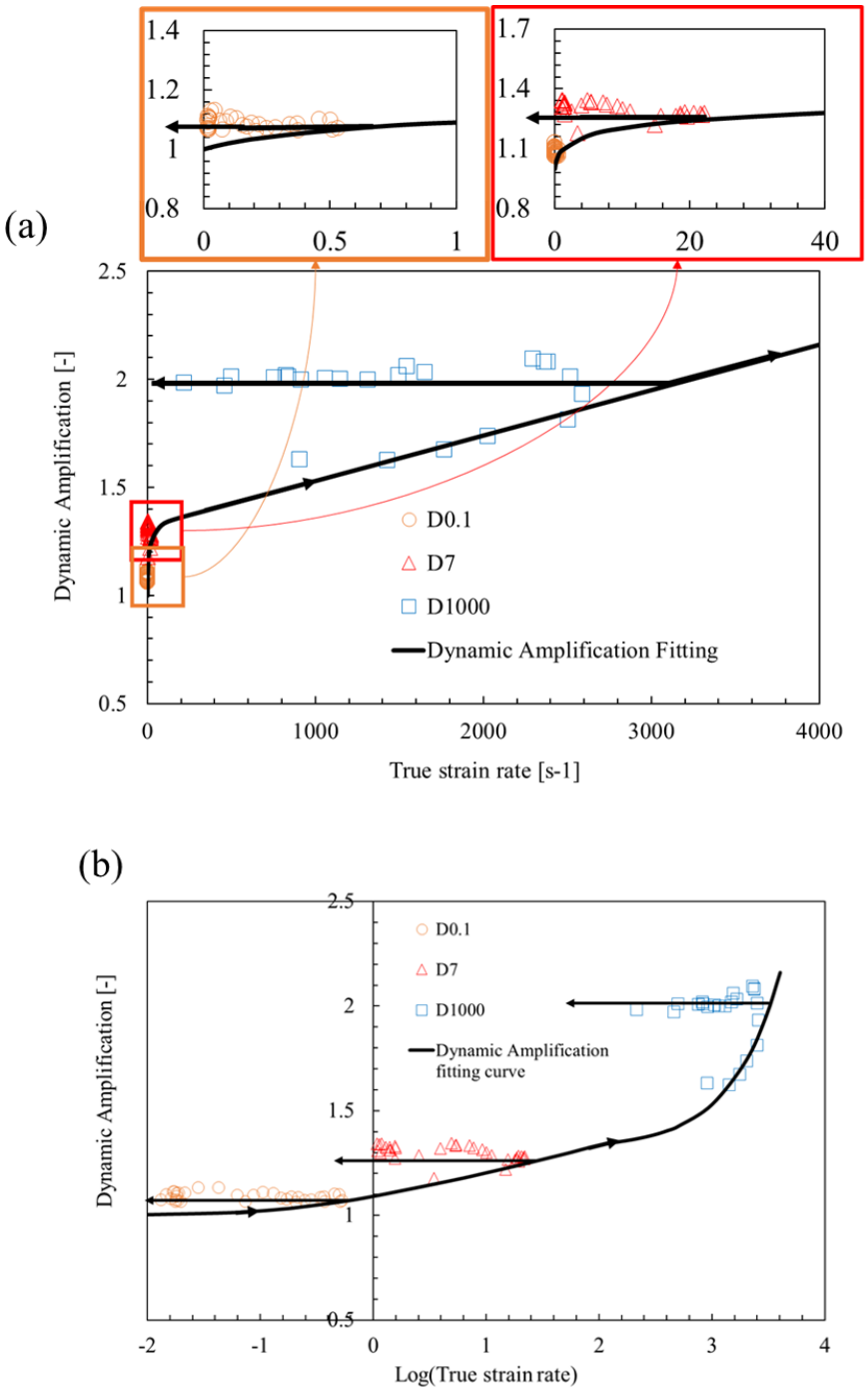


Figure 117: Dynamic Amplification of Polycarbonate vs true strain rate: a) True strain rate in linear scale; b) True strain rate in logarithmic scale.

Therefore, the dynamic amplification of Polycarbonate can be modeled as follows:

79) $$A(\varepsilon_{True}, \dot{\varepsilon}_{True}) = \begin{cases} f(\dot{\varepsilon}_{True}) & if \quad \frac{d\dot{\varepsilon}_{True}}{d\varepsilon_{True}} \geq 0 \\ \max\limits_{[0,\varepsilon_{True}]}(f(\dot{\varepsilon}_{True})) & if \quad \frac{d\dot{\varepsilon}_{True}}{d\varepsilon_{True}} < 0 \end{cases}$$

where the function *f(dε/dt)* is the fitting of the dynamic amplification data during the increasing strain rate phase, and is defined as follows:

$$80) \quad f(\dot{\varepsilon}_{True}) = \begin{cases} \left(1 + \frac{\dot{\varepsilon}_{True}}{0.175}\right)^{0.045} & if \quad \dot{\varepsilon}_{True} \leq 100\frac{1}{s} \\ 0.00021\dot{\varepsilon}_{True} + 1.32 & if \quad \dot{\varepsilon}_{True} > 100\frac{1}{s} \end{cases}$$

At the end of the procedures outlined in this methodology, all the necessary "components" are available to construct a material model capable of simulating the behavior of Polycarbonate over the experimental strain rate and temperature ranges. This empirical model will be referred to, for simplicity, as the PC-*DynamicAmplificationThermalSoftening* model, or PC-DATS model. This model is, in principle, capable of capturing the key aspects that characterize the elasto-plastic response of Polycarbonate when subjected to the combined effects of strain rate and temperature. By deriving the flow curve equation as a function of both strain rate and temperature, some interesting considerations can be made:

$$81) \quad \frac{d\sigma_{eq}(\varepsilon_{True},\dot{\varepsilon}_{True},T)}{d\varepsilon_{True}} = \frac{\partial\sigma_{eq}(\varepsilon_{True},\dot{\varepsilon}_{True},T)}{\partial\varepsilon_{True}} + \frac{\partial\sigma_{eq}(\varepsilon_{True},\dot{\varepsilon}_{True},T)}{\partial\dot{\varepsilon}_{True}}\frac{\partial\dot{\varepsilon}_{True}}{\partial\varepsilon_{True}} + \frac{\partial\sigma_{eq}(\varepsilon_{True},\dot{\varepsilon}_{True},T)}{\partial T}\frac{\partial T}{\partial\varepsilon_{True}}$$

By computing the partial derivatives and dividing both sides by the flow stress, the following expression is obtained:

$$82) \quad \frac{1}{\sigma_{eq}(\varepsilon_{True},\dot{\varepsilon}_{True},T)}\frac{d\sigma_{eq}(\varepsilon_{True},\dot{\varepsilon}_{True},T)}{d\varepsilon_{True}} = \frac{1}{\sigma_{eq_{S,T_0}}(\varepsilon_{True})}\frac{\partial\sigma_{eq_{S,T_0}}(\varepsilon_{True})}{\partial\varepsilon_{True}} + \frac{1}{A(\varepsilon_{True},\dot{\varepsilon}_{True})}\frac{\partial A(\varepsilon_{True},\dot{\varepsilon}_{True})}{\partial\varepsilon_{True}} + \frac{1}{A(\varepsilon_{True},\dot{\varepsilon}_{True})}\frac{\partial A(\varepsilon_{True},\dot{\varepsilon}_{True})}{\partial\dot{\varepsilon}_{True}}\frac{\partial\dot{\varepsilon}_{True}}{\partial\varepsilon_{True}} + \frac{1}{S(\varepsilon_{True},T)}\frac{\partial S(\varepsilon_{True},T)}{\partial T}\frac{\partial T}{\partial\varepsilon_{True}} + \frac{1}{S(\varepsilon_{True},T)}\frac{\partial S(\varepsilon_{True},T)}{\partial\varepsilon_{True}}$$

On the left-hand side of equation (82), there is the ratio between the derivative of the flow curve and the flow curve itself, while the right-hand side contains the sum of the following terms: the first term is the ratio between the derivative of the static flow curve at room temperature and the function itself, while all the other terms are the partial derivatives of the thermal softening and

dynamic amplification functions with respect to strain, strain rate, and temperature. By plotting the ratio $(\partial\sigma_{S,T0}/\partial\varepsilon_{True})/\sigma_{S,T0}$, the following diagram is obtained (Figure 118). Let us now consider the following cases:

Effect of Dynamic Amplification during isothermal test at ambient temperature

If the test is ideally conducted under isothermal conditions at room temperature, then S=1 and $\partial T/\partial\varepsilon=0$. As previously discussed, when the strain rate increases, the dynamic amplification is a monotonically increasing function of the strain rate, which implies that $\frac{\partial A}{\partial \dot{\varepsilon}_{True}} > 0$ and $\partial A/\partial\varepsilon=0$. The equation (82), thus, simplifies to:

83) $$\frac{1}{\sigma_{eq}(\varepsilon_{True},\dot{\varepsilon}_{True},T)}\frac{d\sigma_{eq}(\varepsilon_{True},\dot{\varepsilon}_{True},T)}{d\varepsilon_{True}} = \frac{1}{\sigma_{eq_{S,T_0}}(\varepsilon_{True})}\frac{\partial\sigma_{eq_{S,T_0}}(\varepsilon_{True})}{\partial\varepsilon_{True}} + \frac{1}{A(\varepsilon_{True},\dot{\varepsilon}_{True})}\frac{\partial A(\varepsilon_{True},\dot{\varepsilon}_{True})}{\partial\dot{\varepsilon}_{True}}\frac{\partial\dot{\varepsilon}_{True}}{\partial\varepsilon_{True}}$$

Equation 81 clearly shows that the derivative of the dynamic amplification gives a positive contribution to the ratio between the derivative of the static flow curve and the function itself. This effect can be visualized graphically in Figure 119 c). The red curve represents the sum of the ratio between the derivative of the static flow curve and the static flow stress, and the positive contribution from the derivative of the dynamic amplification. The point at which these curves intersect the horizontal line with intercept 1 corresponds to the Considère condition for necking. As a result, the dynamic amplification delays both the onset of necking and the strain at which the flow stress reaches its peak, effectively shrinking the region where the derivative is negative (softening region).

Effect of Thermal Softening in a constant strain rate test, at fixed temperature

This case describes the effect of thermal softening (assumed to be independent of strain rate) on the derivative of the flow curve. Under the assumptions of constant strain rate and fixed temperature higher than room temperature, equation (82) simplifies to the following expression:

84) $$\frac{1}{\sigma_{eq}(\varepsilon_{True},\dot{\varepsilon}_{True},T)}\frac{d\sigma_{eq}(\varepsilon_{True},\dot{\varepsilon}_{True},T)}{d\varepsilon_{True}} = \frac{1}{\sigma_{eq_{S,T_0}}(\varepsilon_{True})}\frac{\partial\sigma_{eq_{S,T_0}}(\varepsilon_{True})}{\partial\varepsilon_{True}} + \frac{1}{S(\varepsilon_{True},T)}\frac{\partial S(\varepsilon_{True},T)}{\partial\varepsilon_{True}}$$

In contrast to the previous case, since the thermal softening function is decreasing with strain, as inferred from the experimental data of G' Sell et al. [99], its derivative provides a negative contribution to the slope of the flow stress at room temperature. It follows that static thermal softening tends to anticipate the onset of necking and the peak in flow stress, thereby extending the strain range associated with the material's softening behavior (see the solid red curve reported in diagram Figure 119 c)).

Effect of Thermal Softening due to adiabatic self-heating

In the tensile test at a nominal strain rate of 0.1 s^{-1}, it is observed that—although the local strain rate in the range between 0.55 and failure remains constant (around 0.02 s^{-1}) and higher than that of the quasi-static test (approximately 0.002 s^{-1}), the true stress curve (which coincides with the flow curve in this case) D0.1 intersects and lies below the true curve D0.01, with a lower slope. Applying equation (82) to this case, it simplifies to the following expression:

85) $$\frac{1}{\sigma_{eq}(\varepsilon_{True},\dot{\varepsilon}_{True},T)}\frac{d\sigma_{eq}(\varepsilon_{True},\dot{\varepsilon}_{True},T)}{d\varepsilon_{True}} = \frac{1}{\sigma_{eq_{S,T_0}}(\varepsilon_{True})}\frac{\partial\sigma_{eq_{S,T_0}}(\varepsilon_{True})}{\partial\varepsilon_{True}} + \frac{1}{S(\varepsilon_{True},T)}\frac{\partial S(\varepsilon_{True},T)}{\partial T}\frac{\partial T}{\partial\varepsilon_{True}}$$

Also in this case, since $\partial T/\partial\varepsilon$ is certainly positive, as the temperature increase is related to the dissipation of plastic work, the partial derivative $\partial S/\partial T$ is negative, and therefore the effect of adiabatic self-heating naturally tends to lower both the dynamic flow curve and its slope at high plastic strains (see Figure 119 d)).

In the following section, the DATS model previously introduced will be implemented in a Finite Element code, and the results obtained from the FEM simulations will be presented.

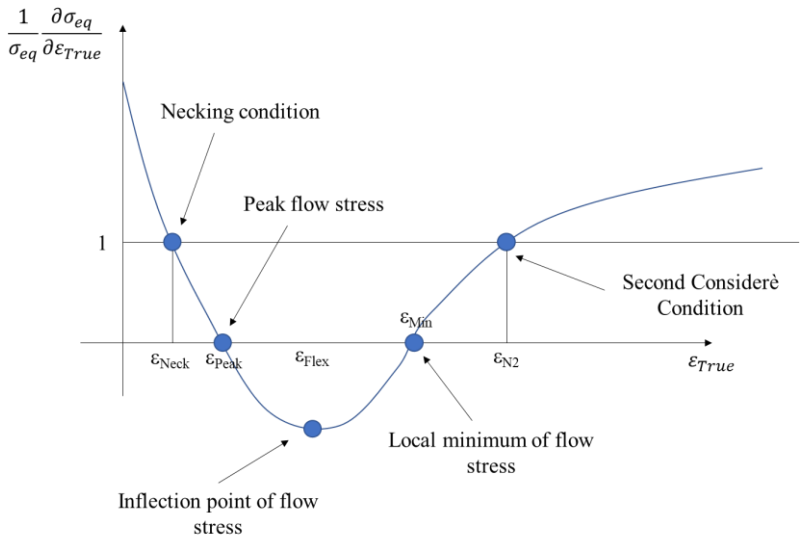


Figure 118: Derivative of flow stress / Flow Stress ratio vs true strain diagram.

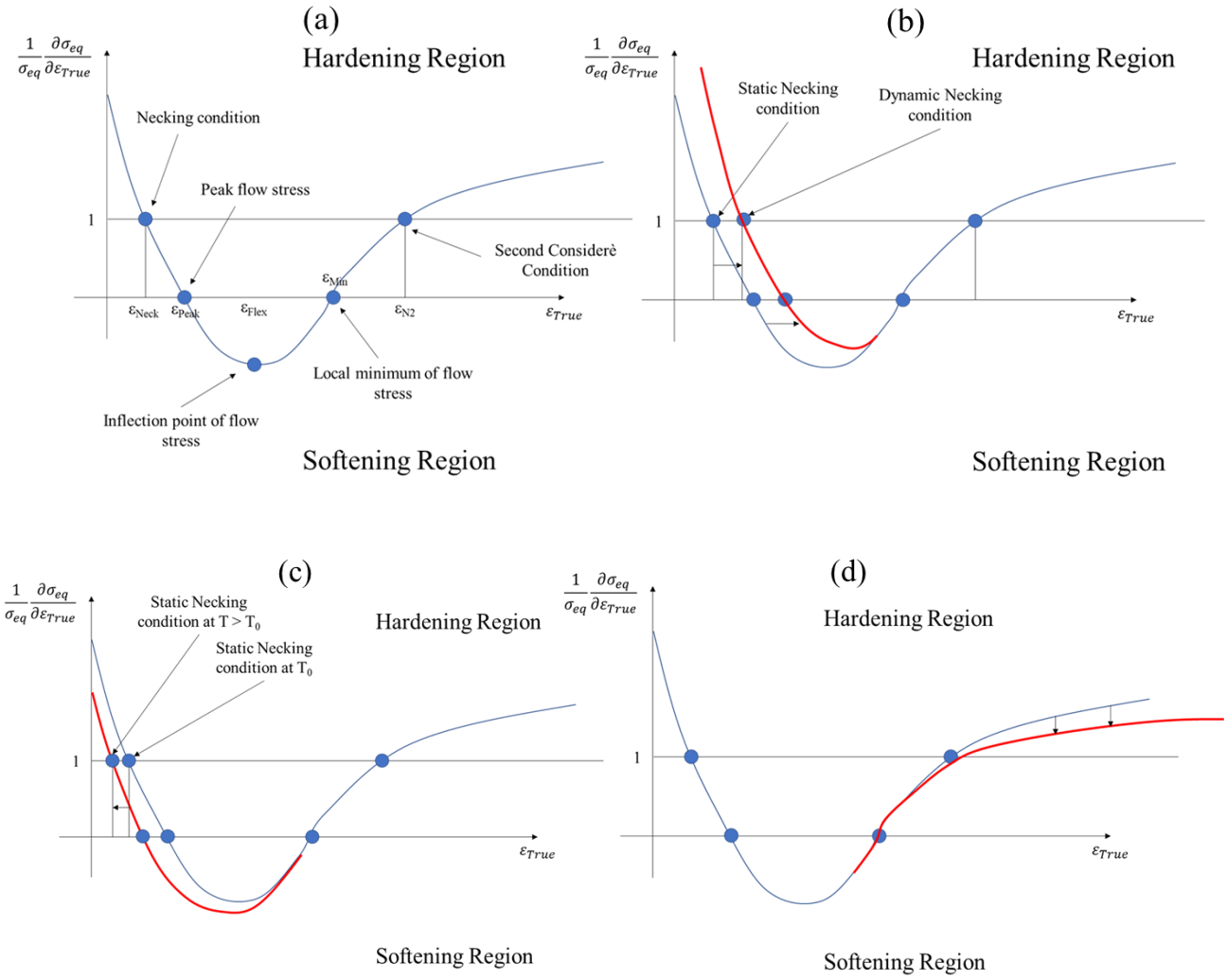


Figure 119: Derivative of flow stress/flow stress ratio vs true plastic strain: a) ratio plotted in quasi-static condition at room temperature; b) Effect of dynamic amplification on the slope of the flow curve; c) Effect of the static thermal softening; d) Effect of the adiabatic self-heating.

8.1 Implementation of the PC-DATS model and results from Finite Element modelling

The DATS model for Polycarbonate analyzed in the present work was implemented in the Finite Element software MSC Marc Mentat® v2023.4 through a user-defined subroutine written in Fortran language.

To account for self-heating effects, all simulations considered an initial uniform temperature of 25 °C, and a fixed Taylor-Quinney coefficient of 0.55. The additional thermal properties used for Polycarbonate were: thermal conductivity equal to 0.2 W/m·K, and specific heat at constant volume equal to 1300 J/kg·K.

The plasticity of Polycarbonate was modeled as J2-plasticity with isotropic hardening. The strain rate and temperature dependent hardening/softening model was implemented via the *uyield_surface* subroutine (2023 version of the former *yiel* subroutine) in Marc Mentat. The subroutine is reported in the appendix of the thesis. The three analyses were performed as thermal/structural implicit dynamic transient simulations. In the models corresponding to tests D0.1 and D7, the displacement along the x-axis was applied to the shoulder nodes at a velocity equal to the nominal velocity of the experimental test, while for the Split Hopkinson Bar test, the incident wave was simulated by applying a step stress to the nodes at the left end of the input bar, with an amplitude of 100 MPa.

The DATS model was used to simulate the specimen conditions for the three strain rate cases previously discussed: nominal strain rates of 0.1 s^{-1}, 7 s^{-1}, and 1000 s^{-1}. To reduce the computational complexity of the simulations, all models were assumed to be axisymmetric and discretized using plane quad4 elements**.**

For the analyses corresponding to the 0.1 s^{-1} and 7 s^{-1} tests, one quarter of the specimen's longitudinal section was modeled (see Figure 72). In contrast, the FEM analysis of the Split Hopkinson Tension Bar (SHTB) tests involved the modeling of both incident and transmission bars, in order to properly account for the wave reflection and transmission phenomena through the specimen.

The bars were discretized using five elements along the radial direction**,** with an aspect ratio length-to-width of 4.5. The threaded specimen was discretized using 33 elements along the radius and 80 elements along the gauge length. The mesh was refined in the specimen region and coarsened in the bars to optimize computational efficiency.

The bars were modeled as purely elastic materials, with a Young's modulus of 71700 MPa**,** a Poisson's ratio of 0.33, and a mass density of 2810 kg/m³, consistent with the properties of the Ergal aluminum used for the experimental setup. The Polycarbonate was modeled as a purely elasto-plastic material, with elastic constants: Young's modulus 2400 MPa and Poisson's ratio 0.33. The density of Polycarbonate was assumed to be 1170 kg/m³.

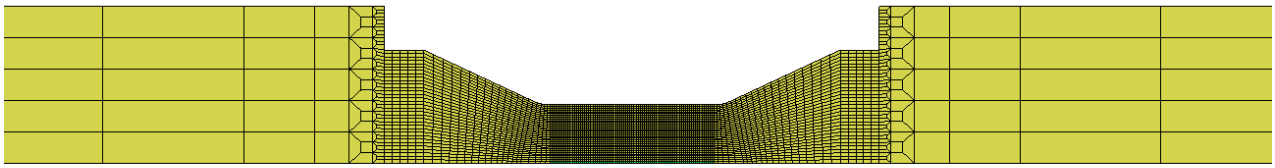


Figure 120: Partial view of the axisymmetric model of SHTB and specimen.

From the FEM simulations, the following data were extracted: the reaction force along the x-direction at the master node, the elongation of a gage length with an initial length of 4 mm centered on the specimen's midsection, and the instantaneous minimum diameter at the necking region. For the simulation involving the Hopkinson bar setup, instead of the tensile force, the transmitted stress wave in the output bar was extracted.

Using these outputs, and applying the same equations employed for the processing of the experimental data, the following results were computed: the true stress-strain curves based on elongation and cross-section area reduction, the area strain vs. elongation strain diagrams, and the local strain rate histories.

As can be seen from Figure 121, the flow curves, locally extracted at the center node of the mesh of the specimen, generated by the DATS model closely reproduce the "fixed" flow curves obtained by correcting the experimental true curves solely for the effect of stress triaxiality. This confirms that the methodology developed in the present work to decouple the individual contributions of thermal softening and dynamic amplification is suitable, and that the DATS model is capable of predicting the flow curves of the material during tensile tests in which both strain rate and temperature may vary locally over time.

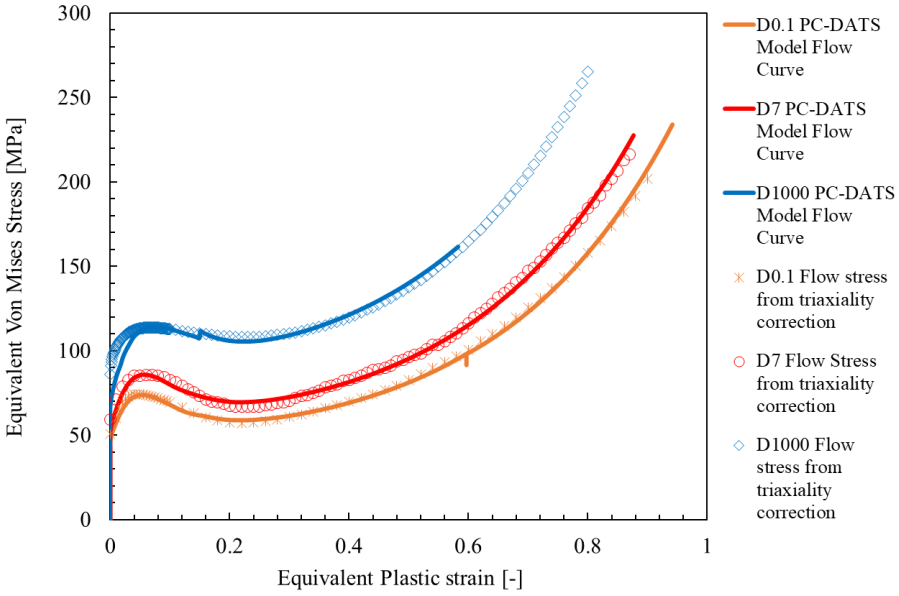


Figure 121: Comparison between the flow curves obtained by correcting the experimental true stress curves from the triaxiality effect (dotted curves) and the ones generated by the PC-DATS model, extracted at the center of necking section.

The results of the FEM simulations are shown in Figure 124, Figure 125Figure 126. The proposed model is able to accurately simulate the true stress-strain curves based on both area reduction and elongation, across low, medium, and high strain rates. Thanks to this model, it becomes possible to simulate characteristic phenomena governed by the combined effects of strain rate and temperature, such as the delay in the onset of necking and the strain at peak stress, the broadening of the constitutive peak with increasing strain rate, the "freezing" of dynamic amplification once the local strain rate starts to decrease, and the effect of adiabatic self-heating at high strains.

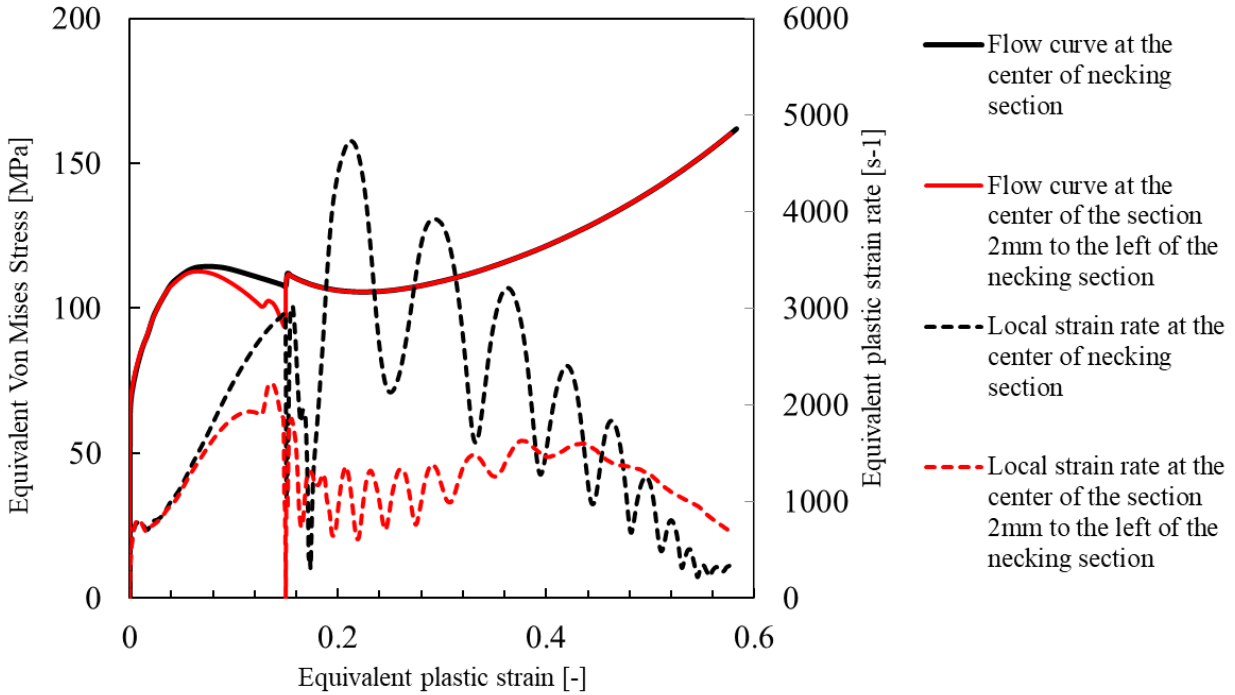


Figure 122: Polycarbonate flow curves generated by the PC-DATS model, extracted at the center of two different cross-section.

If the flow curve is extracted at a central node of a section different from that of the first necking (see Figure 122), some differences emerge with respect to the curve extracted at the center of the first necking section, especially in the material's softening phase. In fact, before the necking strain, the strain rate histories are coincident and monotonically increasing up to approximately 1100 s^{-1} (close to the nominal value). After the onset of necking, the two flow curves diverge due to the different evolution of the strain rate history (higher at the center of the first necking, lower in the section outside the necking). At a plastic strain of 0.15, the two curves suddenly converge again due to the freezing of the strain rate modeled through the subroutine. It is evident that the discontinuity introduced in the modeling of the dynamic amplification law is not related to any physical phenomenon, but rather represents a strategy to maintain the flow curves at a certain level of dynamic amplification during the post-decreasing phase of the local strain rate. What remains to be clarified is whether and how the viscoelastic effects of the material during softening are connected to, and possibly influence, this effect of strain rate freezing.

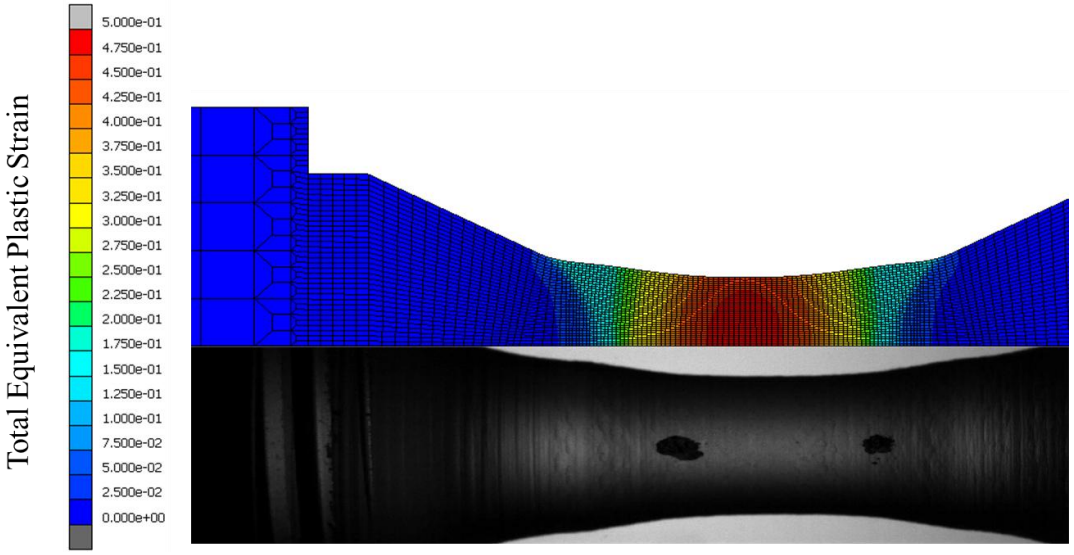


Figure 123: Comparison between the specimen's shape during the test at 1000 s^{-1} predicted by the PC-DATS model (on the top), and the experiment (on the bottom). The pictures are taken at an elongation strain of 0.40.

The DATS model also successfully captures the shape of the necking region at high strain rates, confirming that the higher is the local strain rate, the lower is the tendency of necking to localize (see Figure 123).

A limitation of the model lies in the discontinuity present in the dynamic amplification function, which naturally introduces discontinuities in the constitutive response as well. These discontinuities have a practically negligible effect on the numerical results of the 0.1 s^{-1} and 7 s^{-1} tests, but they induce noticeable non-physical oscillations in the 1000 s^{-1} simulation. This issue could be mitigated by properly accounting for the damping effects associated with the material's internal viscosity, which should act as a "brake" during the force drop in the material's softening phase, and is expected to dampen internal vibrations within the specimen.

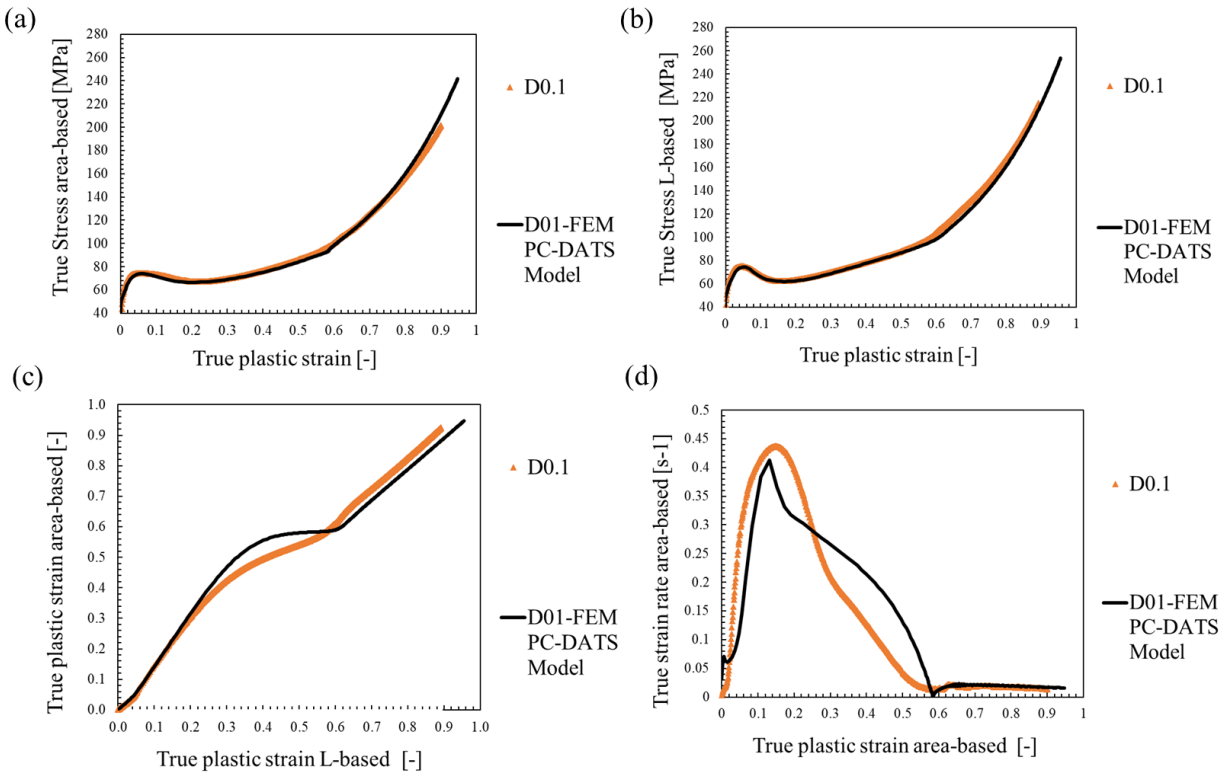


Figure 124: Comparison between the results from FEM simulation (black line) using the PC-DATS model and the experimental data (orange dots) for the test at 0.1 s^{-1}. a) True stress area-based curve; b) True stress elongation-based curve; c) area strain vs elongation strain diagram; d) True strain rate history.

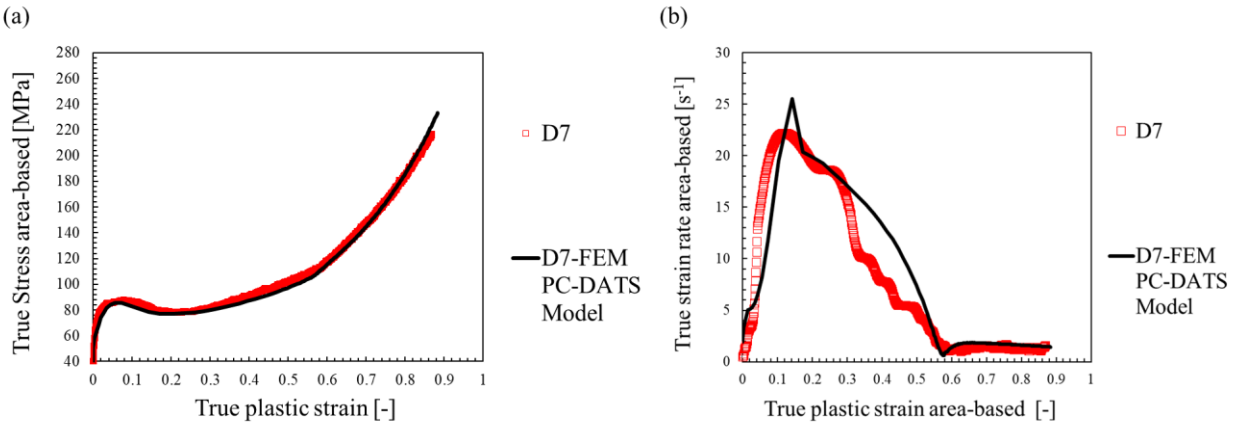


Figure 125: Comparison between the results from FEM simulation (black line) using the PC-DATS model and the experimental data (red dots) for the test at 7 s^{-1}. a) True stress area-based curve; b) True stress elongation-based curve; c) area strain vs elongation strain diagram; d) True strain rate history.

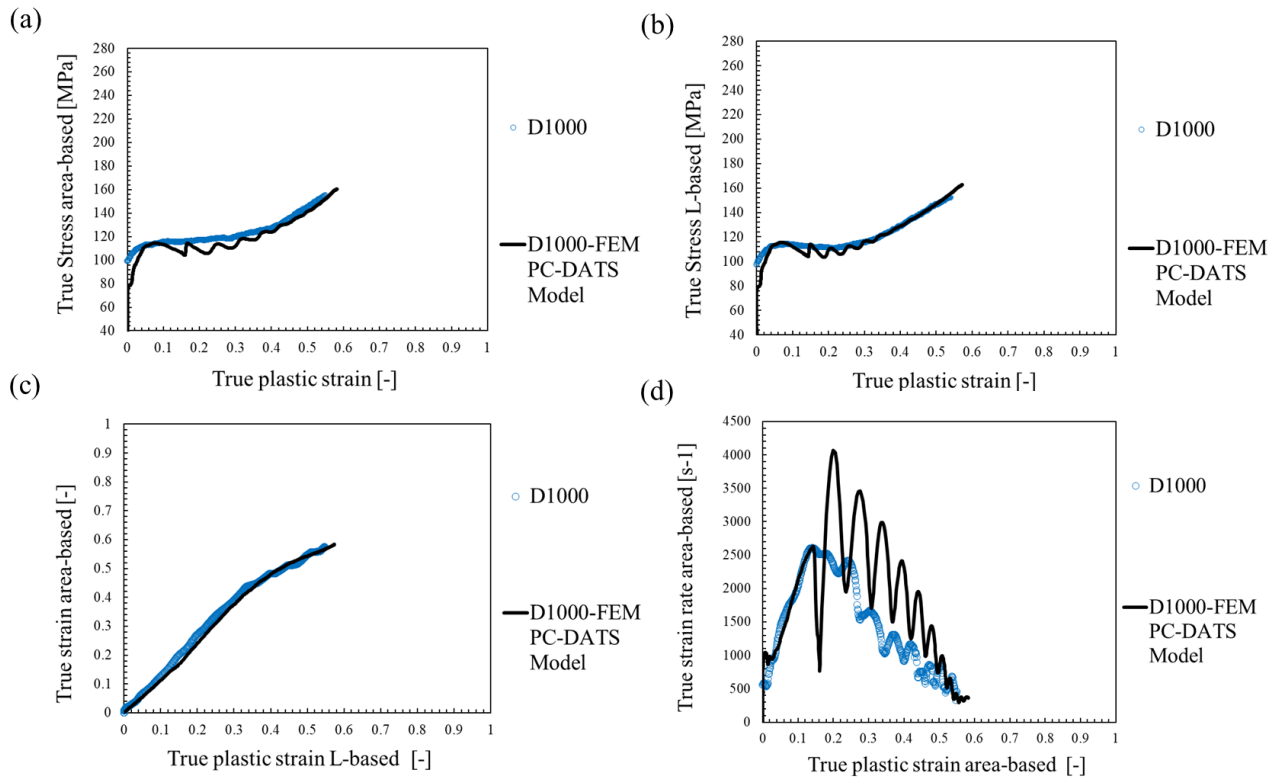


Figure 126: Comparison between the results from FEM simulation (black line) using the PC-DATS model and the experimental data (blue dots) for the test at 1000 s^{-1}. a) True stress area-based curve; b) True stress elongation-based curve; c) area strain vs elongation strain diagram; d) True strain rate history.

Although the simulations of dynamic tests using "fixed flow curves" already gave satisfactory results, the adoption of a more general hardening-softening model like the PC-DATS one is essential to allow the modeling, for the same material, of deformation histories differing from those of the tensile tests corresponding to each fixed curve.

In fact, the suitability of the fixed curve to model the corresponding dynamic tests is just due to the coincidence between the rate-temperature histories originating the "fixed" flow curve of an experiment, and the rate-temperature histories of the same simulated experiment: e.g., it is quite obvious that the fixed flow curve from the 0.1/s test would not be suitable for simulating the 1000/s test. And, likely, the same fixed flow curve would not be even suitable for simulating the 0.1/s test of a notched Polycarbonate specimen or another generally-shaped component strained at the same rate. On the contrary, the DATS model can deliver the current flow stress, depending on the instantaneous combination of strain, strain rate and temperature, which generally varies with time at each point, and from point to point at each instant of the test.

Summarizing, the fixed flow curves, derived by correcting the proper experimental true curves through either a Bridgman-like correction [92,93] or the three-parameters correction proposed by Mirone et al. [89] are then the necessary intermediate step of the characterization process, essential to "sample" the effective flow stress at the different combinations of current rate-temperature, corresponding to the rate and temperature histories of each test.

After this set of quadruplets of data (strain, strain rate, temperature, flow stress) is properly derived, the postprocessing approach of identifying the effects of thermal softening and dynamic amplification can be made, according to many possible models, like the known Johnson-Cook model [105] and the coupled DATS model, originally proposed in Mirone et al. [95] for a stainless steel and recalled in this work for the Polycarbonate, by renaming it as PC-DATS.

8.2 Conclusions

In the present chapter, the mechanical characterization of Polycarbonate at high strain rates was addressed. From the experimental stress–strain curves, by applying the direct triaxiality correction according to Bridgman's approach, it was possible to derive the so-called "fixed" flow curves. These are flow curves considered at a given nominal strain rate, which result from a complex history of strain rate and temperature variation, point by point and at each instant of the test. The "fixed" flow curves proved to be suitable for modeling and reproducing a single dynamic tensile test on a given specimen's geometry (round, in this case). However, they cannot be directly transferred for simulating different geometries and/or other models subjected to different strain rate and temperature histories (e.g., projectile–plate impact tests on Polycarbonate, dynamic tests on notched specimens, etc.).

In order to account for the combined dependence of the material response on strain rate and temperature, a multiplicative material model was developed, referred to as the PC-DATS model, in which the two effects of dynamic amplification and thermal softening were decoupled. Using the "fixed" flow curves, the local strain-rate histories, the temperature histories from adiabatic heating, and the flow curves at constant strain rates and elevated temperatures, two functions were constructed to model the phenomena of dynamic amplification and thermal softening. The parameters of these functions were directly calibrated from the available experimental data.

This decoupling methodology enabled the identification of a peculiar feature of Polycarbonate, known as *freezing of the strain rate effect*. According to this phenomenon, the dynamic amplification of the material (strain rate effect) increases with the local true strain rate, but

then remains approximately constant, “frozen” at the value reached at the maximum strain rate, even when the localization rate decreases or stabilizes during the post-necking propagation stage.

The freezing effect thus reveals the tendency of the material not to reduce its tensile strength during the reduction of the local strain rate. Conversely, the adiabatic heating of the specimen, due to the dissipation of 50 % of plastic work into heat, leads to a reduction of the flow stress at large strains.

Possible future developments of this work could include the investigation of the viscoelastic effect of the material and how it is influenced by strain rate and temperature. Moreover, it would be of interest to further analyze the shifting phenomenon of the area-based strain vs. elongation-based strain diagram away from the 45° line in the post-propagation stage, possibly related to changes in the elastic properties of the material during tensile testing. Density measurements conducted on fractured specimens revealed no significant variation in the material density, confirming that the plastic component of deformation remains incompressible and ruling out the possibility of pressure-dependent yielding. Furthermore, a complete characterization of the material should also include the study of its response under different stress states (e.g., compression, torsion, shear, mixed-mode) in order to confirm or disprove the assumption that the J2 plasticity model is valid for Polycarbonate.

Chapter 9: Tensile response of anisotropic sheet metals

Sheet metals are engineered materials designed to combine high strength, ductility, formability, and lightness, which make them suitable for applications across various fields, including the automotive, aeronautical, and military sectors. The rolling process to which these alloys are subjected confer anisotropic mechanical properties to them, meaning that the material response depends on the direction of the applied load.

The mechanical characterization of sheet metals is essential to investigate their behavior within the elastic–plastic regime. In general, the ductility of these materials is such that local plastic strains at fracture may exceed 100%, while the strain at necking remains relatively low, typically between 4% and 25%. This implies that approximately 90% of the material response lies in the post-necking regime.

To apply the direct or inverse characterization methods previously discussed for Polycarbonate or proposed in the literature, it is first necessary to determine the local (area-based) true stress–strain curve from tensile tests performed along a specific material direction (e.g., rolling direction or transverse direction). For isotropic materials, obtaining the experimental true curve is relatively straightforward. Indeed, in the case of cylindrical specimens, the instantaneous diameter measurement is sufficient to evaluate the resistant cross-section area. Conversely, for isotropic rectangular specimens, it has been observed that the specimen thickness t evolves proportionally to the width w, thus preserving the initial aspect ratio. However, if the material's response is anisotropic the circular cross-section of cylindrical specimens becomes elliptical, as reported in several studies [106,107]. On the other hand, for anisotropic flat specimens, the thickness-to-width ratio does not remain constant throughout the test.

In theory, investigating the anisotropic behavior of a material requires complex experimental setups, such as 3D Digital Image Correlation (DIC) with multiple cameras for strain measurement [108]. Other authors, such as Sasso et al. [109], combined two-dimensional DIC with Moiré interferometry to measure the out-of-plane displacements at the specimen's surface, with the aim of reconstructing the instantaneous necking section. In the work of Mirone et al. [107], two orthogonal cameras were employed to capture the instantaneous minimum cross-section of anisotropic cylindrical specimens of X100 steel.

In addition to anisotropy, when the material undergoes large plastic deformations, the rectangular cross-section does not maintain its shape up to failure, but rather distorts by bending inward, thereby reducing the net area compared to the gross rectangular one estimated from width

and thickness measurements alone. The phenomenon of distortion is strongly related to localized necking, which typically occurs in thin flat specimens with a width-to-thickness ratio smaller than three [110].

The aim of the present work is to propose a methodology for processing optical strain measurements derived during tensile tests on metal sheets, in order to identify both the anisotropy parameters and the distortion of the necking cross-section, by employing only one camera in the experimental setup. The main objective is to accurately estimate the effective resistant area and derive reliable local true stress–strain curves, which can subsequently be converted into flow curves of the material. The proposed methodology was applied to four metal sheets manufactured through different rolling processes, using specimens cut along the rolling direction. Naturally, this methodology can be easily extended to the post-processing of tensile tests performed on specimens cut along other directions. The results of this work, together with the details of the proposed methodologies, have been published in the following articles: *A simple procedure for the post-necking stress–strain curves of anisotropic sheet metals* [111] and *An enhanced approach for high-strain plasticity in flat anisotropic specimens with progressively distorting necking section* [112].

9.1 Methodologies for the mechanical characterization of ductile sheet metals

Modern metallic alloys are engineered to combine high strength with high ductility, enabling lightweight structures that resist nominal loads while sustaining large deformations under exceptional conditions to absorb energy before failure. High strength generally promotes an earlier onset of necking, whereas high ductility is associated with higher fracture strains; consequently, such materials typically undergo pronounced post-necking phase during their deformation history.

For round specimens, necking mainly affects the conversion of true stress into the material's flow stress as discussed for Polycarbonate, while in flat or thin-sheet specimens it also complicates the determination of true stress-strain curve from experiments. Indeed, the main issue related to the experimental true curve of sheet metals relies in the correct estimation of the specimen's resistant cross section during necking evolution. The rectangular geometry would require at least two orthogonal cameras for tracking the instantaneous reduction in the width and thickness. Moreover, if the alloy exhibits large plastic strain, the specimen's resistant cross section does not maintain its

rectangular shape throughout the tests, but tends to bend toward the center becoming progressively distorted, reducing the gross area estimated with the two cameras.

Although the reconstruction of post-necking flow curves from experimental data has been widely investigated, the accurate derivation of the experimental true curve after necking has received less attention, despite the significant challenges it poses for flat specimens.

In the case of a smooth rectangular specimen (Figure 127), the true strain and true stress are defined as the section-averaged axial strain and stress, as expressed in eqs. (86) and (87), where F is the tensile load, and $A_0=w_0t_0$ and $A=wt$ are the initial and current cross-sectional areas.

(86) $$\varepsilon_{True} = ln\left(\frac{A_0}{A}\right)$$

(87) $$\sigma_{True} = \frac{F}{A}$$

For a smooth tensile specimen with a rectangular cross-section, the true stress–strain curve can be derived through five post-processing methods, being various grades of approximation of the true stress and the true strain. Since many high-strength alloys exhibit early necking strain (e.g., minor than 0.05) and late failure (e.g., at effective local strain greater than 0.5), the choice of the methodology becomes critical. Moreover, the intrinsic anisotropy of most rolled sheet metals further limits the possibility of arbitrarily selecting among these approaches. The five approaches used for the derivation of the true curve are reported below.

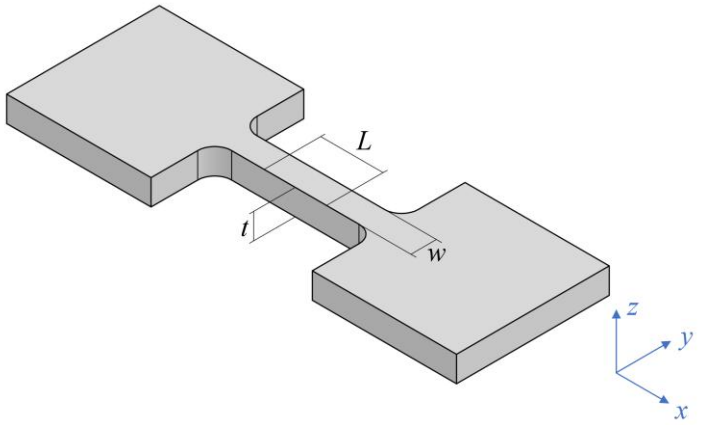


Figure 127: Schematic representation of the rectangular specimen cut from metallic sheet.

ELONGATION-BASED (L-BASED) APPROACH

The most common approach to determine the true stress–strain curve is the elongation-based (L-based) method, which assumes the conservation of the volume of the gage length throughout the test. Under this hypothesis, $AL=A_0L_0$, leading to the expressions for true strain and true stress reported below (eqs. (88) and (89)).

(88) $$\varepsilon_{True_L} = ln\left(\frac{L}{L_0}\right)$$

(89) $$\sigma_{True_L} = \frac{F}{A_0}\frac{L}{L_0}$$

This method is widely adopted because elongation measurements are simple, but its accuracy decreases after necking, when the specimen develops an hourglass shape or exhibits localized shear bands.

DIGITAL IMAGE CORRELATION-BASED (DIC-BASED) APPROACH

An alternative method for the determination of the true stress-strain curve for sheet metals relies on the measurements of the local peak axial strain on the specimen's surface, by means of the Digital Image Correlation (DIC) technique, already presented in the section 6.1.1.

The approximation of the DIC-based approach lies in the assumption to consider the "local" peak axial strain equal to the cross-section averaged axial strain (eqs. (90) and (91)).

(90) $$\varepsilon_{True_{DIC}} = \varepsilon_{z_{peak}}$$

(91) $$\sigma_{True_{DIC}} = \frac{F}{A_0} exp\ (\varepsilon_{z_{peak}})$$

Although this technique can occasionally yield accurate results, the DIC peak axial strain could be affected by an error: depending on the cross-section aspect ratio (width-to-thickness ratio) and the material's hardening behavior, the DIC peak strain may overestimate or underestimate the true strain in the post-necking phase. In general, thin specimens tend to give higher peak values, while thicker ones give lower values (Figure 128). For each material, there exist a specific value of the width-to-thickness ratio that aligns the DIC peak with the effective true strain, but its determination requires prior knowledge of the hardening behavior, which is precisely the unknown under investigation.

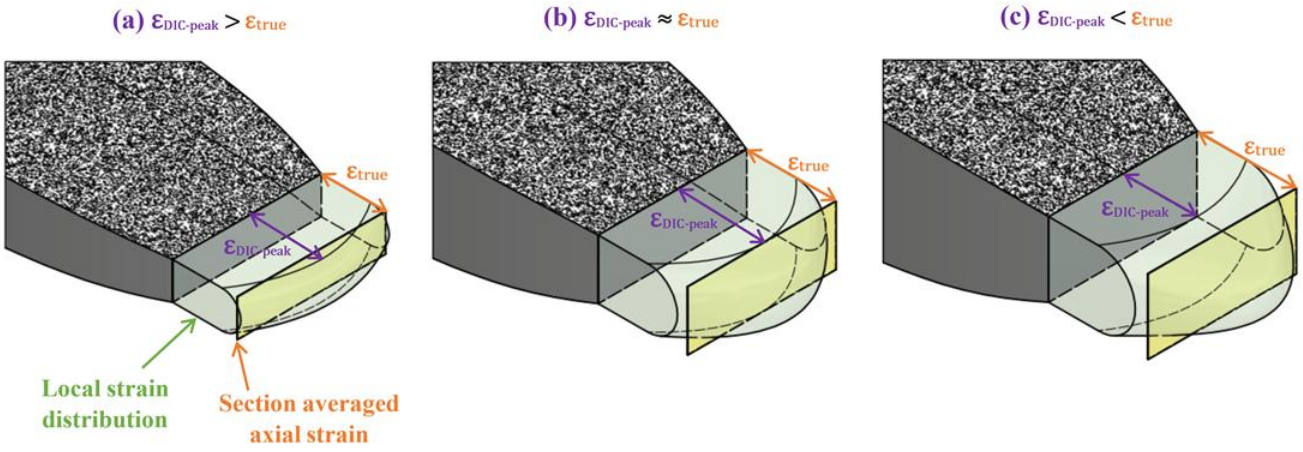


Figure 128: Comparison between the local axial strain distribution, the averaged value (true strain), and the DIC local peak strain in three different cross section geometries: a) thin specimen; b) w/t such that $\varepsilon_{DIC}=\varepsilon_{True}$; c) thick specimen.

ISOTROPIC WIDTH-BASED (w_{iso}-BASED) APPROACH

For isotropic materials, neglecting the distortion of the specimen's cross-section in the post-necking phase, the thinning ratio t/t_0 remains approximately equal to the shrinking ratio w/w_0 throughout the entire deformation history, up to fracture. Under this assumption, the thickness can be estimated as $t=(t_0/w_0)w$, leading to a cross-section area $A=(t_0/w_0)w^2$. Substituting this expression into eqs. (86) and (87), the following true strain and stress can be computed:

$$\varepsilon_{True_w} = 2\,ln\left(\frac{w_0}{w}\right) \tag{92}$$

$$\sigma_{True_w} = \frac{F}{\left(\frac{t_0}{w_0}\right)w^2} \tag{93}$$

This w-based method improves the accuracy of the elongation-based approach because, for isotropic materials, it allows the true curve to be extended beyond necking and up to failure, assuming the necking section remains rectangular. This approach allows to estimate the resistant cross-section by viewing only the specimen's width with a frontal camera. However, in some cases the minimum cross-section distorts into a curved quadrilateral, limiting the accuracy of this methos. Importantly, for anisotropic materials, the loss of accuracy in the w-based curve is generally less severe than the underestimation inherent in the elongation-based method after necking.

ANISOTROPIC WIDTH-BASED (w_{aniso}-BASED) APPROACH

In anisotropic materials, the constancy of the ratio thickness-to-width ratio is not preserved during deformation ($t_0/w_0 \neq t/w$), since the thickness may decrease at a slower or faster rate than the width (Figure 129).

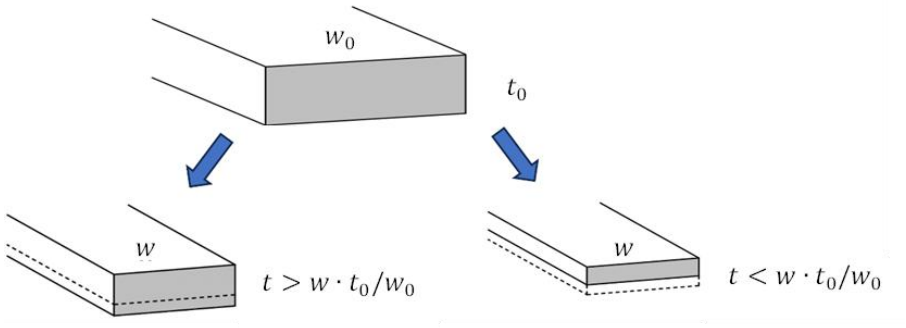


Figure 129: Anisotropic straining of cross-sections: thinning rate smaller (left side) or greater (right side) than isotropic shrinking ratio.

As a result, the thickness cannot be derived from simple width measurements, making the w-based method inaccurate both before and after necking. In this case, the addition of a second camera orthogonal to the thickness, or the utilization of the elongation-based procedure remain the only approaches valid in the pre-necking regime. However, no reliable formulation of the true curve has been available for the post-necking phase.

To address this limitation, a new method combining length and width measurements is proposed. Before necking, assuming volume conservation, the thinning ratio is given by equation (94).

$$\frac{t}{t_0} = \frac{w_0}{w}\frac{L_0}{L} \tag{94}$$

After necking, this relation no longer holds, since the specimen deviates from a parallelepiped shape. For isotropic materials, thinning and shrinking follow the linear relation $t/t_0=w/w_0$.

In contrast, anisotropic materials exhibit a different relationship, which can be identified observing the pre-necking data of the thinning ratio plotted against the evolving shrinking ratio w/w_0. In the literature, the measurement of the anisotropic behavior of a sheet metal is given by the so-called *Lankford coefficient R*. It is defined as the ratio between the two transversal components of the plastic strain tensor:

(95) $$R = \frac{ln\left(\frac{w}{w_0}\right)}{ln\left(\frac{t}{t_0}\right)}$$

If R > 1, then the thinning ratio is smaller than the shrinking ratio. Obviously, R=1 is the Lankford coefficient for isotropic materials, which means that the thickness-to-width ratio remains constant as discussed before. From the definition of the Lankford coefficient R, it follows that the thinning ratio evolves according as a power law:

(96) $$\frac{t}{t_0} = \left(\frac{w}{w_0}\right)^z$$

where the exponent *z*, determined from the pre-necking data, corresponds to the inverse of the *R* coefficient.

Once identified, this power-law relation can be extrapolated to the post-necking regime, and refined using direct thickness measurements, either from fractured specimens or from in-situ side-view imaging.

Equation (96) allows to account for the anisotropic effect of the material on the resistant cross-section, throughout the deformation history.

$$\mathrm{A} = \mathrm{wt} = \mathrm{wt}_0 \left(\frac{w}{w_0}\right)^z = w_0 t_0 \left(\frac{w}{w_0}\right)^{z+1}$$

This effective necking area, accounting for anisotropic thinning and shrinking, can then be introduced into the standard definitions of area-based stress and strain, thus providing the anisotropy-aware true curve:

(97) $$\varepsilon_{True_{Aniso}} = (z+1)\, ln\left(\frac{w_0}{w}\right)$$

(98) $$\sigma_{True_{Aniso}} = \frac{F}{A_0}\left(\frac{w_0}{w}\right)^{z+1}$$

ANISOTROPY AND DISTORTION-BASED (Aniso+Dist-BASED) APPROACH

The fifth characterization method represents another improvement of the novel approach introduced before. The anisotropic width-based approach still relies on the simplifying assumption that the neck cross-section remains rectangular until failure, with its area estimated considering the

power-law evolution of the thinning ratio as reported in equation (96). In reality, depending on the initial aspect ratio t_0/w_0 and the material ductility, diffuse and localized necking progressively distort the section, which loses its rectangular geometry and develops inward-curved edges, assuming an hourglass-like profile similar to that of the specimen surface (Figure 130).

As a result, the effective resisting neck area becomes smaller than the nominal rectangular one. The distorted section, denoted as $A_{aniso+dist}$ may therefore differ significantly from the nominal anisotropic area $A_{aniso}=wt$, calculated only from width and thickness values according to the latter procedure. To account for this difference, a distortion coefficient D is introduced in the following equation:

$$D = \frac{A_{aniso+dist}}{A_{dist}} \quad (99)$$

Before necking, the cross-section remains undistorted ($D=1$). At failure, D_f can be evaluated from fracture surface measurements using image analysis. Between necking onset

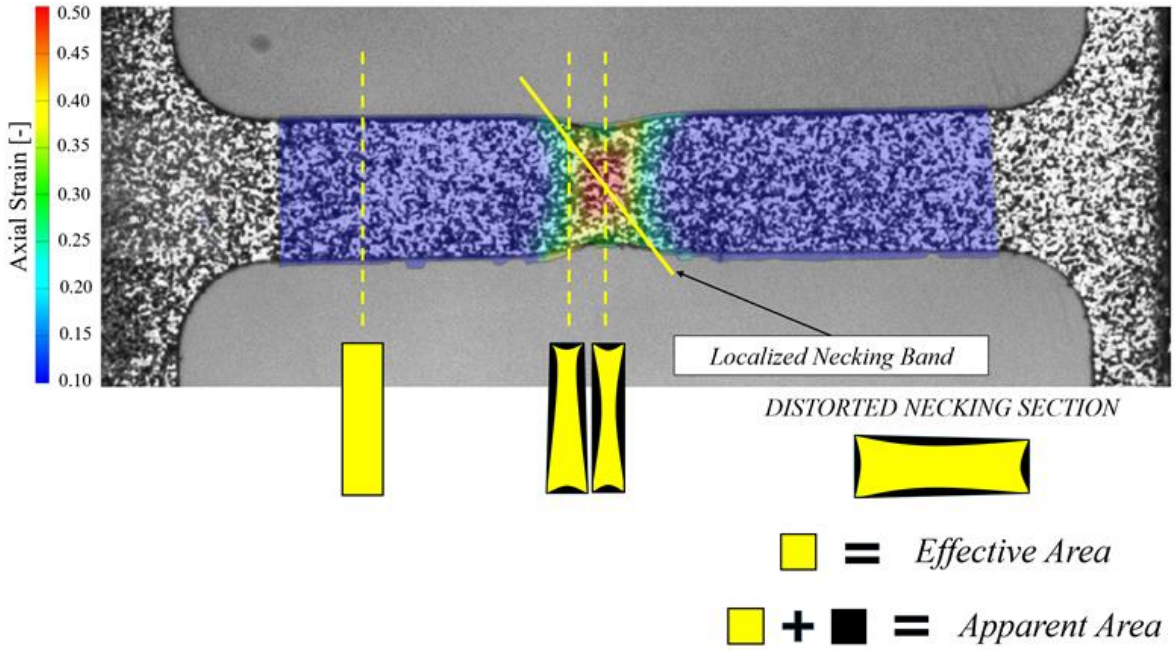


Figure 130: Effect of localized necking on the minimum cross-section of the specimen.

and failure, the evolution of D is estimated through a polynomial law (Equation (100)), with the quadratic ($\phi = 2$) form adopted here as the simplest option ensuring smooth transition and consistency with boundary conditions.

(100) $$D = \begin{cases} 1 & before\ necking\ onset \\ 1 - (1 - D_f)\left(\frac{w - w_{neck}}{w_{failure} - w_{neck}}\right)^{\phi} & after\ necking\ onset \end{cases}$$

The effective distorted area is then obtained as follows:

$$\mathrm{A_{aniso+dist}} = \mathrm{DA_{aniso}} = \mathrm{D\ wt_0}\left(\frac{w}{w_0}\right)^{z} = D\ w_0 t_0 \left(\frac{w}{w_0}\right)^{z+1}$$

Substituting this area into equations (86) and (87) yields the enhanced *Aniso+Dist* approach, proposed in this work.

(101) $$\varepsilon_{True_{Aniso+Dist}} = (z+1)\, ln\left(\frac{w_0}{w}\right) - ln\,(D)$$

(102) $$\sigma_{True_{Aniso+Dist}} = \frac{F}{DA_0}\left(\frac{w_0}{w}\right)^{z+1}$$

While the methods listed in the previous sections provide accurate curves at low strains, this latter procedure is essential at large deformations, where a reliable description of plasticity is a prerequisite for the material's characterization, ductile damage modeling and failure prediction.

9.2 Materials and experimental setup

The experimental campaign presented in this work was carried out through quasi-static tensile tests on smooth specimens manufactured from four different automotive steels. The investigated materials include two low-carbon ferritic mild steels, one produced by cold rolling (hereafter referred to as CR04) and the other by hot rolling (HR12), as well as two high-strength steels: a martensitic grade (MTC1300T) and a ferrite/bainite matrix steel subjected to a quenching and partitioning treatment (FORTIFORM 1180, hereafter simply denoted as FORTIFORM).

Each of these steels is typically employed in specific automotive applications according to its mechanical performance. In particular, CR04 is commonly used for deep-drawn inner panels of doors and hoods; MTC1300T is adopted for side-impact reinforcement bars within the doors; HR12 is

utilized for supporting brackets for the attachment of small components to the chassis; and FORTIFORM is designed for energy-absorbing crash components, such as side spars.

The nominal mechanical properties of the selected steels, as provided by the manufacturer in the rolling direction, are reported in Table 17, while their chemical compositions are summarized in Table 18.

Grade	*Yield Stress [MPa]*	*Ultimate Tensile Strength [MPa]*	*Elongation at Break [-]*
CR04	161.9	294.9	46%
HR12	236.3	312.8	42%
MTC1300T	1059.6	1372.8	6.6%
FORTIFORM	912.1	1249.6	15.8%

Table 17: Mechanical properties of the four tested steels provided by the manufacturer.

Mild Steels	***C***	***Si***	***Mn***	***P***	***S***	***Ti***	***Cu***	***Al***
	%max	***%max***	***%max***	***%max***	***%max***	***%max***	***%max***	***%min***
CR04	0.08	0.5	0.5	0.025	0.02	0.3	0.25	0.01
HR12	0.1	0.5	0.5	0.025	0.03	0.3	0.25	0.01
High strength steels	***C***	***Si***	***Mn***	***P***	***S***	***Ti+Nb***	***Cu***	***Al***
	%max	***%max***	***%max***	***%max***	***%max***	***%max***	***%max***	***%min***
MTC1300T	0.35	2.2	3	0.02	0.025	0.15	0.2	0.01
FORTIFORM	0.26	2.2	2.9	0.04	0.01	0.15	0.2	0.01

Table 18: Chemical composition of the four tested steels.

All specimens were waterjet-cut along the rolling direction from the investigated sheet metals, maintaining a common in-plane geometry (Figure 131) and adopting thicknesses consistent with the original sheets (CR04: 1.2 mm, HR12: 3.5 mm, MTC1300T: 1.3 mm, FORTIFORM: 1.6 mm). The specimen design ensured an initial width-to-thickness ratio $w_0/t_0<3$, even for thinner sheets, in order to limit premature failure and excessive localized necking that would otherwise underestimate ductility. A square-like cross-section is ideal, but flat specimens with $w_0/t_0<3$ already provide a reliable post-necking response. The uniform gage length was chosen five times the specimen width to promote uniaxial stress conditions and minimize shoulder effects.

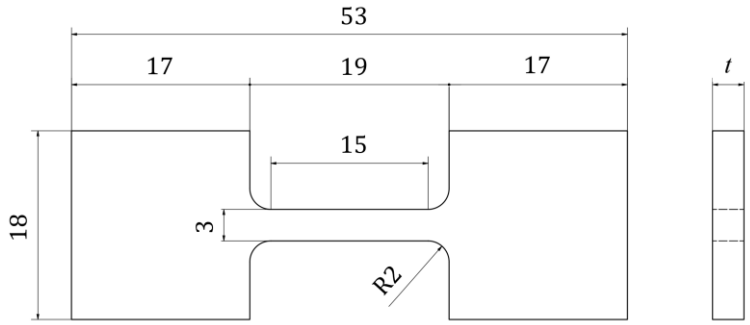


Figure 131: Specimen's geometry. The thickness t depends on the tested sheet.

Quasi-static tensile tests were conducted at University of Catania at a nominal strain rate of 3×10^{-4} s^{-1} using an Instron 8872 hydraulic machine (25 kN load cell), with three repetitions per material. Two high-resolution cameras recorded the tests from frontal and lateral views, enabling the possibility to apply optical technique for measuring strains as Digital Image Correlation (DIC) and pixels count. The thickness evolution was validated via side-view image analysis, ensuring accuracy within 3% for width and within 5% for thickness at failure, despite the severe thinning observed in ductile steels such as CR04.

The acquired data supported the derivation of true stress–strain curves according to the five methodologies, explained before. Neck distortion effects were further quantified through post-mortem image analysis of the fractured specimens (Figure 133), where the effective resisting area and dimensionless ratios such as *t/w* and the distortion coefficient D_f were extracted for each material series.

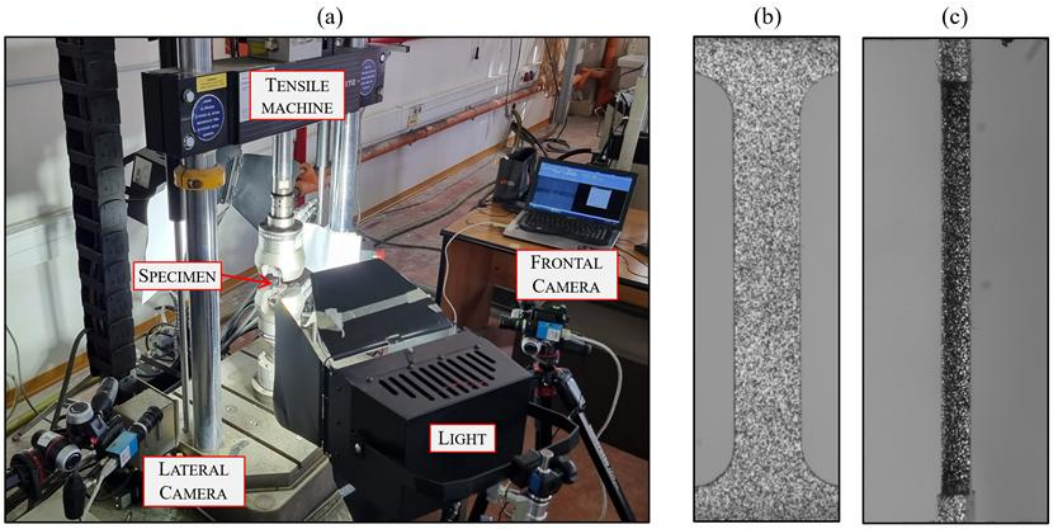


Figure 132: a) Experimental setup used for the tests; b) frontal view of the painted specimen; c) lateral view of the specimen.

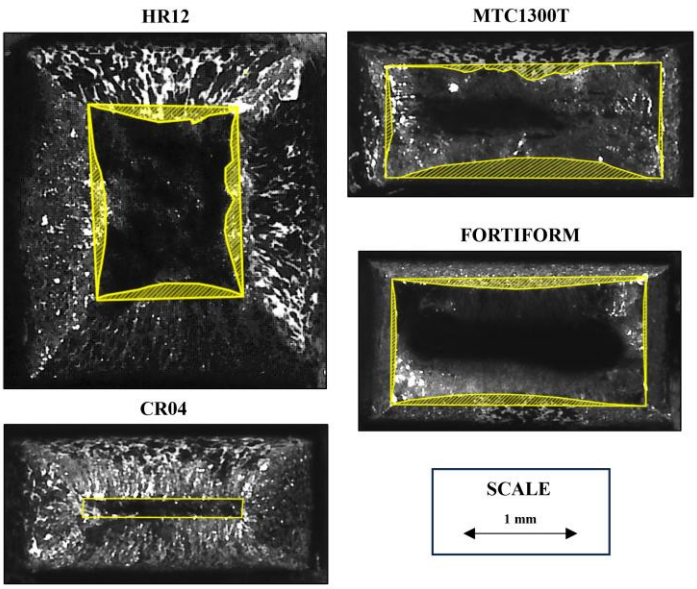


Figure 133: Post-mortem images of the specimens' fracture surface. The yellow region distinguishes the net resistant cross-section from the gross one.

9.3 Experimental data and results

The experimental results were first employed to evaluate material anisotropy by analyzing the thinning–shrinking relationship of the specimens, following the anisotropic width-based approach. The thickness t was estimated using the volume conservation hypothesis and the measurements of gage length elongation and width (eq. (*94*)). Figure 134 reports the normalized thickness t/t_0 versus the normalized width w/w_0, showing that volume conservation holds only up to necking, while post-necking data (i.e., the data that deviates from the red line in the diagrams) must be interpreted differently. Thinning and shrinking values at failure (green triangles in Figure 134) were obtained from fracture surface measurements after the tests. The power-law fits (red lines) were applied to pre-necking data to determine the exponent z, related to the Lankford coefficient ($R=1/z$). For three steels, this constant exponent provided reliable predictions up to failure.

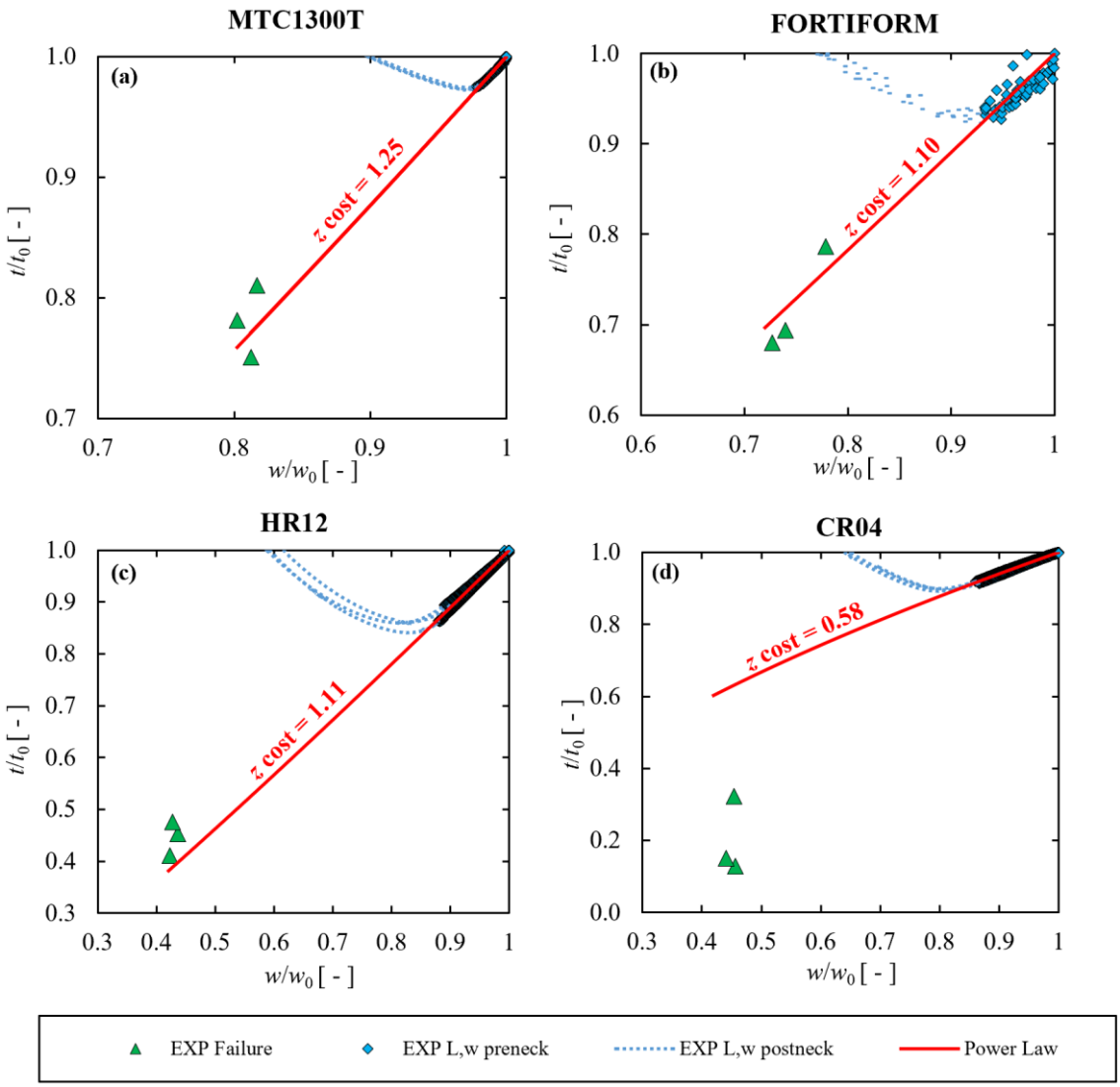


Figure 134: Experimental data of thickness ratio vs width ratio during a tensile test on anisotropic sheet metal. The diamond dots are related to the pre-necking phase of the material. The green triangles are obtained from the post-mortem measurement of the specimen's fracture surface. The red line is the fitting of the pre-neck data using the power-law having the exponent equal to the Lankford coefficient R.

For CR04 steel, it is possible to observe a strong deviation of the data at failure from the power-law fitting, which could mean the anisotropic coefficient R does not remain constant in the post-necking phase. Then, a variable exponent formulation (eq. (103)) was introduced to capture its peculiar high thinning behavior after necking.

$$z\left(\frac{w}{w_0}\right) = \begin{cases} z_{neck} & before\ necking\ onset \\ z_{neck} + \left(z_{fail} - z_{neck}\right)\left(\frac{w - w_{neck}}{w_{failure} - w_{neck}}\right)^{m} & after\ necking\ onset \end{cases} \tag{103}$$

By adding the thickness measurements from the lateral camera, the variability of the anisotropic exponent z is confirmed, as reported in the following Figure 135.

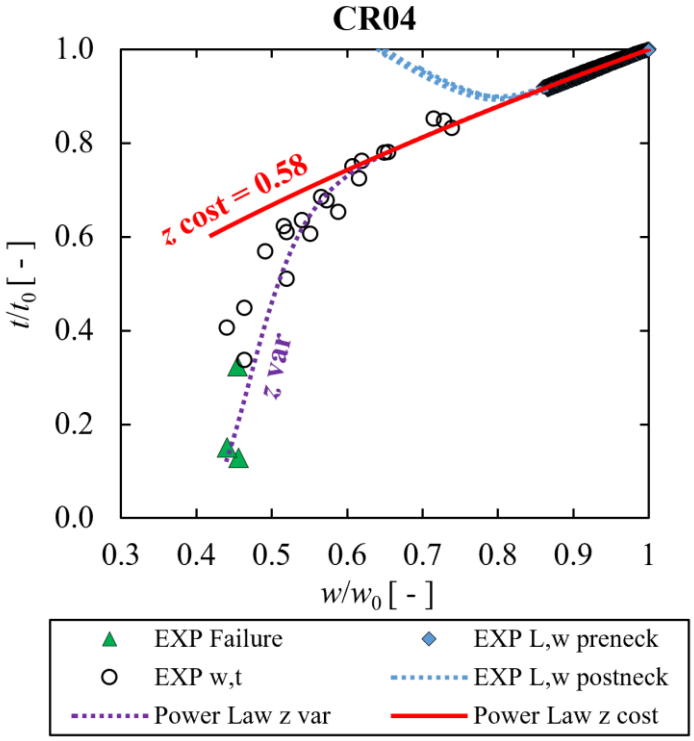


Figure 135: Experimental data of the thickness vs width evolution during the tensile tests performed on CR04 steel. The black circles were obtained from the direct measurements of the thickness by means of a lateral camera. The trend of the black circles deviates from the power-law fitting (constant anisotropic coefficient). The violet dashed line corresponds to a power-law fitting with a variable anisotropic exponent z.

These information are essential to apply the methodologies for deriving the true stress-strain curves of sheet metals, accounting for the effect of the anisotropic behavior of the material and the distortion of the necking section. The anisotropic and distortion parameters for each steel are summarized in the following Table 19.

	CR04	***HR12***	***MTC1300T***	***FORTIFORM***
w_f/w_0	0.450	0.428	0.810	0.748
t_f/t_0	0.200	0.448	0.781	0.720
z pre-neck	0.58	1.11	1.25	1.10
R pre-neck	1.72	0.90	0.80	0.91
m	7.3	0	0	0
$D_f = \frac{A_{Dist+Aniso}}{A_{Aniso}}\Big\vert_{fail}$	1	0.84	0.84	0.86

Table 19: Anisotropy and distortion parameters of the four tested steels.

The different cross-section estimations are the basis for the five true stress–strain curve approximations (Figure 136), ranging from the simplest elongation length-based to the most comprehensive anisotropy + distortion approach. Among them, the latter procedure proved the most accurate, since it accounts for necking effect, anisotropy, and distortion simultaneously, while the others systematically underestimate or misrepresent the post-necking response. The comparison revealed that length-based curves significantly underestimate material's hardening after only 10–30% of the strain life depending on the necking strain, whereas the DIC-based and isotropic width-based approaches may slightly over or underestimate the tensile response, depending on specimen's width-to-thickness aspect ratio and anisotropy.

Distortion was negligible for CR04 but highly relevant for MTC1300T, where neglecting it led to errors up to 20% in fracture strain, compared to the simple anisotropic-based approach.

Strain at necking was found to be quite consistent across all procedures, while strain at failure varied considerably depending on the approximation, with errors approximately equal to 200% for the most ductile materials (Figure 137).

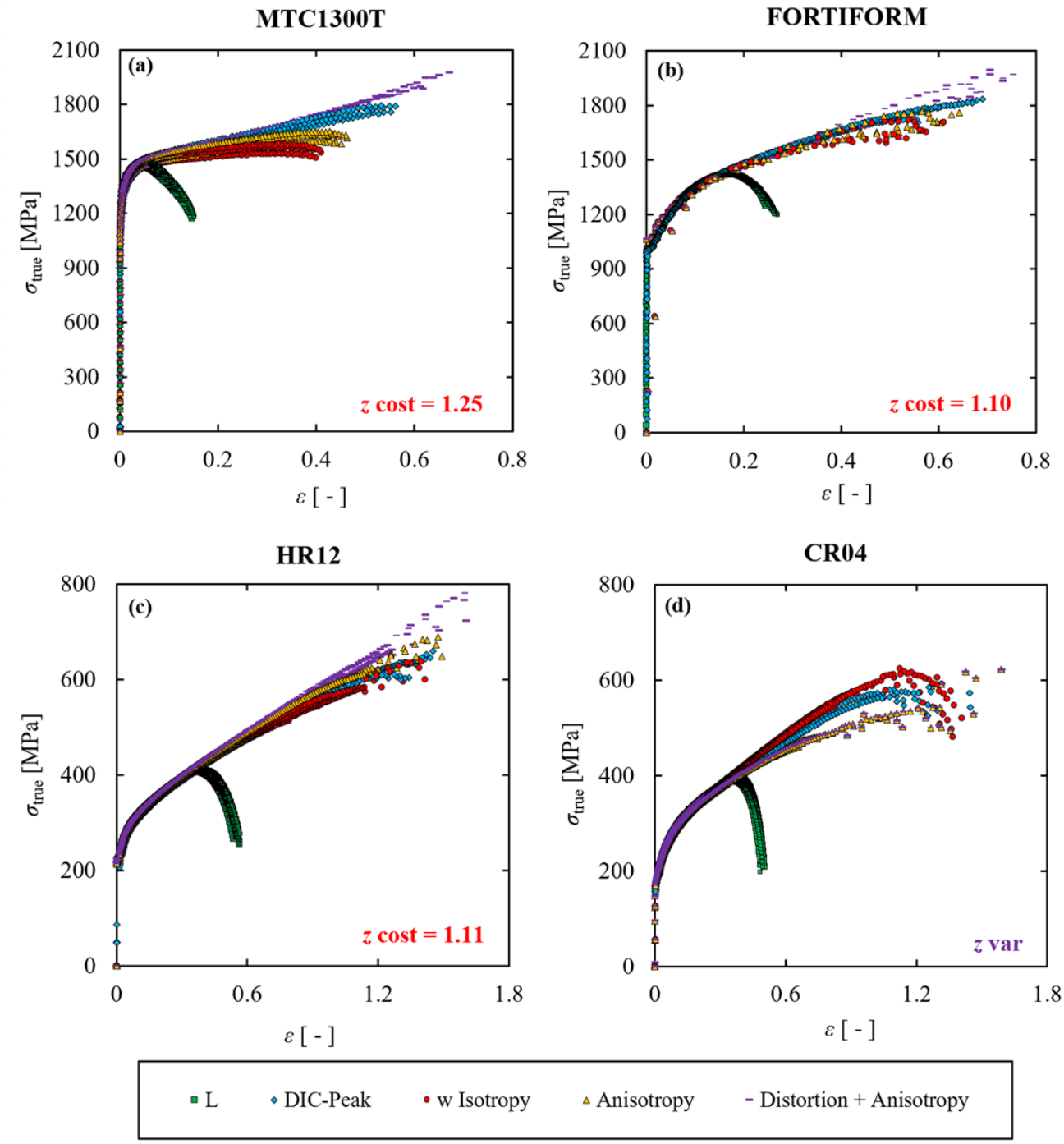


Figure 136: True stress-strain curves for the tested anisotropic sheets, obtained from the five approaches proposed in the present work .

Finally, the different methods for estimating the Lankford coefficient (e.g., DIC-Peak, L–w ratios, power-law fits) are compared in the following Figure 138. Results shows that CR04 is the unique steel having R > 1, while HR12 and FORTIFORM, subjected to high-temperature processing, displayed nearly isotropic behavior with R≈1.

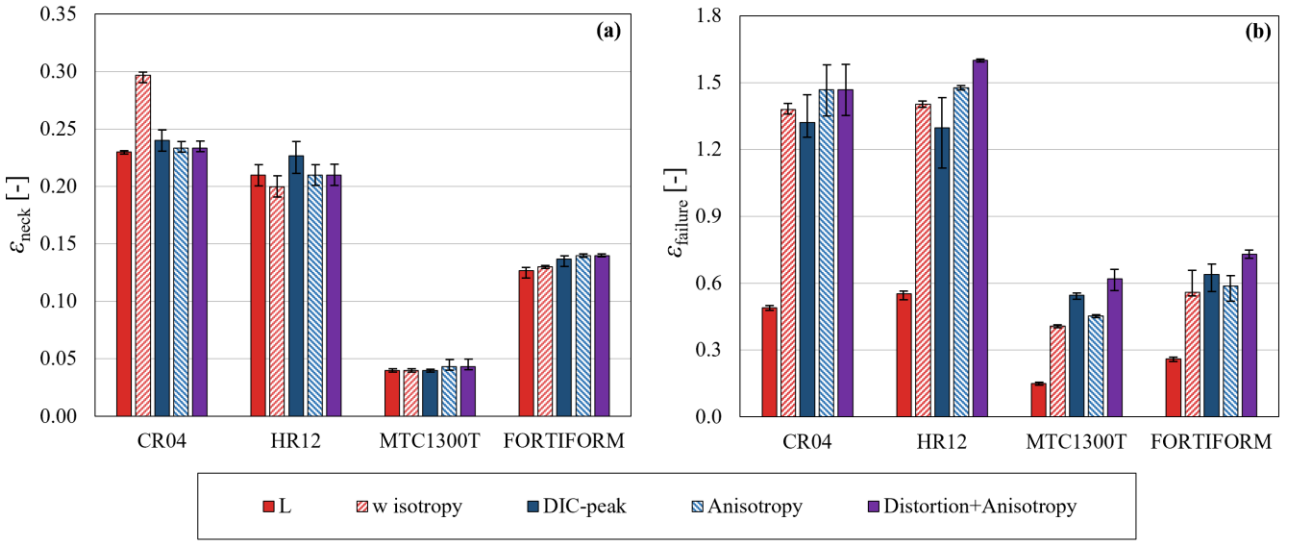


Figure 137: Mean values and corresponding scattering of the necking strain and failure strain estimated by the five approaches proposed in this work.

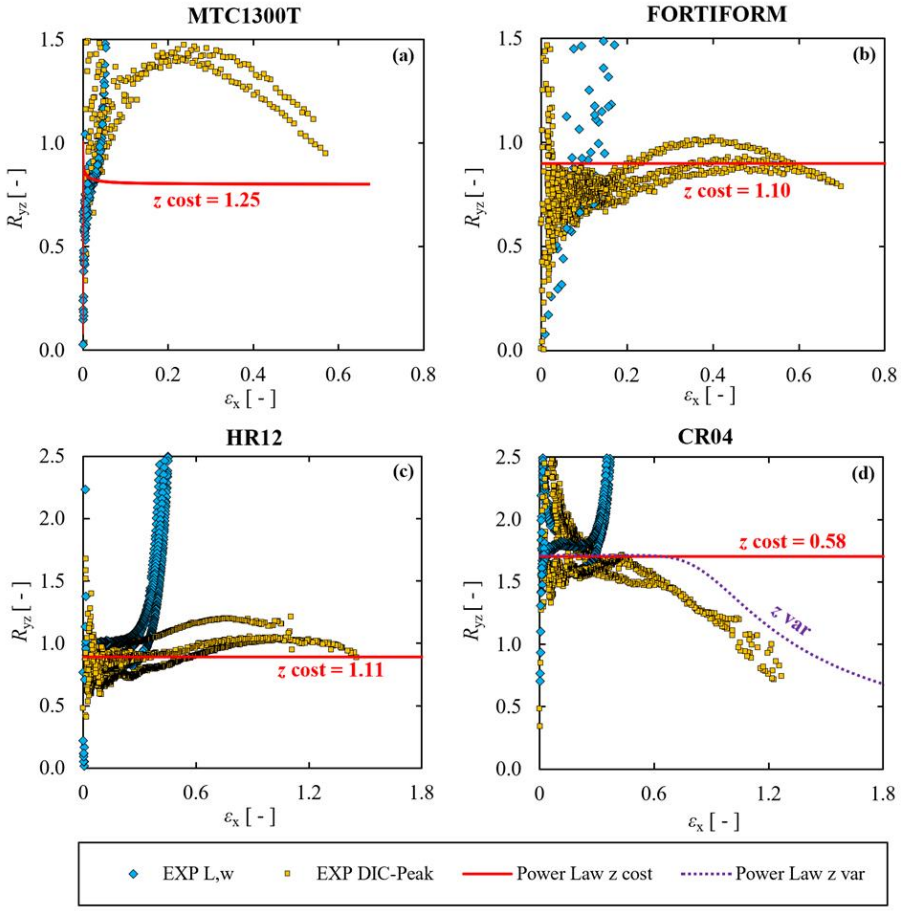


Figure 138: Comparison between the Lankford coefficient derived from elongation and width measurements (blue diamonds), DIC strain measurements (yellow squares), and power-law fitting (red line).

9.4 Conclusions

In the present chapter, the tensile mechanical behavior of four anisotropic sheets under quasi-static conditions was investigated. Since the determination of the experimental true stress–strain curve is essential for the subsequent material characterization, two novel methodologies were proposed for this aim. These approaches account for both the anisotropy of the material and the distortion of the necking section in the estimation of the resistant cross-section area of rectangular specimens.

Starting from the definition of the Lankford coefficient *R*, which represents a measure of anisotropy in a given material direction, it was demonstrated that the thickness evolution of the specimen as a function of its width follows a power law, whose exponent is exactly the reciprocal of this coefficient. If the material's anisotropy remains constant throughout the tensile test, then the pre-necking thinning ratio vs. shrinking ratio data, as well as the post-fracture analyses, can be fitted by a power law with a constant exponent. For three of the four tested steels (e.g., MTC1300T, HR12, and FORTIFORM), the Lankford coefficient remained constant over the entire test, whereas for CR04 steel, both the post-fracture data and the thickness measurements obtained from the second lateral camera demonstrated that anisotropy in this material varies in the post-necking phase.

Moreover, the localized necking phenomenon occurring in flat specimens induces a distortion of the necking section, which does not remain rectangular up to fracture. From the analysis of the fracture surface, the distortion parameter at failure was estimated, thus including the contribution of this phenomenon in the assessment of the specimen's net resistant area. The proposed *Aniso+Dist* methodology enabled the extension of the true stress–strain curves of the materials into the post-necking regime, providing an accurate estimation of the averaged axial strain across the section and the material's hardening, compared with elongation-based or DIC-based approaches, which may either underestimate or overestimate the true strain.

Conclusions, main contributions of the present work, and future developments

This doctoral thesis has progressed along two interconnected research branches: the advanced thermo-mechanical modeling of Power Electronics packages and the implementation of experimental-numerical methodologies for the elastoplastic characterization of structural materials. The present thesis addressed complex issues related to the reliability of power electronic devices and the fundamental understanding of material behavior under various loading conditions. The main scientific and methodological contributions of this work can be summarized as follows:

1. *Analysis of Geometry and Defect Effects*: The significant impact of passivation layer deposition geometry (sharp vs. rounded edges) and process-induced defects like "dry spots" on local stress distributions at critical package interfaces was demonstrated, providing quantitative insights for design optimization.
2. *Development of Efficient Modeling Approaches (Global-Local)*: A Global-Local FEM strategy was implemented and validated, enabling accurate analysis of stress concentrations in specific package regions (e.g., passivation corners), reducing computational cost compared to full-domain fine-mesh modeling. The beneficial role of the polyimide layer in mitigating stress gradients was also highlighted.
3. *Simulation of Manufacturing Process (RTM)*: An innovative FEM procedure was proposed to simulate the Resin Transfer Molding (RTM) process, modeling the evolution of the resin's thermo-mechanical properties during curing and its interaction with the substrate. This approach allowed quantification of permanent deformations (warpage) and residual stresses induced by the manufacturing process, which are often neglected in standard reliability analyses.
4. *Implementation and Comparison of Damage Models:* Various damage models were implemented and compared: Cohesive Zone Models (CZM) for interfacial delamination (e.g., Copper/Resin, Si_3N_4/Resin), a Modified Tresca (MT) criterion for brittle fracture in the resin, and the analysis of critical parameters (accumulated plastic strain, triaxiality factor) for ductile damage in metals (Solder, Copper, Polyimide). A sensitivity analysis on CZM parameters was conducted, providing guidelines for their calibration. The crucial importance of elastoplastic

modeling over purely elastic approaches for accurately predicting residual stresses and strain accumulation was emphasized.

5. *Analysis under Spatial Thermal Gradients:* The package's thermo-mechanical response under spatial thermal gradients -both constant and time-varying, characteristic of active power cycles- was investigated, demonstrating the impact of such gradients on stress distributions and plastic strain accumulation.
6. *Characterization of Polycarbonate (PC) under Static and Dynamic Regimes:* The complex tensile behavior of Polycarbonate (PC), characterized by necking, strain propagation, and post-propagation hardening phenomena, was studied in detail, analyzing the influence of specimen geometry (round vs. flat) and strain rate (from quasi-static up to 1000 s^{-1}, utilizing a Split Hopkinson Tension Bar).
7. *Development of Methodologies for Flow Curve Derivation (PC):* Two experimental-numerical methodologies were proposed and validated (a direct one based on Bridgman/Siebel theory for round specimens, and a semi-inverse one based on the "Generalized Necking" concept for flat specimens) to correct experimental true stress-strain curves (from area or elongation measurements) by eliminating the effect of stress state triaxiality, thereby obtaining the constitutive material flow curve.
8. *Coupled Rate-Temperature Constitutive Modeling for PC (PC-DATS):* A multiplicative constitutive model (PC-DATS) was developed and implemented (via Fortran subroutine) for Polycarbonate, decoupling and quantifying the combined effects of strain rate (dynamic amplification, including the "freezing" phenomenon) and temperature (static thermal softening and adiabatic self-heating). The model was validated against experimental data across a wide range of strain rates.
9. *Characterization of Anisotropic Sheet Metals:* An enhanced methodology ("Aniso+Dist") was proposed to extend the true stress-strain curve of sheet metals into the post-necking regime, simultaneously accounting for material anisotropy (estimated via the Lankford coefficient, potentially variable) and the progressive distortion of the minimum cross-section due to localized necking. This was successfully applied to four different automotive steels.

It is noteworthy that the suitability of Finite Element Analyses as a tool for the advanced mechanical design of power modules and for the prediction of their durability under operating conditions, strongly depends on the effectiveness of the material models implemented in simulating complex behaviours, (e.g. the elastoplastic response of the solder also reflecting on its ductile damageability or the adhesion

at the resin-copper interface joining materials with very different mechanical properties. Therefore, the present doctoral work opens several avenues for future investigations, both in the field of power module modeling and in material characterization.

- *Advanced Modeling of Manufacturing Processes:* The procedure developed for the Resin Transfer Molding process could be extended to include other critical manufacturing stages, such as die attach soldering or wire bonding processes for obtaining a more comprehensive estimation of the initial stress/strain state of the package before the operating life. Experimental validation of the predicted residual warpage would also be valuable.
- *Evolution of damage due to thermal fatigue:* The implemented damage models (CZM, MT) could be further developed to incorporate evolutionary laws describing damage accumulation cycle by cycle (thermo-mechanical fatigue), especially for solder joints and interfaces, enabling more accurate fatigue life predictions for the device.
- *Experimental validation of the results regarding the FEM analyses:* It would be crucial to complement the simulations with targeted experimental validation. Techniques such as *in-situ* optical methods (Digital Image Correlation, Moiré interferometry) during thermal cycling could measure strain fields and warpage, while post-mortem microstructural analyses could correlate damage predictions with actual degradation.
- *Characterization of the materials at elevated temperatures:* A further contribution in the mechanical modeling of power modules might be the experimental characterization of materials, particularly polymers like polyimide and epoxy resins, as well as solder alloys, to relevant power module operating temperatures (up to 150-200°C or higher for future SiC/GaN generations) is essential, including phenomena such as creep and glass transition.
- *Modeling of the mechanical response of Polycarbonate:* The PC-DATS constitutive model could be enhanced by incorporating viscoelastic effect exhibited by Polycarbonate, providing a more accurate description of the softening behavior of the material and investigating the potential evolution of elastic constants following large plastic deformations. Furthermore, its validation could be extended to multi-axial stress states such as: compression, shear, and biaxial state.

References

1. Yang, Y.; Dorn-Gomba, L.; Rodriguez, R.; Mak, C.; Emadi, A. Automotive Power Module Packaging: Current Status and Future Trends. *IEEE Access* **2020**, *8*, 160126–160144, doi:10.1109/ACCESS.2020.3019775.
2. Huazhong University of Science and Technology; Chen, C. A Review of SiC Power Module Packaging: Layout, Material System and Integration. *CPSS Trans. Power Electron. Appl.* **2017**, *2*, 170–186, doi:10.24295/CPSSTPEA.2017.00017.
3. Lee, H.; Smet, V.; Tummala, R. A Review of SiC Power Module Packaging Technologies: Challenges, Advances, and Emerging Issues. *IEEE J. Emerg. Sel. Top. Power Electron.* **2020**, *8*, 239–255, doi:10.1109/JESTPE.2019.2951801.
4. Ji, S.; Zhang, Z.; Wang, F. Overview of High Voltage Sic Power Semiconductor Devices: Development and Application. *CES Trans. Electr. Mach. Syst.* **2017**, *1*, 254–264, doi:10.23919/tems.2017.8086104.
5. Homberger, J.; Lostetter, A.B.; Olejniczak, K.J.; McNutt, T.; Lal, S.M.; Mantooth, A. Silicon-Carbide (SiC) Semiconductor Power Electronics for Extreme High-Temperature Environments. In Proceedings of the 2004 IEEE Aerospace Conference Proceedings (IEEE Cat. No.04TH8720); IEEE: Big Sky, MT, USA, 2004; Vol. 4, pp. 2538–2555.
6. Kabaar, A.B.; Buttay, C.; Dezellus, O.; Estevez, R.; Gravouil, A.; Gremillard, L. Characterization of Materials and Their Interfaces in a Direct Bonded Copper Substrate for Power Electronics Applications. *Microelectron. Reliab.* **2017**, *79*, 288–296, doi:10.1016/j.microrel.2017.06.001.
7. Mishra, S.; Sharma, A.; Jung, D.H.; Jung, J.P. Recent Advances in Active Metal Brazing of Ceramics and Process. *Met. Mater. Int.* **2020**, *26*, 1087–1098, doi:10.1007/s12540-019-00536-4.
8. Mirone, G.; Sitta, A.; D'Arrigo, G.; Calabretta, M. Material Characterization and Warpage Modeling for Power Devices Active Metal Brazed Substrates. *IEEE Trans. Device Mater. Reliab.* **2019**, *19*, 537–542, doi:10.1109/TDMR.2019.2932971.
9. Pichon, P.-Y.; Brandelero, J. Relative Importance of Solder and Wire Bond Defects on the Maximum Junction Temperature of IGBT Devices. *Microelectron. Reliab.* **2021**, *126*, 114250, doi:10.1016/j.microrel.2021.114250.
10. Wang, L.; Zhang, T.; Yang, F.; Ma, D.; Zhao, C.; Pei, Y.; Gan, Y. Cu Clip-Bonding Method With Optimized Source Inductance for Current Balancing in Multichip SiC MOSFET Power Module. *IEEE Trans. Power Electron.* **2022**, *37*, 7952–7964, doi:10.1109/TPEL.2022.3141373.
11. Lee, C.-C.; Chen, M.-T.; Chuang, J.-C. Process-Induced Influences on Epoxy-Based Encapsulated Reliability of High Power Modules. *Int. J. Mech. Sci.* **2025**, *297–298*, 110394, doi:10.1016/j.ijmecsci.2025.110394.

12. Donetti, L.; Mauro, S.; Sequenzia, G.; Calabretta, M.; Sitta, A. Effects of the Pin-Fins Cooler Roughness on the Thermo-Fluid Dynamics Performance of a SiC Power Module. *Int. J. Thermofluids* **2024**, *22*, 100609, doi:10.1016/j.ijft.2024.100609.
13. Mirone, G.; Barbagallo, R.; Bua, G.; Sitta, A.; Calabretta, M.; Sequenzia, G. Thermal-Structural Modeling of Power Electronic Package: Effects of Deposition Geometry and Dry Spot on the Stress Distributions. *IOP Conf. Ser. Mater. Sci. Eng.* **2024**, *1306*, 012012, doi:10.1088/1757-899X/1306/1/012012.
14. Mirone, G.; Barbagallo, R.; Corallo, L.; Bua, G.; La Rosa, G.; Fargione, G.; Giudice, F. Nonlinear Elastoplastic Response and Damage Modeling in Power Electronics Packages Under Thermal Cycling. In Proceedings of the AIAS 2024; MDPI, April 16 2025; p. 50.
15. JEDEC STANDARD JESD22-A104E-TCT, October 2014.
16. ECPE Guideline AQG 324 Qualification of Power Modules for Use in Power Electronics Converter Units in Motor Vehicles.
17. Ciappa, M. Selected Failure Mechanisms of Modern Power Modules. *Microelectron. Reliab.* **2002**, *42*, 653–667, doi:10.1016/S0026-2714(02)00042-2.
18. Chen, Y.; Lan, X.; Li, L.; Li, X.; Zhang, Z.; Xin, G. Failure Evolution Analysis of SiC Power Modules in Electric-Thermal-Mechanical Multi-Physical Fields. *Microelectron. Reliab.* **2025**, *169*, 115751, doi:10.1016/j.microrel.2025.115751.
19. Hung, T.-Y.; Huang, C.-J.; Lee, C.-C.; Wang, C.-C.; Lu, K.-C.; Chiang, K.-N. Investigation of Solder Crack Behavior and Fatigue Life of the Power Module on Different Thermal Cycling Period. *Microelectron. Eng.* **2013**, *107*, 125–129, doi:10.1016/j.mee.2012.09.014.
20. Otiaba, K.C.; Bhatti, R.S.; Ekere, N.N.; Mallik, S.; Ekpu, M. Finite Element Analysis of the Effect of Silver Content for Sn–Ag–Cu Alloy Compositions on Thermal Cycling Reliability of Solder Die Attach. *Eng. Fail. Anal.* **2013**, *28*, 192–207, doi:10.1016/j.engfailanal.2012.10.008.
21. Roumanille, P.; Ben Romdhane, E.; Pin, S.; Nguyen, P.; Delétage, J.-Y.; Guédon-Gracia, A.; Frémont, H. Evaluation of Thermomechanical Fatigue Lifetime of BGA Lead-Free Solder Joints and Impact of Isothermal Aging. *Microelectron. Reliab.* **2021**, *126*, 114201, doi:10.1016/j.microrel.2021.114201.
22. Alaferdov, A.; Yoshioka, R.T.; Nunes, C.C.P.; Sousa, M.D.; Carvalho, V.; Namba, I.F.; Coral, C. Strategies for Avoiding Delamination in System-in-Packaging Devices. *Microelectron. Eng.* **2023**, *281*, 112089, doi:10.1016/j.mee.2023.112089.
23. Miyazakia, H.; Iwakiri, S.; Hirao, K.; Fukuda, S.; Izu, N.; Yoshizawa, Y.; Hyuga, H. Effect of High Temperature Cycling on Both Crack Formation in Ceramics and Delamination of Copper Layers in Silicon Nitride Active Metal Brazing Substrates. *Ceram. Int.* **2017**, *43*, 5080–5088, doi:10.1016/j.ceramint.2017.01.020.
24. Mirone, G.; Barbagallo, R.; Bua, G.; La Rosa, G. Finite Element Simulation and Sensitivity Analysis of the Cohesive Parameters for Delamination Modeling in Power Electronics Packages. *Materials* **2023**, *16*, 4808, doi:10.3390/ma16134808.

25. Marc 2023.4 Volume A: Theory and User Information.
26. Dudek, R.; Doering, R.; Pufall, R.; Kanert, W.; Seiler, B.; Rzepka, S.; Michel, B. Delamination Modeling for Power Packages by the Cohesive Zone Approach. In Proceedings of the 13th InterSociety Conference on Thermal and Thermomechanical Phenomena in Electronic Systems; IEEE: San Diego, CA, USA, May 2012; pp. 187–193.
27. Gschwandl, M.; Fuchs, P.F.; Mitev, I.; Yalagach, M.; Antretter, T.; Qi, T.; Schingale, A. Modeling of Manufacturing Induced Residual Stresses of Viscoelastic Epoxy Mold Compound Encapsulations. In Proceedings of the 2017 IEEE 19th Electronics Packaging Technology Conference (EPTC); IEEE: Singapore, December 2017; pp. 1–8.
28. Bua, G. Caratterizzazione e Modellazione Termo-Meccanica di Moduli di Potenza. **2022**.
29. Kabaar, A.B.; Buttay, C.; Dezellus, O.; Estevez, R.; Gravouil, A.; Gremillard, L. Characterization of Materials and Their Interfaces in a Direct Bonded Copper Substrate for Power Electronics Applications. *Microelectron. Reliab.* **2017**, *79*, 288–296, doi:10.1016/j.microrel.2017.06.001.
30. Agag, T.; Koga, T.; Takeichi, T. Studies on Thermal and Mechanical Properties of Polyimide–Clay Nanocomposites. *Polymer* **2001**, *42*, 3399–3408, doi:10.1016/S0032-3861(00)00824-7.
31. Khatibi, G.; Betzwar Kotas, A. Mechanical Properties and Life Time of High Pb-Containing Solder Joints. In Proceedings of the 2017 21st European Microelectronics and Packaging Conference (EMPC) & Exhibition; IEEE: Warsaw, September 2017; pp. 1–6.
32. Yang, K.; Zhou, L.; Wu, F.; Yang, G.; Ding, L.; Li, K.; Li, X. Simulation of Crack Propagation in Solder Layer of IGBT Device under Temperature Shock by Viscoplastic Phase Field Method. *Eng. Fract. Mech.* **2023**, *284*, 109260, doi:10.1016/j.engfracmech.2023.109260.
33. Huang, T.; Singh, B.P.; Liu, Y.; Norrga, S. Failure Characterization of Discrete SiC MOSFETs under Forward Power Cycling Test. *Energies* **2024**, *17*, 2557, doi:10.3390/en17112557.
34. Munro, R.G. Material Properties of a Sintered α-SiC. *J. Phys. Chem. Ref. Data* **1997**, *26*, 1195–1203, doi:10.1063/1.556000.
35. *Tailoring of Mechanical Properties of Si3N4 Ceramics*; Hoffmann, M.J., Petzow, G., NATO, Eds.; NATO ASI series Series E, Applied sciences; Kluwer Academic: Dordrecht London, 1994; ISBN 978-0-7923-3119-3.
36. Wiederhorn, S.M.; Anne Fields, B.; Hockey, B.J. Fracture of Silicon Nitride and Silicon Carbide at Elevated Temperatures. *Mater. Sci. Eng. A* **1994**, *176*, 51–60, doi:10.1016/0921-5093(94)90958-X.
37. Bouzakis, K.-D.; Tsiafis, I.; Michailidis, N.; Tsouknidas, A. Determination of Epoxy Resins' Mechanical Properties by Experimental-Computational Procedures in Tension. *J. Balk. Tribol. Assoc.* **2009**, *15*.
38. Liu, Y.; Liu, Y.; Yuan, Z.; Chen, T.; Lee, K.; Belani, S. Warpage Analysis and Improvement for a Power Module. In Proceedings of the 2013 IEEE 63rd Electronic Components and Technology Conference; IEEE: Las Vegas, NV, USA, May 2013; pp. 475–480.

39. Zhu, N.; Van Wyk, J.D.; Liang, Z.X. Thermal-Mechanical Stress Analysis in Embedded Power Modules. In Proceedings of the 2004 IEEE 35th Annual Power Electronics Specialists Conference (IEEE Cat. No.04CH37551); IEEE: Aachen, Germany, 2004; pp. 4503–4508.
40. Ye, H.; Lin, M.; Basaran, C. Failure Modes and FEM Analysis of Power Electronic Packaging. *Finite Elem. Anal. Des.* **2002**, *38*, 601–612, doi:10.1016/S0168-874X(01)00094-4.
41. Sitta, A.; Renna, M.; Messina, A.; Mirone, G.; D'Arrigo, G.; Calabretta, M. *Power Module Ceramic Substrates: Mechanical Characterization and Modeling*; 2020; p. 5;.
42. Abuelnaga, A.; Narimani, M.; Bahman, A.S. A Review on IGBT Module Failure Modes and Lifetime Testing. *IEEE Access* **2021**, *9*, 9643–9663, doi:10.1109/ACCESS.2021.3049738.
43. Valdoleiros, J.; Akhavan-Safar, A.; Maleki, P.; Videira, P.F.C.; Carbas, R.J.C.; Marques, E.A.S.; Karunamurthy, B.; Da Silva, L.F.M. Effects of Temperature on the Fracture Response of EMC-Si Interface Found in Multilayer Semiconductor Components. *Surfaces* **2025**, *8*, 2, doi:10.3390/surfaces8010002.
44. Benabou, L.; Sun, Z.; Dahoo, P.R. A Thermo-Mechanical Cohesive Zone Model for Solder Joint Lifetime Prediction. *Int. J. Fatigue* **2013**, *49*, 18–30, doi:10.1016/j.ijfatigue.2012.12.008.
45. Li, S.; Thouless, M.D.; Waas, A.M.; Schroeder, J.A.; Zavattieri, P.D. Mixed-Mode Cohesive-Zone Models for Fracture of an Adhesively Bonded Polymer–Matrix Composite. *Eng. Fract. Mech.* **2006**, *73*, 64–78, doi:10.1016/j.engfracmech.2005.07.004.
46. Ibrahim, A.H.; Watson, B.; Jahed, H.; Rezaee, S.; Royer, C.; Cronin, D.S. Prediction of Bonded Asymmetric Metallic Cross-Tension and Single Lap Shear Joints Using Finite Element Model with Material-Level Adhesive Properties and Cohesive Zone Method. *Int. J. Adhes. Adhes.* **2023**, *120*, 103298, doi:10.1016/j.ijadhadh.2022.103298.
47. Carneiro Neto, R.M.; De Medeiros Sales, F.; Sampaio, E.M.; Akhavan-Safar, A.; De Assis, J.T.; Da Silva, L.F.M. Cohesive Zone Models for the Shear Creep Life Assessment of Bonded Joints. *Mech. Time-Depend. Mater.* **2023**, *27*, 1139–1152, doi:10.1007/s11043-022-09548-x.
48. Calabretta, M.; Sitta, A.; Oliveri, S.M.; Sequenzia, G. Copper to Resin Adhesion Characterization for Power Electronics Application: Fracture Toughness and Cohesive Zone Analysis. *Eng. Fract. Mech.* **2022**, *266*, 108339, doi:10.1016/j.engfracmech.2022.108339.
49. Liu, S.; Yan, Y.; Zhou, Y.; Han, B.; Wang, B.; Zhang, D.; Xue, S.; Wang, Z.; Yu, K.; Shi, Y.; et al. Thermal Induced Interface Mechanical Response Analysis of SMT Lead-Free Solder Joint and Its Adaptive Optimization. *Micromachines* **2022**, *13*, 908, doi:10.3390/mi13060908.
50. Lall, P.; Yihua Luo; Nguyen, L. De-Bonding Simulation of Cu-Al Wire Bond Intermetallic Compound Layers. In Proceedings of the 2016 15th IEEE Intersociety Conference on Thermal and Thermomechanical Phenomena in Electronic Systems (ITherm); IEEE: Las Vegas, NV, USA, May 2016; pp. 862–870.
51. Long, H.; Liu, Y.; Wei, Y. Debonding Characterization of Stiff Film/Compliant Substrate Systems Based on the Bilinear Cohesive Zone Model. *Eng. Fract. Mech.* **2022**, *265*, 108363, doi:10.1016/j.engfracmech.2022.108363.

52. Kleinendorst, S.M.; Fleerakkers, R.; Cattarinuzzi, E.; Vena, P.; Gastaldi, D.; Van Maris, M.P.F.H.L.; Hoefnagels, J.P.M. Micron-Scale Experimental-Numerical Characterization of Metal-Polymer Interface Delamination in Stretchable Electronics Interconnects. *Int. J. Solids Struct.* **2020**, *204–205*, 52–64, doi:10.1016/j.ijsolstr.2020.08.011.
53. Msolli, S.; Baazaoui, A.; Alexis, J.; Kim, H.S. Identification of Damage and Fracture Modes in Power Electronic Packaging from Experimental Micro-Shear Tests and Finite Element Modeling. *Eng. Fract. Mech.* **2018**, *188*, 470–492, doi:10.1016/j.engfracmech.2017.09.014.
54. Dudek, R.; Döring, R.; Mathew, A.; Otto, A.; Rzepka, S. Modelling Thermal Fatigue in Power Electronics. In Proceedings of the 2022 23rd International Conference on Thermal, Mechanical and Multi-Physics Simulation and Experiments in Microelectronics and Microsystems (EuroSimE); April 2022; pp. 1–11.
55. Gurson, A.L. Continuum Theory of Ductile Rupture by Void Nucleation and Growth: Part I—Yield Criteria and Flow Rules for Porous Ductile Media. *J. Eng. Mater. Technol.* **1977**, *99*, 2–15, doi:10.1115/1.3443401.
56. Tvergaard, V.; Needleman, A. Analysis of the Cup-Cone Fracture in a Round Tensile Bar. *Acta Metall.* **1984**, *32*, 157–169, doi:10.1016/0001-6160(84)90213-X.
57. Lemaitre, J. Micro-Mechanics of Crack Initiation. *Int. J. Fract.* **1990**, *42*, 87–99, doi:10.1007/BF00018615.
58. Bonora, N. A Nonlinear CDM Model for Ductile Failure. *Eng. Fract. Mech.* **1997**, *58*, 11–28, doi:10.1016/S0013-7944(97)00074-X.
59. McClintock, F.A. A Criterion for Ductile Fracture by the Growth of Holes. *J. Appl. Mech.* **1968**, *35*, 363–371, doi:10.1115/1.3601204.
60. Rice, J.R.; Tracey, D.M. On the Ductile Enlargement of Voids in Triaxial Stress Fields∗. *J. Mech. Phys. Solids* **1969**, *17*, 201–217, doi:10.1016/0022-5096(69)90033-7.
61. Bao, Y.; Wierzbicki, T. On Fracture Locus in the Equivalent Strain and Stress Triaxiality Space. *Int. J. Mech. Sci.* **2004**, *46*, 81–98, doi:10.1016/j.ijmecsci.2004.02.006.
62. Cockcroft, M.G.; Lathan, D.J. *Ductility and the Workability of Metals*; 1968;
63. Mirone, G.; Corallo, D. A Local Viewpoint for Evaluating the Influence of Stress Triaxiality and Lode Angle on Ductile Failure and Hardening. *Int. J. Plast.* **2010**, *26*, 348–371, doi:10.1016/j.ijplas.2009.07.006.
64. Xue, L. Damage Accumulation and Fracture Initiation in Uncracked Ductile Solids Subject to Triaxial Loading. *Int. J. Solids Struct.* **2007**, *44*, 5163–5181, doi:10.1016/j.ijsolstr.2006.12.026.
65. Coppola, T.; Cortese, L.; Folgarait, P. The Effect of Stress Invariants on Ductile Fracture Limit in Steels. *Eng. Fract. Mech.* **2009**, *76*, 1288–1302, doi:10.1016/j.engfracmech.2009.02.006.
66. Krieger, W.E.R.; Raghavan, S.; Sitaraman, S.K. Experiments for Obtaining Cohesive-Zone Parameters for Copper-Mold Compound Interfacial Delamination. *IEEE Trans. Compon. Packag. Manuf. Technol.* **2016**, *6*, 1389–1398, doi:10.1109/TCPMT.2016.2589223.

67. Hu, Y.; Xia, Z.; Ellyin, F. The Failure Behavior of an Epoxy Resin Subject to Multiaxial Loading. In Proceedings of the Pipelines 2006; American Society of Civil Engineers: Chicago, Illinois, United States, July 28 2006; pp. 1–8.
68. Morelle, X.P.; Chevalier, J.; Bailly, C.; Pardoen, T.; Lani, F. Mechanical Characterization and Modeling of the Deformation and Failure of the Highly Crosslinked RTM6 Epoxy Resin. *Mech. Time-Depend. Mater.* **2017**, *21*, 419–454, doi:10.1007/s11043-016-9336-6.
69. Krieger, W.E.R.; Raghavan, S.; Sitaraman, S.K. Experiments for Obtaining Cohesive-Zone Parameters for Copper-Mold Compound Interfacial Delamination. *IEEE Trans. Compon. Packag. Manuf. Technol.* **2016**, *6*, 1389–1398, doi:10.1109/TCPMT.2016.2589223.
70. Adler, C.; Morais, P.; Akhavan-Safar, A.; Carbas, R.J.C.; Marques, E.A.S.; Karunamurthy, B.; Da Silva, L.F.M. Cohesive Properties of Bimaterial Interfaces in Semiconductors: Experimental Study and Numerical Simulation Using an Inverse Cohesive Contact Approach. *Materials* **2024**, *17*, 289, doi:10.3390/ma17020289.
71. Miklowitz, J. The Initiation and Propagation of the Plastic Zone along a Tension Specimen of Nylon. *J. Colloid Sci.* **1947**, *2*, 193–215, doi:10.1016/0095-8522(47)90021-4.
72. G'sell, C.; Jonas, J.J. Determination of the Plastic Behaviour of Solid Polymers at Constant True Strain Rate. *J. Mater. Sci.* **1979**, *14*, 583–591, doi:10.1007/BF00772717.
73. G'sell, C.; Aly-Helal, N.A.; Jonas, J.J. Effect of Stress Triaxiality on Neck Propagation during the Tensile Stretching of Solid Polymers. *J. Mater. Sci.* **1983**, *18*, 1731–1742, doi:10.1007/BF00542069.
74. Buisson, G.; Ravi-Chandar, K. On the Constitutive Behaviour of Polycarbonate under Large Deformation. *Polymer* **1990**, *31*, 2071–2076, doi:10.1016/0032-3861(90)90078-D.
75. Neale, K.W.; Tuğcu, P. Analysis of Necking and Neck Propagation in Polymeric Materials†. *J. Mech. Phys. Solids* **1985**, *33*, 323–337, doi:10.1016/0022-5096(85)90032-8.
76. Hutchinson, J.W.; Neale, K.W. Neck Propagation. *J. Mech. Phys. Solids* **1983**, *31*, 405–426, doi:10.1016/0022-5096(83)90007-8.
77. Zhang, Z.L.; Hauge, M.; Ødegård, J.; Thaulow, C. Determining Material True Stress–Strain Curve from Tensile Specimens with Rectangular Cross-Section. *Int. J. Solids Struct.* **1999**, *36*, 3497–3516, doi:10.1016/S0020-7683(98)00153-X.
78. Mirone, G. A New Model for the Elastoplastic Characterization and the Stress–Strain Determination on the Necking Section of a Tensile Specimen. *Int. J. Solids Struct.* **2004**, *41*, 3545–3564, doi:10.1016/j.ijsolstr.2004.02.011.
79. Le Roy, G.; Embury, J.D.; Edwards, G.; Ashby, M.F. A Model of Ductile Fracture Based on the Nucleation and Growth of Voids. *Acta Metall.* **1981**, *29*, 1509–1522, doi:10.1016/0001-6160(81)90185-1.
80. Sarva, S.; Boyce, M. Mechanics of Polycarbonate during High-Rate Tension. *J. Mech. Mater. Struct.* **2007**, *2*, 1853–1880, doi:10.2140/jomms.2007.2.1853.

81. Mulliken, A.D.; Boyce, M.C. Mechanics of the Rate-Dependent Elastic–Plastic Deformation of Glassy Polymers from Low to High Strain Rates. *Int. J. Solids Struct.* **2006**, *43*, 1331–1356, doi:10.1016/j.ijsolstr.2005.04.016.
82. Richeton, J.; Ahzi, S.; Vecchio, K.S.; Jiang, F.C.; Makradi, A. Modeling and Validation of the Large Deformation Inelastic Response of Amorphous Polymers over a Wide Range of Temperatures and Strain Rates. *Int. J. Solids Struct.* **2007**, *44*, 7938–7954, doi:10.1016/j.ijsolstr.2007.05.018.
83. Bergstrom, J. Constitutive Modeling of the Large Strain Time-Dependent Behavior of Elastomers. *J. Mech. Phys. Solids* **1998**, *46*, 931–954, doi:10.1016/S0022-5096(97)00075-6.
84. Safari, K.H.; Zamani, J.; Ferreira, F.J.; Guedes, R.M. Constitutive Modeling of Polycarbonate during High Strain Rate Deformation. *Polym. Eng. Sci.* **2013**, *53*, 752–761, doi:10.1002/pen.23315.
85. Cao, K.; Ma, X.; Zhang, B.; Wang, Y.; Wang, Y. Tensile Behavior of Polycarbonate over a Wide Range of Strain Rates. *Mater. Sci. Eng. A* **2010**, *527*, 4056–4061, doi:10.1016/j.msea.2010.03.088.
86. Tzibula, S.; Lovinger, Z.; Rittel, D. Dynamic Tension of Ductile Polymers: Experimentation and Modelling. *Mech. Mater.* **2018**, *123*, 30–42, doi:10.1016/j.mechmat.2018.04.014.
87. Zhang, L.; Pellegrino, A.; Townsend, D.; Petrinic, N. Temperature Dependent Dynamic Strain Localization and Failure of Ductile Polymeric Rods under Large Deformation. *Int. J. Mech. Sci.* **2021**, *204*, 106563, doi:10.1016/j.ijmecsci.2021.106563.
88. Foster, M.; Love, B.; Kaste, R.; Moy, P. The Rate Dependent Tensile Response of Polycarbonate and Poly-Methylmethacrylate. *J. Dyn. Behav. Mater.* **2015**, *1*, 162–175, doi:10.1007/s40870-015-0020-8.
89. Mirone, G.; Barbagallo, R.; Bua, G. Experimental Characterization and Plastic Modeling of Polycarbonate at Static and Dynamic Rates. *Int. J. Impact Eng.* **2025**, *203*, 105329, doi:10.1016/j.ijimpeng.2025.105329.
90. Sato, Y.; Yoshida, M.; Nagayama, K.; Horie, Y. Stress–Strain Relationships of Polycarbonate over a Wide Range of Strain Rate, Including a Shock Wave Regime. *Int. J. Impact Eng.* **2008**, *35*, 1778–1783, doi:10.1016/j.ijimpeng.2008.07.045.
91. Xu, Y.; Gao, T.; Wang, J.; Zhang, W. Experimentation and Modeling of the Tension Behavior of Polycarbonate at High Strain Rates. *Polymers* **2016**, *8*, 63, doi:10.3390/polym8030063.
92. Bridgman, P.W. *Studies in Large Plastic Flow and Fracture*; With Special Emphasis on the Effects of Hydrostatic Pressure; Harvard University Press, 1964; ISBN 978-0-674-73134-9.
93. Siebel, E.; Schwaigerer, S. Zur Mechanik des Zugversuchs. *Arch. Für Eisenhüttenwes.* **1948**, *19*, 145–152, doi:10.1002/srin.194805749.
94. Barbagallo, R.; Mirone, G.; Landi, L.; Bua, G. Tensile Behavior of Polycarbonate: Key Aspects for Accurate Constitutive Modelling and Simulation. *Appl. Eng. Sci.* **2024**, *18*, 100183, doi:10.1016/j.apples.2024.100183.

95. Mirone, G.; Barbagallo, R.; Corallo, L. Combined Rate-Temperature Effects in Postnecking Plasticity of A2-70 Stainless Steel. *Int. J. Mech. Sci.* **2024**, *262*, 108754, doi:10.1016/j.ijmecsci.2023.108754.
96. G'Sell, C.; Hiver, J.M.; Dahoun, A.; Souahi, A. Video-Controlled Tensile Testing of Polymers and Metals beyond the Necking Point. *J. Mater. Sci.* **1992**, *27*, 5031–5039, doi:10.1007/BF01105270.
97. Mulliken A.D., Mechanics of Amorphous Polymers and Polymer Nanocomposites during High Rate Deformation, PhD Thesis, 2006.
98. Song, P.; Chapman, D.; Graham, A.; Trivedi, A.; Siviour, C.R. Thermomechanical Coupling during Large Strain Deformation of Polycarbonate: Experimental Study. *J. Mech. Phys. Solids* **2025**, *196*, 105976, doi:10.1016/j.jmps.2024.105976.
99. G'Sell, C.; Hiver, J.M.; Dahoun, A.; Souahi, A. Video-Controlled Tensile Testing of Polymers and Metals beyond the Necking Point. *J. Mater. Sci.* **1992**, *27*, 5031–5039, doi:10.1007/bf01105270.
100. Walley, S.M.; Proud, W.G.; Rae, P.J.; Field, J.E. Comparison of Two Methods of Measuring the Rapid Temperature Rises in Split Hopkinson Bar Specimens. *Rev. Sci. Instrum.* **2000**, *71*, 1766–1771, doi:10.1063/1.1150534.
101. Li, Z.; Lambros, J. Strain Rate Effects on the Thermomechanical Behavior of Polymers.
102. Shao, G.; Zhu, S.; Wang, Y.; Zhao, Q. An Internal State Variable Thermodynamic Model for Determining the Taylor-Quinney Coefficient of Glassy Polymers. *Int. J. Mech. Sci.* **2017**, *126*, 261–269, doi:10.1016/j.ijmecsci.2017.03.026.
103. Kapoor, R.; Nemat-Nasser, S. Determination of Temperature Rise during High Strain Rate Deformation. *Mech. Mater.* **1998**, *27*, 1–12, doi:10.1016/S0167-6636(97)00036-7.
104. Mirone, G.; Barbagallo, R.; Giudice, F. Locking of the Strain Rate Effect in Hopkinson Bar Testing of a Mild Steel. *Int. J. Impact Eng.* **2019**, *130*, 97–112, doi:10.1016/j.ijimpeng.2019.04.009.
105. Johnson, G.R.; Cook, W.H. A Constitutive Model And Data For Metals.
106. Madi, Y.; Garcia, J.-M.; Proudhon, H.; Shinohara, Y.; Helfen, L.; Besson, J.; Morgeneyer, T.F. On the Origin of the Anisotropic Damage of X100 Line Pipe Steel: Part I—In Situ Synchrotron Tomography Experiments. *Integrating Mater. Manuf. Innov.* **2019**, *8*, 570–596, doi:10.1007/s40192-019-00165-0.
107. Mirone, G.; Corallo, D. Stress–Strain and Ductile Fracture Characterization of an X100 Anisotropic Steel: Experiments and Modelling. *Eng. Fract. Mech.* **2013**, *102*, 118–145, doi:10.1016/j.engfracmech.2013.02.027.
108. Zhu, F.; Bai, P.; Zhang, J.; Lei, D.; He, X. Measurement of True Stress–Strain Curves and Evolution of Plastic Zone of Low Carbon Steel under Uniaxial Tension Using Digital Image Correlation. *Opt. Lasers Eng.* **2015**, *65*, 81–88, doi:10.1016/j.optlaseng.2014.06.013.

109. Sasso, M.; Rossi, M.; Chiappini, G.; Palmieri, G. Sheet Metals Testing with Combined Fringe Projection and Digital Image Correlation.
110. Zhang, Z.L.; Ødegård, J.; Søvik, O.P.; Thaulow, C. A Study on Determining True Stress–Strain Curve for Anisotropic Materials with Rectangular Tensile Bars. *Int. J. Solids Struct.* **2001**, *38*, 4489–4505, doi:10.1016/S0020-7683(00)00302-4.
111. Mirone, G.; Barbagallo, R.; Bua, G.; De Caro, D.; Ferrea, M.; Tedesco, M.M. A Simple Procedure for the Post-Necking Stress-Strain Curves of Anisotropic Sheet Metals. *Metals* **2023**, *13*, 1156, doi:10.3390/met13071156.
112. Mirone, G.; Barbagallo, R.; Bua, G.; Licignano, P.; Tedesco, M.M. An Enhanced Approach for High-Strain Plasticity in Flat Anisotropic Specimens with Progressively Distorting Neck Sections. *Metals* **2024**, *14*, 578, doi:10.3390/met14050578.

Appendix

Fortran Subroutine for the implementation of the Modified Tresca Damage Model

```
% Calling of the variables from FEM results

      subroutine plotv(v,s,sp,etot,eplas,ecreep,t,m,nn,kcus,ndi,
     * nshear,jpltcd)

     implicit real*8(a-h,o-z)
     integer jpltcd, kcus, m, ndi, nn, nshear
     dimension s(*),etot(*),eplas(*),ecreep(*),sp(*),m(2),kcus(2),
     *   t(*),princ_stresses(3),var_array(3)

      parameter ne=16176, ng=8, dd=3

      include 'concom'
      common/comdata/vet(ne,ng,14)

      ICODE=27                          !!!total equivalent plastic strain
           call elmvar(icode,m(1),nn,kcus,var)
           eeq=var

      ICODE=17                          !!!sigma equivalent
           call elmvar(icode,m(1),nn,kcus,var)
           seq=VAR

      ICODE=18                          !!! sigma hydrostatic
           call elmvar(icode,m(1),nn,kcus,var)
           sh=VAR

      ICODE=318                          !!! Principal values of stress tensors
           call elmvar(icode,m(1),nn,kcus,var_array)
           princ_stresses=var_array


% Modified Tresca Damage Model


      princ_MAX=maxval(princ_stresses)
      princ_MIN=minval(princ_stresses)
      princ_MEAN=3*sh - princ_MAX - princ_MIN
      OMT_tau_cr=43.5
      OMT_ni=-0.275

      if (inc==0.) then
```

```
        OMT_D=0.
!        OMT_old=0.
          else
              OMT_D=(abs(princ_MAX-princ_MIN)/2. - OMT_ni*sh)/OMT_tau_cr
    endif


    if (OMT_D>=vet(m(1),nn,6)) then
        vet(m(1),nn,6)=OMT_D
    else
        OMT_D=vet(m(1),nn,6)
    endif


% Variables in output


    vet(m(1),nn,1)=eeq                ! total equivalent plastic strain
    vet(m(1),nn,2)=princ_MAX          ! maximum principal stress
    vet(m(1),nn,3)=princ_MIN          ! minimum principal stress
    vet(m(1),nn,4)=princ_MEAN         ! mean principal stress
    vet(m(1),nn,5)=sh                 ! hydrostatic stress
    vet(m(1),nn,6)=OMT_D              ! damage


    if(jpltcd.eq.1)v=vet(m(1),nn,2)  !  Max princ
    if(jpltcd.eq.2)v=vet(m(1),nn,3)  !  Min princ
    if(jpltcd.eq.3)v=vet(m(1),nn,4)  !  Mean princ
    if(jpltcd.eq.4)v=vet(m(1),nn,5)  !  sh
    if(jpltcd.eq.5)v=vet(m(1),nn,6)  !  OMT_D
    if(jpltcd.eq.6)v=vet(m(1),nn,7)  !  OMT_D

    return
    end
```

Marc Mentat uyield_surface user subroutine for the implementation of the PC-DATS model

```
      subroutine uyield_surface (yiel,m,nn,kcus,yld,temp,eplas,erate,
     %                           mats,jprops)
% The subroutine takes in input the element's ID, the node's ID, temperature at each node, the plastic strain, and the plastic strain rate
      implicit real*8 (a-h,o-z)
      integer, intent(in) :: m,nn,kcus(2),mats,jprops
      real*8, intent(in) :: yld, temp, eplas, erate
      real*8, intent(inout) :: yiel
% In these lines, I reported the parameters for the static flow curve, the thermal softening function, and the dynamic amplification function
      parameter ne=3000, ng=4, p=0.175, q=0.045, er=100, f=0.000205,
     % g=1.316, a=98.21, b=27.14, c=1.967, h=1.976, n=1.326
% Definition of the static flow curve at room temperature
      strue=48.5*(1+a*(eplas**n)*exp(-b*eplas))*exp(c*eplas**h)
% Definition of the dynamic amplification function
     if(erate<=er) then
       R=(1+erate/p)**q
        else
       R=g+f*erate
        endif
      if(eplas>=0.15)then
       R=Rmax   %Rmax depends on the maximum strain rate reached during the test. Taken from the experimental data
      endif
% Definition of the thermal softening function (approximated at its asymptotic function)
```

```
    S=1.1783-0.0068*temp
% PC Flow Stress
    yiel=strue*R*S
    return
    end
```

Acknowledgments

I wish to dedicate this Doctoral thesis, which marks the completion of my studies, to my parents and to Simona for their precious support and love.

A special thank goes to my second family of the University of Catania: the Machine Design Research Group; to Professor Giuseppe Mirone, an excellent supervisor and teacher; to Professor Raffaele Barbagallo, a great friend and colleague; and to Mr. Rosario Mazza, the affectionate technician of the Mechanics laboratory.

I also thank another special group of people, great researchers and scientists, who hosted and welcomed me at the University of Freiburg, Germany: the INATECH Research Group, led by Professor Stefan Hiermaier and Dr. Georg Ganzenmuller.

I thank ST Microelectronics and the engineers of the R&D Automotive and Discrete Group: Prof. Michele Calabretta and Dr. Alessandro Sitta, for funding my Doctoral research and for supporting me in the work related to the mechanical modeling of power modules.

I thank everyone who has been part of my academic journey and beyond, without whom I would not be who I am today.